

8-8-2013

Siloles Bearing Coordination-Active 2,5-Substituents: Synthesis, Reactivity, Structural and Spectral Properties.

James Bryan Carroll

University of Missouri-St. Louis, jbc6wc@mail.umsl.edu

Follow this and additional works at: <https://irl.umsl.edu/dissertation>

 Part of the [Chemistry Commons](#)

Recommended Citation

Carroll, James Bryan, "Siloles Bearing Coordination-Active 2,5-Substituents: Synthesis, Reactivity, Structural and Spectral Properties." (2013). *Dissertations*. 285.

<https://irl.umsl.edu/dissertation/285>

This Dissertation is brought to you for free and open access by the UMSL Graduate Works at IRL @ UMSL. It has been accepted for inclusion in Dissertations by an authorized administrator of IRL @ UMSL. For more information, please contact marvinh@umsl.edu.

**Siloles Bearing Coordination-Active 2,5-Substituents: Synthesis, Reactivity,
Structural and Spectral Properties.**

By

James B. Carroll II

A dissertation submitted in partial fulfillment of the requirements for the degree of
Doctor of Philosophy (Chemistry)

University of Missouri – St. Louis

August 2013

II

This is dedicated to my parents, my partner Holly Pope, and all of my family and friends. Your love, encouragement, and support have encouraged me and have kept me going through all my years of learning; the culmination thereof, represented as this document, would have been impossible without you.

To many more years of learning!

Acknowledgements

I would like to acknowledge here the people who have contributed graciously to the completion of my project and my development as a chemist. I would first like to thank Dr. Janet Braddock-Wilking for her advisement both during my undergraduate and graduate schooling. Through your willingness to help me during my projects when I needed it, and allowing me to work out some of my projects on my own, I now have invaluable experience in designing projects, as well as investigating how to better execute those projects through rigorous analyses; these skills will greatly benefit me through my future endeavors. Moreover, through your friendliness and ease of communication, I could count on you as both an advisor, and a friend.

My gratitude goes to my committee for the helpful comments: Dr. Eike Bauer, Dr. Wes Harris, and Dr. Nigam Rath. In particular, Dr. Harris helped me to elucidate a plausible mechanism for metal binding on one of my compounds, and Dr. Rath graciously assisted me in learning many aspects of X-ray crystallography.

I would like to thank the following for contributing to my research: Dr. Nigam Rath, Dr. Rensheng Luo, Dr. Rudolph E.K. Winter, Joe Kramer, David Osborn, and Dan Zhou. I also would like to thank the faculty and staff of the Department of Chemistry and Biochemistry for being so helpful and student-oriented; it was the main reason why I chose to continue on into graduate education. I will forever cherish the education and personal support I have received from you.

Finally, I would like to thank my family, friends, and my partner Holly Pope, for their love, encouragement, and support, all of which providing me the motivation to succeed and realize my doctoral degree.

Table of Contents

Acknowledgements.....	III
Table of Contents.....	IV
List of Abbreviations.....	X
Table of Figures.....	XII
Chapter 1 Figures.....	XII
Chapter 2 Figures.....	XIII
Chapter 3 Figures.....	XV
Chapter 5 Figures (See Chapter).....	XVII
Chapter 6 Figures.....	XVIII
Table of Schemes.....	XVIII
Chapter 1 Schemes.....	XVIII
Chapter 2 Schemes.....	XIX
Chapter 3 Schemes.....	XIX
Chapter 6 Schemes.....	XIX
Table of Equations.....	XX
Chapter 2 Equations.....	XX
Chapter 3 Equations.....	XX
Table of Tables.....	XXI
Chapter 1 Tables.....	XXI

Chapter 2 Tables	XXI
Chapter 3 Tables	XXI
Chapter 5 Tables (See Chapter).....	XXII
Abstract.....	XXIII
Chapter 1. Introduction.....	1
1.1. Synthetic Overview of group 14 metalloles, including siloles.	2
1.1.1. Early synthesis of siloles and other metalloles.	2
1.1.2. Synthesis of siloles and precursors from metallacycle intermediates.	4
1.1.3. The Tamao procedure for synthesis of 2,5-aryl-3,4-diphenylsiloles.	5
1.2. The optoelectronics of siloles, and the effect of substitution thereon.	7
1.2.1. Substituents at the 1,1-position.....	10
1.2.2. Substituents at the 3,4-position.....	11
1.2.3. Substituents at the 2,5-position.....	13
1.3. Overview of siloles and their coordination to metal centers.	15
1.3.1. Siloles and group 14 metalloles as cyclopentadienyl analogues.	15
1.3.2. Platinum centers covalently bound to the 2,5-position of silole.....	17
1.3.3. Metal coordination to 2,5-substituents.	18
1.4. Overview of the photoinduced charge-transfer effect (PCT).	21
1.5. Statement of the problem.....	24
1.6. References.....	25

Chapter 2. Results and Discussion – 1,1-disubstituted germoles and germole-like compounds: Structural Characterization and Aggregation-Induced Emission.....	28
2.1. General Introduction.....	28
2.2. Synthesis and spectral characterization of germoles and their precursors.	30
2.2.1 Generation of lithiated compounds for synthesis of germoles.	30
2.2.2. Synthesis and characterization of 1,1-dichloro-2,3,4,5-tetraphenylgermole, G1.....	33
2.2.3. Synthesis of 1,1-disubstituted-2,3,4,5-tetraphenylgermoles.....	35
2.2.4. Preliminary study of coordination of G4 with (COD)PtCl ₂	38
2.3. SEM study on the effect of cooling a melt on crystallinity and optical properties.....	40
2.4. X-ray crystallography of 2,3,4,5-tetraphenyl-1,1-disubstituted germoles.....	44
2.4.1. General comments on molecular structures.....	44
2.4.2. Packing arrangements of the tetraphenylgermoles.	49
2.5. X-ray crystallography of differently substituted germafluorenes.....	53
2.5.1. General comments on molecular structures.....	53
2.5.2. Packing arrangement of the germafluorenes studied.....	56
2.6. Summary.....	61
2.7. References.....	62
Chapter 3. Results and Discussion – Siloles with 2,5-substituents have coordinative ability, and their interactions with metal cations	64

VII

3.1. General Introduction.....	64
3.2. Synthesis and Characterization of Symmetrical 2,5-Substituted Siloles.....	66
3.2.1. Difficulties with the Tamao procedure and characterization of byproducts	67
3.2.2. Synthesis and General Comments.....	74
3.2.3. Characterization of the siloles by NMR spectroscopy.....	77
3.2.4. Characterization of the siloles by optical spectra.....	79
3.2.5. X-ray crystallography of symmetric siloles.....	81
3.3. Attempted preparation of α -quinolate substituted 2,5-tolylsilole.....	84
3.4. Synthesis of unsymmetric silole precursors and attempted preparation of asymmetric siloles.....	89
3.5. Study of interactions of S1-S4 with Ni(II), Cu(II), and Hg(II) ions.....	97
3.5.1. UV-vis and fluorescence studies. ¹⁵	98
3.5.2. Spectrophotometric titration study of S3 with Hg(II).....	104
3.6. Preliminary calculations of S3 with varying stoichiometries of metal coordination.....	112
3.7. Summary.....	115
3.8. References.....	117
Chapter 4. Experimental Section.....	120
4.1. Synthesis and reactivity of several 1,1-disubstituted germales.....	123
4.2. Synthesis of symmetrical 2,5 substituted siloles.....	127

VIII

4.2.1. Synthesis of precursors and starting materials to symmetrical 2,5 substituted siloles.....	127
4.2.2. Synthesis of some symmetric siloles.....	128
4.3. Synthesis of unsymmetrical silole precursors.....	135
4.4. References.....	139
Chapter 5. Appendices.....	141
Table of Figures.....	141
Table of Tables.....	149
5.1. NMR Spectra of compounds.....	149
5.1.1. NMR spectra of several 1,1-disubstituted germales.....	149
5.1.2. NMR spectra of symmetrical silole precursors.....	162
5.1.3. NMR spectra of symmetrical siloles.....	166
5.1.4. NMR spectra of unsymmetrical silole precursors.....	180
5.2. MS Spectra and Chromatograms of compounds.....	188
5.2.1. MS of symmetrical siloles.....	188
5.2.2. MS of unsymmetrical siloles and precursors.....	195
5.3. X-ray crystal structures of compounds.....	198
5.3.1. X-ray crystallography of 2,3,4,5-tetraphenyl-1,1-disubstituted-germales.....	198
5.3.2 X-ray crystallography of differently substituted germafluorenes.....	212
5.3.3. X-ray crystallography of symmetric 2,5-substituted siloles.....	217

5.4. UV-vis and fluorescence spectra with Ni(II), Cu(II), and Hg(II).....	221
5.4.1. Interactions of metal salts with the siloles listed.	221
5.4.2. Titration spectra and related calculations.	233
Chapter 6. Addendum: Platinum and Palladium complexes for use as Precursors for M-Sn nanoparticles.	242
6.1. Background.....	242
6.2. Insertion of tin chloride into a platinum or palladium-chloride bond	243
6.2.1. Introduction.....	243
6.2.2. Synthetic efforts with tin(II) chloride insertion.	243
6.2.3. Summary.....	248
6.3. Attempted preparation of platinum-tin halide clusters.	248
6.3.1. Introduction.....	248
6.3.2. Attempted synthesis of a platinum tin cluster.....	249
6.3.3. Summary.....	251

List of Abbreviations

Abs	absorbance or absorption
acac	acetylacetonate
ACQ	Aggregation-caused Quenching
addn	addition
AIE	Aggregation-induced Emission
B3LYP	Becke, three-parameter, Lee-Yang-Parr (an exchange correlation functional in computational chemistry)
BHT	butylated hydroxytoluene
Bu	butyl
CCD	charge-coupled device
CFL	Compact Fluorescent Light bulb
COD	1,5-cyclooctadiene
Cp	cyclopentadienyl-
Cp*	pentamethylcyclopentadienyl
CSD	Cambridge Structural Database
cycl	cyclization
DEPT	Distortionless Enhancement by Polarization Transfer
DFT	density functional theory
DIPA	diisopropylamine
dppf	1,1'-(diphenylphosphino)ferrocene
Et	ethyl
eV	electron-volt
Fl	fluorescence
GC-MS	Gas Chromatography-Mass Spectrometry
HOMO	Highest Occupied Molecular Orbital
incomp	incomplete
iPr	isopropyl
LiNaphth	lithium naphthalenide
λ_{\max}	wavelength of maximum absorption/emission

XI

LUMO	lowest unoccupied molecular orbital
Me	Methyl
MeOH	Methanol
N ₂ O/O ₂ N	nitro- substituent
NBS	<i>N</i> -bromosuccinimide
NCP	<i>N</i> -chlorophthalimide
nm	nanometer
NMR	Nuclear Magnetic Resonance
OFET	Organic Field-Effect Transistor
OLED	Organic Light Emitting Diode
OTf	trifluoromethanesulfonate, or triflate
PCT	Photoinduced Charge Transfer
Ph	Phenyl
PM3	Parameterized Model number 3, a semi-empirical method in computational chemistry
rt	room temperature
SEM	Scanning Electron Microscopy
THF	tetrahydrofuran
TMEDA	<i>N,N,N',N'</i> -tetramethylethylenediamine
TPS	1,1-dimethyl-2,3,4,5-tetraphenylsilole
UV-vis	UV-visible spectroscopy
XRD	X-ray Diffraction

Table of Figures

Chapter 1 Figures

Figure 1-1. The general structure of a) silole, and b) cyclopentadiene. The general substituents, denoted by “R”, are subscripted by the positional numeration typically employed for siloles.....	2
Figure 1-2. A qualitative drawing of the HOMO-LUMO portion of the molecular overlap of the silylene and butadiene portions of the silole ring, along with orbital phases and their symmetries; this shows the stabilizing effect that the silylene has on the LUMO (The figure is an adaptation from Ref. 18)	8
Figure 1-3. The siloles synthesized by Marder’s group to determine the effect of conjugation of substituents at the 3,4-position. ²⁷	11
Figure 1-4. The siloles investigated theoretically by Yin <i>et al.</i> ²⁹	12
Figure 1-5. The comparison of the degree of conjugation of the 2,5-substituents, and its effect on the optical spectra obtained. ¹⁷	13
Figure 1-6. Comparison of the phenyl substituent to the naphthyl substituent, the latter showing a hypsochromic shift due to the increased dihedral angle. ¹⁷	14
Figure 1-7. The effect of strong π -donors and acceptors on the optical spectra of siloles. ¹⁷	14
Figure 1-8. The a) poly(platinayne) polymer and b) its monomeric analogue. ³⁷	17
Figure 1-9. The siloles studied by Wang’s group. ³⁸	19
Figure 1-10. Some of the phosphine-linked siloles synthesized by our group. For siloles A-E, the phosphine oxide was also synthesized. ⁴⁰	19

Figure 1-11. The terpyridine siloles synthesized by Tang's group. Compound A showed good selective fluorescence enhancement in the presence of zinc(II). ⁴¹	20
Figure 1-12. A schematic representation of a donor-acceptor fluorophore undergoing photoinduced-charge transfer upon excitation. ⁴²	22
Figure 1-13. A representation of the effects of cation binding to the "donor" or "acceptor" moieties of the fluorophore. Also included in the figure are a summary of the effects observed in each situation. ⁴³	23
Figure 1-14. The structure of the calcium detection fluorophore Indo-1, which shows hypsochromic shifts in optical spectra upon binding, a hallmark of the PCT effect.	24
Chapter 2 Figures	
Figure 2-1. General structure for a group 14 metallole.	28
Figure 2-2. A crystal structure of 1-methyl-1,2,3,4,5-pentaphenylsilole, which shows the arrangement of the substituents preventing parallel orientation of the π -system intermolecularly.	30
Figure 2-3. Example of the plots used to estimate completion time of the reaction to synthesize L1.	32
Figure 2-4. Germales synthesized for this study.	35
Figure 2-5. Expanded $^{13}\text{C}\{^1\text{H}\}$ NMR spectrum of G4 demonstrating the ^{31}P - ^{13}C coupling; shifts are assigned to the ethynyl carbons on G4.	37
Figure 2-6. The reaction of (COD)PtCl ₂ with G4.	39
Figure 2-7. The proposed geometry and composition of the product of G4 and (COD)PtCl ₂ , based on $^{31}\text{P}\{^1\text{H}\}$ data.	40

Figure 2-8. Normalized fluorescence spectra of G2 after two different cooling modes from a melt of a thin film, and an additional thin film were no heating was performed. . 41

Figure 2-9. Sample 1 at magnifications of a) 25X and b) 250X. Images acquired using an acceleration voltage of 15 kV, a working distance of 15 mm, a probe current setting of #3, an aperture setting of #3, and using the lower SE detector..... 42

Figure 2-10. Sample 2 at magnifications of a) 250X and b) 5000X. Images acquired using an acceleration voltage of 15 kV, a working distance of 15 mm, a probe current setting of #3, an aperture setting of #3, and using the lower SE detector..... 42

Figure 2-11. Sample 3 at magnifications of a) 250X and b) 7500X. Images acquired using a) an acceleration voltage of 15 kV, a working distance of 15 mm, a probe current setting of #3, an aperture setting of #3, and using the lower SE detector; b) an acceleration voltage of 15 kV, a working distance of 8 mm, a probe current setting of #3, an aperture setting of #3, and using the upper SE detector..... 43

Figure 2-12. The additional tetraphenylgermoles studied crystallographically. 44

Figure 2-13. The structure of G2, with the perspective a) perpendicular to the germole ring, and b) parallel to the germole ring, the latter of which demonstrates the propeller-like arrangement of the 2,3,4,5- phenyl substituents. Hydrogens have been removed for clarity..... 50

Figure 2-14. The structure of G14, with the perspective a) perpendicular to the germole ring, and b) parallel to the germole ring, the latter of which demonstrates the unique opposing arrangement of the 2,3,4,5- phenyl substituents. Hydrogens have been removed for clarity..... 51

Figure 2-15. The extended packing for the G8 lattice, which shows minimal parallel interactions between aryl groups, which limits π - π interactions in the solid state (a main requirement for ACQ).....	52
Figure 2-16. The closest aryl group interaction in G2. The non-parallel arrangement indicates any π -interactions are weak, if not non-existent (some measurements are included in the Figure).....	53
Figure 2-17. The fundamental structure of germafluorene, as analogous to the all-carbon analogue, fluorene.....	54
Figure 2-18. The germafluorenes that were determined by X-ray crystallography for this study.....	54
Figure 2-19. Two views, a) perpendicular to the germafluorene core and b) parallel to the germafluorene core, of the closest packing arrangement between two molecules of G16 in the crystal lattice. Hydrogens are removed for clarity.....	57
Figure 2-20. A depiction of G16, enlarged to show the additional potential π -interaction site. Hydrogens are removed for clarity, and a line indicating the distance measured is included.....	58
Figure 2-21. Two views, a) perpendicular to the germafluorene core and b) parallel to the germafluorene core, of the closest packing arrangement between two molecules of G17 in the crystal lattice. Hydrogens are removed for clarity.....	59
Figure 2-22. The packing arrangement of G18 in the crystal lattice.....	60
Chapter 3 Figures	
Figure 3-1. Two of the siloles synthesized by Tamao, along with their optical λ_{max} values, demonstrating the range of values obtained. ²	64

Figure 3-2. The bipyridyl amine substituted silole that was studied by Wang and Gerbier. ^{4,5}	65
Figure 3-3. Molecular structure of S6.....	68
Figure 3-4. Expanded Si-Me region of a crude ¹ H NMR of S6.	69
Figure 3-5. The a) crystal structure of the hydrolyzed silole byproduct, and b) the molecular drawing thereof. Hydrogens are removed except for the vinyl, amine, and silanol positions.	71
Figure 3-6. The siloles synthesized and fully characterized for study.	75
Figure 3-7. A selected portion of S2 that shows potential C-H/ π interactions.....	82
Figure 3-8. The crystal structures of a) S1, b) S2, and c) S5. Selected measurements for each compound are given in section 5.3.3 in the Appendix.....	83
Figure 3-9. A stacked ¹ H NMR spectrum comparing the silole S5 with the product generated from reaction with BBr ₃ . The assigned structure of this product (D) is inset.	87
Figure 3-10. Some desired unsymmetric silole targets, with potential to bind to metal centers.	90
Figure 3-11. The terminal alkynes synthesized for initial study.	93
Figure 3-12. The optical spectra of S1-S4 and the mixtures with 10 equiv of the metal perchlorate; the color correspondence is: mercury(II) (red), copper(II) (blue), nickel(II) (green), pure silole (black). a) The UV-Vis (dashed) and fluorescence (solid) spectra of S1 with metal solutions. b) The UV-Vis (dashed) and fluorescence (solid) spectra of S2 with metal solutions. c) The UV-Vis spectra of S3 with metal solutions. d) The fluorescence spectra of S3 with metal solutions. e) The UV-Vis (dashed) and fluorescence (solid) spectra of S4 with metal solutions. The wavelengths for	

fluorescence excitation are: 365 nm (S1), 390 nm (S2), 415 nm (S3), and 383 nm (S4).	100
Figure 3-13. Compound S3 (5×10^{-5} M in dichloromethane) with 1-10 equiv of copper(II) perchlorate solution (in methanol).....	101
Figure 3-14. Selected titration data of a solution of S3 in THF (6×10^{-5} M), titrated with 1.3×10^{-2} M mercury(II) perchlorate solution in THF. The values in parentheses in the legend represent the equivalencies of mercury(II) in solution.....	102
Figure 3-15. The absorbance versus mercury(II) concentration, along with the 1:1 and 2:1 Hg(II):S3 fit curves, for the titration in dichloromethane/methanol. Statistical data is provided Figure A-93 after in the appendix (Section 5.4.2).....	105
Figure 3-16. The titration data extract from the raw data (Figure A-94) at 503 nm. The total $[\text{Hg}^{2+}]$ was calculated from the initial volume of S3 (3 mL), plus the volume added by the titrant (i.e., Hg(II) perchlorate in THF). The fit curves for one-cation and two-cation binding are displayed, along with their R^2 values in the legend.	108
Figure 3-17. The titration data extract from the raw data (Figure A-94) at 355 nm. The total $[\text{Hg}^{2+}]$ was calculated from the initial volume of S3 (3 mL), plus the volume added by the titrant (i.e., Hg(II) perchlorate in THF).	109
Figure 3-18. The plot of absorbance versus the concentration of Hg(II), after subtracting 4×10^{-4} M to account for the previously coordinated Hg(II) (see text).....	110
Chapter 5 Figures (See Chapter)	

Chapter 6 Figures

Figure 6-1. The hydride region of the product of <i>trans</i> -(Ph ₃ P) ₂ Pt(H)Cl and tin(II) chloride. The structure and coupling constants are inset.	245
Figure 6-2. ¹⁹ F{ ¹ H} NMR spectrum of (FMes)Pd(COD)Cl.....	247
Figure 6-3. The ¹¹⁹ Sn{ ¹ H} NMR spectrum of the crystalline species obtained from the reaction mixture reported in this section.....	250

Table of Schemes**Chapter 1 Schemes**

Scheme 1-1. The synthetic route employed for most early siloles, germales, and other main-group metalloces. ^{6,7,8}	2
Scheme 1-2. Synthesis of metalloces from dihalobutadienes.	4
Scheme 1-3. The synthesis of dihalobutadiene precursors via a titanacycle intermediate. ¹¹	4
Scheme 1-4. The synthesis of dihalobutadiene precursors via a zirconacycle intermediate. ^{12,13}	5
Scheme 1-5. The mechanism proposed for the formation of the silole through reductive cyclization. ¹⁵	6
Scheme 1-6. The Tamao synthesis, using ZnCl ₂ (TMEDA) and cross-coupling under Negishi conditions. ¹⁷	6
Scheme 1-7. The reaction of a several siloles with iron carbonyl to generate the η ⁴ -complex. ³¹	15
Scheme 1-8. The synthesis of the bis(η ⁴ -silolyl)nickel complex reported by Carré <i>et al.</i> ³²	16

Scheme 1-9. The synthesis of the first η^5 -coordinated silole complex..... 16

Chapter 2 Schemes

Scheme 2-1. Attempted routes to coupling G5 with (4-bromophenyl)-
diphenylphosphine..... 36

Chapter 3 Schemes

Scheme 3-1. The attempted preparation routes for C from pre-formed siloles S5 and
S6..... 84

Scheme 3-2. The synthetic route for unsymmetric donor-acceptor siloles.³³ 89

Scheme 3-3. The synthesis of the terminal alkynes used for study. 94

Scheme 3-4. A representation of the metal binding sites as suggested through the
spectrophotometric titration studies..... 111

Chapter 6 Schemes

Scheme 6-1. The complex synthesized for preliminary thermolysis studies..... 242

Scheme 6-2. The mechanism of insertion of tin(II) chloride into the Pt-Cl bond.⁵ 243

Scheme 6-3. Our planned reaction sequence upon isolation of a trichlorostannyl-
platinum complex..... 244

Scheme 6-4. The balanced redox reaction of platinum(II) chloride and tin(II)
chloride to form the triplatinum-tin cluster.¹⁰ 249

Table of Equations

Chapter 2 Equations

Equation 2-1. Synthesis of the key dilithiobutadiene intermediate L1.....	31
Equation 2-2. Isomerization of the desired precursor yields the unwanted naphthalene compound.	31
Equation 2-3. Synthesis of G1.....	33
Equation 2-4. General route for the synthesis of the 1,1-disubstituted germoles in this study.....	35

Chapter 3 Equations

Equation 3-1. Tamao's synthesis of 2,5-substituted siloles. ²	66
Equation 3-2. The mechanism for the intramolecular cyclization of dimethylbis(phenylethynyl)silane by lithium naphthalenide. ²	66
Equation 3-3. The proposed route for formation of the "partially reduced" silane. ..	70
Equation 3-4. The route proposed for the hydrolyzed product with an m/z of 280. .	71
Equation 3-5. Proposed reaction route for formation of the "partially coupled" species, with a molecular weight of 352 amu.	72
Equation 3-6. The synthesis of SP2.....	88

Table of Tables

Chapter 1 Tables

Table 1-1. The calculated probability density, energies, and bandgaps between the HOMO and LUMO orbitals for 1,1-dimethyl-2,3,4,5-tetraphenylsilole and -cyclopentadiene. The geometry was minimized using semi-empirical methods (PM3), while the energy was minimized using DFT calculations (B3LYP/6-31G*). Wavefunction Spartan '04 computational chemistry software was used for these calculations. 9

Chapter 2 Tables

Table 2-1. Optical data for germoles G2 to G4. 38

Chapter 3 Tables

Table 3-1. Selected ^1H and $^{13}\text{C}\{^1\text{H}\}$ NMR data and assignments, and literature values for known siloles..... 78

Table 3-2. UV-visible and fluorescence spectral data for the reported compounds.^a ^aSpectral data from siloles in a 1:1 mixture of $\text{CH}_2\text{Cl}_2/\text{MeOH}$, 5×10^{-5} M. ^bWith reference to 9,10-diphenylanthracene. ^cWith reference to fluorescein. ^dLiterature values are listed in parentheses, see Ref. 2. ^eLiterature values are listed in parentheses, see Ref. 14a. ^fLiterature values are listed in parentheses, see Ref. 14c. 79

Table 3-3. Conditions used to attempt the conversion of siloles S5 or S6 into the α -bromotolylsilole B (Scheme 3-1). References for the procedures are listed in the Table. 85

Table 3-4. The probability densities of the HOMO and LUMO orbitals for S3, S3+2Cu, and S3+3Cu. Calculation details are outlined in the text. Hydrogen atoms have been omitted for clarity. 113

Chapter 5 Tables (See Chapter)

Abstract

Siloles, or silacyclopentadienes and other group 14 metalloles are structurally analogous to their all-carbon analogue, cyclopentadiene, except for the heavy group 14 element (i.e., Si, Ge, Sn, and Pb) in the 1-position. The placement of the heavy element in this position allows for unique properties, such as high electron affinity, mobility, and bathochromically shifted optical spectra, as compared to cyclopentadienes, and the relatively low-lying lowest-unoccupied molecular orbital (LUMO) helps to account for these properties. The substituents about the silole have a significant impact on the electronics and properties observed, with 2,5-substituents inducing the most substantive changes. Even as many 2,5-substituents are known, and could possess potential to bind to metal cations, very few reports to date have studied metal binding effects on the optoelectronics of siloles.

The goal of this investigation is to synthesize siloles with 2,5-substituents that could potentially coordinate metal centers, and study the optical changes upon addition of metal solutions. Several symmetric 2,5-substituted siloles were synthesized and characterized by various means, and showed modest to significant changes upon addition of metal centers. The most significant changes were observed with a *p*-dimethylaminophenyl substituted silole. The binding of this silole was studied in further detail through spectrophotometric titration, which suggested two binding events occurring at different locations on the silole. These studies also reveal the binding constant of the second, weaker binding event. The results of the studies suggest an appropriate explanation from the phenomenon of photoinduced-charge transfer, to which metal cations can significantly interfere, and helps to explain the changes in the spectral data observed.

Additionally, the crystal structures of a series of germales and germafluorenes have been acquired, and their packing affects with respect to potential for aggregation-induced emission studies are explored. The attempted synthesis of siloles with potential for “off-on” fluorescent behavior upon exposure to metals, as well as asymmetric 2,5-substituted siloles with coordinative ability, are also addressed, and briefly discussed.

Chapter 1. Introduction

Siloles, or 1-silacyclopentadienes, are a class of fluorescent molecules that have received significant interest.¹ They are related to the all-carbon analogue, cyclopentadiene, and the general structure is provided in Figure 1-1. Though typically the 2,5- and 3,4-substituents are equivalent, up to all of the substitutions can be inequivalent; however, inequivalent 1,1-positions are more common due to the relatively facile adjustment of precursors compared to the other positions. Because of their unique electronics, siloles closely related cyclic organosilicon species have found in diverse applications such as organic field-effect transistors (OFETs),² organic light-emitting diodes,³ photovoltaics,⁴ and sensors.⁵ This chapter gives a general synthetic history of siloles, a discussion of the unique optoelectronic phenomena of siloles compared to the all-carbon analogues, and finally an overview of siloles and their coordination to metal ions; the latter subject concerns the research object of this manuscript. Included in the discussion of metal coordination with siloles is an overview of the concept of photoinduced-charge transfer (PCT), which is important for explaining some of the changes in optical spectral properties of siloles upon interaction with metal centers (Chapter 3).

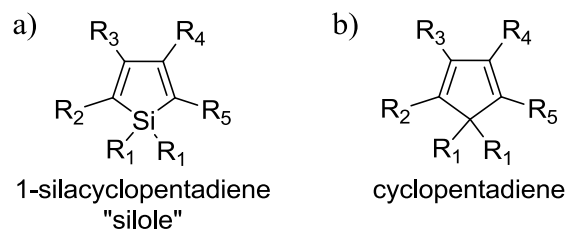


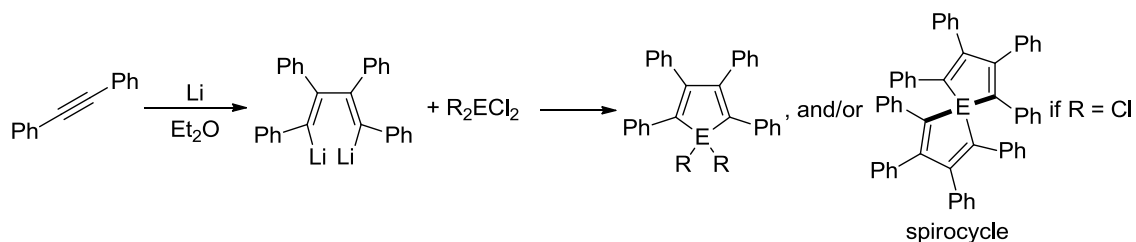
Figure 1-1. The general structure of a) silole, and b) cyclopentadiene. The general substituents, denoted by “R”, are subscripted by the positional numeration typically employed for siloles.

1.1. Synthetic Overview of group 14 metalloles, including siloles.

Corey gives a comprehensive overview of the synthesis of siloles;^{1c} some of the more common reactions for synthesizing siloles, related metalloles, and important precursors are addressed briefly in this section.

1.1.1. Early synthesis of siloles and other metalloles.

Main group-containing metalloles were first synthesized by Leavitt *et al.* in 1959,⁶ with the first silole being synthesized by Braye and Hübel one year later.⁷ A decade later, Curtis synthesized a series of siloles and analogous germoles using a similar synthetic protocol,⁸ which is described in Scheme 1-1, and is sometimes referred to as “the Curtis method”.^{1c}

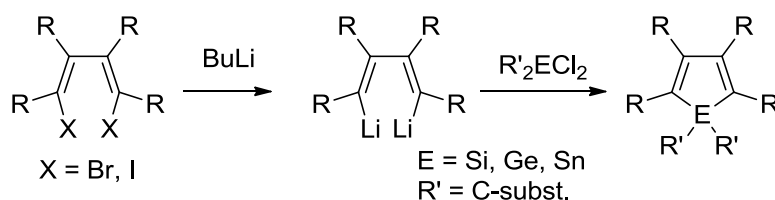


Scheme 1-1. The synthetic route employed for most early siloles, germoles, and other main-group metalloles.^{6,7,8}

All of these early syntheses, as shown above, used the same lithiated species, 1,4-dithio-1,2,3,4-tetraphenyl-1,3-butadiene, reacted with a dichlorometallane species in a salt-metathesis reaction to generate the desired metalloles. If the metallane is substituted with four chlorides, as were some of the reagents used in the above studies, then the spirocycle could be formed, and could be the major product if the metallane was added to the dilithiobutadiene solution. Curtis was able to minimize the amount of spirogermole formed by modifying the procedure to add the dilithiospecies into a diethyl ether solution of germanium tetrachloride,⁸ reversing the addition that prior researchers had used. The 1,1-dichlorogermole formed precipitates in diethyl ether, preventing its subsequent reaction with additional dilithiobutadiene to form the spirocycle. The related 1,1-dichlorosilole would not be reported until much later,⁹ as it would generally continue to react with the dilithiobutadiene under standard addition procedures, forming the spirocycle. Special modifications are necessary to successfully synthesize the 1,1-dichlorosilole from this route; for example, adding silicon tetrachloride to a frozen matrix of the dilithiobutadiene in diethyl ether, followed by slowly warming to room temperature, allowed the silicon tetrachloride to have slow access to the dilithiobutadiene, allowing for successful synthesis of the 1,1-dichlorosilole.¹⁰ Additionally, it is noted here that the procedure to make the dilithiobutadiene precursor requires special considerations for optimizing reaction yields; these are addressed in Section 2.2.1; Chapter 2 includes synthesis of 1,1-dialkynylgermoles, of which the precursor reported by Curtis, 1,1-dichloro-2,3,4,5-tetraphenylgermole,⁸ is used extensively.

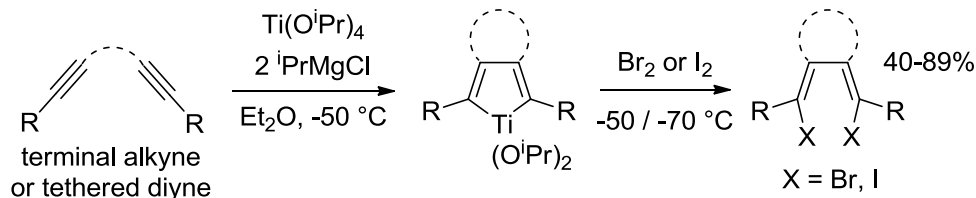
1.1.2. Synthesis of siloles and precursors from metallacycle intermediates.

Another route commonly taken in forming siloles and other metalloles employs the synthesis of 1,4-dihalobutadienes, which are usually then lithiated, and reacted with the dichlorometallane in a salt-metathesis reaction (Scheme 1-2). The reaction to generate the requisite dihalobutadiene can be achieved through two routes, and both involve early transition metal intermediates.



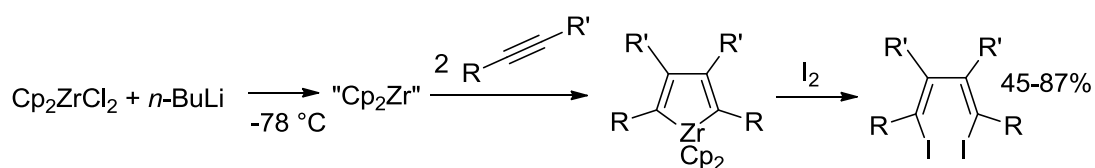
Scheme 1-2. Synthesis of metalloles from dihalobutadienes.

One method to form the necessary dihalobutadiene involves the synthesis of an intermediate titanacycle through the reaction of titanium isopropoxide with alkynes; two alkynes coordinate to the reduced titanium, and the alkynes are oxidatively coupled forming the metallacycle, which is then quenched with the halogen (bromine or iodine) to achieve the dihalobutadiene.¹¹ The reaction is depicted in Scheme 1-3. Following this synthesis, the dihalobutadiene can then be reacted as shown in Scheme 1-2.



Scheme 1-3. The synthesis of dihalobutadiene precursors via a titanacycle intermediate.¹¹

Another method to form the dihalobutadiene involves the synthesis of a zirconacycle, where zirconocene dichloride (Cp_2ZrCl_2) is reduced with *n*-BuLi to form a low valent complex ("Cp₂Zr") that efficiently coordinates two alkynes, oxidatively cyclizes,¹² and is quenched with iodine to form a diiodobutadiene,¹³ which can be lithiated and reacted with dichlorometallanes as in Scheme 1-2. A depiction of this reaction is given in Scheme 1-4.



Scheme 1-4. The synthesis of dihalobutadiene precursors via a zirconacycle intermediate.^{12,13}

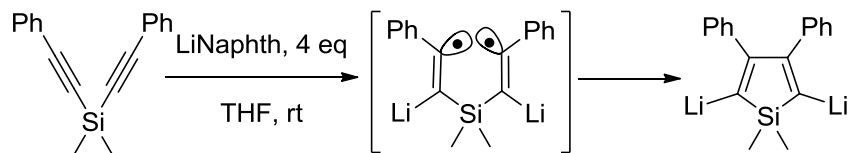
Fagan's group also demonstrated that germoles could be formed by a direct reaction of the zirconacycle with a dichlorogermane,¹⁴ but this reaction does not proceed with dichlorosilanes.

1.1.3. The Tamao procedure for synthesis of 2,5-aryl-3,4-diphenylsiloles.

Another avenue for synthesis of siloles was discovered by Tamao's group, where a silane with two phenylethynyl-substituents could be reductively cyclized using an excess of lithium naphthalenide, thus giving a 2,5-dilithio-3,4-diphenylsilole (Scheme 1-5).¹⁵

The dilithio-silole is believed to be formed by the radical coupling of a diradical intermediate, itself formed through addition of the silane into an "electron pool" created from the lithium naphthalenide. Interestingly, this proceeds in an *endo-endo* cyclization, where the carbons tether away from the silicon center and places the cyclizing metal (lithium) without the cyclized ring; this is exactly opposite behavior compared to the

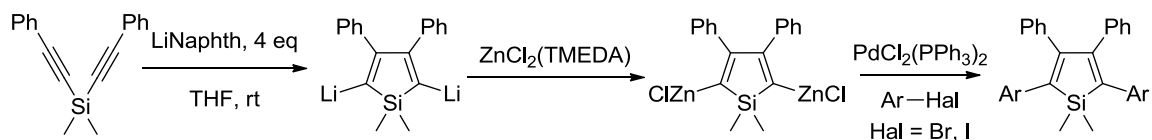
much more common *exo-exo* mode,¹⁵ which tethers the carbons of the diyne such that the metal is within the ring system (e.g., the titanacycle and zirconacycle systems above).



Scheme 1-5. The mechanism proposed for the formation of the silole through reductive cyclization.¹⁵

The 2,5-dilithiosilole species could then serve a platform for several manipulations, most of which involved electrophile reaction with this species.¹⁵ For example, after quenching the dilithiosilole solution to remove excess lithium naphthalenide, bromine could be added to make the 2,5-dibromosilole, which then acts as a typical aryl bromide, serving as a cross coupling partner with (tributyltin)acetylides under Stille conditions to give the 2,5-dialkynylsilole in excellent yields.^{15,16}

By far the most often used derivative of the Tamao method in use today involves a transmetalation of the dilithiosilole with ZnCl_2 or $\text{ZnCl}_2(\text{TMEDA})$, and then reacting the newly formed 2,5-dizincsilole with aryl halides under Negishi conditions¹² to form 2,5-aryl-3,4-diphenylsiloles (Scheme 1-6); this method too was reported by Tamao's group, using common aryl halides to develop a series of such siloles.¹⁷



Scheme 1-6. The Tamao synthesis, using $\text{ZnCl}_2(\text{TMEDA})$ and cross-coupling under Negishi conditions.¹⁷

Early syntheses involving the dilithiosilole involved quenching the excess lithium naphthalenide with bulky chlorosilanes, such as triphenylchlorosilane or *tert*-butyldiphenylchlorosilane, followed by transmetallation with $\text{ZnCl}_2(\text{TMEDA})$.^{16,17} However, it was then discovered that $\text{ZnCl}_2(\text{TMEDA})$ itself could be used for both the quenching and transmetallation species. Thus, quenching the reaction mixture with approximately four equiv of $\text{ZnCl}_2(\text{TMEDA})$ based on starting bis(phenylethynyl)silane allowed excellent yields of the cross-coupled product, without having to address siloxane contamination from the chlorosilane quenching agents.¹⁷ This method for developing 2,5-arylsiloles is by far the most used for the Tamao procedure presently, and enjoys broad applications;^{1c} it is also the method used for much of the synthetic efforts for compounds in Chapter 3.

1.2. The optoelectronics of siloles, and the effect of substitution thereon.

Siloles have long been studied for their unique optical and electronic qualities.¹ Compared to related cyclopentadienes, siloles and heavier group 14 metalloles have bathochromic shifts in their absorption and fluorescence spectra. The reason now accepted for these effects is that the LUMO of siloles is greatly stabilized in energy compared to the all-carbon analogues.¹⁸ A qualitative representation of this overlap is provided in Figure 1-2.

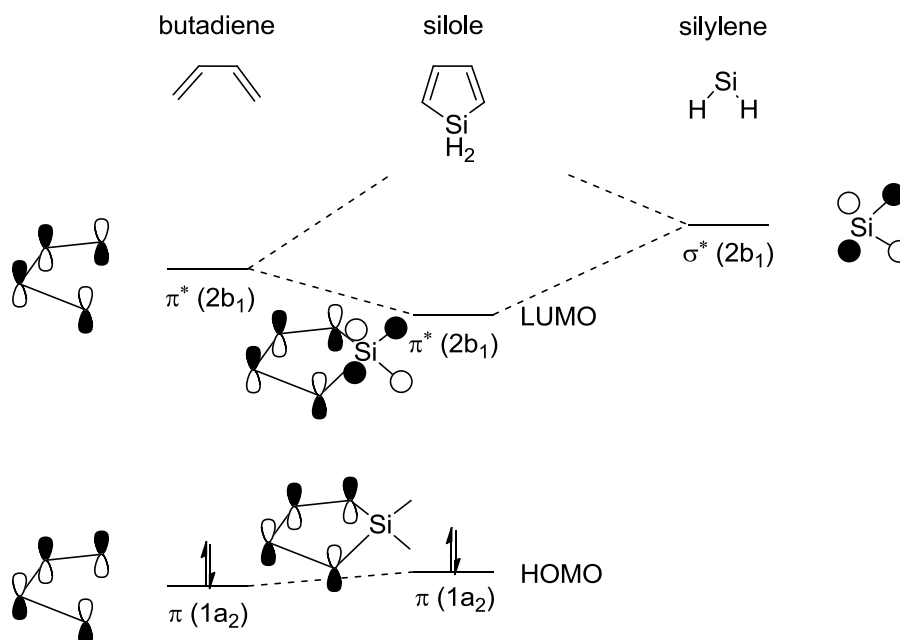


Figure 1-2. A qualitative drawing of the HOMO-LUMO portion of the molecular overlap of the silylene and butadiene portions of the silole ring, along with orbital phases and their symmetries; this shows the stabilizing effect that the silylene has on the LUMO (The figure is an adaptation from Ref. 18)

The silylene σ^* orbital shown in drawing matches the symmetry ($2b_1$) of the π^* orbital of the butadiene fragment; in addition, the energies are close enough for efficient interaction, resulting in the stabilizing effect. In comparison, the σ^* orbital of the carbene moiety in cyclopentadiene is much too high in energy to interact with the butadiene; thus, no stabilization is possible, resulting in wider bandgaps and higher energy absorption and emission spectra.¹⁹

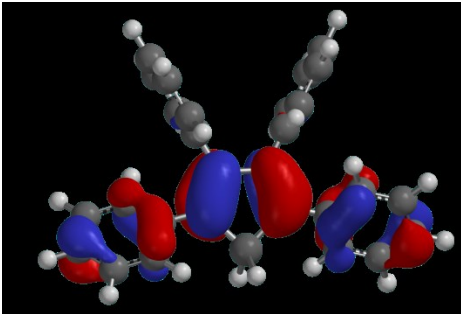
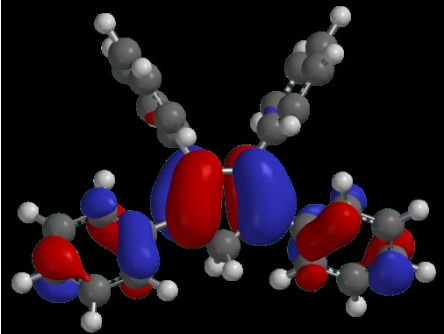
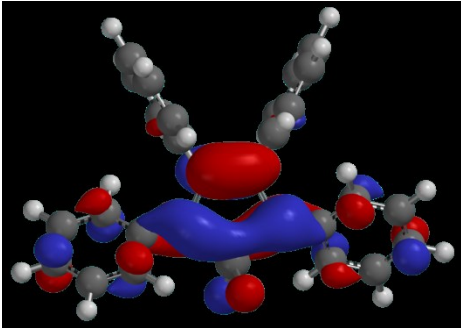
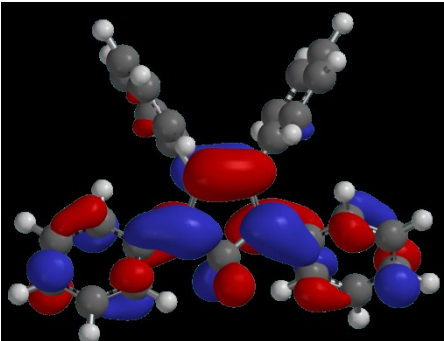
	1,1-dimethyl-2,3,4,5-tetraphenylsilole	1,1-dimethyl-2,3,4,5-tetraphenylcyclopentadiene
HOMO	 -5.38 eV	 -5.12 eV
LUMO	 -1.63 eV	 -1.08 eV
Bandgap	3.75 eV	4.04 eV

Table 1-1. The calculated probability density, energies, and bandgaps between the HOMO and LUMO orbitals for 1,1-dimethyl-2,3,4,5-tetraphenylsilole and -cyclopentadiene. The geometry was minimized using semi-empirical methods (PM3), while the energy was minimized using DFT calculations (B3LYP/6-31G*). Wavefunction Spartan '0420 computational chemistry software was used for these calculations.

This is also graphically represented in Table 1-1, in which our group calculated the probability density of the HOMO and LUMO for a more realistic 1,1-dimethyl-2,3,4,5-tetraphenylsilole and -cyclopentadiene. The HOMO of each looks very similar, with all of the probability on the butadiene ring, as shown by Tamao's group.¹⁸ The LUMO for each, however, is significantly different about the pentadienyl ring system. The silole has

appreciable probability density distributed across the silicon center due to the σ^* interaction, whereas none exists in the cyclopentadiene fragment.

The values for the silole calculated above in Table 1-1 compare well to an analogous tolyl-substituted silole reported by Tracy's group.²¹ His group also determined the bandgaps electrochemically and optically, and found that the calculations actually suggest slightly larger bandgap values than those obtained in other methods, by roughly 0.3 eV. Nevertheless, the significantly lower LUMO in siloles and other heavy group 14 metalloles allows for many unique properties, including a high electron affinity,²² which allows them, for example, to be easily reduced to anions and dianions in the presence of alkali metals.^{1a,23}

Marder's group provides a good overview of the substituent effect on the electronics of siloles;²⁴ these subsections below summarize and supplement his review.

1.2.1. Substituents at the 1,1-position.

The alteration of substituents at the silicon atom (1,1-position) generally seems to bring about slight changes, which Tamao's group has shown through Hartree-Fock calculations to be inductive in nature; significantly electronegative groups tend to cause a slight bathochromic shift in the optical spectra because of their ability to affect the σ^* of the silylene unit and thus slightly stabilize the LUMO of the silole.²⁵ In the same work, a series of differing substitutions at the 1,1-position of a 2,5-bis(trimethylsilyl)-3,4-dimethylsilole were performed, and the 1,1-difluorosilole was found to have the lowest energy absorption λ_{\max} value (318 nm), while the 1,1-dihydridosilole was found to have the highest (305 nm).²⁵ Our own group's investigations into a series of different substitutions at the 1,1-position of a 2,3,4,5-tetraphenylgermole found similar modest

changes in the absorption maxima,²⁶ suggesting this phenomenon is general to group 14 metalloles.

1.2.2. Substituents at the 3,4-position.

Not as many studies have been performed for a systematic determination of the effect of 3,4-substituent changes and their effects on the electronics of the silole, partly due to the challenges in synthesizing differently-substituted siloles at this position.²⁴ Marder reported the synthesis of both 2,3,4,5-tetrafluorenyl- and 2,5-difluorenyl-3,4-diphenylsiloles (Figure 1-3).²⁷ Though the fluorenyl substituent has an extended π -conjugated system compared to the phenyl-substituent, comparison of the 3,4-diphenyl substituted silole with the 3,4-difluorenyl-substituted silole yielded little difference in HOMO/LUMO values.²⁷ This is partly due to the orthogonal arrangement of the π -systems of the 3,4-substituent and the silole ring; at the torsional angles typical of siloles,^{1c} the π -systems of each are not in alignment symmetrically. Therefore, modest inductive effects appear to dominate the electrical contributions of this group, as was the case for 1,1-substituents.

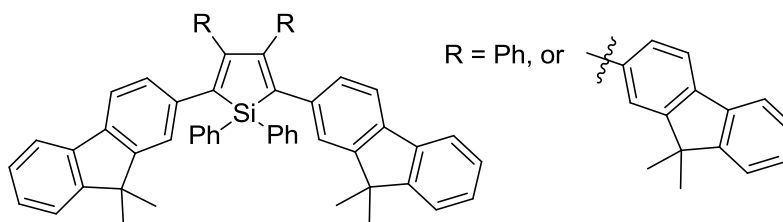


Figure 1-3. The siloles synthesized by Marder's group to determine the effect of conjugation of substituents at the 3,4-position.²⁷

Though substituents at this position do not contribute greatly to the electronics of the silole, they can make a significant impact on the quantum yields of siloles in solution and in the solid state. Smaller substituents at these positions, such as hydrogen, allow for

high quantum yields in solution.¹¹ Moderately bulky substituents at this position, such as phenyl groups, yield siloles with relatively low quantum yields in solution, but aggregate in such a way that they exhibit high quantum yields as solids. This effect is generally opposite of the behavior of most fluorophores, and has been coined as “aggregation-induced emission” (AIE); the phenomenon has led to broad applications for the detection of various properties and molecules.²⁸ To understand the mechanism behind AIE, Yin *et al.* investigated the degree of emissive and nonemissive relaxation to the ground state of two siloles,²⁹ shown in Figure 1-4.

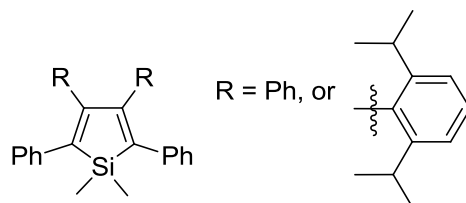


Figure 1-4. The siloles investigated theoretically by Yin *et al.*²⁹

The diisopropylphenyl-substituent was expected to be able to rotate much less freely than the phenyl-substituent, and the barrier to free rotation for the former was indeed high. Along with this lowered rotational ability, it was found that the diisopropylphenyl-substituent also was much more liable to undergo radiative (or emissive) relaxation to the ground state (i.e., a higher quantum yield in solution). The radiationless relaxation of the phenyl-substituted silole was found to be 2-3 orders of magnitude greater than the radiative decay rate.²⁹ Thus, the free rotation of the phenyl groups in the solution phase, and the subsequent increase in radiationless relaxation, is the cause behind the lowered quantum yields in solution, while the arrangement thereof is also the reason behind the high quantum yields in the solid state, due to the prevention of π -stacking.²⁸

1.2.3. Substituents at the 2,5-position.

Compared with the other positions discussed above, substitution at the 2,5-position has the most dramatic impact to the overall electronics of the silole.²⁴ Because changing the substitution at these positions separately has been made possible through the development of the Tamao method,^{15,17} research on the effect of substitution on the electronics of the silole has been extensive.^{1c,24} From the large amount of data gathered, it has been found that there are three factors that combined can affect the optoelectronic properties of siloles, and these are discussed below.

One substituent property that affects the electronics of siloles at this position is the degree of conjugation. Figure 1-5 shows the comparison of the 2,3,4,5-tetraphenylsilole with 2,5-bis(biphenyl)-3,4-diphenylsilole,¹⁷ along with their respective optical data. Increasing the degree of conjugation leads to bathochromic shifts in the optical spectra, so long as the other properties discussed below are not significantly changed.

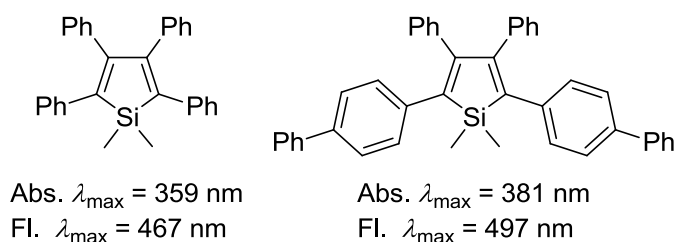


Figure 1-5. The comparison of the degree of conjugation of the 2,5-substituents, and its effect on the optical spectra obtained.¹⁷

Another substituent property that effects the optoelectronics is the dihedral angle. A comparison is shown as an example in Figure 1-6. Though the naphthyl-substituent might be initially expected to also cause a bathochromic shift in the optical spectra due to increased conjugation, the spectra actually absorb and emit at a higher energy.

Presumably, the sterics of the naphthyl-substituent causes an increase in the dihedral angle, reducing the degree of π -overlap between the substituent and the silole ring, and thus causing a hypsochromic shift in the optical spectra.²⁴

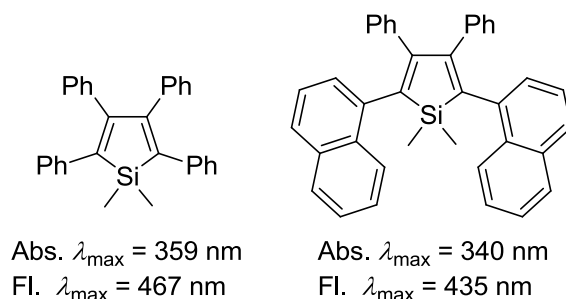


Figure 1-6. Comparison of the phenyl substituent to the naphthyl substituent, the latter showing a hypsochromic shift due to the increased dihedral angle.¹⁷

The third factor that affects the optoelectronics of siloles from the 2,5-position is the degree of π -resonance contribution of the silole. Both strong π -donors (such as *p*-Me₂N-phenyl) and strong π -acceptors (such as *p*-O₂N-phenyl) induce large bathochromic shifts in the spectra (Figure 1-7), the former also allowing for facile oxidation, whereas the latter yields facile reduction, compared to the unsubstituted phenyl-silole.²⁴

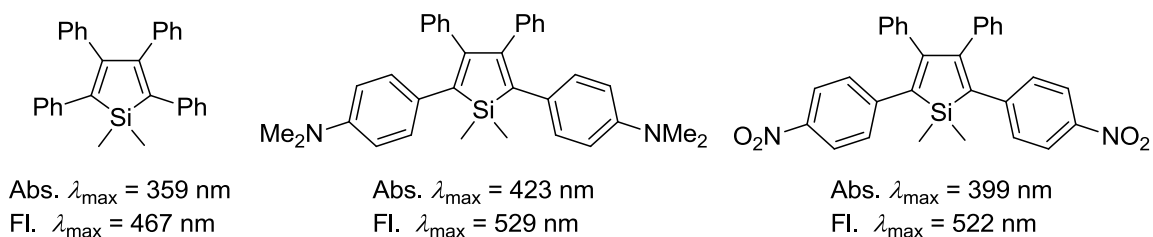
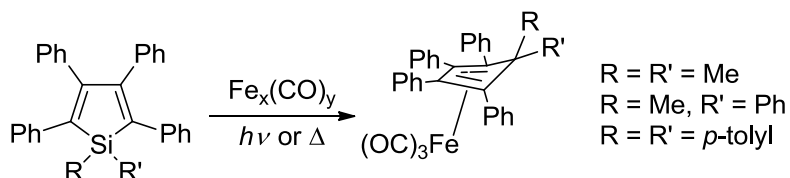


Figure 1-7. The effect of strong π -donors and acceptors on the optical spectra of siloles.¹⁷

1.3. Overview of siloles and their coordination to metal centers.

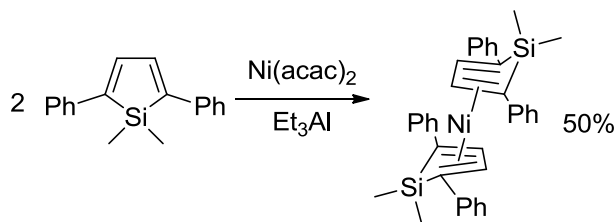
1.3.1. Siloles and group 14 metalloles as cyclopentadienyl analogues.

The first interest of siloles and heavier group 14 metalloles as ligands was in trying to replicate the behavior of cyclopentadiene, in order to determine the degree of aromaticity present in heavier analogues of cyclopentadiene. Indeed, one of the motivations behind Curtis' synthesis of germoles and siloles (Section 1.1.1) initially was to siloles and germoles into ions, and reacting them with iron chloride to make the silole and germole analogues of ferrocene.⁸ However, the reactions reported in his account did not yield the sandwich complex, but rather the germole-hydride. Nevertheless, investigations by other researchers continued, and found initial success at forming discrete silole-metal complexes,³⁰ for example, through reaction of 2,3,4,5-tetraphenylsiloles with iron(0) carbonyl complexes to generate η^4 -sandwich complexes (Scheme 1-7).³¹



Scheme 1-7. The reaction of a several siloles with iron carbonyl to generate the η^4 -complex.³¹

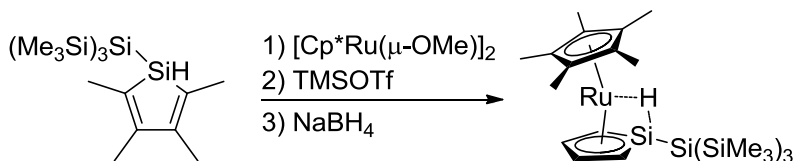
Carré *et al.* reported 2,5-diphenylsiloles and their use as ligands. Reaction of 1,1-dimethyl-2,5-diphenylsilole with nickel(acetylacetonate)₂ and triethylaluminum gave the sandwich complex bis(silole)nickel (Scheme 1-8);³² however, the crystal structure obtained of this complex indicated the silole was 20° out of plane from the butadiene moiety, suggesting η^4 -complexation of the siloles to the metal center.



Scheme 1-8. The synthesis of the bis(η^4 -silolyl)nickel complex reported by Carré *et al.*³²

Most early attempts yielded complexes that were only η^4 -coordinated with the butadiene backbone of the silole ring, rather than η^5 -coordinated as is the case with cyclopentadienyl-substituents. Several years after the reports above, Tilley's group reported the first germole with properties suggestive of η^5 -coordination as a mixed sandwich complex with ruthenium,³³ followed shortly thereafter by an analogous mixed sandwich complex, (2,3,4,5-tetramethylsilolyl)(Cp*)Ru (Scheme 1-9), with a crystal structure showing a planar silole as a ligand, also suggestive of η^5 -coordination; the complex was formed by oxidative addition of the silole to a ruthenium complex precursor, followed by removal of the methoxy groups from the ruthenium, and finally reduction with sodium borohydride (Scheme 1-9).³⁴

Several years after these reports, Tilley's group also reported another synthesis of siloles that were η^5 -coordinated with hafnium centers and lithium in a "tri-sandwich complex",³⁵ however, attempts at isolating non-lithiated products from this species caused the formation of more common η^4 -coordinated siloles.



Scheme 1-9. The synthesis of the first η^5 -coordinated silole complex.

1.3.2. Platinum centers covalently bound to the 2,5-position of silole.

Despite the significant electronic effects imparted on siloles from the 2,5-substituents, there has been comparatively little study on coordination or attachment of metal center to 2,5-substituents. The covalent attachment of platinum to 2,5-alkynylphenyl substituents is discussed briefly in this section.

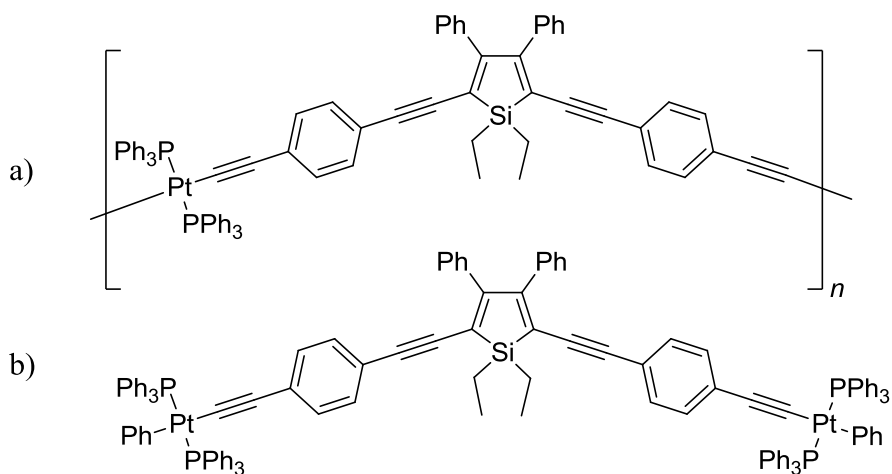


Figure 1-8. The a) poly(platinayne) polymer and b) its monomeric analogue.³⁷

The research of Wong's group focuses on the synthesis of poly(platinumacetylenes), where terminal acetylenes containing aromatic spacers are attached covalently to platinum phosphine centers, with the spacer chosen for the ultimate aim of lowering the bandgap of these metallopolymers.³⁶ They were able to achieve this by using a silole as the aromatic spacer (Figure 1-8), forming both the polyplatinayne and the monomeric analogue.³⁷

Due to the high electron affinity of siloles,²² it was found that the band gap for the monomer and the polymer were 2.18 eV and 2.10 eV, respectively; the slightly smaller value for the polymer is attributed to the much greater extension of the conjugation.³⁷ The value obtained for the polymer using the silole as a spacer greatly reduces the

bandgap compared to other spacers, from a reduction of 0.6 eV for the thiophenyl group to 1.0 eV for the diphenylsilyl group.³⁷

1.3.3. Metal coordination to 2,5-substituents.

As mentioned above, though 2,5-substituents have significant electronic impact on the properties of siloles (Section 1.2.3), and many siloles have been made that could have coordinative ability (e.g., bipyridyl and amine-substituents),^{1c,17} there have been relatively few studies on the coordination of metal centers to 2,5-substituents. Several studies outlining the field are summarized below.

To our knowledge, the earliest account of metal coordination dealing specifically with 2,5-substituents was work by Wang's group on the coordination of zinc to two 2,5-functionalized siloles, which are shown in Figure 1-9.³⁸ While the primary goal of the research was to develop materials for use in OLEDs, the response in the optical spectra for each species was observed in response to coordination by zinc(II).

Both substituents **A** and **B** contain nitrogens that have potential to bind to metal centers. Based on the optical spectra observed, coordination of zinc(II) to the silole with substituent B (n=1) induces a hypsochromic shift in the absorbance (by 20 nm) and fluorescence (by 19 nm) spectra. Based on the crystal structure obtained of the zinc(II) coordinated compound, the 2,5-aryl rings have a larger torsional angle with the silole ring. The authors suggest that this might be explained by the metal reducing the overall conjugation of the molecule on coordination, which causes the removal of electronic communication between the 2,5- substituents and the silole core, increasing the bandgap and thus raising the energy of both the absorption and emission bands.³⁸

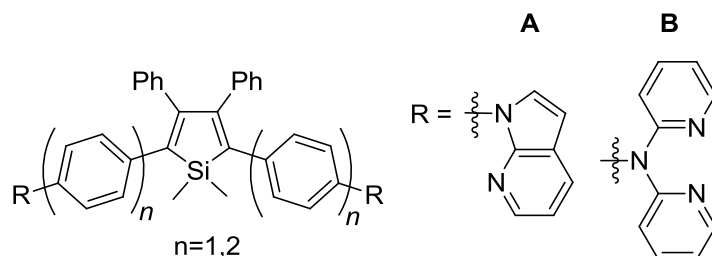


Figure 1-9. The siloles studied by Wang's group.³⁸

Very shortly after the report above, Gerbier's group reported the optical properties of the same compound (Figure 1-9B, $n=1$) of which Wang obtained a crystal structure.

Gerbier compared the silole with the silole and a solution of ZnCl_2 and CuCl_2 .³⁹

Dramatic differences in the fluorescence spectra were observed. Addition of ZnCl_2 caused an increase in emission intensity, but not a significant shift in wavelength, as was reported by Wang for $\text{Zn}(\text{OTf})_2$ salts (*vide infra*). When CuCl_2 was added, however, the fluorescence of the silole was almost completely quenched; the weak fluorescence bands were also significantly shifted to shorter wavelengths.³⁹

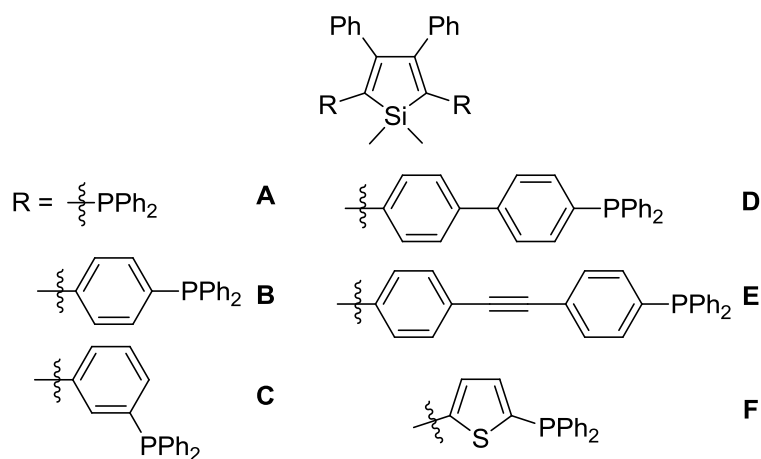


Figure 1-10. Some of the phosphine-linked siloles synthesized by our group. For siloles A-E, the phosphine oxide was also synthesized.⁴⁰

Recently, our group took interest in siloles with coordinating ability, synthesizing a series of phosphine-linked siloles and studying their effects on coordination with platinum and gold centers.⁴⁰ The siloles synthesized are shown in Figure 1-10.

Though the coordination of **B** to platinum centers induced modest shifts in the optical spectra,^{40a} coordination of the same compound to gold centers caused an appreciable hypsochromic shift in the absorption spectrum (by 19 nm), and a large hypsochromic shift in the emission spectrum (by 87 nm).^{40b}

Very recently, Tang's group reported the synthesis of two terpyridine-substituted siloles (Figure 1-11).⁴¹ They tested these siloles against a range of metal centers, with a notable enhancement of the fluorescence of the bis(terpyridine) silole when coordinated with zinc; determination of the stoichiometry through Job's Method suggested a 1:1 binding mode, which in the case of the bis(terpyridine)silole means that an oligomeric species had formed. The oligomer causes reduced solubility, and this aggregation is likely the cause of the enhanced fluorescence due to the AIE effect.^{5a,28}

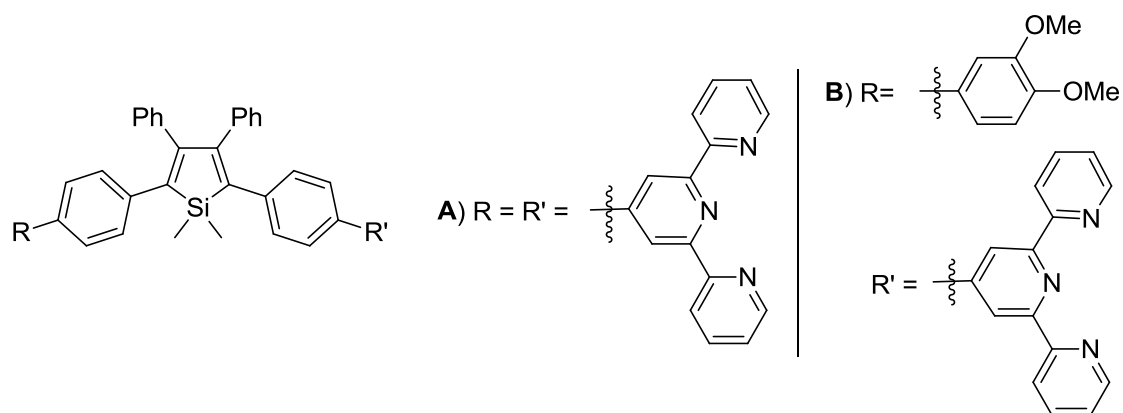


Figure 1-11. The terpyridine siloles synthesized by Tang's group. Compound **A** showed good selective fluorescence enhancement in the presence of zinc(II).⁴¹

Our group has also reported on the interactions of several siloles in solution with Ni(II), Cu(II), and Hg(II) metal centers; this research is also covered in Chapter 3 of this thesis.⁴²

1.4. Overview of the photoinduced charge-transfer effect (PCT).

Some fluorophores have electronics in them that can be considered to have “donor” and “acceptor” moieties. Donor ends typically consist of amines, where the lone pair of the nitrogen atom is π -symmetric with the aromatic system of fluorophore. Acceptor ends are much more varied, and many times consist of the fluorophore itself; typically the acceptor moiety has more of a π -withdrawing drawing effect, consisting of π -symmetric substituents that, through resonance, tend to retain more partial electron density from the fluorophore. Many times, the electronics of the fluorophore are such that the accepting moiety is the fluorophore itself.⁴³

During the process of excitation for these molecules, there is a momentary transfer of charge from the donor to the acceptor portions of the fluorophore. This results in a partial positive charge on the donor, and a partial negative charge on the acceptor, in the excited state (Figure 1-12). This process of charge transfer in the excited state is known as photo-induced charge transfer, or PCT.⁴³ This charge transfer in the excited state has the effect of inducing bathochromic shifts in optical spectra, as a notable example.

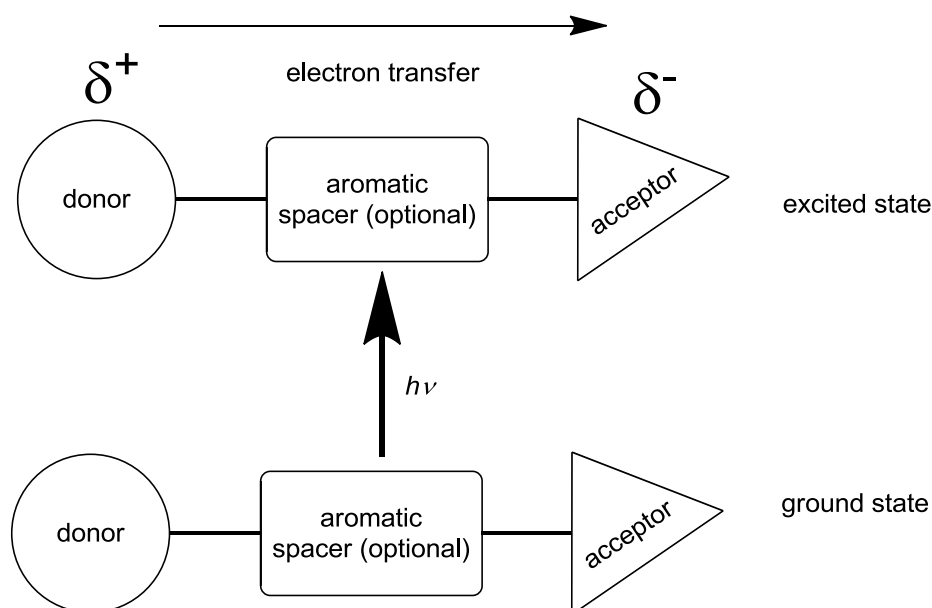


Figure 1-12. A schematic representation of a donor-acceptor fluorophore undergoing photoinduced-charge transfer upon excitation.⁴²

As the PCT effect is highly sensitive to the nature of both the donor and acceptor moieties, a metal center binding to either side can be expected to alter the optoelectronics of the fluorophore significantly; indeed, extensive research into the effect of coordination on PCT has shown this to be true.⁴³ The cation generally can bind to the donor or acceptor moieties, and the optical changes observed will vary greatly depending on where binding occurs. If the cation binds to the donor end, the lone pairs that contributed to the charge transfer in the excited state are now contributing to the binding; thus, the charge transfer is mitigated, leading to hypsochromic shifts in optical spectra, and a lower molar absorptivity, compared to the unbound fluorophore. Intuitively, binding to the acceptor portion of the fluorophore brings about opposing effect. When the cation binds here, the acceptor moiety can be considered to have a more “positive-like” state in the ground state, and when excitation and subsequent charge transfer occurs, the charge difference

across the fluorophore is greater; therefore, the effects of PCT are amplified, causing further bathochromic shifts and higher molar absorptivities, compared to the unbound fluorophore. A depiction of each event is listed in Figure 1-13.

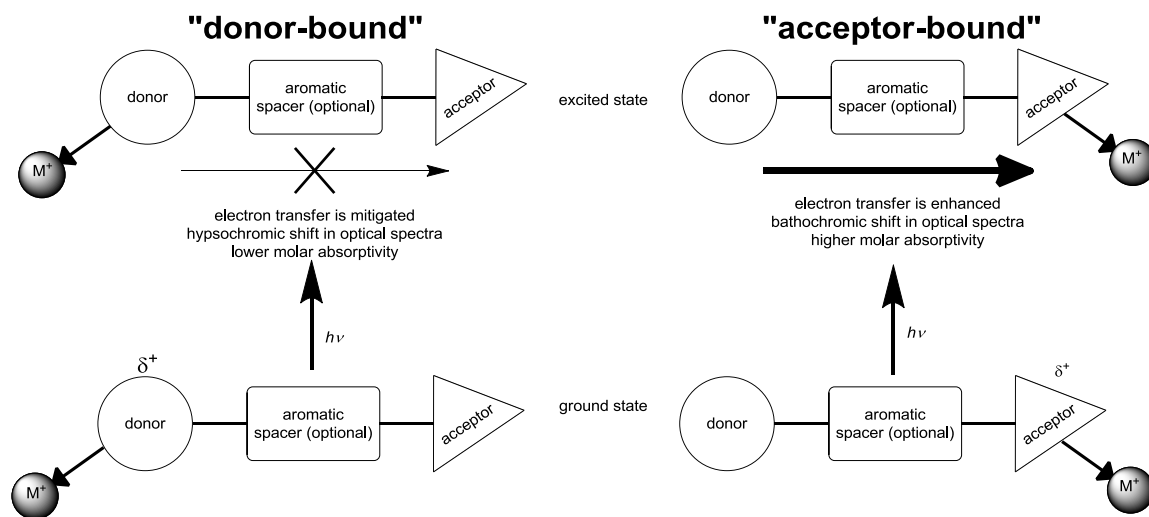


Figure 1-13. A representation of the effects of cation binding to the “donor” or “acceptor” moieties of the fluorophore. Also included in the figure are a summary of the effects observed in each situation.⁴³

An example of a molecule that exhibits this effect on binding to calcium is known as Indo-1, a commercially available fluorescent calcium sensor.⁴⁴ The structure is shown in Figure 1-14. Upon binding to calcium (which is very strong from the chelating ligand structure on the donor end), the lone pairs of the nitrogen on the donor side are restricted from undergoing PCT across the fluorophore, and therefore, the absorbance and fluorescence maxima are hypsochromically shifted compared to the unbound fluorophore by 18 and 65 nm, respectively.⁴⁴ This concept of PCT becomes particularly important for explaining the causal factors behind the optical changes of some of the siloles studied in Chapter 3.

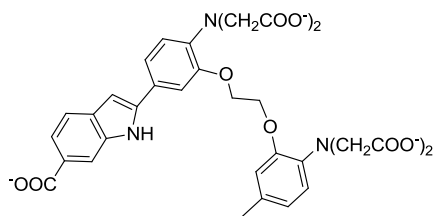


Figure 1-14. The structure of the calcium detection fluorophore Indo-1, which shows hypsochromic shifts in optical spectra upon binding, a hallmark of the PCT effect.

1.5. Statement of the problem.

There are many avenues for research into the optical, structural and electronic effects of siloles and other group 14 metalloles.^{1,28} During the course of this research two classes of group 14 metalloles were studied. Germales, and their structural related analogues germafluorenes, became a focus of our group from our desire to determine to what degree they could exhibit the phenomenon of aggregation-induced emission (AIE), which was already well-established for siloles.²⁸ Though there are several characterization methods important to AIE studies, the molecular structures of these compounds, and their packing behavior in the crystal lattice, have proved to be vital pieces of information to explain the high quantum yields AIE-active molecules in the crystalline/solid state.²⁸ Therefore, Chapter 2 of this thesis addresses the crystal structures and packing behavior of several germafluorenes, as well as a series of differently-substituted 1,1-germales synthesized by our group.²⁶ The crystal structures are then assessed for any potential intermolecular interactions, particularly for the presence or absence of π - π stacking effects.

Substituent effects at the 2,5-positions of siloles have been extensively studied,²⁴ and even though many of the substituents chosen seem to have good potential to act as ligands to metal centers, there have been relatively few studies on metal binding to these

positions, and subsequent optical changes.³⁸⁻⁴¹ Therefore, Chapter 3 details the synthesis and molecular structures of several symmetric 1,1-dimethyl-2,5-substituted-3,4-diphenylsiloles, along with their characterization by numerous means. The synthesis of siloles using the Tamao method can cause some yield-limiting byproducts to occur; these byproducts are herein extensively characterized, along with a discussion of possible alterations to the procedure to ensure the best possible yields. Additionally, the interaction of the symmetric siloles with Ni(II), Cu(II), and Hg(II) in solution are investigated by UV-visible and fluorescence spectroscopy, along with a discussion on the potential causes of the changes observed, which include mechanisms related to PCT.⁴² Additionally, spectrophotometric titrations are performed on one silole with Hg(II) in order to quantitatively determine the binding characteristics between the silole and metal. The attempted syntheses of asymmetric siloles, as well as a benzylquinolate silole envisioned to have “off-on” capabilities, are also discussed.

1.6. References

- (1) For some extensive reviews see: (a) Dubac, J.; Guerin, C.; Meunier, P. Wiley, 1998; Vol. 2, pp. 1961–2036; (b) Hissler, M.; Dyer, P. W.; Réau, R. *Coord. Chem. Rev.* **2003**, *244*, 1–44; (c) Corey, J. Y. In *Advances in Organometallic Chemistry*; Anthony F. Hill and Mark J. Fink, Ed.; Academic Press, 2011; Vol. Volume 59, pp. 1–180.
- (2) (a) Usta, H.; Lu, G.; Facchetti, A.; Marks, T.J. *J. Am. Chem. Soc.* **2006**, *128*, 9034–9035; (b) Wu, J.-S.; Cheng, Y.-J.; Lin, T.-Y.; Chang, C.-Y.; Shih, P.-I.; Hsu, C.-S. *Adv. Funct. Mater.* **2012**, *22*, 1711–1722; (c) Wang, Y.; Hou, L.; Yang, K.; Chen, J.; Wang, F.; Cao, Y. *Macromol. Chem. Phys.* **2005**, *206*, 2190–2198; (d) Huang, H.; Youn, J.; Ortiz, R.P.; Zheng, Y.; Facchetti, A.; Marks, T. *Chem. Mater.* **2011**, *23*, 2185–2200.
- (3) (a) Murata, H.; Kafafi, Z.H. *Appl. Phys. Lett.* **2002**, *80*, 189–191; (b) Tamao, K.; Uchida, M.; Izumizawa, T.; Furukawa, K.; Yamaguchi, S. *J. Am. Chem. Soc.* **1996**, *118*, 11974–11975; (c) Kim, W.; Palilis, L.C.; Uchida, M.; Kafafi, Z.H. *Chem. Mater.* **2004**, *16*, 4681–4686.

-
- (4) (a) Zhang, Z.-G.; Min, J.; Zhang, S.; Zhang, J.; Zhang, M.; Li, Y. *Chem. Commun.* **2011**, 9474–9476; (b) DiCarmine, P.M.; Wang, X.; Pagenkopf, B.L.; Semenikhin, O.A. *Electrochemistry Communications* **2008**, *10*, 229–232; (c) Hou, J.; Chen, H.-Y.; Zhang, S.; Li, G.; Yang, Y. *J. Am. Chem. Soc.* **2008**, *130*, 16144–16145; (d) Wang, F.; Luo, J.; Yang, K.; Chen, J.; Huang, F.; Cao, Y. *Macromolecules* **2005**, *38*, 2253–2260.
- (5) (a) Li, Z.; Dong, Y.Q.; Lam, J.W.Y.; Sun, J.; Qin, A.; Häußler, M.; Dong, Y.P.; Sung, H.H.Y.; Williams, I.D.; Kwok, H.S.; Tang, B.Z. *Adv. Funct. Mater.* **2009**, *19*, 905–917; (b) Wang, M.; Zhang, D.; Zhang, G.; Tang, Y.; Wang, S.; Zhu, D. *Anal. Chem.* **2008**, *80*, 6443–6448; (c) Sohn, H.; Calhoun, R.M.; Sailor, M.J.; Trogler, W.C. *Angew. Chem. Int. Ed.* **2001**, *40*, 2104–2105.
- (6) Leavitt, F. C.; Manuel, T. A.; Johnson, F. *J. Am. Chem. Soc.* **1959**, *81*, 3163–3164.
- (7) Braye, E. H.; Hübel, W.; Caplier, I. *J. Am. Chem. Soc.* **1961**, *83*, 4406–4413.
- (8) Curtis, M. D. *J. Am. Chem. Soc.* **1969**, *91*, 6011–6018.
- (9) Jutzi, P.; Karl, A. *J. Organomet. Chem.* **1981**, *214*, 289–302.
- (10) Joo, W.-C.; Park, Y. C.; Kang, S. K.; Hong, J. H.; Kong, Y.-K. *Bull. Korean Chem. Soc.* **1987**, *8*, 271.
- (11) Yamaguchi, S.; Jin, R.-Z.; Tamao, K.; Sato, F. *J. Org. Chem.* **1998**, *63*, 10060–10062.
- (12) Negishi, E.; Cederbaum, F. E.; Takahashi, T. *Tetrahedron Lett.* **1986**, *27*, 2829–2832.
- (13) (a) Buchwald, S. L.; Nielsen, R. B. *J. Am. Chem. Soc.* **1989**, *111*, 2870–2874; (b) Ashe III, A. J.; Kampf, J. W.; Al-Taweel, S. M. *J. Am. Chem. Soc.* **1992**, *114*, 372–374; (c) Xi, C.; Huo, S.; Afifi, T. H.; Hara, R.; Takahashi, T. *Tetrahedron Lett.* **1997**, *38*, 4099–4102.
- (14) (a) Fagan, P. J.; Nugent, W. A. *J. Am. Chem. Soc.* **1988**, *110*, 2310–2312 (b) Fagan, P. J.; Nugent, W. A.; Calabrese, J. C. *J. Am. Chem. Soc.* **1994**, *116*, 1880–1889.
- (15) Tamao, K.; Yamaguchi, S.; Shiro, M. *J. Am. Chem. Soc.* **1994**, *116*, 11715–11722.
- (16) Yamaguchi, S.; Iimura, K.; Tamao, K. *Chemistry Letters* **1998**, 89–90.
- (17) Yamaguchi, S.; Endo, T.; Uchida, M.; Izumizawa, T.; Furukawa, K.; Tamao, K. *Chem. Eur. J.* **2000**, *6*, 1683–1692.
- (18) Yamaguchi, S.; Tamao, K. *Bull. Chem. Soc. Jpn.* **1996**, *69*, 2327–2334.
- (19) Yamaguchi, S.; Itami, Y.; Tamao, K. *Organometallics* **1998**, *17*, 4910–4916.
- (20) Spartan '08. Wavefunction, Inc.; Irvine, CA.
- (21) Bozeman, T. C.; Edwards, K. A.; Fecteau, K. M.; Verde, M. G.; Blanchard, A.; Woodall, D. L.; Benfaremo, N.; Ford, J. R.; Mullin, J. L.; Prudente, C. K.; Tracy, H. J. *J. Inorg. Organomet. P.* **2011**, *21*, 316–326.
- (22) Zhan, X.; Risko, C.; Amy, F.; Chan, C.; Zhao, W.; Barlow, S.; Kahn, A.; Brédas, J.-L.; Marder, S.R. *J. Am. Chem. Soc.* **2005**, *127*, 9021–9029
- (23) Colomer, E.; Corriu, R. J.; Lheureux, M. *Chemical Reviews* **1990**, *90*, 265–282.

-
- (24) Zhan, X.; Barlow, S.; Marder, S. R. *Chem. Comm.* **2009**, 1948–1955.
- (25) Yamaguchi, S.; Jin, R.-Z.; Tamao, K. *J. Organomet. Chem.* **1998**, *559*, 73–80.
- (26) Bandrowsky, T. L.; Carroll, J. B.; Braddock-Wilking, J. *Organometallics* **2011**, *30*, 3559–3569.
- (27) Zhan, X.; Haldi, A.; Risko, C.; Chan, C. K.; Zhao, W.; Timofeeva, T. V.; Korlyukov, A.; Antipin, M. Y.; Montgomery, S.; Thompson, E.; An, Z.; Domercq, B.; Barlow, S.; Kahn, A.; Kippelen, B.; Brédas, J.-L.; Marder, S. R. *J. Mater. Chem.* **2008**, *18*, 3157.
- (28) Liu, J.; Lam, J. W. Y.; Tang, B. Z. *J. Inorg. Organomet. P.* **2009**, *19*, 249–285.
- (29) Yin, S.; Peng, Q.; Shuai, Z.; Fang, W.; Wang, Y.-H.; Luo, Y. *Phys. Rev. B* **2006**, *73*, 205409.
- (30) Abel, E. W.; Blackmore, T.; Whitley, R. J. *J. Chem. Soc., Dalton Trans.* **1976**, *0*, 2484–2489.
- (31) McMahon, R. J. *Coord. Chem. Rev.* **1982**, *47*, 1–14.
- (32) Carré, F.; Colomer, E.; Corey, J. Y.; Corriu, R. J.; Guerin, C.; Henner, B. J.; Kolani, B.; Wong Chi Man, W. W. C. *Organometallics* **1986**, *5*, 910–917.
- (33) Freeman, W. P.; Tilley, T. D.; Rheingold, A. L.; Ostrander, R. L. *Angew. Chem. Int. Ed.* **1993**, *32*, 1744–1745.
- (34) Freeman, W. P.; Tilley, T. D.; Rheingold, A. L. *J. Am. Chem. Soc.* **1994**, *116*, 8428–8429.
- (35) Dysard, J. M.; Tilley, T. D. *J. Am. Chem. Soc.* **2000**, *122*, 3097–3105.
- (36) Wong, W.-Y.; Harvey, P. D. *Macromol. Rapid Comm.* **2010**, *31*, 671–713.
- (37) Wong, W.-Y.; Wong, C.-K.; Poon, S.-Y.; Lee, A. W.-M.; Mo, T.; Wei, X. *Macromol. Rapid Comm.* **2005**, *26*, 376–380.
- (38) Lee, J.; Liu, Q.-D.; Motala, M.; Dane, J.; Gao, J.; Kang, Y.; Wang, S. *Chem. Mater.* **2004**, *16*, 1869–1877.
- (39) Aubouy, L.; Huby, N.; Wantz, G.; Vignau, L.; Hirsch, L.; Guérin, C.; Gerbier, P. *C. R. Chimie* **2005**, *8*, 1262–1267.
- (40) (a) Braddock-Wilking, J.; Gao, L.-B.; Rath, N. P. *Dalton Trans.* **2010**, *39*, 9321–9328. (b) Braddock-Wilking, J.; Gao, L.-B.; Rath, N. P. *Organometallics* **2010**, *29*, 1612–1621.
- (41) Yin, S.; Zhang, J.; Feng, H.; Zhao, Z.; Xu, L.; Qiu, H.; Tang, B. *Dyes and Pigments* **2012**, *95*, 174–179.
- (42) Carroll, J. B.; Braddock-Wilking, J. *Organometallics* **2013**, *32*, 1905–1912
- (43) A very good discussion of these effects is in Section 3 of: Valeur, B.; Leray, I. *Coord. Chem. Rev.* **2000**, *205*, 3–40.
- (44) Gryniewicz, G.; Poenie, M.; Tsien, R. Y. *J. Biol. Chem.* **1985**, *260*, 3440–3450.

Chapter 2. Results and Discussion – 1,1-disubstituted germoles and germole-like compounds: Structural Characterization and Aggregation-Induced Emission

2.1. General Introduction

Group 14-metalloles, particularly those including heavier group 14 elements (Figure 2-1), enjoy broad research regarding their synthesis, reactivity, and especially study of their unique optoelectronic properties.¹ While siloles have been studied at length ever since interest was renewed following Tamao's extremely useful syntheses of 2,5-substituted siloles,² the related germoles (i.e., metalloles with a germanium at the 1-position) remain relatively much less studied.

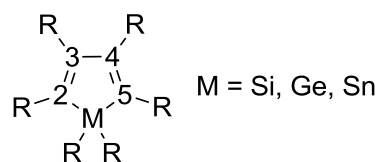


Figure 2-1. General structure for a group 14 metallole.

While studying some well-known siloles, Tang and co-workers discovered their unique attribute of aggregation-induced emission (AIE);³ the siloles were found to be weakly emissive in the solution phase, but the emission *increased* in the solid state, which could be demonstrated by decreasing the compound's solubility through introduction of an anti-solvent. This behavior is unusual in that fluorophores typically fluoresce strongly in the solution state, but this emission is quenched significantly when in the solid state. The reverse in behavior for siloles is due mainly to two factors: the difference in substituent rotational motion in the solution and solid state (referred to as

restricted intramolecular rotation, or RIR), and the non-planarity of packing in the crystalline/solid state, and are discussed briefly below.

The phenyl substituents on the siloles, particularly at the 3,4-positions, play a significant role in the degree of radiationless relaxation to the ground state upon excitation; when in solution, these groups are free to rotate, and this rotation causes the excited-state metallole to relax through this movement. When the silole is in the solid state, this rotation is greatly mitigated, and as such the radiationless pathway is prevented, forcing the excited-state silole to relax to the ground state through a radiative pathway (i.e., fluorescence potential greatly increases).⁴

The fluorescence potential in siloles in the solid state is also more fully realized than other fluorophores because of non-planar arrangement of the molecule. Classical fluorophores are generally planar molecules, as the planarity imparts a rigidity that allows for high radiative emission. This planarity, however, also allows for the parallel stacking of molecules in the solid/crystalline state, and this arrangement can cause the development of excimers that can relax through mostly non-radiative means. This combined affect is known colloquially as aggregation-caused quenching (ACQ).⁵ It was later found that siloles in particular have significantly higher yields than most other fluorophores in the solid state. The arrangement of the substituents on the silole, particularly the phenyl groups at the 2,3,4,5-positions (Figure 2-2) disallows for any significant parallel orientation between the π -system of the molecules (which, along with interplanar distance, is the main requirement for π -stacking quenching effects to occur).

Our group decided to work on germales, which are analogous to siloles except for the placement of germanium at the 1-position instead of silicon. It was noticed that

several known crystal structures exhibited similar substituent arrangements; given that they are generally less studied than siloles, we desired to investigate the structures of several known and new germanium compounds in order to determine how germoles behaved similarly or differently to siloles that exhibited AIE.

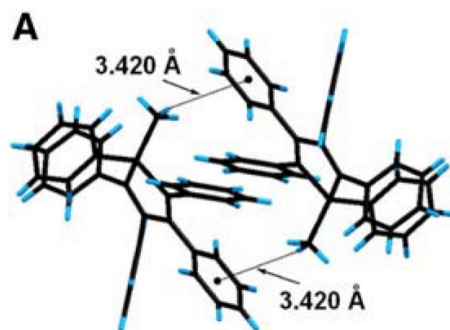
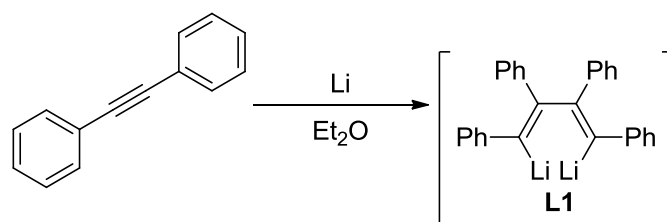


Figure 2-2. A crystal structure of 1-methyl-1,2,3,4,5-pentaphenylsilole, which shows the arrangement of the substituents preventing parallel orientation of the π -system intermolecularly.⁶

2.2. Synthesis and spectral characterization of germoles and their precursors.

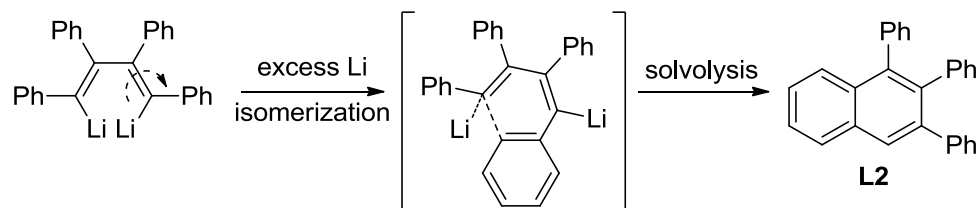
2.2.1 Generation of lithiated compounds for synthesis of germoles.

Many of the compounds that were investigated were variations of the 2,3,4,5-tetraphenylgermole, where the exocyclic substituents at the germanium center (1-position) were varied. Most of the germoles studied have identical 1,1-substituents, though some were synthesized that have differing substituents here and have a slightly different synthesis. All syntheses based on the tetraphenyl system, however, require the generation of 1,2,3,4-tetraphenyl-1,4-dilithio-1,3-butadiene (**L1**), generated from diphenylacetylene (tolan) and lithium under inert atmosphere in diethyl ether (Et_2O) (Equation 2-1).



Equation 2-1. Synthesis of the key dilithiobutadiene intermediate **L1**.

The reaction for the dilithio- intermediate has a distinct history of being fickle, with researchers in the early- to mid-20th century studying its formation and byproducts in significant detail;⁷ a reading of different literature accounts show that conversions, reaction times, and appearance of the mixture varied from group to group. The primary difficulty of the reaction is in the isomerization of the product on extended reaction times or (more commonly) excess lithium; in such cases the main product formed is (on alcoholysis) 1,2,3-tetraphenyl naphthalene (**L2**). A representation of this conversion is shown in Equation 2-2.



Equation 2-2. Isomerization of the desired precursor yields the unwanted naphthalene compound.⁸

Interestingly, other researchers as well as our group have noted that the two compounds, **L1** and lithio-**L2**, are never seen as mixtures.^{7b,8} This suggests that excess lithium, or a solvent with significant donation ability such as THF,⁸ can catalytically drive the conversion, which, once started, cannot be reversed. Therefore, a method was developed to optimize the conversion to the desired compound **L1**, while minimizing the

chances for isomerization to the undesired material, as well as estimating the time to complete reaction in order to reduce the number of aliquots needed. Figure 2-3 shows an example of the method, where several aliquots were taken early in the reaction, the percent conversion by GC versus time was plotted, and a fit curve was applied to estimate approximate completion.

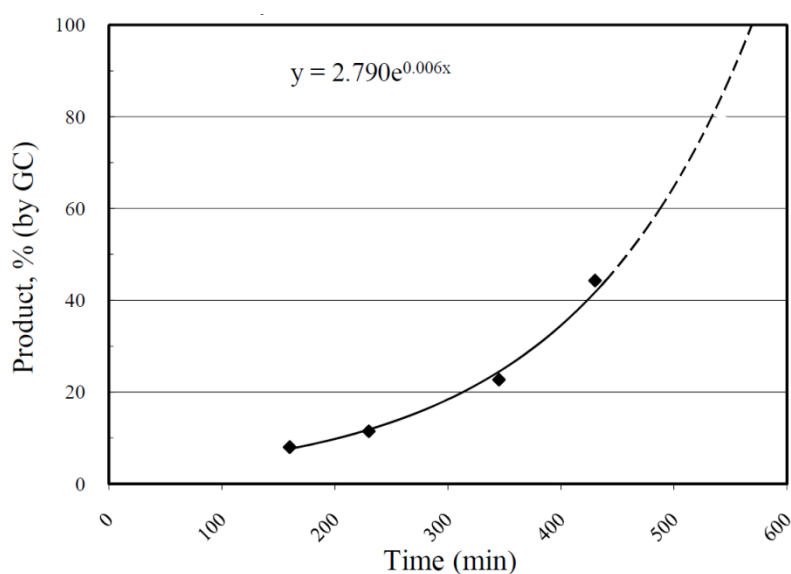
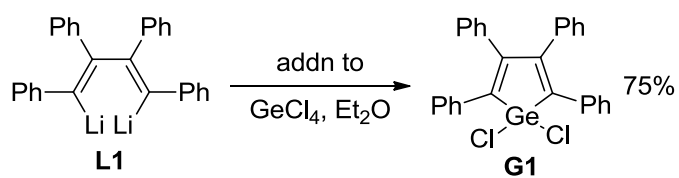


Figure 2-3. Example of the plots used to estimate completion time of the reaction to synthesize **L1**.

During the course of reaction attempts, the most optimal conditions that gave reproducibly high conversions were determined as follows: the amount of lithium added should never exceed one equiv of diphenylacetylene (an excess of diphenylacetylene is acceptable and can ensure that the material does not convert to unwanted side products). Diethyl ether is the best choice for solvent in the reaction as well as the quenching dihalometallane. Good results are obtained if the reaction is allowed to occur at room temperature. Heating the material gave a significant amount of solvolyzed precursor as

1,2,3,4-tetraphenyl-1,3-butadiene, and using THF during reaction⁸ gave a complex mixture on quenching with group-14 chloride. It should also be noted that the reaction typically had an induction period, with the conversion accelerating until completion; therefore, aliquots must be taken, at least for the first few hours, in order to determine the appropriate time for quenching. The induction period varied at each attempt, sometimes significantly.

2.2.2. Synthesis and characterization of 1,1-dichloro-2,3,4,5-tetraphenylgermole, **G1**.



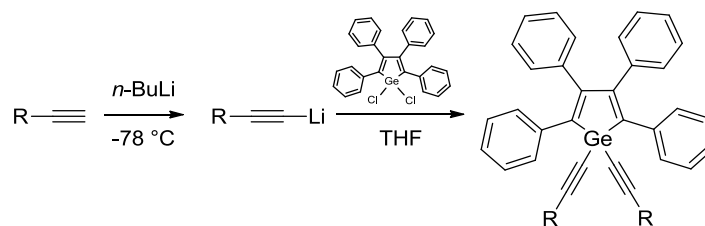
Equation 2-3. Synthesis of **G1**.

Synthesis. Once the precursor **L1** is successfully synthesized, the preparation of the germole that serves as a precursor to other 1,1-disubstituted germoles, 1,1-dichloro-2,3,4,5-tetraphenylgermole (**G1**), can be carried out using the method developed by Curtis.⁹ Originally, it was reported that addition of germanium(IV) chloride to the slurry of **L1** was unsuccessful in synthesizing **G1**;^{7b} however, Curtis reversed this addition, giving good yields on workup for the target compound (Equation 2-3). The benefit of this route is that **G1** is poorly soluble in ether, so the product crashes out of solution immediately as a bright yellow powder and limits its further reaction with additional **L1** towards the other two chlorine atoms on the germanium center. Once the reaction was complete, the material could be isolated through evacuation of the ether, dissolving the material in dichloromethane, and filtering off the lithium salts; concentration of the filtrate followed by cooling in a freezer precipitated pure large crystals of **G1** in several

crops. The reaction scales well and was repeated on several scales up to 20 g theoretical yield with yields ranging from 50-75%. Notably, isolation of **G1** could be done in open air, and the compound exhibits unexpected air/moisture stability in the solid state, as well as moderate stability in solution. This stability is counter to the silicon analogue of **G1**, 1,1-dichloro-2,3,4,5-tetraphenylsilole,¹⁰ which requires that, for both its synthesis and isolation, the system remain stringently free of moisture; it is only moderately stable to moisture in the atmosphere as a solid, and decomposes rapidly in solution on exposure to moisture in the environment.

Characterization. Once **G1** was isolated, it was characterized by NMR and melting point, the latter of which agreed well with the literature.⁹ The ¹H NMR spectrum (Figure A-1) displays a complex mixture of signals in the aromatic region; the integration, which matches the ratio expected for tetraphenyl-substituted metalloles (16:4, total of 20 protons expected), and the region of the shifts observed are generally suggestive of **G-1**. The ¹³C{¹H} spectrum (Figure A-2) displays 10 signals as expected from the symmetry within **G1**, and more importantly exhibits a shift at 150.1 ppm, which is an identifying shift of group 14 metalloles and corresponds to the 3,4-carbons in the germole ring. A melting point was also obtained (198–201 °C), and this agreed reasonably well the melting point reported by Curtis (197–199°C).⁹ Once the synthesis of **G1** was confirmed, it was then used as the precursor for the 1,1-disubstituted germoles prepared by our group (Section 2.2.3).

2.2.3. Synthesis of 1,1-disubstituted-2,3,4,5-tetraphenylgermoles.



Equation 2-4. General route for the synthesis of the 1,1-disubstituted germoles in this study.

The optimized synthesis of **G1** allowed for a useful precursor that could be easily modified. This research project focuses on germanium-carbon bond formation by a facile salt metathesis reaction of a lithium acetylide with **G1** to form 1,1-diethynyl-substituted 2,3,4,5-tetraphenylgermoles; yields for these compounds ranged from 44-70%. The germoles synthesized for this project initially were chosen for their abilities to potentially coordinate to metal centers, or could be synthesized as precursors to do so, and are shown in Figure 2-4.

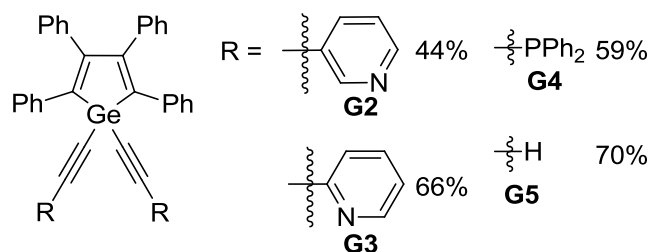
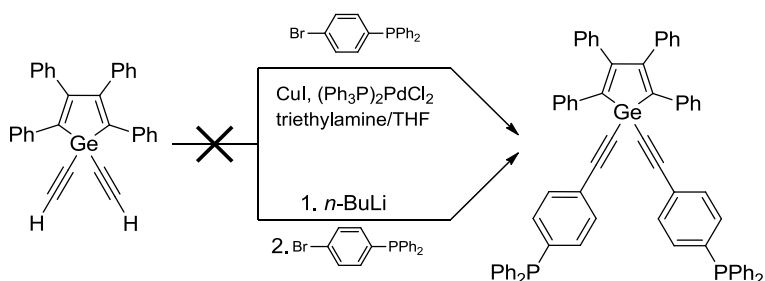


Figure 2-4. Germoles synthesized for this study.

The compounds **G2** and **G3** have pyridine moieties for binding, and **G4** contains the diphenylphosphino- moiety that has been shown to be a good choice of substituent on siloles for coordination with platinum and gold centers by our group.¹¹

The compound **G5**¹² was synthesized as a precursor for extending the coordinating substituents outward away from the germole moiety, as a way of removing potential steric strain on coordination; Sonogashira coupling was performed on 1-ethynyl substituted siloles with aryl iodides to achieve similar results.¹³ In our hands, Sonogashira coupling with (4-bromophenyl)diphenylphosphine produced no reaction, and attempts to lithiate at the terminal ethynyl carbons in order to perform a nucleophilic aromatic substitution on the same aryl bromide yielded a complex mixture (Scheme 2-1).



Scheme 2-1. Attempted routes to coupling **G5** with (4-bromophenyl)-diphenylphosphine.

Isolation. The germoles **G2** to **G5** were initially purified by column chromatography, and further purified for additional analysis (e.g., X-ray crystallography and elemental analysis) by crystallization from solvents, as needed. Experimental Section 4.1 details these isolation procedures. The pyridinyl-substituted germoles **G2** and **G3** needed more polar solvents (dichloromethane and methanol, respectively) in order to begin elution from the silica gel column. This allowed for efficient isolation of the targets with less than typical amounts (*ca.* 60 g/g of compound) of silica gel.

Characterization: NMR. The germoles **G2** to **G5** were all characterized by ¹H NMR and ¹³C{¹H}, as well as ³¹P{¹H} for **G4** (Figure A-3 to Figure A-9, Figure A-10, Figure A-11). The ¹H NMR for these compounds all contained complex aromatic

resonances. Compounds **G2** and **G3** also had shifts downfield of those expected for metalloles, with resolved coupling patterns indicative of their substitution. Compound **G5**¹² also included a terminal alkyne shift at 2.63 ppm, at an integration ratio close to the typical value of terminal acetylenes. The $^{13}\text{C}\{^1\text{H}\}$ NMR shifts, broadly considered, match up to expected shift counts, with the identifying 3,4-carbon shifts on the germole ring present at *ca.* 155 ppm, with **G2** and **G3** having resonances also in that region (assigned to the pyridine ring). Initially, **G4** has more shifts than expected, but this is due to 1-2 bond coupling between the carbon and phosphorus atoms, the latter of which is a 100% abundant NMR-active nucleus (^{31}P). An expanded spectrum of the alkynyl-carbon region is provided in Figure 2-5 to demonstrate this phenomenon.

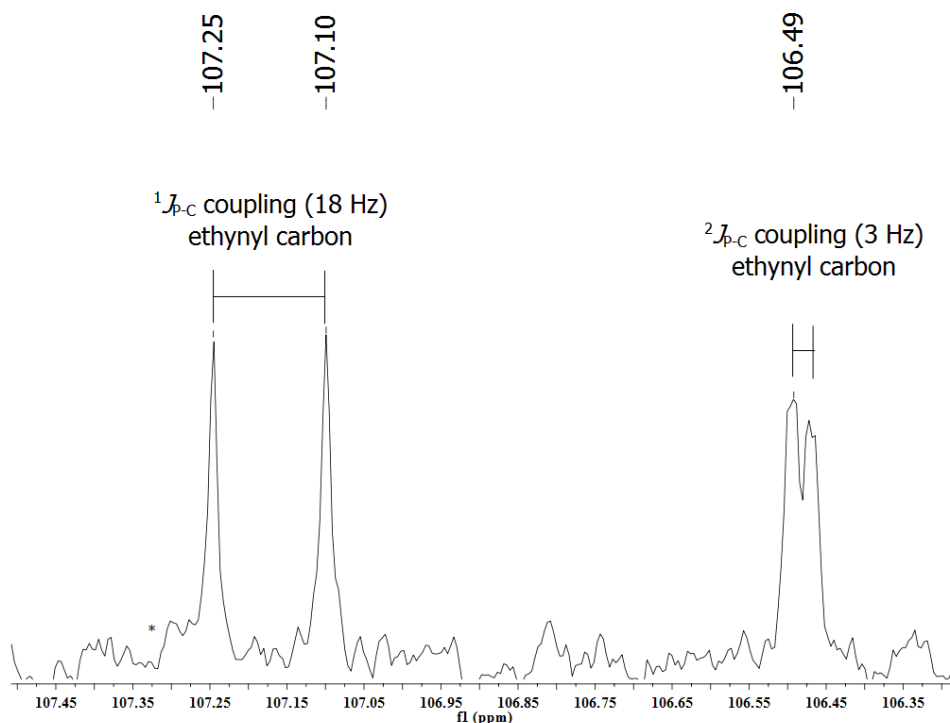


Figure 2-5. Expanded $^{13}\text{C}\{^1\text{H}\}$ NMR spectrum of **G4** demonstrating the ^{31}P - ^{13}C coupling; shifts are assigned to the ethynyl carbons on **G4**.

Characterization: UV-vis and Fluorescence. Compounds **G2** to **G4** were characterized by UV-vis and fluorescence spectroscopies, along with quantum yield determinations (relative to 9,10-diphenylanthracene), in order to gauge the effect that various 1,1-substituents had on these parameters.¹⁴ The data for these germoles is provided in Table 2-1.

Compound	Abs. λ_{\max} , nm	Em. λ_{\max} , nm	Φ_F , % ^a
G2	368	487	0.63
G3	369	486	0.67
G4	369	487	0.71

Table 2-1. Optical data for germoles **G2** to **G4**.

^aWith reference to 9,10-diphenylanthracene.

The optical data reveal little change in the values, even with significant changes in the substituent electronic properties, as well as the overall steric bulk of each substituent. These modest changes in the optical properties on varying 1,1-substituents were noted for siloles;¹⁵ the influence was mainly attributed to subtle inductive effects that changed the electronics of the silole slightly and becomes much less influential as the substituents are more remote from the silole ring. The optical data acquired for this study and by other researchers in our group¹⁴ would suggest that this explanation also carries over for germoles.

2.2.4. Preliminary study of coordination of G4 with (COD)PtCl₂.

The germoles synthesized in this study were initially chosen for their potential to coordinate to metal centers, with the intent to study this coordination structurally. As an example of this, we chose to initially study **G4**, as its phosphine substituents would be a

good potential ligand for, e.g., platinum and palladium centers. Our group studied siloles substituted with diphenylphosphino- groups *para* to the silole ring, and observed optical changes upon coordination to platinum and gold centers.¹⁶ The compound **G4** was reacted with 1 equiv of (COD)PtCl₂ in a dichloromethane solution, and stirred overnight under argon, in a standard ligand substitution reaction of the labile cyclooctadiene for a strongly bound phosphine (Figure 2-6).

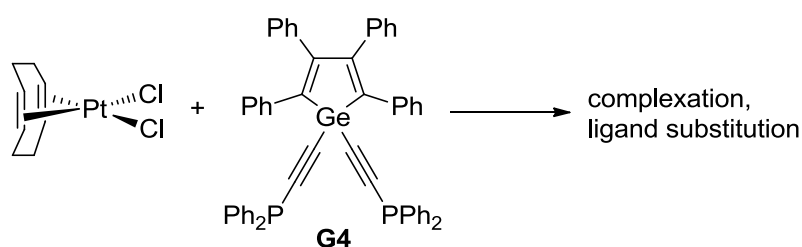


Figure 2-6. The reaction of (COD)PtCl₂ with **G4**.

This yielded a light yellow powder that was significantly insoluble in a range of solvents. A ³¹P{¹H} NMR Spectrum (Figure A-12) was taken of the material in CDCl₃ (a large number of scans were taken in order to get an acceptable signal). The spectrum indicates that, for what could dissolve in solution, there seems to be only one phosphorus environment, downfield of the “free” germole with obvious platinum satellites; all of these would be expected for metal coordination and matches behavior characterized by our group for phosphine-linked siloles and metal centers.^{16b} The shift of the peak in the spectrum (-9.2 ppm) and the ¹J_{PtP} coupling constant (3673 Hz) very closely match a related complex, *cis*-Cl₂Pt(Ph₂P-C≡C-Ph)₂, whose analogous data are -10.8 ppm and 3765 Hz, respectively.¹⁷ Therefore, our tentative assignment based on the NMR data is of a *cis* species of the phosphorus-coordinated **G4** with the platinum center, possibly

oligomeric due to the poor solubility and single phosphorus environment, and a representative figure for the geometry is provided in Figure 2-7.

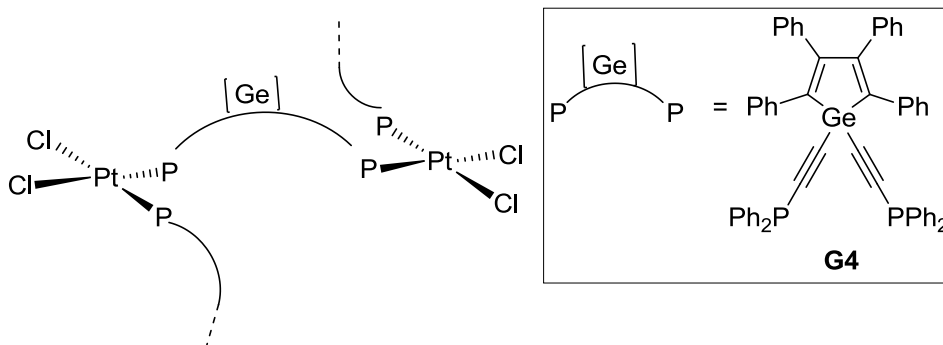


Figure 2-7. The proposed geometry and composition of the product of **G4** and (COD)PtCl₂, based on ³¹P{¹H} data.

2.3. SEM study on the effect of cooling a melt on crystallinity and optical properties.

Tang's group noted for related siloles that the degree of crystallinity in the solid state could induce small hypsochromic or bathochromic shifts from the amorphous sample, and demonstrated this through exposing an amorphous thin film to solvent vapors and showing more crystalline features on removal from the vapors.¹⁸

One way to control the crystallinity of the sample is to melt amorphous material, and vary the degree of cooling. For an example, a sample of **G2** was dissolved in dichloromethane and the solution was deposited on a smooth quartz surface, and then allowed to evaporate into a thin film. Several films were made in order to vary the degree of cooling. Sample 1 was left unheated as a control. Sample 2 was heated in a muffle furnace at 20 °C/min to 235 °C, and then cooled at 2 °C/min to room temperature. Sample 3 was heated at the same rate to 235 °C, cooled to 190 °C, and then removed from the heat.

The solid samples were analyzed for fluorescence by a Varian Cary Eclipse fluorospectrometer, collecting in the fluorescence mode. All samples were excited at 372 nm, and emission was monitored at 400-700 nm. The results are shown in Figure 2-8.

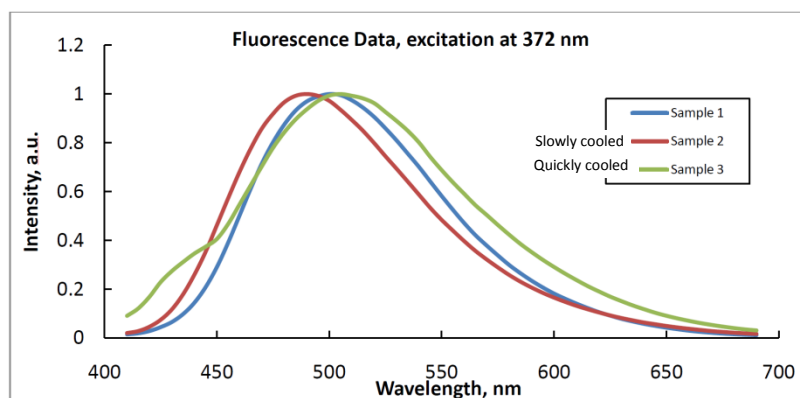


Figure 2-8. Normalized fluorescence spectra of **G2** after two different cooling modes from a melt of a thin film, and an additional thin film where no heating was performed.

As can be seen in Figure 2-8, the emission for the slowly cooled sample (Sample 2) shows a hypsochromic shift from the initial amorphous sample (*ca.* 20 nm), while the quickly cooled sample (Sample 3) shows a similar emission maximum but a broader peak than the amorphous material. This phenomenon was also observed for related silole systems, suggesting that increased crystallinity can induce small electronic changes in the molecules.⁶

The data above suggests that the slowly cooled sample is likely more crystalline than the quickly cooled sample. In order to confirm this, SEM imaging was performed on each of the samples. As the compound is non-conductive, each sample had to be coated in gold using a Hummer 6 Sputtering System, after being evacuated for several hours. The coated samples were analyzed using a JEOL 6320F Field Emission SEM. After standard startup and alignment procedures, each sample was imaged by attempting

several different parameters. The best images were acquired at working distances of 8 and 15 mm, using an accelerating voltage of 15 kV. The resulting images are shown in Figure 2-9, Figure 2-10, and Figure 2-11.

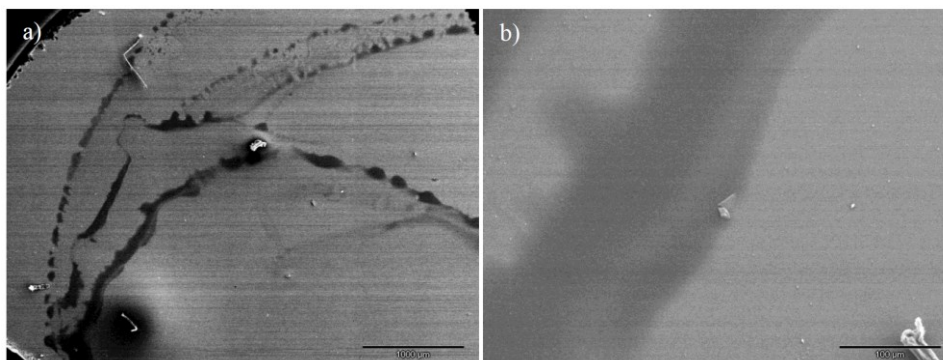


Figure 2-9. Sample 1 at magnifications of a) 25X and b) 250X. Images acquired using an acceleration voltage of 15 kV, a working distance of 15 mm, a probe current setting of #3, an aperture setting of #3, and using the lower SE detector.

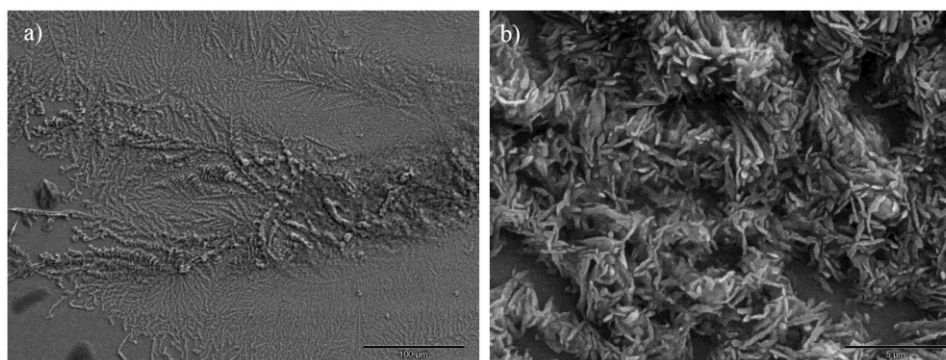


Figure 2-10. Sample 2 at magnifications of a) 250X and b) 5000X. Images acquired using an acceleration voltage of 15 kV, a working distance of 15 mm, a probe current setting of #3, an aperture setting of #3, and using the lower SE detector.

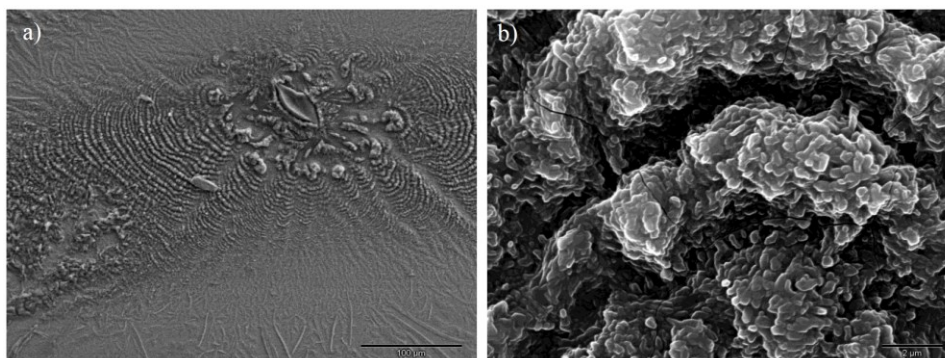


Figure 2-11. Sample 3 at magnifications of a) 250X and b) 7500X. Images acquired using a) an acceleration voltage of 15 kV, a working distance of 15 mm, a probe current setting of #3, an aperture setting of #3, and using the lower SE detector; b) an acceleration voltage of 15 kV, a working distance of 8 mm, a probe current setting of #3, an aperture setting of #3, and using the upper SE detector.

As can be seen in the above figures, there is a definite change in the appearance of the samples. Sample 1 is completely amorphous; even at very high magnifications no crystalline features could be detected. Sample 2 is the most crystalline, with needle-shaped microcrystals easily shown. Sample 3, as suspected, shows an intermediate stage of crystal formation. The macrostructure looks rather amorphous, but upon increasing the magnification (Figure 2-11b), some secondary features are noticeable, as if crystal growth was arrested and small globular surfaces formed instead. The intermediate nature of the solid might explain the broadened emission; if **G2** was polymorphous in Sample 2, the emission might be a combination of emissions from several polymorphs of the same material. By comparison, emission spectra of Samples 1 and 3 are significantly sharper, indicating a more ordered crystal structure for Sample 3 and a well-averaged environment for Sample 1.

2.4. X-ray crystallography of 2,3,4,5-tetraphenyl-1,1-disubstituted germoles.

2.4.1. General comments on molecular structures.

In addition to the tetraphenyl-substituted compounds shown above, our group also synthesized a series of other similar compounds with even more variations at the 1,1-positions. Figure 2-12 shows the range of compounds synthesized; all but the thiophenyl-substituted germole was characterized structurally in this study (it having been characterized by another researcher in our group), and each compound is addressed individually below (data reference for compounds **G2-G14** is included in Table A-1).

Most of the crystal mounting, centering, and data collection and reduction were performed with the assistance of Teresa Bandrowsky, while the data solution and refinement was performed by this researcher. Generally, the bond distances and other parameters were within the expected range for germoles,¹⁹ and selected measurements for the structures can be found in Sections 5.3.1 in the Appendix.

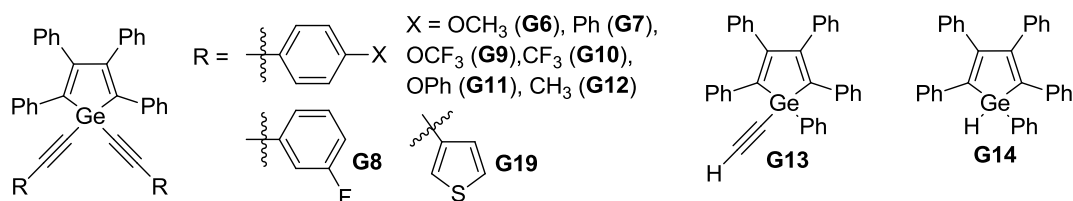


Figure 2-12. The additional tetraphenylgermoles studied crystallographically.

Refinements were performed using the ShelX package;²⁹ as such, terms used to describe restraints and special refinement instructions are alluded to below; a brief description of the instructions used in refinement are therefore presented herein.²⁰ A PART instruction in SHELXL is used to model disorder, and accounts for electron density from a disordered portion of the molecule from two or more orientations.

Generally the occupancies are linked such that the total occupancy of all disordered sections adds to unity. A DELU instruction applies a restraint on atoms in a bond such that the components of the anisotropic parameters of these atoms are similar with a defined standard of deviation (i.e., the ellipses are oriented along a similar direction, commonly called a “rigid bond” restraint). A DFIX restraint restricts the distance between atoms to a certain value, within a standard of deviation set by the operator. An ISOR restraint restricts the anisotropically modeled atoms to behave as approximately isotropic, within a standard of deviation set by the operator. A DANG restraint restricts the distance of atoms connected by an intermediate atom, and is used to set the angle formed by these atoms within a standard of deviation set by the operator. An AFIX constraint sets the arrangement of a group of atoms to a particular geometry, e.g., t-butyl groups, benzene rings, and others.

Compounds **G2** (Figure A-49) and **G3** (Figure A-50) yielded very crystalline material on slow crystallization from diffusion of hexane into a dichloromethane solution, and the structural and refinement details (Table A-1) indicate strong, highly resolved data.

Compound **G4** (Figure A-51) also crystallized well from slow evaporation of a diethyl ether solution. Its data were collected at room temperature; therefore, the ellipses (indicating 50% probability of electron density at each atom, Figure A-51) are notably expanded compared to the others taken at lower temperature. Also likely because of the temperature of collection, some resolvable disorder exists, including the phosphorus atom and a phenyl ring at one of the diphenylphosphino- moieties (P1 and C33–C38). These atoms were therefore split into separate parts (using PART). Initial refinements included

the AFIX 66 constraint at the phenyl rings (i.e., a regular hexagon) until the model was further settled, and was then removed in the final refinement stages. The occupancies between these two parts were linked, a DELU restraint was applied to each disordered phenyl ring, and finally refined to a ratio of *ca.* 58:42, improving the ultimate R_1 to 3.90% (initially from more than 5%).

Compound **G6** (Figure A-52) was crystallized from a THF/methanol solution by slow diffusion. Therefore, the compound crystallized with THF in the lattice in a ratio of 1:1 **G6**/THF (Figure A-52). Initial refinements assumed one orientation of the THF molecule; however, refinement would not converge, and there existed significant electron density about the THF molecule (*ca.* $3 \text{ e } \text{\AA}^{-3}$). It was suspected that this electron density could be indicative of a disordered THF molecule, so the largest unassigned peak was assigned as the oxygen of the disordered THF, and additional unassigned peaks of appropriate geometry were assigned to the carbon atoms of the disordered THF. The disorder was modeled using the PART function, and the occupancies of the two parts were linked. The DFIX and ISOR restraints were applied to restrain the disordered THF molecule to chemically sensible geometries. This greatly improved the residual density value ($0.65 \text{ e } \text{\AA}^{-3}$, more closely matching the magnitude of the hole value), and significantly improved the model overall, decreasing R_1 from 5.43% to 3.92%. The disordered THF molecule refined to a ratio of its parts of 58:42.

Crystals for compound **G7** (Figure A-53) were difficult to obtain, but ultimately a small crystal was isolated that proved suitable for crystallography. Usable reflections could only be collected out to $2\theta = 34^\circ$, and the relatively high $R(\text{int})$ value is indicative of the weakly diffracting data. Nevertheless, the model was refined adequately with the

limited data available, enough to firmly establish connectivity (Figure A-53). The asymmetric unit contains 3 molecules of **G7**, and overall $Z = 12$. Platon²¹ ADDSYM was performed on the model to ensure no additional symmetry was missed in initial refinements; the calculations did not suggest any higher symmetry space groups.

Compound **G8** (Figure A-54) crystallized very well from a slow evaporation of a dichloromethane/hexanes mixed-solvent system. The reflection data were strong, indicated by a high $I/\sigma(I) = 28.2$, and was solved and refined well in the triclinic $P-1$ space group.

Crystals of **G9** (Figure A-55) were also difficult to crystallize; plate-like crystals ultimately formed after several months of very slow evaporation from a capped vial. Nevertheless, obtaining a suitable crystal for diffraction still proved a challenge, and the data collected on the crystal chosen was of moderate quality. Usable reflections could be collected past $2\theta = 50^\circ$, but the $R(\text{int}) = 0.0707$ indicates moderate diffraction quality. The structure was solved with 2 molecules of **G9** in the asymmetric unit. The Olex2 software package²⁴ indicated a centrosymmetric space group could be possible ($P2/c$), but the structure was unsolvable in this space group. There remains some high electron density near each molecule ($3 \text{ e } \text{\AA}^{-3}$), and very weak residual electron density peaks indicate an arrangement that closely resembles the germole ring, and immediate substituents attached to it; this is probably a result of the weak data collected.

Compound **G10** (Figure A-56) solved and refined well from good reflection data. Disorder was apparent on the $-\text{CF}_3$ substituents. The fluorine atoms were split and assigned to different PART fragments, and the C-F distances were restrained using DFIX restraints. The restraints ISOR and DANG were also used during refinement for the

disordered groups. Once the disorder was addressed, the model refined well, with the two separate $-\text{CF}_3$ groups at each 1,1-substituent refining to a ratio of 52:48.

Compound **G11** (Figure A-57) also crystallized well, and good reflection data were obtained. The structure was solved in the non-centrosymmetric (polar) space group Cc (Flack parameter = 0.390(19)).

Compound **G12** (Figure A-58) crystallized well, with good reflection data. The structure was solved and refined in the triclinic space group $P-1$.

Compound **G13** (Figure A-59) was solved and refined in the monoclinic $P2_1/c$ space group, and contains two molecules in the asymmetric unit. The data were of moderate quality, as indicated by the $R(\text{int})$ value; however, usable reflections were collected to $2\theta = 50.28^\circ$, and the model refined well with the data obtained. This compound was synthesized as a precursor to cross-couple with various aryl-halides for differing functionalization, in a route similar to the analogous silole.¹³

Compound **G14** (Figure A-60) also refined in the monoclinic $P2_1/c$ space group. The $R(\text{int})$ value indicated moderate data quality (due to the temperature controller having an error around 75% collection), but the model solved and refined well with the data available, with 98.9% completeness. This structure was synthesized as a precursor in order to functionalize the germole through a hydrogermylation reaction of alkynes, similar in approach to reactions performed with the analogous silole by Trogler's group.²²

Some averaged measurements of the germoles above were compared to the Cambridge Structural Database data of other known germacyclopentadienes.²³ The averaged angle between the germanium and the carbons directly bonded to it on the germole ring were 91.3° , matching the average value from the database at 91.3° . The

average C=C and C-C bond lengths for the germoles in this study are 1.358 and 1.518 Å, respectively, which are both close matches to the CSD data of 1.350 and 1.507 Å, if not slightly longer. The average magnitude of the torsions for the 2,5-phenyl and 3,4-phenyl groups was 34.8° and 63.8°, respectively; these are both agreeable with the analogous torsions of siloles, being ~30° and ~70°, respectively.⁶

2.4.2. Packing arrangements of the tetraphenylgermoles.

As previously discussed, the arrangement of the 2,3,4,5-tetraphenyl-substituents of siloles proved to significantly affect the packing in their crystal structures, and also prevented the parallel arrangement of silole molecules that otherwise would have decreased their emission quantum yield in the solid state (through aggregation-caused quenching, or ACQ).⁶ Moreover, these fluorescent molecules undergo a hypsochromic shift upon increasing crystallinity, which again is opposite behavior to most chromophores. In the SEM study performed above (Section 2.3), it was observed that the slowly cooled sample underwent the same hypsochromic shift, and this correlated to an increased crystallinity upon analysis by SEM. Therefore, understanding the packing arrangement of these compounds in the crystalline state is important to explain this behavior.

The packing of these molecules is mainly guided by the propeller-shaped arrangement of the phenyl substituents. For example, Figure 2-13 demonstrates this orientation for **G2**.

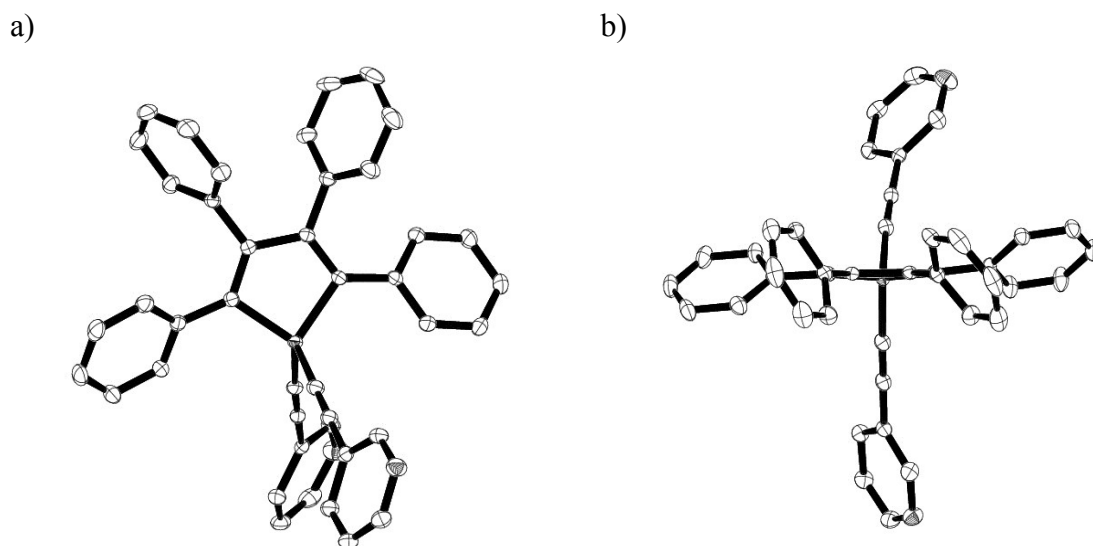


Figure 2-13. The structure of **G2**, with the perspective a) perpendicular to the germole ring, and b) parallel to the germole ring, the latter of which demonstrates the propeller-like arrangement of the 2,3,4,5- phenyl substituents. Hydrogens have been removed for clarity

It should be noted that almost all of the tetraphenyl-substituted germoles in this structural study had a similar arrangement of the phenyl substituents, except for **G14**,⁹ which curiously has the 2,3- phenyl groups rotating in the opposite direction as the 4,5- phenyl groups. This is depicted in Figure 2-14. The main difference between this compound and the other germoles studied is that only one exocyclic substituent at the germanium center has significant steric influence; therefore, this unsymmetric influence, upon crystallization, may be involved in the unique arrangement due to packing considerations.

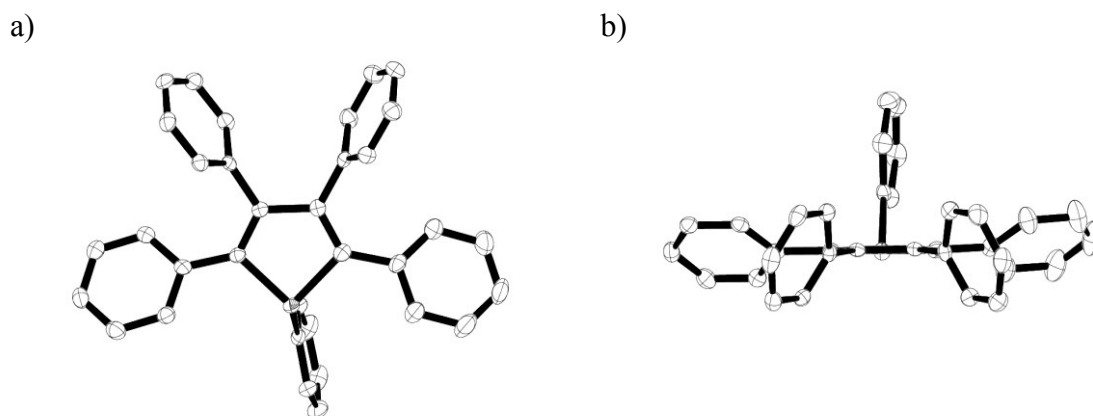


Figure 2-14. The structure of **G14**, with the perspective a) perpendicular to the germole ring, and b) parallel to the germole ring, the latter of which demonstrates the unique opposing arrangement of the 2,3,4,5- phenyl substituents. Hydrogens have been removed for clarity.

In a similar way to many analogous 2,3,4,5-tetraphenylsiloles,⁶ the phenyl substituents on the germoles studied seem to influence crystallization in a way that minimizes any parallel arrangement of aromatic groups, and as a consequence would likely limit any π - π stacking and exciplex formation as noted for many planar fluorophores. An example of this effect is provided in Figure 2-15, which shows the arrangement of **G8** in the crystal lattice, and also shows the minimal parallel aryl group interactions intermolecularly. This is the main cause for both crystallization enhanced emission and absence of aggregation-caused quenching in this class of molecules.

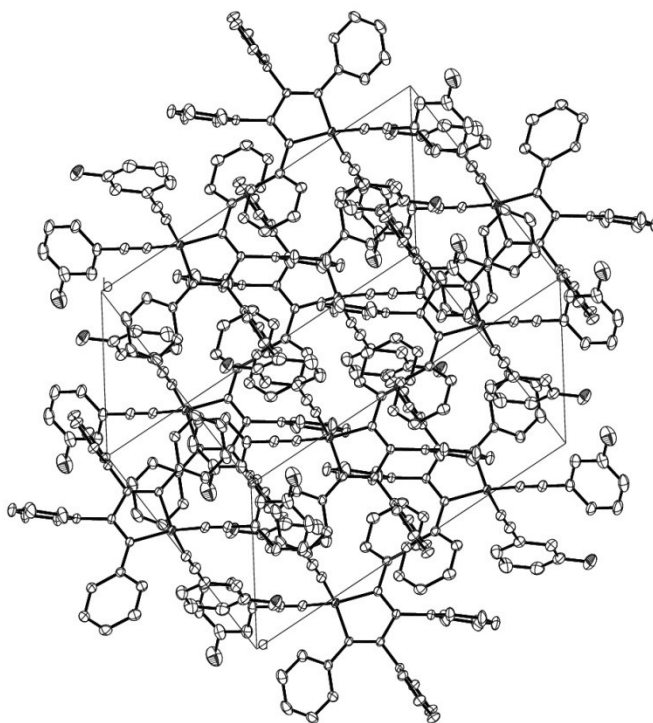


Figure 2-15. The extended packing for the **G8** lattice, which shows minimal parallel interactions between aryl groups, which limits π - π interactions in the solid state (a main requirement for ACQ).

The Olex2 crystallography software program²⁴ includes a tool for searching for π -systems, and whether or not these have any potential for interaction intermolecularly (the tool is referred to in the program as “Analyze π - π interactions”). In the case of **G8**, this tool also did not discover any π - π interactions with the usual requirements,²⁵ which reflects the qualitative inspection of the crystal packing. The closest distance between the centroids of the germole 5-membered rings in **G8** is 7.4 Å, which is much too far away for any significant interactions. Most of the germoles studied indicated no aryl group interactions, except, for instance, the pyridine-substituted germoles, including **G2**, where the pyridine ring is within the required distance from a phenyl group on another molecule

in the crystal (at 3.44 Å); however, the non-parallel arrangement suggests that this interaction is weak, and could possibly be a consequence of crystal packing (Figure 2-16).

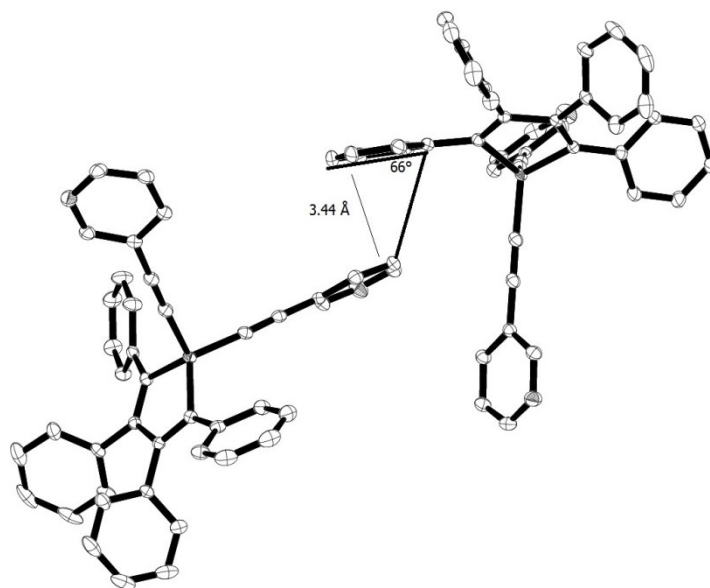


Figure 2-16. The closest aryl group interaction in **G2**. The non-parallel arrangement indicates any π -interactions are weak, if not non-existent (some measurements are included in the Figure).

2.5. X-ray crystallography of differently substituted germafluorenes.

2.5.1. General comments on molecular structures.

In addition to study of tetraphenyl-substituted germafluorenes, our group also has studied another class of cyclic germanium compounds referred to as germafluorenes, which are analogous to fluorene, where a germanium atom replaces the carbon at the 9-position (Figure 2-17). These molecules were synthesized in a similar fashion to related silafluorenes;²⁶ the optical spectra of which were found to be similarly red-shifted (compared to fluorene) due to the special orbital overlap conveyed by the silicon center, similar to the effect seen on siloles. Most of the crystal mounting, centering, and data

collection and reduction were performed with the assistance of Teresa Bandrowsky, while the structure solution and refinement was performed by this researcher. Generally, the bond distances and other parameters were within the expected range, and selected measurements for the structures can be found in Sections 5.3.2 in the Appendix.

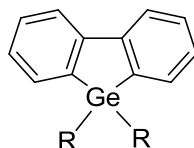


Figure 2-17. The fundamental structure of germafluorene, as analogous to the all-carbon analogue, fluorene.

During the course of study by our group, four germafluorene molecules were synthesized that were suitable for study by X-ray crystallography. These are depicted in Figure 2-18. Compounds **G15** and **G16** were both synthesized from the precursor germafluorene **G17** using Sonogashira conditions and the appropriate terminal acetylene.²⁷ Compound **G18** was synthesized as a precursor for which Sonogashira conditions could be applied to functionalize the germafluorene core at the 3,6-position with acetylene-based groups, in order to study optoelectronic changes comparing between these and the 2,7-substituted analogues such as **G15** and **G16**. The individual molecular structures obtained are described below.

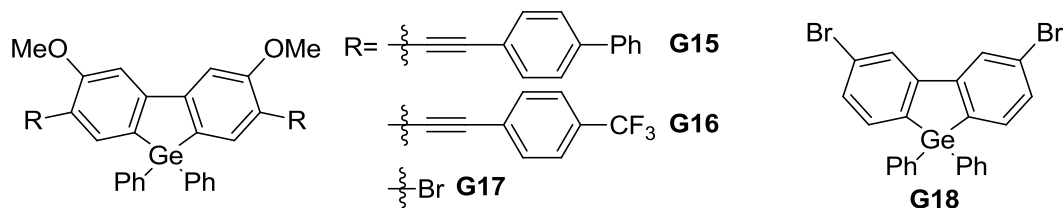


Figure 2-18. The germafluorenes that were determined by X-ray crystallography for this study.

Compound **G15** (Figure A-61), like the biphenyl-substituted germole **G7**, proved difficult to crystallize, but a crystal of adequate quality was obtained, and the structure was able to be solved. The data for **G15** in Table A-2 show that the crystal was only just suitable enough to obtain connectivity; the $R(\text{int})$ value (0.2036), combined with the significant difference between $R_1(I > 2\sigma)$ and $R_1(\text{all data})$ (10.82% and 26.67%, respectively), indicates weakly diffracting data. This may also explain the large deviations from expected angle for the *sp* carbons to the germafluorene core (164° and 173° , ca. 175° for similarly substituted group 14 fluorenes²⁸). The torsions of the methoxy- substituents are very small, and in plane with the germafluorene core. The phenyl groups directly attached to the *sp* carbons are also close to planar with the core, while the most removed phenyl substituents begin to display some twisting. These substituent arrangements become important for considerations on the packing ability of this molecule (*vide infra*).

Compound **G16** (Figure A-62), as opposed to the germafluorene above, was crystallized and gave strong diffraction data, as indicated by its values in Table A-2. The structural model as solved has the germanium atom on a special position ($\frac{1}{2}, y, \frac{1}{4}; y=0.780467$) with C_2 site symmetry; the structure, therefore, has only half of the molecule in the asymmetric unit. The molecular structures displayed, e.g. Figure A-62, are symmetrically generated to reveal the full molecule, as suggested by the numbering of the atoms. The molecule is considerably planar, with the trifluoromethylphenyl-substituent in plane with the germafluorene core, and as was the case with **G15**, has important considerations in packing. The trifluoromethyl-substituent is relatively

ordered compared to those of **G10**; no disorder instructions were necessary for refinement.

Compound **G17** (Figure A-63) was the precursor used to synthesize both **G15** and **G16**, and was crystallized from a cross-coupling reaction mixture, and the crystal chosen for analysis yielded good diffraction data, crystallizing in the monoclinic space group $P2_1/c$. The methoxy-substituents are in the plane of the germafluorene core, as indicated by the small torsion angles observed (less than 10° in magnitude for both), and are similarly arranged to the subsequently synthesized germafluorenes above.

Compound **G18** is another germafluorene synthesized such that the bromo-substituents are at the 3,6-positions, instead of the 2,7-positions, and replace the methoxy-substituents of the previous germafluorenes. The diffraction data suggest an intermediate quality compared to other germafluorenes studied. The structural model solved and refined with 2 molecules in the asymmetric unit, also in the monoclinic space group $P2_1/c$. It should be noted that the second weight parameter in the ShelXL²⁹ refinement is very large (*ca.* 92.1); the PLATON-based IUCr checkcif utility³⁰ suggested possible twinning could explain this; however, both the TwinRotMatrix package included in the PLATON²¹ executable and the twinning analysis included in Olex2²⁴ did not suggest alternatives that significantly improved this parameter. The mostly likely cause is the intermediate quality of the crystals chosen for diffraction.

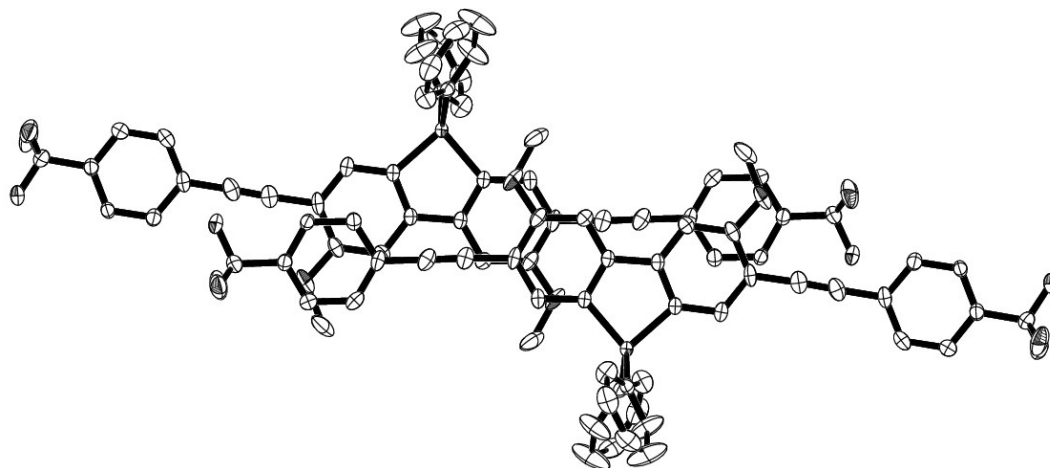
2.5.2. Packing arrangement of the germafluorenes studied.

The packing arrangement of the germafluorenes is also of interest because of future potential applications for AIE active compounds. Therefore, an analysis of any potential π -stacking interactions can be used to anticipate their utility in this regard, as well as

offering useful data to improve their performance. The packing of each molecule will be described briefly below.

Both germafluorenes **G15** and **G16** are considerably planar molecules. An analysis of the distances between the closest arrangements for these molecules in the lattice will reveal if there are any potential π - π interactions. The closest packing arrangement for **G16** is provided in Figure 2-19 as an example, with two orientations.

a)



b)

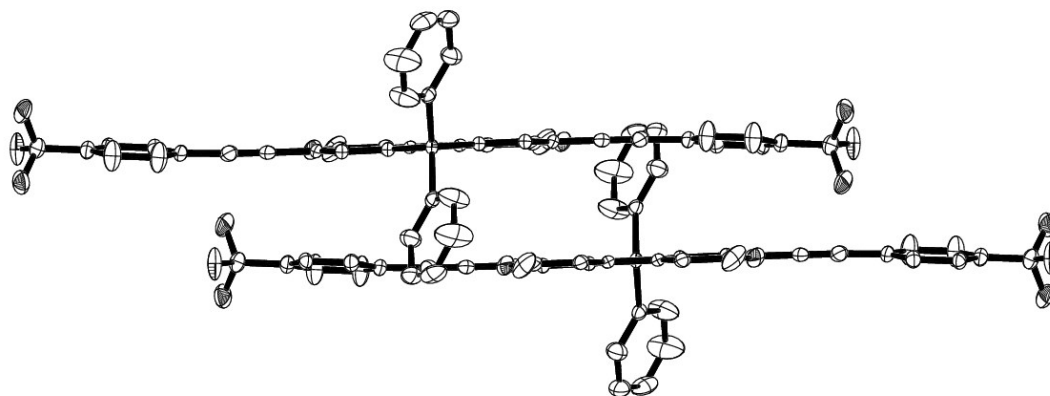


Figure 2-19. Two views, a) perpendicular to the germafluorene core and b) parallel to the germafluorene core, of the closest packing arrangement between two molecules of **G16** in the crystal lattice. Hydrogens are removed for clarity.

The germafluorene cores are offset from one another in order to minimize steric repulsion from the out-of-plane phenyl substituents on the germanium atom. These phenyl groups are also angled towards opposite directions from one another for this reason. Olex2 was used to calculate the mean plane of the germafluorenes for distance analysis. Accounting for the shift in the planes, the distance between the two was 3.67 Å, which is probably representative of the average distance between the π -systems of the two molecules overall, and is within the range of 3–4 Å required for π - π interactions; the two molecular planes are also parallel to each other, which is another requirement. Olex2 also detected additional potential π - π interactions between the outermost phenyl groups of adjacent molecules. The angle between the planes indicates that these are close to parallel (*ca.* 10° between planes), with an average distance of 3.8 Å. This interaction is depicted in Figure 2-20, and also explains the higher degree of twisting for this outer phenyl group versus the same substituent on the opposing side of the molecule.

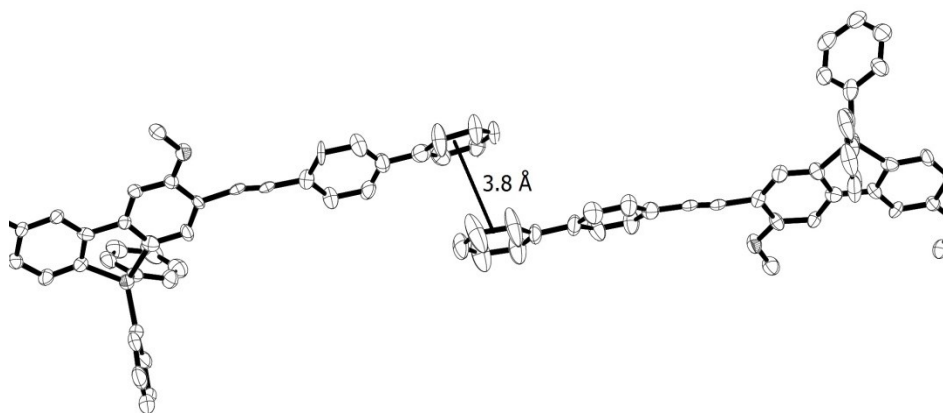


Figure 2-20. A depiction of **G16**, enlarged to show the additional potential π -interaction site. Hydrogens are removed for clarity, and a line indicating the distance measured is included.

Additional optical spectroscopic analysis would be required to determine if this arrangement in the crystalline state could potentially cause aggregation-caused quenching, or is a coincidence of packing effects. Additional substitution at the germafluorene core would potentially be necessary in order to break this parallel arrangement by increasing steric repulsion between germafluorene cores in a method similar to the 2,3,4,5-tetraphenyl systems above.

The closest packing arrangement of **G17** is depicted in Figure 2-21, and is similar in arrangement the prior two germafluorenes, with the germafluorene cores staggered and phenyl groups opposed so as to minimize steric repulsion intermolecularly. Figure 2-21b gives a more readily apparent depiction of the oppositely oriented phenyl groups at the germanium center that was exhibited for the prior germafluorenes.

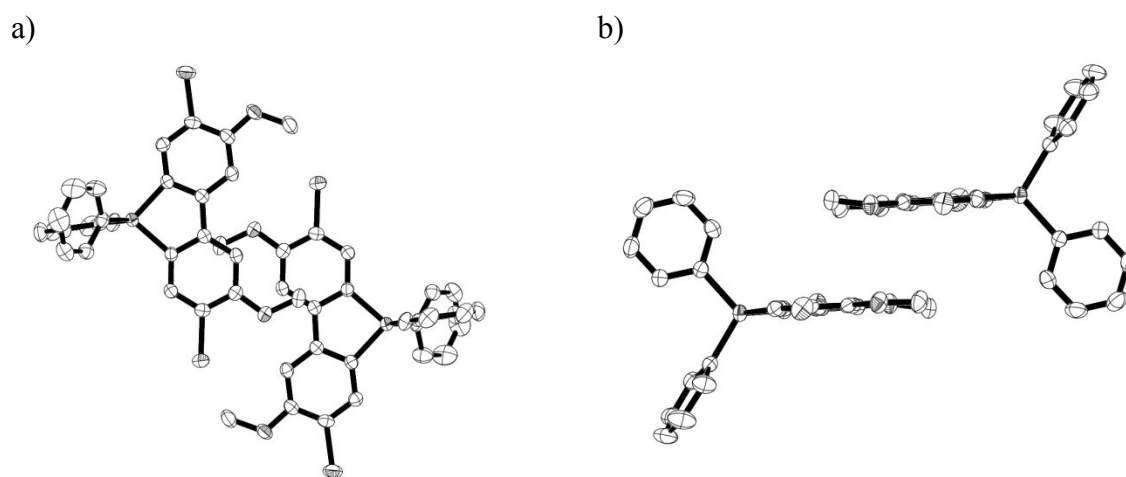


Figure 2-21. Two views, a) perpendicular to the germafluorene core and b) parallel to the germafluorene core, of the closest packing arrangement between two molecules of **G17** in the crystal lattice. Hydrogens are removed for clarity.

The intermolecular distance between the planes of the germafluorene core in **G17**, accounting for the offset, is 3.45 Å, which is closer than the previous examples, probably because the bromine substituent is considerably less sterically demanding than the trifluoromethylphenyl substituent as above. However, Figure 2-21a indicates that these molecules may be offset enough to limit π - π interactions.

Compound **G18** packs slightly differently than the other germafluorenes studied, as show in Figure 2-22. The 3,6-bromo substituents are oriented such that they are close to one another, forming a “channel” arrangement that extends throughout the extended packing of the molecule. Instead of packing such that the phenyl groups are alternately opposed, as with the other germafluorenes studied, **G18** packs such that the two most closely packed germafluorenes have their phenyl substituents staggered on the same side, as indicated in Figure 2-22. The distance between the planes formed by the germafluorene core, as calculated by Olex2, is 3.6 Å, around the same value as the other germafluorenes studied.

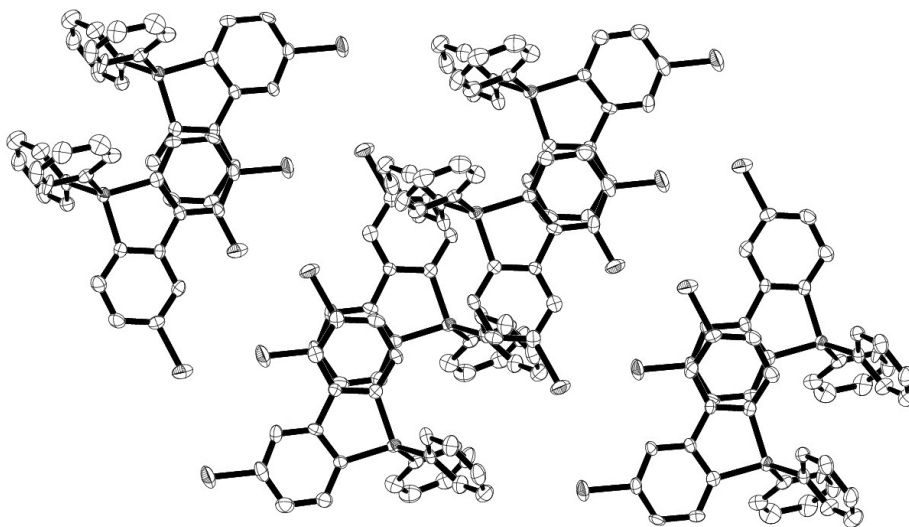


Figure 2-22. The packing arrangement of **G18** in the crystal lattice.

2.6. Summary

Several new 2,3,4,5-tetraphenylgermoles, with 1,1-substituents chosen for their potential behavior as ligands to metal centers, were synthesized and fully characterized by multinuclear NMR, UV-vis, and fluorescence spectroscopies, X-ray crystallography, and elemental analysis. A study of crystallization-enhanced emission was performed on **G2** via scanning electron microscopy analysis of several melts cooled at different rates. The slowly cooled melt showed much more crystalline features, along with a blue shift in the solid fluorescence spectrum as was observed for several analogous tetraphenylsiloles.⁵

Along with the tetraphenylgermoles synthesized for this study, our group synthesized a series of other germoles with various 1,1-substituents. All of the germoles synthesized were able to be characterized crystallographically, and generally yielded good structures, except for **G7** and **G9**, the structures of which were only of appropriate quality to establish connectivity. Additionally, the packing of the germoles in the crystal lattice was investigated in order to confirm the absence of any potential π - π interactions; generally, the structures were found to pack in such a way as to limit the close contact of the germole ring system in a similar fashion to related silole systems.⁶

Four new germafluorene compounds were also synthesized by our group, and characterized crystallographically for this study. Compound **G15** gave rather poor data, but was enough to establish connectivity of the molecule. Compounds **G16** and **G17** crystallized well with strong data, while **G18** gave data quality intermediate between **G15** and **G16/G17**, enough to establish the connectivity but not without some special parameters in refinement (*vide supra*). The packing of this class of compounds was also

analyzed to compare similarities and differences with the tetraphenylgermole class compounds. As analyzed here, all compounds were found to pack in a stacked arrangement, due to their relatively planar structures. The closest packed intermolecular distances ranged from 3.45 – 3.8 Å, within the distance for potential π - π interactions, along with having a parallel arrangement of the π -system. Additional studies would be needed to confirm the presence or absence of these effects in relation to fluorescence quenching in the solid state.

2.7. References

- (1) Hissler, M.; Dyer, P. W.; Réau, R. *Coord. Chem. Rev.* **2003**, *244*, 1–44.
- (2) (a) Tamao, K.; Yamaguchi, S.; Shiro, M. *J. Am. Chem. Soc.* **1994**, *116*, 11715–11722; (b) Yamaguchi, S.; Endo, T.; Uchida, M.; Izumizawa, T.; Furukawa, K.; Tamao, K. *Chem. Eur. J.* **2000**, *6*, 1683–1692.
- (3) Luo, J.; Xie, Z.; Lam, J. W. Y.; Cheng, L.; Tang, B. Z.; Chen, H.; Qiu, C.; Kwok, H. S.; Zhan, X.; Liu, Y.; Zhu, D. *Chem. Comm.* **2001**, 1740–1741.
- (4) (a) Chen, J.; Law, C. C. W.; Lam, J. W. Y.; Dong, Y.; Lo, S. M. F.; Williams, I. D.; Zhu, D.; Tang, B. Z. *Chem. Mater.* **2003**, *15*, 1535–1546; (b) Yin, S.; Peng, Q.; Shuai, Z.; Fang, W.; Wang, Y.-H.; Luo, Y. *Phys. Rev. B.* **2006**, *73*, 205409.
- (5) Hong, Y.; Lam, J. W. Y.; Tang, B. Z. *Chem. Comm.* **2009**, 4332.
- (6) Liu, J.; Lam, J. W. Y.; Tang, B. Z. *J. Inorg. Organomet. P.* **2009**, *19*, 249–285.
- (7) (a) Smith, L. I.; Hoehn, H. H. *J. Am. Chem. Soc.* **1941**, *63*, 1184–1187; (b) Leavitt, F. C.; Manuel, T. A.; Johnson, F.; Matternas, L. U.; Lehman, D. S. *J. Am. Chem. Soc.* **1960**, *82*, 5099–5102.
- (8) *Organometallic Syntheses*; Eisch, J.J.; King, R.B. Eds.; Academic Press: New York, 1981, 98-100.
- (9) Curtis, M. D. *J. Am. Chem. Soc.* **1969**, *91*, 6011–6018.
- (10) (a) Jutzi, P.; Karl, A. *J. Organomet. Chem.* **1981**, *214*, 289–302; (b) Joo, W. C.; Park, Y. C.; Kang, S. K.; Hong, J. H.; Kong, Y. K. *Bull. Korean Chem. Soc.* **1987**, *8*, 270–2.
- (11) (a) Braddock-Wilking, J.; Gao, L.-B.; Rath, N. P. *Dalton Trans.* **2010**, *39*, 9321–9328. (b) Braddock-Wilking, J.; Gao, L.-B.; Rath, N. P. *Organometallics* **2010**, *29*, 1612–1621.
- (12) (a) Lebedev, B. V.; Milov, V. I.; Kiparisova, E. G.; Sladkov, A. M.; Luneva, L. K. *Zh. Fiz. Khim.* **1975**, *49*, 2716–17; (b) Vasneva, N. A.; Gavrilova, O. N.; Sladkov, A. M. *Izv. Akad. Nauk SSSR, Ser. Khim.* **1978**, 2149–51.

-
- (13) Li, Z.; Dong, Y. Q.; Lam, J. W. Y.; Sun, J.; Qin, A.; Häußler, M.; Dong, Y. P.; Sung, H. H. Y.; Williams, I. D.; Kwok, H. S.; Tang, B. Z. *Adv. Funct. Mater.* **2009**, *19*, 905–917.
- (14) Bandrowsky, T. L.; Carroll, J. B.; Braddock-Wilking, J. *Organometallics* **2011**, *30*, 3559–3569.
- (15) Zhan, X.; Barlow, S.; Marder, S. R. *Chem. Comm.* **2009**, 1948–1955.
- (16) (a) Braddock-Wilking, J.; Gao, L.-B.; Rath, N. P. *Dalton Trans.* **2010**, *39*, 9321–9328; (b) Braddock-Wilking, J.; Gao, L.-B.; Rath, N. P. *Organometallics* **2010**, *29*, 1612–1621.
- (17) Johnson, D. K.; Rukachaisirikul, T.; Sun, Y.; Taylor, N. J.; Canty, A. J.; Carty, A. J. *Inorg. Chem.* **1993**, *32*, 5544–5552.
- (18) Dong, Y.; Lam, J.W.Y.; Qin, A.; Li, Z.; Sun, J.; Dong, Y.; Tang, B.Z. *J. Inorg. Organomet. Polym.* **2007**, *17*, 673–678.
- (19) Cambridge Structural Database (CSD version 5.32) search performed on 07/12/2013.
- (20) Sheldrick, G.M. User guide to crystal structure refinement with SHELXL. http://shelx.uni-ac.gwdg.de/SHELX/shelxl_user_guide.pdf (accessed 07/12/2013)
- (21) Spek, A.L. *Acta Cryst.* **2009**, *D65*, 148–155.
- (22) (a) Sanchez, J. C.; Urbas, S. A.; Toal, S. J.; DiPasquale, A. G.; Rheingold, A. L.; Trogler, W. C. *Macromolecules* **2008**, *41*, 1237–1245; (b) Sanchez, J. C.; Trogler, W. C. *Macromol. Chem. Phys.* **2008**, *209*, 1527–1540.
- (23) Cambridge Structural Database (CSD version 5.32) search performed on 02/24/2011.
- (24) Dolomanov, O.V.; Bourhis, L.J.; Gildea, R.J.; Howard, J.A.K.; Puschmann, H. *J. Appl. Cryst.* **2009**, *42*, 339–341.
- (25) (a) Hunter, C. A.; Sanders, J. K. *J. Am. Chem. Soc.* **1990**, *112*, 5525–5534; (b) Sinnokrot, M. O.; Valeev, E. F.; Sherrill, C. D. *J. Am. Chem. Soc.* **2002**, *124*, 10887–10893.
- (26) Wong, W. W.; Hooper, J. F.; Holmes, A. B. *Aust. J. Chem.* **2009**, *62*, 393–401.
- (27) For a review of Sonogashira cross-coupling protocols see: Chinchilla, R.; Nájera, C. *Chem. Rev.* **2007**, *107*, 874–922.
- (28) Cambridge Structural Database (CSD version 5.32) search performed on 07/15/2013.
- (29) Sheldrick, G. M. *Acta Cryst.* **2007**, *64*, 112–122.
- (30) Checkcif CIF validation Utility. International Union of Crystallography. <http://checkcif.iucr.org/> (accessed May 28, 2013).

Chapter 3. Results and Discussion – Siloles with 2,5-substituents have coordinative ability, and their interactions with metal cations

3.1. General Introduction.

As described in Chapter 1, siloles (or 1-silacyclopentadienes, Figure 2-1, M=Si), have unique optical features that are also heavily dependent on the nature of their substituents; in particular, the substituents at the 2,5-positions have a dramatic effect on the ultimate properties observed.¹ Changing the π -symmetric electron-donating or –withdrawing ability of substituents at this position can, for example, shift the λ_{\max} of the absorption and emission. Tamao's group, in some of their initial investigations of altering silole 2,5-substitution, found that the ultimate absorption and emission spectra could shift by *ca.* 100 nm (Figure 3-1), and differently substituted siloles could be made using similar conditions to easily make a wide library of compounds.²

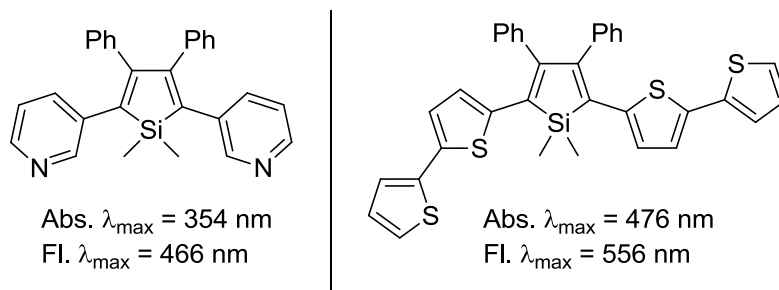


Figure 3-1. Two of the siloles synthesized by Tamao, along with their optical λ_{\max} values, demonstrating the range of values obtained.²

Because of the rich electronic variations that siloles present, we desired to investigate several changes in optoelectronic properties upon interaction with metal ions. A significant amount of substituents that affect the properties of the silole can also be envisioned to have some coordinating ability to metal ions. Appreciable changes in

properties can then be explored for potential chemosensor applications. Though covalent coordination of metal centers directly to the silole ring, both in η^4 and η^5 modes, have been known for many years,³ coordination of metals at groups bound to the 2,5- positions have been a relatively recent development. Wang and co-workers reported the synthesis of two siloles with nitrogen containing substituents that could coordinate to zinc,⁴ and a short time later Gerbier's group reported one of the same siloles (**A**, Figure 3-2) along with optical data on coordination with both zinc and copper;⁵ the compound exhibited stark differences in fluorescence depending on the metal center employed. When Zn(II) solution was added to a solution of **A** the fluorescence was slightly enhanced, however when Cu(II) was added, the fluorescence was almost entirely quenched.

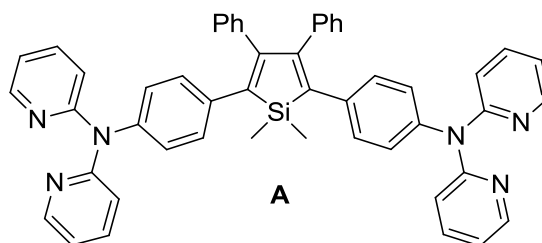


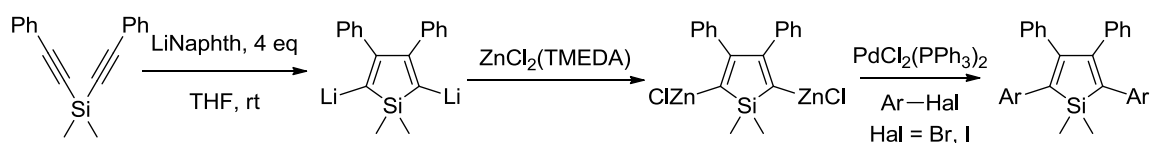
Figure 3-2. The bipyrindyl amine substituted silole that was studied by Wang and Gerbier.^{4,5}

Recently, Tang and co-workers synthesized a terpyridine-substituted silole that showed selective fluorescent enhancement for zinc.⁶ Our group has also investigated some phosphine-linked siloles and their optical changes upon coordination to gold and platinum.⁷ Some subtle changes with platinum were observed, however gold was found to cause appreciable hypsochromic shifts upon coordination.

This chapter addresses the preparation of some known and new siloles chosen for their potential to bind to metal cations, or as precursors to do so, along with optical

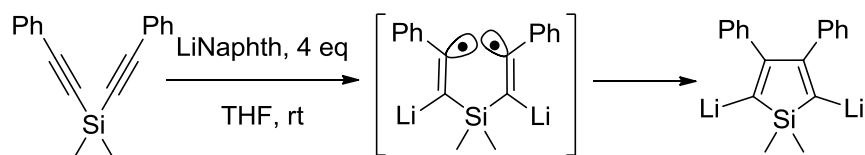
spectra outlining the differences in the changes observed based on the metal and silole employed. For our initial studies the perchlorate salts of nickel(II), copper(II), and mercury(II) were chosen in order to study the effects of paramagnetic or heavy atom species. The synthesis, characterization, and metal interaction studies are described in their respective sections below.

3.2. Synthesis and Characterization of Symmetrical 2,5-Substituted Siloles



Equation 3-1. Tamao's synthesis of 2,5-substituted siloles.^{2,8}

The one-pot synthesis of 2,5-aryl-3,4-diphenylsiloles was discovered and developed by Tamao.^{2,8} The synthesis typically begins with dimethylbis(phenylethynyl)silane, added as a solution to a pre-made solution of lithium naphthalenide in an inert atmosphere. This allows for a unique *endo-endo* intramolecular reductive cyclization to yield the intermediate dilithio-silole. This process is mechanistically shown in Equation 3-2.



Equation 3-2. The mechanism for the intramolecular cyclization of dimethylbis(phenylethynyl)silane by lithium naphthalenide.²

The excess of lithium naphthalenide causes the immediate formation of the intermediate diradical, which then couples itself to ultimately form the dilithio-silole. As this is a radical-based reaction, an aryl group, almost always phenyl, must be present on

the silane in order for the reaction to proceed. It was generally found that absent these aryl groups, the reaction mixture would be complex.² It is thought that the aryl groups stabilize the diradical species long enough to complete the coupling step. Importantly, the silane must be added to a large excess of lithium naphthalenide. If reaction is reversed, or if the amount of naphthalenide is stoichiometric, a monoradical species is formed that is ultimately unstable; the only characterizable product was formed by cleavage of the silicon-carbon bond as lithio-phenylacetylene.² Not only is the synthesis complicated in itself, the nature of reagents used is also critical, particularly the grade/additives in the lithium. Pagenkopf noted, in his group's detailed experimental observations of the synthesis of 2,5-dibromo-siloles using the Tamao cyclization procedure,⁹ that lithium without additional sodium content (0.5-1.0%) caused the reaction to fail. In our group's research on this class of compounds, lithium with copper added as stabilizer was also found to cause this cyclization to fail. After the addition of zinc(II) chloride or (*N,N,N',N'*-tetramethylethylenediamine)zinc(II) chloride ($\text{ZnCl}_2(\text{TMEDA})$), the reaction usually is found to proceed smoothly under standard Negishi conditions.¹⁰

3.2.1. Difficulties with the Tamao procedure and characterization of byproducts

Because the reaction to make these is one-pot, there are several areas that need to be optimized and monitored to ensure the best possible yields. During the course of study in synthesizing several compounds using this procedure, several aspects of the reaction yielded peculiar byproducts, leading to low yields that necessitated a study into their formation, and possible causes thereof. These studies, as well as representative characterization methods used during assignment of these byproducts, are addressed in this section.

Most of the optimization and characterization was performed en route to synthesizing compound **S6** (originally reported by Tamao²), which was to be an intermediate in further modifications at the benzylic position (*vide infra*). The synthesis was performed using the standard Tamao procedure (Equation 3-1), using 4-iodotoluene as the cross-coupling reagent in the Negishi step.

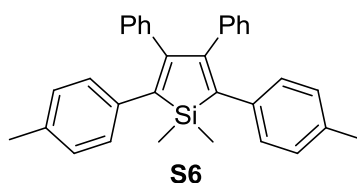


Figure 3-3. Molecular structure of **S6**.

During initial syntheses of **S6**, yields would generally be limited to approximately 30%, despite changing several of the parameters in the cross-coupling step, such as reaction time. Moreover, analysis of the crude material by ¹H NMR typically showed three distinct shifts in the Si-Me region (i.e., between 0-0.8 ppm). Generally, the integrations of these would be close to 1:1:1. Figure 3-4 shows an example of the crude NMR in the Si-Me proton region.

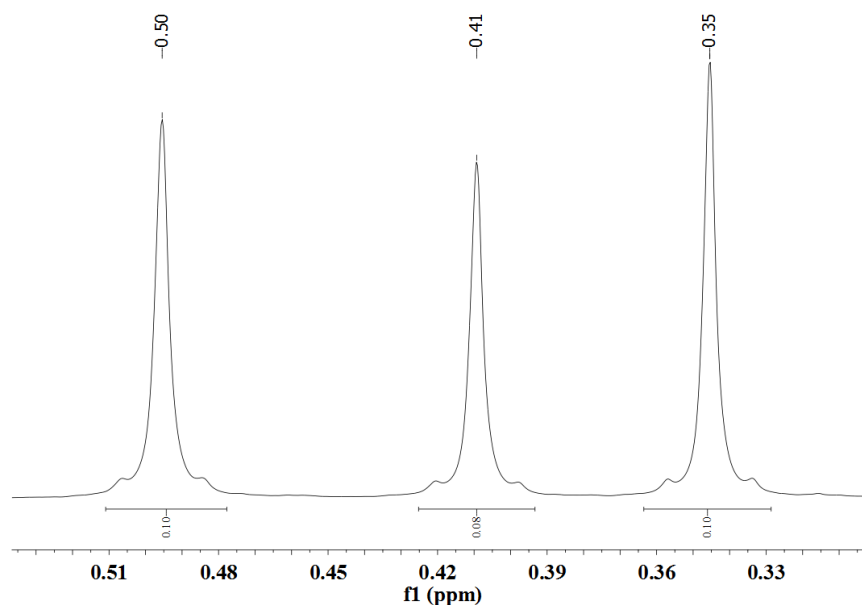


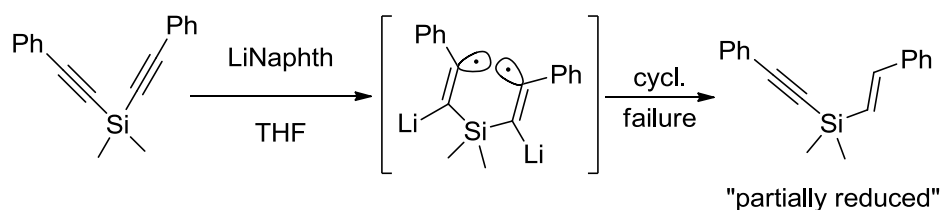
Figure 3-4. Expanded Si-Me region of a crude ^1H NMR of **S6**.

Assuming that the most downfield shift of these three peaks is the silole (0.50 ppm, in the above figure, 0.47 ppm in the purified spectrum in Figure A-30), the integrations of these three shifts, which all are indicative of Si-Me compounds due to the small 2J silicon satellites (7 Hz), suggest that the other upfield shifts at 0.41 and 0.35 are potentially incompletely-reacted byproducts or byproducts from decomposition. The ratios of integration would also explain the cause behind the limited yields initially observed.

To identify these byproducts further, and to relate their probable structures with pitfalls in the reaction, GC-MS of the crude mixture was performed after filtration through a silica gel plug. An example of the analysis is shown in Figure A-40 through Figure A-45. The naphthalene (Figure A-40) and **S6** (Figure A-45) retentions are easily identified by their chromatogram M^+ traces (128 and 442 m/z, respectively). The retention at 7.57 (Figure A-41) had a chromatogram trace with an apparent M^+ signal of 182 m/z. This matched the molecular weight of the “homocoupled” byproduct, 4,4’-

dimethylbiphenyl; these homocoupled species are common Negishi cross-coupling reactions.¹¹ A large secondary signal at 167 m/z is 15 m/z less than the parent ion, indicative of a loss of a methyl group.

The next major retention in the chromatogram has a parent ion of 262 m/z (Figure A-42). This is two mass units greater than the silane starting material, dimethylbis(phenylethynyl)silane. This is assigned as a “partially reduced” silane, where only one triple bond of the starting material reduced to a double bond (adding two protons), and the complete cyclization was arrested (Equation 3-3). It is not clear exactly why this partially reduced species arises from the reaction mixture; it was found in almost every silole produced using the Tamao procedure and analyzed by GC-MS. Some of our analyses indicated trace amounts of butylated hydroxytoluene (BHT), which is the stabilizer supplied with our THF, and surprisingly seems to have co-distilled somewhat with the THF. In significant enough quantities, this may arrest cyclization, as BHT is a radical inhibitor, and the cyclization depends on the intermediate formation of a diradical species.



Equation 3-3. The proposed route for formation of the “partially reduced” silane.

The next noteworthy retention in the GC-MS occurs near 10 min (Figure A-43), and has an m/z value of 280, 18 units higher than the “partially reduced” species. Originally it was hypothesized that this species was a hydroxylated analogue of the partially reduced

species; however, another species, the “partially coupled” silane (*vide infra*), also would at times have analogue 18 mass units higher present, indicating that the formation of this byproduct might be more general. In some preliminary investigations of formation of a 2,5-*p*-aniline substituted silole, some crystals of a byproduct were isolated. X-ray crystallography of this species revealed a silanol had formed, likely via hydrolysis of a partially coupled mono-zinc silole.

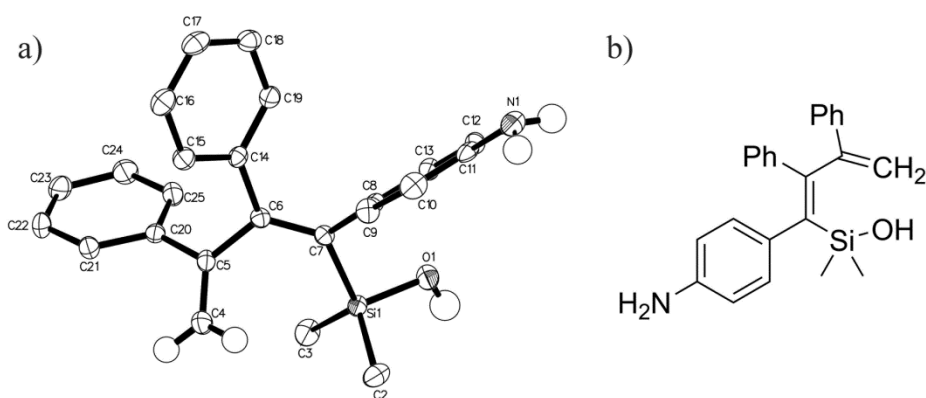
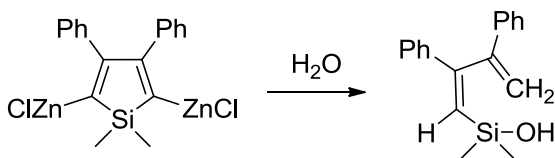


Figure 3-5. The a) crystal structure of the hydrolyzed silole byproduct, and b) the molecular drawing thereof. Hydrogens are removed except for the vinyl, amine, and silanol positions.

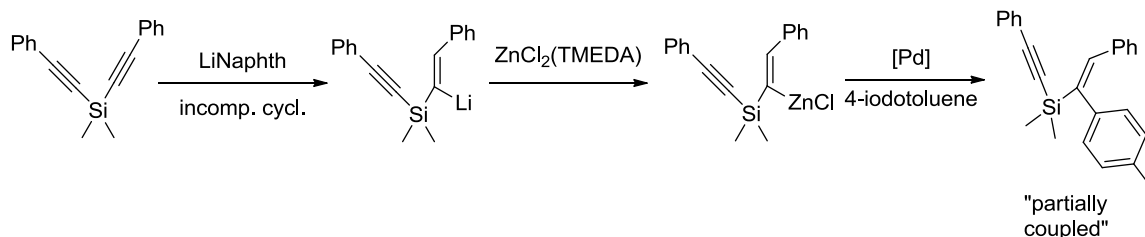
This hydrolyzed analogue of the partially reduced silane produced in synthesizing **S6**, therefore, is probably not generated directly from the lithiation step, but from the dizinc-silole intermediate; this reaction pathway is shown in Equation 3-4.



Equation 3-4. The route proposed for the hydrolyzed product with an *m/z* of 280.

The next significant retention peak is at 12 min, having an *m/z* value of 352. This value matches well to the “partially coupled” product shown below. The product is

suspected to be formed from a reaction of the partially reduced species with $\text{ZnCl}_2(\text{TMEDA})$, followed by cross-coupling Negishi conditions (Equation 3-5).



Equation 3-5. Proposed reaction route for formation of the “partially coupled” species, with a molecular weight of 352 amu.

Therefore, the reaction step that seems to affect the yield the most in this sequence is the first step, i.e., the reductive cyclization of the silane using lithium naphthalenide. Though initial reports claim an addition time for the silane to the naphthalenide solution of less than 5 min,² Pagenkopf *et al* report a time of 20 min at minimum is needed for addition; at the scales in their procedure, this works out to an approximate drip rate of 1 drop/sec or slower.⁹ They also report that any addition rate faster than this seems to greatly reduce yield.⁹ Though they do not characterize the byproducts formed from failed reactions in their report, it appears plausible that too quick an addition does not allow sufficient time for the silane to complete the reductive cyclization, as a significant excess of the reducing naphthalenide solution was already reported to be necessary for successful cyclization.⁸ An addition rate that is too rapid might make the local concentration of the silane momentarily too high for efficient conversion, leading the partially reduced species, and subsequently the partially coupled species described in the above account. Therefore, later reactions performed using the Tamao route reduced the rate of addition of the silane, and this generally improved yields to around 50-60%.

Additionally, optimizing the preparation of the lithium naphthalenide solution was necessary in order to reliably achieve these yields. Many accounts report simple stirring of lithium wire and naphthalene under inert conditions for *ca.* 5 h was sufficient for the formation of the naphthalenide solution; however, in our hands, the yields obtained for siloles generated using this method proved highly variable. Pagenkopf also noted such fickle behavior in his report on the reductive cyclization.⁹ One way to greatly improve the synthesis of the required naphthalene was through sonication, as reported by Pagenkopf.⁹ The vessel containing lithium (of appropriate composition, *vide supra*), naphthalene, and dry THF was sonicated in a sonicating bath for at least 1 h. Pagenkopf reported that the mixture was titrated after 1 h in order to confirm complete reaction; for the reactions completed in this report, a sonication time of 2 h was generally sufficient to form the naphthalenide without titration, in order to reproducibly form the target siloles in sufficient yields.

Another issue faced occasionally throughout the Tamao silole synthesis was gelation of the solution upon addition of $\text{ZnCl}_2(\text{TMEDA})$, which would sometimes make the suspension viscous enough that rotation of the magnetic stir bar was arrested. The reagents used to this point were carefully purified (through recrystallization of the solids and distillation of the THF), so it appeared impurities seemed unlikely be the cause. Ultimately, however, the gelation was determined to be caused by trace amounts of TMEDA left from the synthesis of $\text{ZnCl}_2(\text{TMEDA})$, even though the sample was recrystallized several times.¹² A sample of the material that caused gelation in a prior reaction was oven dried for several days at 70 °C. This same material ceased to cause gelation in further reactions. If the noticeable odor of TMEDA is present, it is likely

enough to cause gelation, and further oven drying is needed. Gelation was also noticed during the synthesis of the precursor material 4-bromo-1,2-bis(methylthio)benzene, which requires addition of TMEDA to cold solution containing *n*-butyllithium.¹³ Therefore, it appears that TMEDA, or potentially an impurity contained therein, interacts with organolithium species in a way that causes temporary polymerization and increased viscosity.

If gelation did occur during the Tamao silole synthesis, the suspension was treated with a sonicating bath for several seconds until the viscosity was reduced, and then the reaction sequence was continued. Also noteworthy was the observation that yields generally did not suffer greatly if gelation occurred, indicating that this process is not necessarily due to degradation or decomposition of the active organozinc intermediates.

3.2.2. Synthesis and General Comments.

After the various steps in the Tamao procedure were optimized, several siloles were synthesized and characterized by NMR and other methods (*vide infra*). The siloles that were synthesized and fully characterized are shown below in Figure 3-6; Siloles **S3**,² **S4**,¹⁴ and **S6**² are known compounds; siloles **S1** and **S2** have been reported by our group.¹⁵

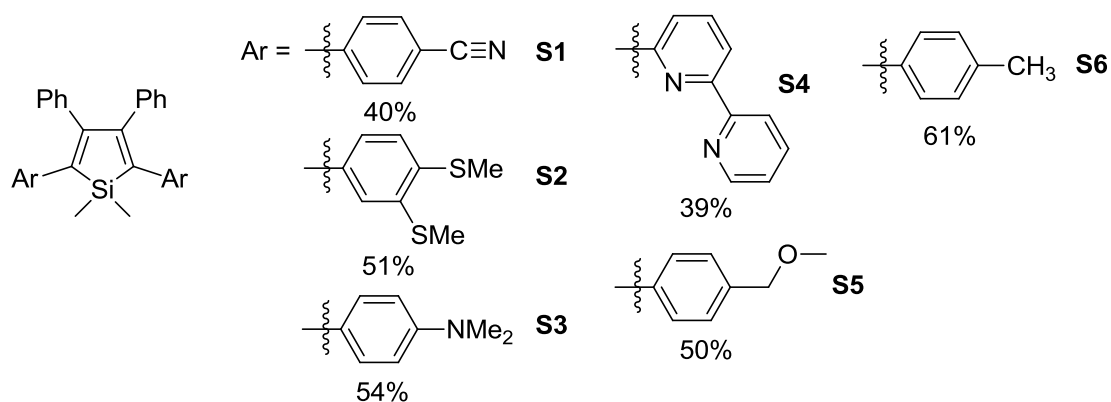


Figure 3-6. The siloles synthesized and fully characterized for study.

In general, the compounds were purified by silica gel, either through a full column or silica gel plug. The compounds were then further purified via recrystallization, typically by either slow evaporation or slow diffusion of an anti-solvent through a solution of the silole. Siloles **S1** and **S2** were also characterized by elemental analysis and the values obtained agreed well with predicted values. The melting points of the new siloles **S1**, **S2**, and **S5** were also taken, and were found to be in the general silole range (*ca.* 200 °C), and of narrow temperature range, indicative of their purity (Section 4.2.2). Both siloles **S2** and **S3** tended to precipitate out on the silica gel column prior to elution; the use of significantly polar solvents (e.g., ethyl acetate) was needed in order to redissolve the solids and make elution possible. This solidification was actually beneficial in that most of the other byproducts eluted much earlier in the columning procedure. Compound **S3** was also further purified through trituration of the deep yellow-orange powder with diethyl ether, from which a dark red-brown supernate was removed, yielding pure **S3**. Additionally, the standard quenching of the crude reaction mixture with 1 M HCl appeared to cause protonation of the amine groups in **S3**, as the aqueous layer on workup had clear plate-like crystals that, on basification, yielded a bright yellow powder of **S3**,

which was extracted and combined with the other fractions in the organic layer of the aqueous extraction. Generally, purification for the other siloles in this study was less intensive than for **S2** and **S3**, and column chromatography followed by recrystallization yielded very pure compounds. Section 4.2.2 details the isolation of the individual siloles.

Compound **S3** was also synthesized using a modified Tamao procedure, using an adaptation from the work of Knochel and Kienle,¹⁶ which detailed the use of 2-iodopropane to greatly accelerate Negishi reactions. The authors propose that the iodopropane co-catalyst causes a radical organopalladium species to catalyze the reaction at much greater rates than traditionally observed (e.g., 5 min instead of at least 12 h). Generally, degassed iodopropane was added to the zinc species, the contents were stirred for several minutes, and then the palladium catalyst and the cross-coupling aryl halide were added. The palladium catalyst chosen for this alternate synthesis was (dppf)PdCl₂, the large bite angle of which allows for efficient coupling of traditionally difficult systems,¹⁷ e.g., deactivated aryl halides such as 4-bromo-*N,N*-dimethylaniline, the precursor used for **S3**. When 2 equiv of degassed 2-iodopropane was added to the solution containing the dizinc intermediate (Equation 3-1), the appearance of the mixture changed from a black suspension to a deep red solution after 5 min of reaction. Addition of (dppf)PdCl₂ and 4-bromo-*N,N*-dimethylaniline to this solution cause another color change to deep brown/black, which changed to black with intense yellow overtones after several hours at rt. This was refluxed overnight to ensure complete reaction. Isolation of the silole indicated slightly improved overall yields, with less apparent homocoupled product noticeable by NMR analysis of the crude product. The successful synthesis of

S3, along with the apparent faster reaction times at rt, might warrant further study of this alternate reaction method for silole synthesis.

3.2.3. Characterization of the siloles by NMR spectroscopy

All of the pure siloles, **S1** through **S6**, were characterized by ^1H and $^{13}\text{C}\{^1\text{H}\}$ NMR spectroscopy (Figure A-17 to Figure A-30), except for **S6**; the ^1H NMR and GC-MS spectra were acquired for general purity considerations. The important shifts are described in Table 3-1; known values are also listed and compared to the values obtained in this study. Additionally, the $^{29}\text{Si}\{^1\text{H}\}$ NMR (DEPT) data have been reported for the new compounds **S1**, **S2**, and **S6**, and the shifts are between 0-10 ppm, and within the range of the resonances reported for similar siloles.⁷ The identifying shifts in the ^1H NMR spectrum included the methyl group resonances at the silicon center, the methyl group resonances at the 2,5-substituents for **S2**, **S3**, **S5**, and **S6**, and the downfield shifted aromatic resonances for the bipyridine moiety in **S4**. The aromatic region was usually complicated from the 3,4-phenyl substituents, as well as the aromatic protons on the 2,5-position, though integration helped to reveal whether the assignments were accurate. The important identifying resonances in the $^{13}\text{C}\{^1\text{H}\}$ NMR included the 3,4-carbons (sometimes referred to as the β -carbons), typically around 150 ppm, and the SiMe carbons, typically around -3 ppm, as well as the methyl carbons on the 2,5-substituents.

^1H NMR Data		
Silole	Shift (ppm), Integration (literature value, if applicable)	Assignment
S1	0.48, 6H	SiMe
S2	2.44, 6H	SMe
	1.97, 6H	SMe
	0.51, 6H	SiMe
S3	2.89, 12H (lit. ² 2.87)	NMe
	0.51, 6H (lit. ² 0.49)	SiMe
S4	8.67, 8.42, 8.10, 7.85, 7.39, 7.30; 12H (lit. ^{14a} 8.68-8.66, 8.44-8.41, 8.10, 7.87-7.82, 7.39, 7.38-7.32)	pyH
	0.80	SiMe
	(lit. ^{14a} 0.79)	
S5	4.35, 4H	benzylH
	3.37, 6H	OMe
	0.46, 6H	SiMe
S6	2.25, 6H (lit. ² 2.24)	tolylH
	0.47, 6H (lit. ² 0.45)	SiMe
$^{13}\text{C}\{^1\text{H}\}$ NMR Data		
Silole	Shift (ppm)	Assignment
S1	156.0	β -carbon
	-4.0	SiMe
S2	154.4	β -carbon
	16.5	SMe
	15.7	SMe
	-3.1	SiMe
S3	151.8 (lit. ² 151.6)	β -carbon
	40.5 (lit. ² 40.4)	NMe
	-2.6 (lit. ² -2.7)	SiMe
S4	155.4 (lit. ^{14a} 155.6)	β -carbon
	-2.2 (lit. ^{14a} -2.3)	SiMe
S5	154.1	β -carbon
	74.8	benzyl-carbon
	58.4	OMe
	-3.7	SiMe

Table 3-1. Selected ^1H and $^{13}\text{C}\{^1\text{H}\}$ NMR data and assignments, and literature values for known siloles.

The values reported in the literature match those of the known siloles, as characterized in this research project, very well.

3.2.4. Characterization of the siloles by optical spectra

The UV-visible and fluorescence spectra and quantum yields for the new siloles **S1** and **S2** were recorded and are listed in Table 3-2. Also listed are the optical spectral data for known siloles **S3** and **S4** along with the literature values.

Compound	λ_{\max} , absorbance (nm)	$\log \varepsilon$	λ_{\max} , fluorescence (nm)	Φ_f , %
S1	365	4.12	482	0.25 ^b
S2	390	4.29	511	1.58 ^c
S3 ^d	415 (423)	4.32 (4.33)	549 (529)	(0.251)
S4	382 (386) ^e	3.99	472 (489) ^e	(<0.1) ^f

Table 3-2. UV-visible and fluorescence spectral data for the reported compounds.^a ^aSpectral data from siloles in a 1:1 mixture of CH₂Cl₂/MeOH, 5×10⁻⁵ M. ^bWith reference to 9,10-diphenylanthracene. ^cWith reference to fluorescein. ^dLiterature values are listed in parentheses, see Ref. 2. ^eLiterature values are listed in parentheses, see Ref. 14a. ^fLiterature values are listed in parentheses, see Ref. 14c.

The optical data of **S1** indicate that the cyano- substituent has a relatively modest effect on the electronics of the silole; comparing to 1,1-dimethyl-2,3,4,5-tetraphenylsilole (**TPS**, abs. λ_{\max} = 358 nm, fl. λ_{\max} = 488 nm),¹⁸ there is a 7 and 12 nm bathochromic shift in the absorbance and fluorescence λ_{\max} values, respectively. This corroborates with the very similar structural features of **S1** and **TPS** (*vide infra*). It appears that the cyano- substituent is not suitably positioned to be an effective π -withdrawing group (relative to the 2,5-phenyl moieties); the ability to either be a π -donor or -acceptor has the most effect on the electronics of siloles.¹ Tang's group used dicyanovinyl substitution, allowing the withdrawing cyano- groups to interact more effectively with the π system of the silole;

this group affected significant bathochromic shifts relative to the parent silole **TPS**.¹⁹ The moderate communication of the cyano- group in **S1** will also be addressed in the metal interaction section (*vide infra*).

The optical spectra of **S2** show further shifts to lower energy compared to **S1**. In solution, the largest contribution to this observation is likely the modest donating ability of the lone pairs of the sulfurs on the methylthio- substituents. The related methoxy substituent, situated *para* to the silole ring on the 2,5-phenyl groups, induces a bathochromic shift of 12 nm in the absorption λ_{\max} compared to the methyl analogue for this reason.² Compound **2** also exhibits a significantly higher solution quantum yield. While higher steric hindrance from a methylthio- group *meta* to the silole could help explain this observation,²⁰ the solid state arrangement of this substituent, preferring an orientation that suggests some interaction with the 3,4-phenyl groups (Figure 3-7), could also help explain this increase.

Siloles **S3** and **S4** both were characterized by UV-vis and fluorescence spectroscopy and agreed reasonably well with the literature values. The slight differences in λ_{\max} of the absorbance and fluorescence are most likely from differences in solvent polarity (literature sources used chloroform² for **S3** and THF^{14a} for **S4**). Compound **S3** exhibits significant bathochromic shifts from **TPS** due to the strong π -symmetric donating ability of the dimethylamino- substituent.¹ Compound **S4** exhibits a redshift in the absorbance maximum compared to **TPS**, but a fluorescence blueshift. In the known crystal structure,^{14c} the torsional angles between the silole core and the adjoining pyridine moieties in **S4** are between 26° and 36°, in the approximate range of the silole structures presented herein. Therefore, the extended conjugation brought on by the bipyridine

moiety does not significantly affect the electronics of the silole, probably due to its own strong tendencies as a π -accepting unit. The siloles containing 2,5-di(pyridine-3-yl) and 2,5-di(pyridine-2-yl) groups² also affected a slight bathochromic shift in the absorbance spectrum and had little effect on the fluorescence spectrum compared to **TPS**.

3.2.5. X-ray crystallography of symmetric siloles.

Crystals of sufficient quality for the new siloles **S1**, **S2**, and **S5** were grown by slow evaporation or slow diffusion (see Experimental Section, Section 4.2.2). Compound **S2** refined with 3 molecules of dichloromethane per molecule of **S2**. The structures were solved and refined to reasonable geometries and residual electron densities. Table A-3 in the appendix lists the crystallographic data for compounds **S1**, **S2**, and **S5**.

The molecular structures of **S1**, **S2** and **S5** are shown in Figure 3-8. Compound **S1** exhibits a structure that is very similar to the unsubstituted-phenyl compound **TPS**.¹⁹ Both compounds exhibit the propeller-like arrangement characteristic of 2,3,4,5-tetraphenylsiloles and their analogues.¹⁹ Given that the cyano- substituent on the 2,5-phenyl groups is *para* to the silole ring, steric influence on the geometry is minimal. The magnitude of the phenyl torsion angle for **S1** at the 2,5- positions is 36.5° and 53.7°, while for **TPS** they are 34.8° and 48.8°. ¹⁹ The torsional angles at the 2,5- positions of **S2**, however, are slightly smaller, with a magnitude of 28°. Counter to an assumption that **S2** would pack to minimize steric strain, the methylthio substituent *meta* to the silole ring turns toward the 3,4-phenyl groups. Based on steric assumptions alone, this observation is unexpected. Though hydrogen atom positions are calculated, the difference Fourier map suggests that the hydrogen atoms on the thio- methyl groups are accurately placed; one of these atoms is oriented towards the centroid of the 3,4-phenyl rings in a manner

that suggests some possible C-H $\cdots\pi$ interactions.²¹ A depiction of this interaction is shown in Figure 3-7, where only the hydrogen on the thiomethyl group that could potentially be interacting with the 3,4-phenyl substituents is shown with appropriate measurements in the drawing. The distance (3.073 Å) is on the higher end of the typical range of values found (average of 2.75 Å for sp^3 -CH/ π interactions²¹), but the [C-H/normal of π system] angle (151.52°) compares closely with the average of crystal structures in this system (148°).²¹ This interaction is rather weak on its own (most times weaker than the classic X-H-X hydrogen bond system), however the intramolecular arrangement between substituents likely helps to enforce the orientation of the molecule in the crystal structure.

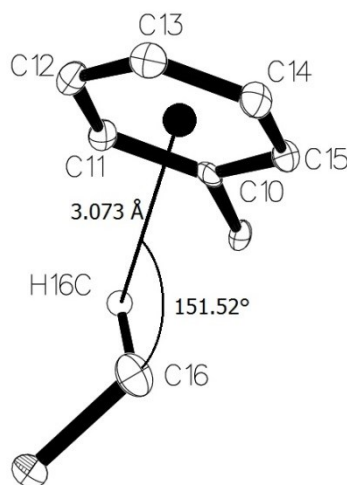


Figure 3-7. A selected portion of **S2** that shows potential C-H/ π interactions.

Compound **S2** also has a larger torsional magnitude of the 3,4-phenyl substituents (64.0°) compared to **S1** (56.5°), perhaps to accommodate for the thiomethyl substituent. These observations, viz., the smaller 2,5- torsional angle and weak intersubstituent interactions, may help explain some of the photometric data recorded for **S2** (*vide supra*).

Compound **S2** crystallized with three dichloromethane solvent molecules per molecule. One chlorine atom on one solvent molecule was disordered; this was addressed by refinement of the chlorine molecules over two positions at a ratio of 93:7 of their partial occupancies. Another dichloromethane molecule has a chlorine atom that was symmetrically generated and the special position constraints were suppressed; the molecule also has partial occupancy of 0.5. EADP constraints were employed on the chlorine atoms. The silicon atom in **S2** is on a special position with C_2 symmetry; for figures displayed in this manuscript, the molecule was grown from the asymmetric unit.

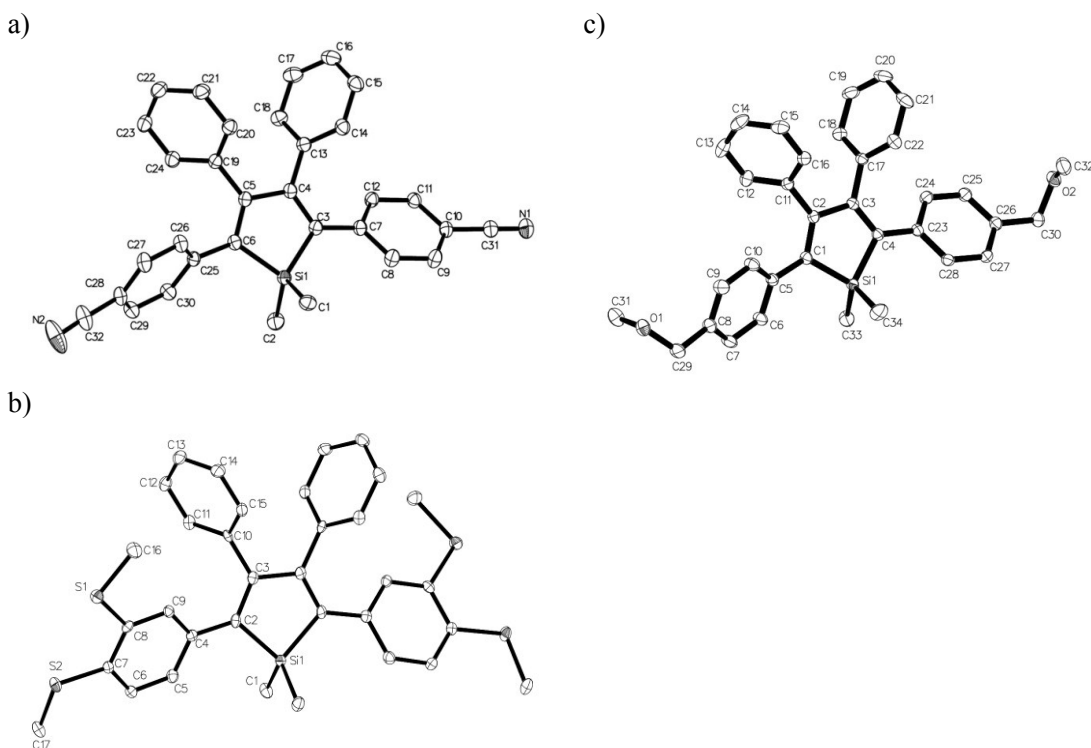
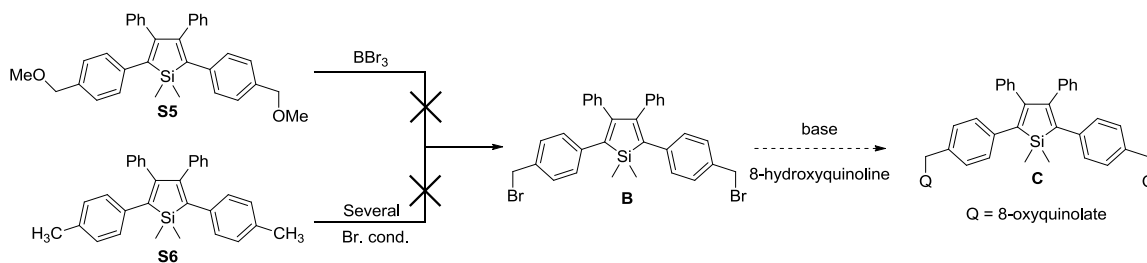


Figure 3-8. The crystal structures of a) **S1**, b) **S2**, and c) **S5**. Selected measurements for each compound are given in section 5.3.3 in the Appendix.

The compound **S5** was originally synthesized as a precursor to attempt synthesis of an α -bromotolyl substituted silole (Section 3.3), and crystals of sufficient quality for

crystallography were acquired (Figure 3-8c). As was the case for the prior siloles, the propeller arrangement of the 2,3,4,5-aryl groups was retained for **S5**. Compared to **TPS**, this compound has a smaller absolute torsional angle of the 2,5-aryl groups (27 and 32°), and the 3,4-phenyl groups also have a smaller absolute torsional angle (68° and 60°, versus 71° and 69° for **TPS**¹⁹). Inspection of the crystal packing by the structure does not suggest intramolecular C-H/ π interactions, as was the case for **S2**; the methoxymethyl substituent is too small, and too far removed from the rest of the molecule for these types of interactions. Compound **S2** has a thiomethyl group in the *meta* position that allows for an orientation that might take advantage of the C-H/ π interaction (*vide supra*), whereas with **S5** the orientation of the methoxymethyl-group *para* to the silole core prevents such intramolecular weak interactions. There is some short contact (i.e., sum of van der Waal radii, as measured by the visualization program Mercury) between the oxygen atom and a hydrogen atom of the 3,4-phenyl group on an adjacent molecule, though this might be due to simple packing effects.

3.3. Attempted preparation of α -quinolate substituted 2,5-tolylsilole.



Scheme 3-1. The attempted preparation routes for **C** from pre-formed siloles **S5** and **S6**.

During our investigations of siloles that could interact with metal cations, our group desired to make siloles that had potential to have quenched fluorescence absent of metal

ions, due to photo-induced or other charge transfer effects (Section 1.4). Upon coordination, the metal changes the electronics or structure of the ligand that originally quenched the fluorophore emission. This is colloquially referred to as an “off-on” metal detection system.²² An example of this system is a coumarin-quinolate fluorophore, linked together via a non-conjugated C-O bond; this non-conjugation is generally considered important so that the fluorophore and quenching moiety remain electronically separate systems. The system showed good fluorescence enhancement, even towards paramagnetic ions that typically cause fluorescence quenching.²³

Silole	Conditions	Reference
S5	BBr ₃ (1.5 eq), -78 °C, inert atm.	24
S6	NBS (2.2 eq), CCl ₄ , AIBN, reflux	25
S6	Br ₂ , H ₂ O/dichloromethane 1:1, 23W CFL, 48 h	26
S6	NaBr (2.2 eq), H ₂ SO ₄ (2 eq), H ₂ O ₂ (3 eq), CHCl ₃ , 24 h	27
S6	H ₂ O ₂ (2.1 eq), HBr (2.2 eq), H ₂ O, 23W CFL, 24 h	28
S6	BBr ₃ , cyclohexane/dichloromethane 1:1, 48 h	29
S6	NBS (2.2 eq), H ₂ O, 23W CFL, 48 h	30
S6	NBS (2.2 eq), EtOAc, 23W CFL, 24 h	31

Table 3-3. Conditions used to attempt the conversion of siloles **S5** or **S6** into the α -bromotolylsilole **B** (Scheme 3-1). References for the procedures are listed in the Table.

Therefore, our group endeavored to use similar synthetic techniques, using a 2,3,4,5-tetraaryl silole as the fluorophore and, initially, 8-oxyquinolate as the quenching/coordinating site; the quinolate was also used as the quenching/coordinating site in Feng’s work.²³ Initial synthetic procedure to synthesize the quinolate-substituted silole **C** are detailed in Scheme 3-1, where siloles **S5** or **S6** were to be converted into the

α -brominated-2,5-tolylsilole **B**, followed by reaction with 8-hydroxyquinolate and base to obtain the target compound **C**. Unfortunately, numerous conditions for bromination were attempted, but none of the reaction methods used yielded clean or isolable conversions to silole **B**. The reaction conditions and their references are listed in Table 3-3.

The reaction of **S5** with BBr_3 yielded clear, crystalline needles on slow diffusion of hexanes into a dichloromethane solution of the reaction product. Comparison of the spectra by NMR (Figure 3-9) shows that the crystalline product does not have the resonances related to the *SiMe* or *OMe* protons in **S5**; however, there is a resonance at 6.25 ppm that is in the range and integration value of 1,3-butadienes, formed by cleavage of the SiMe_2 moiety from the silole ring.² The presence of only benzyl protons (and absence of benzyl alcohol protons) suggests that the *OMe* moiety did react with BBr_3 to yield the desired benzyl bromide, but the reagent continued to react with the silole ring itself to cleave the ring and form the butadiene. The structure assigned of this compound **D** is inset in Figure 3-9.

Most of the bromination conditions attempted for **S6** yielded complex mixtures, with broad, at times featureless resonances in the ^1H NMR, indicative of polymerization. It appears that the extended bromination conditions that the silole was subjected to cause decomposition and polymerization of the species. Some analyses also indicated presence of butadiene contamination, which is only possible from cleaving the Si-C bond with the silole, which also occurred with **S5** and BBr_3 (*vide supra*). Pyridinium tribromide was used as a bromination agent to convert trimethylsilyl positions at the 2,5-positions of the silole to bromo-substituents;³² the Si-C bond, therefore, perhaps cannot withstand

cleavage from the conditions listed in Table 3-3, even the relatively strong bonding within the silole ring.

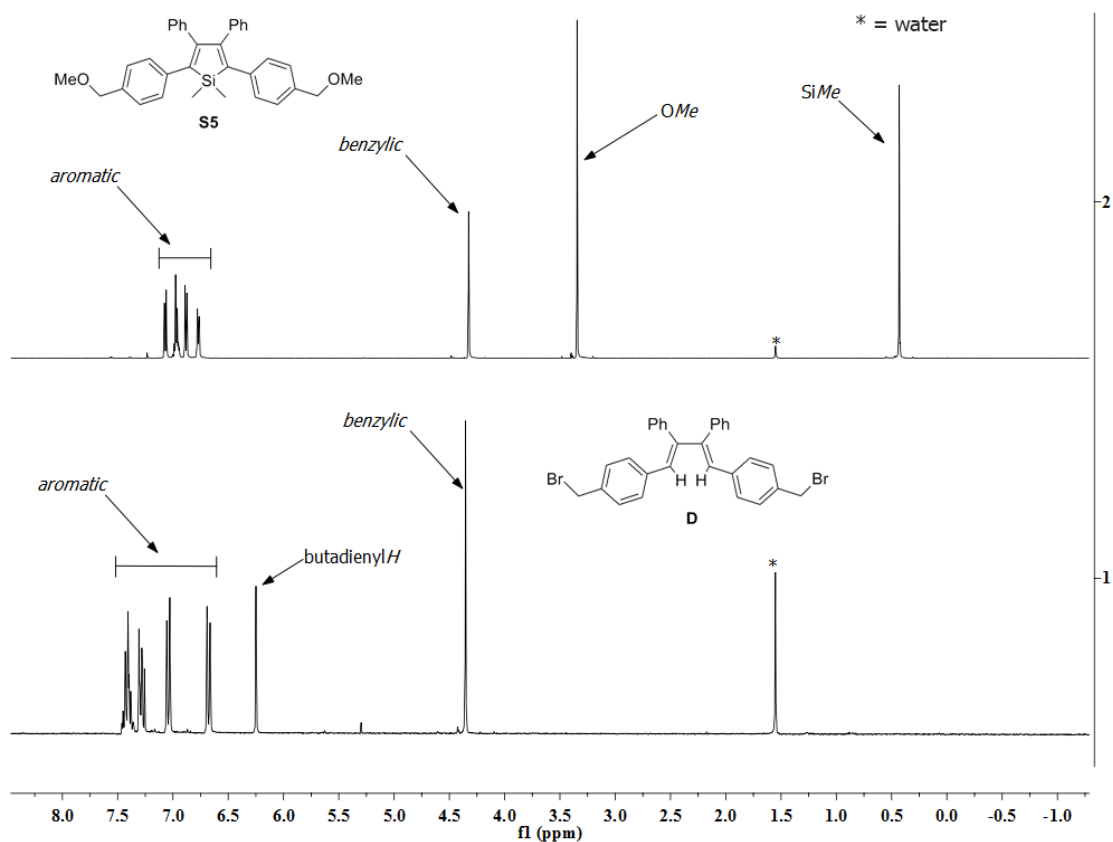
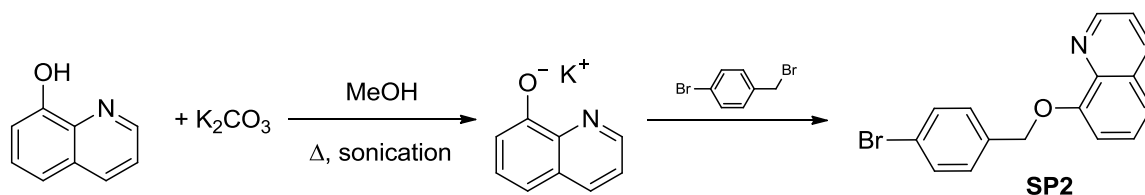


Figure 3-9. A stacked ^1H NMR spectrum comparing the silole **S5** with the product generated from reaction with BBr_3 . The assigned structure of this product (**D**) is inset.

The precursor compound, 8-((4-bromobenzyl)oxy)quinoline, **SP2**, was also synthesized as an alternate reaction pathway to ultimately synthesize **C**. Section 4.2.1 details the synthesis of this precursor, essentially an $\text{S}_{\text{N}}2$ reaction of 4-bromobenzyl bromide with the potassium quinolate (Equation 3-6).



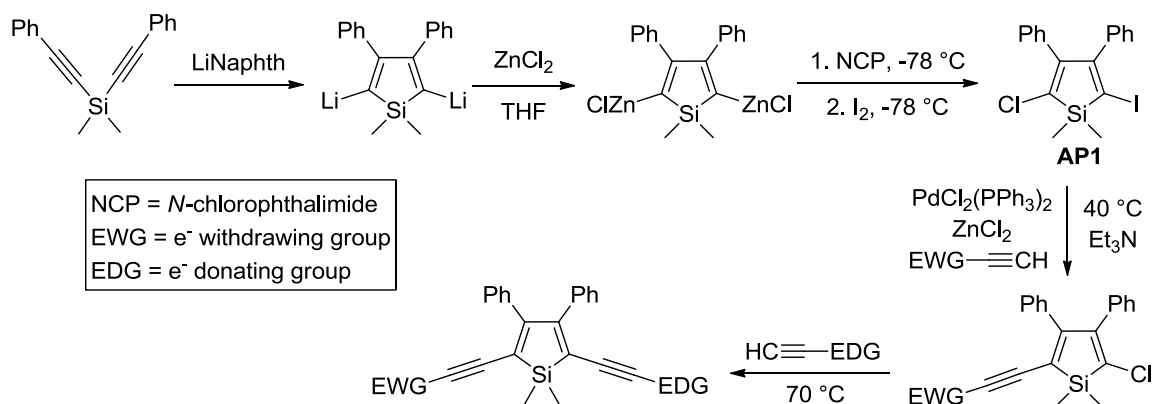
Equation 3-6. The synthesis of **SP2**.

The potassium carbonate was initially slow to react to deprotonate the 8-hydroxyquinoline, therefore it was necessary to heat and sonicate these two compounds in order to ensure complete reaction. The yellow potassium quinolate color changed to a deep red upon addition of the benzyl bromide solution in dichloromethane, and this again changed to purple on filtration and concentration. The compound was recrystallized from methanol to give pure **SP2**. Analyses of the 1H (Figure A-15) and $^{13}C\{^1H\}$ NMR (Figure A-16) spectra, along with the sharp melting point at 124–126 °C, indicate that the white/purple crystalline solid was pure **SP2**.

This compound was reacted with the dizinc intermediate in the standard Tamao procedure (Equation 3-1) in order to attempt to make the quinolate-benzylsilole **C**. Analysis by 1H NMR spectroscopy indicated potential synthesis of **C** due to a resonance at 0.45 ppm, within the range of SiMe resonances for siloles; however, isolation of the compound proved to be difficult. The species appeared to decompose when attempts were made to purify it by column chromatography. Efforts to isolate the species of interest have as of yet failed.

3.4. Synthesis of unsymmetric silole precursors and attempted preparation of asymmetric siloles.

Both strong π -donors (such as $-\text{NMe}_2$ groups) and π -acceptors (such as $-\text{NO}_2$ groups) at the 2,5-positions can affect the electronics of siloles,¹ as discussed in the introduction. Therefore, combining these two types of substituents across the silole unit should have significant effects on the electronics of siloles, creating a “ π -donor/ π -acceptor” system. Pagenkopf was able to develop a synthesis for unsymmetric siloles that was able to realize these unsymmetric siloles, by first synthesizing an unsymmetric 2,5-dihalo silole (**AP1**), which was then reacted with under modified Sonogashira conditions to generate unsymmetric donor-acceptor siloles;³³ this synthesis is detailed in Scheme 3-2.



Scheme 3-2. The synthetic route for unsymmetric donor-acceptor siloles.³³

Within the results and discussion section of a later publication using the same precursor **AP1**, Pagenkopf noted that the Sonogashira conditions typically employed, i.e., using both THF and triethylamine as solvents, generated complex reaction mixtures; it seems that THF might be unstable with regards to the reagents used.³⁴ Unfortunately, the experimental sections of *both* papers^{33,34} explicitly specify that THF *and* triethylamine

were used, *which is a direct contradiction to what was stated in the results and discussion*. This generally made reproduction of their work, already challenging due to the absence of light required, virtually impossible, until THF was removed from the Sonogashira steps. Still, the reaction proved fickle; the results of the synthesis attempts, and characterization of the precursors needed, are discussed below.

Given our group's interest in siloles as ligands for metal centers,^{7,15} we desired to take advantage of the unique electronic arrangement offered by this unsymmetric silole arrangement, by having one position of the silole ring as a strong metal binding site (e.g., a bipyridine moiety), and the other site having either π -donating or accepting moieties, in order to study the effect of metal ligation on the efficiency of, for example, charge-transfer across the molecule. Some targets we desired to synthesize are listed in Figure 3-10. Unfortunately, it was not possible to obtain isolable yields of these desired products (due to the inaccurately reported reaction solvents, *vide supra*), even as some resonances in the crude NMR spectra taken showed trace amounts could have potentially been formed.

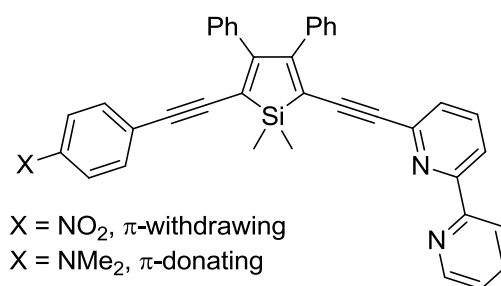


Figure 3-10. Some desired unsymmetric silole targets, with potential to bind to metal centers.

Synthesis and characterization of AP1, the unsymmetric di-halosilole precursor.

The synthesis of 2-chloro-5-iodo-3,4-diphenyl-1,1-dimethylsilole, **AP1**, is outlined in

Scheme 3-2.³³ The synthesis begins in the same manner as the Tamao route (Equation 3-1), with the dimethylbis(phenylethynyl)silane being reductively cyclized using lithium naphthalenide. From here, the dilithio-silole formed is quenched and transmetallated with anhydrous ZnCl_2 in THF, instead of solid $\text{ZnCl}_2(\text{TMEDA})$. After this reaction step, the flask must be wrapped in foil, and the lights turned off, as **API** is rather light sensitive. The reagent *N*-chlorophthalimide (*ca.* 1.1 equiv) is used to exchange one of the organozinc positions with chloride; *N*-chlorosuccinimide gave fickle results for this purpose.³³ The addition must also be made slowly over the course of 1 h at $-78\text{ }^\circ\text{C}$; quicker addition rates significantly impact yields. After stirring for an additional 30 min, iodine is then added as a solid. From this point, the reaction is worked up in the normal aqueous procedure for halogenation reactions (half-saturated NH_4Cl , half-saturated $\text{Na}_2\text{S}_2\text{O}_3$, brine, and drying over MgSO_4). The material is filtered through a very short pad of silica to remove the magnesium salts (washing with ethyl acetate to ensure complete passage), the solvents are removed by rotary evaporation with the flask wrapped in foil, and the solid is redissolved in 20% dichloromethane in hexanes and again filtered through silica to remove the phthalimide byproduct. The literature states a 10% solution of dichloromethane in hexanes is sufficient;³³ however, in our hands this could not remove the target **API** in a reasonable amount of time or solvent. The more polar system reported here appears to still leave the phthalimide insoluble, while being able to filter **API** formed much more quickly. The solvent is again removed by rotary evaporation, yielding an off-white solid that can then be analyzed and used in cross-coupling reactions. Though naphthalene is still in the solid, it generally is innocuous in the next

steps; extensive attempts at removal of naphthalene also could potentially incur decomposition of **AP1**.

All of the reaction and workup must be done with the lab lights out, and as much daylight blocked from windows as possible. Pagenkopf reports **AP1** as very light sensitive, and in our own hands this was the case as well. Exposure of NMR samples for a few minutes to direct sunlight evoked a pale pink discoloration to the solution, evidence of the weak C-I bond cleaving, and general decomposition. The steps during reaction and removal of solvents at the rotary evaporator also have the flasks wrapped in foil as a further precaution. Generally it was not found necessary to wrap the aqueous workup or filtration glassware in foil, as long as much light as possible was excluded from the room, and work was done quickly.

To confirm that **AP1** was formed, ^1H NMR analysis was performed (Figure A-31), along with other analytical methods described below. The naphthalene present in the mixture serves as a convenient internal standard; most of the naphthalene from the naphthalenide step in the reaction is retained through workup, so integration of one of the two multiplets of naphthalene and the integration of the **AP1** SiMe resonance (at 0.45 ppm) is compared with the equivalents of naphthalene and silane the reaction started with. For example, if 4.5 equiv of naphthalene to silane was used, then one of the multiplets of naphthalene would be expected to have an integration ratio of (4.5×4) to 6 (18 to 6) of the SiMe protons for a complete conversion. From this comparison, yields for **AP1** ranged from 40-75%.

Analysis of the $^{13}\text{C}\{^1\text{H}\}$ NMR spectrum (Figure A-32) indicated thirteen peaks for the silole, besides the three large peaks for the naphthalene. The large number of

resonances is due to the unsymmetric nature of **AP1**, causing chemical inequivalency of the carbons. Several resonances of the spectrum could be identified. The peaks at 161 and 154 ppm are likely the β -carbons of the silole ring, again showing two peaks due to chemical inequivalency. The SiMe resonance at -6.2 ppm is slightly more upfield than 2,5-aryl substituted carbons, perhaps due to the iodine present, which provides for additional shielding from magnetic anisotropy of the many electrons in the atom (also sometimes called the “heavy atom effect”). This effect likely can be used to assign the shift of an aromatic resonance at 95 ppm, which is assigned to the carbon on the silole ring that is substituted with iodine, for the same reason as above.

GC-MS analysis yielded several peaks, representing the naphthalene, the target material, and several others relating to decomposition species due sensitivity of the compound towards the high inlet temperature necessary for gas chromatography. Nevertheless, the target retention peak of **AP1** was acquired, displaying its molecular ion (m/z of 422, Figure A-46) in the chromatogram.

Synthesis of the terminal alkynyl precursors for cross-coupling with AP1. Once the synthesis of **AP1** was made reproducible in our hands, the next objective was to synthesize the appropriate terminal alkynes for the unsymmetric siloles desired (Figure 3-10). These are displayed below in Figure 3-11.

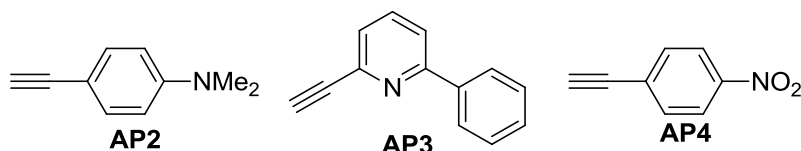
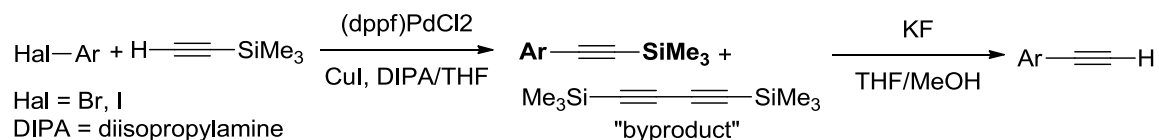


Figure 3-11. The terminal alkynes synthesized for initial study.

All of the precursors, **AP2**,³⁵ **AP3**,³⁶ and **AP4**,³⁷ are known in the literature, but the synthesis for each was modified (see Section 4.3). Typically the catalyst, (dppf)PdCl₂ (**SP1**), was employed in 1-2 mol %, along with a copper iodide co-catalyst with similar loadings (solvent of diisopropylamine or diisopropylamine/THF), in order to couple the aryl halide with (trimethylsilyl)acetylene to form the trimethylsilyl-protected precursor of the terminal acetylene. This was then deprotected with potassium fluoride in a 1:1 mixture of THF and methanol to give the target terminal acetylene. The reaction procedure is shown in Scheme 3-3.



Scheme 3-3. The synthesis of the terminal alkynes used for study.

The reactions generally proceeded in high yields, both for the Sonogashira cross-coupling step and the deprotection step. Upon degassing the reaction solution, some reaction was noted immediately. While **AP2** and **AP3** reactions were also heated to ensure complete reaction, the cross-coupling of *p*-iodonitrobenzene and trimethylsilylacetylene to form **AP4** caused a noticeable exotherm when the components were mixed together, and began precipitating out the amine salt byproduct immediately, to the point that additional THF was added to allow for stirring. Generally, deactivated arenes such as nitrobenzenes are much more reactive in Pd-based oxidative addition/reductive elimination reactions than other species,³⁸ and explains the high reactivity observed here.

Generally, upon filtering the contents of the Sonogashira reactions to remove metal salts, the crude product precipitated as a crystalline solid upon removal of the solvents. Analysis of the crystalline material obtained by ^1H NMR spectroscopy (Section 5.1.4) shows that the product is almost exclusively the desired TMS-protected precursors; the only byproduct noticeable is the bis(trimethylsilyl)diacetylene (Scheme 3-3), which is observed at around 0.19 ppm in the NMR spectrum. The product likely formed because 2 equiv were used per equiv of the aryl halide, for optimal yields. It was not necessary to attempt to remove this byproduct, as its subsequent deprotection would yield diacetylene, volatile enough to be removed from the reaction mixture on evaporation.

Attempted Sonogashira coupling of AP1 with terminal alkynes. With the terminal alkynes in hand, and the synthesis of **AP1** optimized, the Sonogashira cross-coupling of the **AP1** in naphthalene (*vide supra*) with the alkynes was attempted. At first, replication of conditions reported in the experimental sections of Pagenkopf's work was attempted (Scheme 3-2).^{33,34} A solution of the **AP1**/naphthalene reaction mixture in degassed THF (8 mL)/triethylamine (2 mL) was added to a mixture containing $\text{Pd}(\text{PPh}_3)_4$ (10 mol %), ZnCl_2 (1 M in THF, 1.5 equiv), and the "acceptor" alkyne (1.1 equiv, e.g., **AP4**). The vessel was wrapped in foil, and the reaction was brought to 40 °C using a rheostat-controlled oil bath. The reaction was allowed to stir under inert atmosphere for 12 h, then the "donor" alkyne (1.0 equiv, e.g., **AP2**) was added neat under a flow of argon, and the reaction was stirred for 17 h more at 70 °C. The equivalencies listed are based on the estimated NMR yield of **AP1**. The zinc(II) chloride used in this reaction plays the part of co-catalyst, instead of the more traditional copper(I) iodide. Crude NMR

spectra were highly complicated; no identifiable resonances for intact siloles were generally found.

Several reaction conditions were altered to try to improve the outcome. A few palladium catalysts commonly used in cross-coupling conditions were tried: $\text{Pd}(\text{PPh}_3)_4$, $\text{Pd}(\text{PPh}_3)_2\text{Cl}_2$, and $(\text{dppf})\text{PdCl}_2$. Copper(I) iodide was also used, instead of zinc(II) chloride. The reaction times were altered, and both shortening and lengthening the times of cross-coupling was investigated. None of the adjustments attempted seemed to improve the outcomes. Unfortunately, these were all tried in THF, which was mentioned as an aside by Pagenkopf (*vide supra*) to give complex reaction products, so the main cause of the issues faced with the reaction likely overrode whatever adjustments that were investigated.

Later reactions removed THF as a solvent, and were performed in neat triethylamine or diisopropylamine. The crude reaction mixtures were still complex as investigated by NMR spectroscopy, but some SiMe resonances suggestive of silole formation appeared, but the yields based on integration compared with naphthalene suggested that these unconfirmed species were less than 5% of the product formed, not enough to be isolated.

More recently, addition of a very small amount of isopropanol to the reaction was attempted in order to more efficiently reduce the palladium(II) catalysts used into the active palladium(0) species.³⁹ Column chromatography of the crude product from this reaction isolated a fraction that yielded solid which was very insoluble in chloroform. Moreover, this solid noticeably fluoresced a bright red in the solid state but did not fluoresce in dichloromethane solution; this fluorescence behavior is one of the hallmark characteristics of 3,4-phenyl-substituted siloles.⁴⁰

This material crystallized from a slow evaporation of a dichloromethane solution to give orange needle-shaped crystals. The cell determination of the material was performed; unfortunately it turns out to match the cell parameters almost exactly of the dichloromethane solvate of *trans*-PdI₂(PPh₃)₂.⁴¹ The authors of that study were attempting to perform Suzuki coupling with a diodobinaphthyl species. The compound is likely a byproduct of the oxidative addition of the catalytically-active palladium(0) species, where two molecules of **AP1** oxidatively add to the palladium center, and then eliminate to leave the diiodopalladium complex. Nevertheless, the positive indication that **AP1** is undergoing oxidative addition with palladium after addition of isopropanol might warrant further study with greater additions of the alcohol.

3.5. Study of interactions of S1-S4 with Ni(II), Cu(II), and Hg(II) ions.

Compounds **S1-S4** were tested with nickel(II), copper(II), and mercury(II) perchlorate salts. Copper(II) was chosen because of its paramagnetic nature; typically paramagnetic ions cause significant quenching, and we desired to determine to what end this occurred with these compounds. Nickel(II) also has some known quenching ability,⁴² given its ability to form diamagnetic or paramagnetic complexes. The mercury(II) was chosen for several reasons. Being an environmentally harmful ion, potential for selective and sensitive detection has been a steady area of research.⁴³ Also, it too is generally seen as an efficient quencher due to the phenomenon known colloquially as the “heavy-atom effect”.⁴⁴ As shown below, these metal ions have differing abilities to quench (or enhance) fluorescence based on the 2,5-substituent chosen.

3.5.1. UV-vis and fluorescence studies.¹⁵

Figure 3-12 shows the results of each silole upon interaction with 10 equiv of the metal ion. For clarity, the absorbance and emission spectra of **S3** with the metals were separated. Also tested were 1, 2, and 5 equiv, and these spectra are shown in the Appendix (Section 5.4). During these experiments, the total concentration of silole in the system was kept constant at 5×10^{-5} M, and the ratio of the volume of silole solution (in dichloromethane) to metal solution (in methanol) was also 2 mL to 2 mL in order to directly compare the changes on using different metals and different equivalencies. Equivalencies of the metal solution were adjusted by changing the concentration of the metal perchlorate in methanol. In order to get an accurate representation of the silole in the absence of metal ion, the spectrum of each silole was measured with 1:1 dichloromethane/methanol to keep the concentration and overall solvent polarity constant.

Compound **S1** showed slight changes overall in the optical spectra (Figure 3-12a). The absorbance λ_{\max} upon addition of the metals is essentially unchanged. This suggests that, through the combination of the slight communication of the cyano-substituent and the general lability of the group with metal ions, the metal ions studied here do not have significant contribution to the ground state of the silole. The fluorescence spectrum with the metal ions showed variable differences, from none with copper(II) to the most with mercury(II). Interestingly, the fluorescence features are preserved between nickel(II) and mercury(II), and there is no quenching with 10 equiv of copper(II). The slight hypsochromic shift in the fluorescence data along with no discernible changes in the absorbance spectrum might indicate some excited-state de-coordination is occurring,⁴⁵ as

the changes in the overall electronics of the system for this phenomenon generally reflects the observed data for **S1**.

Silole **S2** was synthesized to affect some selectivity among the metals studied. The absorbance spectrum of **S2** also exhibits little change in the presence of the metal ions (Figure 3-12b), indicating that the metals involved do not change the electronics of the silole core significantly. The fluorescence is unaffected by both nickel(II) and copper(II), but there is significant quenching of the emission from mercury(II). It should be noted that quenching was not appreciable on **S2** until 10 equiv of mercury(II) were added (Figure A-79). Complexes containing the di(methylthio)phenyl moiety with mercury ions and compounds are known elsewhere,⁴⁶ but the reported spectra here suggest that even binding to mercury on **S2** is rather labile. Nevertheless, the selectivity of the methylthio-substituents for mercury(II), as predicted by the well-known Pearson acid base theory (HSAB theory),⁴⁷ could make analogues based on **S2** a useful template for selective detection of this ion.

Silole **S3** has the most significant spectral changes of any in the sample of siloles studied herein. With all metals studied, there is a relatively intense absorption peak *ca.* 85 nm lower in energy than the parent silole (Figure 3-12c). Notably, a smaller peak *ca.* 65 nm higher in energy also exists in all cases. The local maxima for the silole with each metal do not vary greatly; this suggests that the new transitions are mainly due to electronic changes in the silole. Figure 3-13 shows an example of **S3** with various equivalents of copper. From this plot the two new absorption bands seem to appear at the same time. In a preliminary titration experiment (Figure 3-14), THF was used for both the silole and metal solutions in order to determine the effects on coordination with a

more coordinating solvent. The blue shifted peak in this experiment appears first, with a similar relative intensity as before, but the lower energy band appears after much more metal ion solution has been added, and at a much lower intensity.

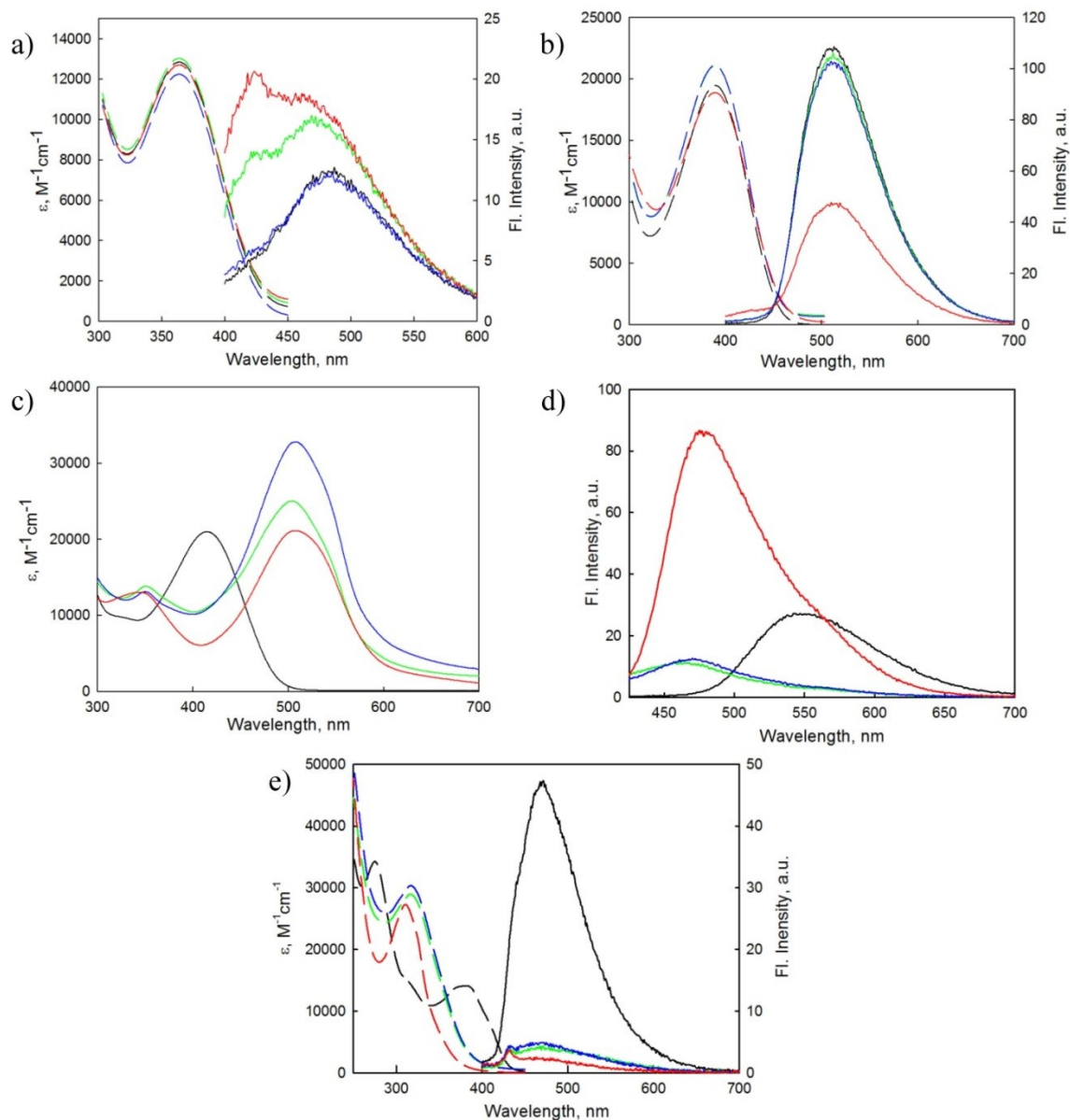


Figure 3-12. The optical spectra of S1-S4 and the mixtures with 10 equiv of the metal perchlorate; the color correspondence is: mercury(II) (red), copper(II) (blue), nickel(II) (green), pure silole (black). a) The UV-Vis (dashed) and fluorescence (solid) spectra of S1 with metal solutions. b) The UV-Vis (dashed) and fluorescence (solid) spectra of S2 with metal solutions. c) The UV-Vis spectra of S3 with metal solutions. d)

The fluorescence spectra of **S3** with metal solutions. e) The UV-Vis (dashed) and fluorescence (solid) spectra of **S4** with metal solutions. The wavelengths for fluorescence excitation are: 365 nm (**S1**), 390 nm (**S2**), 415 nm (**S3**), and 383 nm (**S4**).

Hence, the blue shifted absorption is considerably less dependent on the solvent, but the low-energy band greatly depends on the solvent's coordinating ability. From this data, both bands can be attributed to interaction of **S3** with the metal ion. The reduced intensity, higher energy band (compared to **S3**) is characteristic of reducing the donating abilities of amino-substituents (a photoinduced charge transfer, or PCT, effect),⁴⁸ the absorption λ_{max} is now much closer to that of **TPS**, suggesting deactivation of the amino-group due to coordination. The increased intensity of the lower energy band in non-coordinating solvents also indicates some manipulation of the PCT effect, but through interaction with the acceptor (i.e., the silole ring) by making the PCT from the amino group to the silole more efficient, and thus increasing the absorption coefficient.⁴⁸

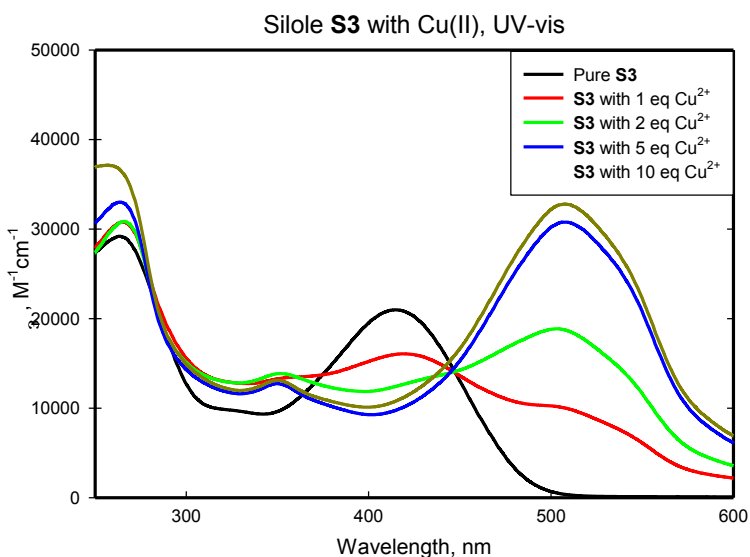


Figure 3-13. Compound **S3** (5×10^{-5} M in dichloromethane) with 1-10 equiv of copper(II) perchlorate solution (in methanol).

Given that the silole ring and accompanying aromatics of the “acceptor” region will likely coordinate with ions through arene interactions, the decrease in intensity in THF can be justified, as this coordination mode can be considered more labile than amine coordination, and will be much more affected by the competing coordinating ability of the solvent.

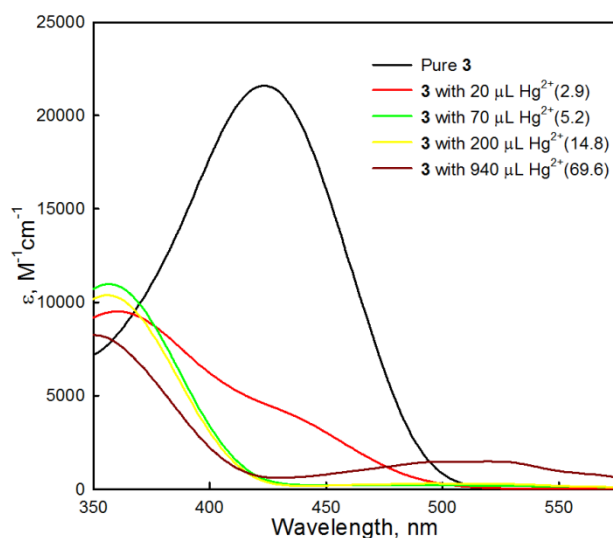


Figure 3-14. Selected titration data of a solution of **S3** in THF (6×10^{-5} M), titrated with 1.3×10^{-2} M mercury(II) perchlorate solution in THF. The values in parentheses in the legend represent the equivalencies of mercury(II) in solution.

The fluorescence spectrum of **3** with the metals has notable differences upon changing the cation studied. Every metal ion studied induces a similar hypsochromic shift in the fluorescence maximum, suggesting that this change is again due to coordination to, and deactivation of, the amino- donating group;⁴⁸ this shift to higher energy corresponds to the initial higher energy shift of **S3** in THF after addition of metal ion solution (Figure 3-14). However, the “acceptor-bound” bathochromic shift in the UV-visible spectrum of **S3** (Figure 3-12c) does not seem to have a correlated shift in the fluorescence spectrum; this is possibly due to the nature of the intra-ligand charge

transfer on excitation. While nickel(II) and copper(II) exhibit a lower intensity than **S3**, mercury(II) is exceptional in its significant increase in the fluorescence intensity. Part of this difference might be due to self-absorption of the fluorescence by the absorbance band near 500 nm, shown in the UV-visible spectrum (Figure 3-12c), which is more intense for copper(II) and nickel(II). The increase in intensity on addition of mercury(II) to **S3** could be due to oligomeric species, as **S3** has two possible coordinating amino-substituents. An increase in the quantum yield on addition of zinc(II) to a terpyridine-substituted silole, reported by Yin *et al*, was attributed to oligomer formation that would reduce intramolecular rotations and thus decrease the amount of non-radiative decay.⁶

The UV-visible spectrum of **S4** (Figure 3-12e) follows a similar trend as the other siloles, in that differences among the metal ions are slight with regard to λ_{max} values. In all cases, a new band appears at *ca.* 315 nm. Though this band is higher in energy than the silole absorbance at 383 nm, it has a significant increase in intensity, which more closely matches the pure silole peak at 275 nm. Pyridine-based groups are considered stronger π -acceptors than siloles,⁶ and therefore this metal-induced shift is likely from the higher energy pure silole band. These factors combined suggest that the metal-silole band is, again, a consequence of the metal binding to the bipyridine moieties and making intramolecular PCT more efficient by increasing the accepting ability of those moieties.⁴⁸ The fluorescence spectra with each metal shows that there is very significant quenching. The UV-visible spectrum indicates the silole band completely disappears, and therefore excitement at the silole peak probably causes a charge transfer to the bipyridine moiety such that fluorescence is attenuated. Bipyridine is a chelating ligand, and so coordination to each ion with **S4** is very efficient; the fluorescence quenching for copper(II) and

mercury(II) is very similar even at 2 equiv (see Figure A-90 and Figure A-91), with nickel(II) exhibiting less quenching (Figure A-89). The exception for nickel(II) is most likely due to its relatively slow ligand exchange kinetics, as ligand exchange of the hexamethanol complex of nickel(II) is approximately four orders of magnitude slower than the copper(II) complex.⁴⁹

3.5.2. Spectrophotometric titration study of **S3** with *Hg(II)*

Of the four siloles studied for interactions with metal salts, silole **S3** showed the most dramatic changes (Figure 3-12). In different solvent systems, these new absorption bands brought on by interaction with metal centers showed remarkably different behavior, particularly for the lower energy band *ca.* 500 nm (Figure 3-13 and Figure 3-14). In order to further understand the binding of the metal centers to **S3**, several spectrophotometric titrations were carried out, and are described below.

The standard representation for a 1:1 metal:ligand binding event is described by the following equation:⁵⁰

$$\frac{A_0 - A}{A - A_{\text{lim}}} = K_1 c_M \quad (1)$$

Where A_0 is the absorbance of the ligand absent any metal, A_{lim} is the absorbance at maximum saturation, K_1 is the binding constant, and c_M is the overall concentration of the cation at a given absorbance (assuming that the amount of free metal is much larger than the amount bound to the ligand). In order to make this equation more amenable to analysis, it is rearranged, such that:

$$A = \frac{A_0 + A_{\text{lim}} K_1 c_M}{1 + K_1 c_M} \quad (2)$$

To make the equation more general, one can also fit multiple metal to ligand binding events such that:

$$A = \frac{A_0 + A_{\text{lim}} K_n c_M^n}{1 + K_n c_M^n} \quad (3)$$

Where n represents the number of metals binding to a ligand.⁵⁰ Therefore, K_1 is the binding constant of one metal center to one ligand, K_2 is the binding constant of 2 metal centers to one ligand, etc. Thus, a plot of the absorbance as a function of the cation concentration would yield a fit curve that, when the difference is minimized against the data, yields the constants A_0 , A_{lim} , and K_n . The fit curves and graphs generated in this section were calculated and displayed using SigmaPlot (version 11) graphing software.

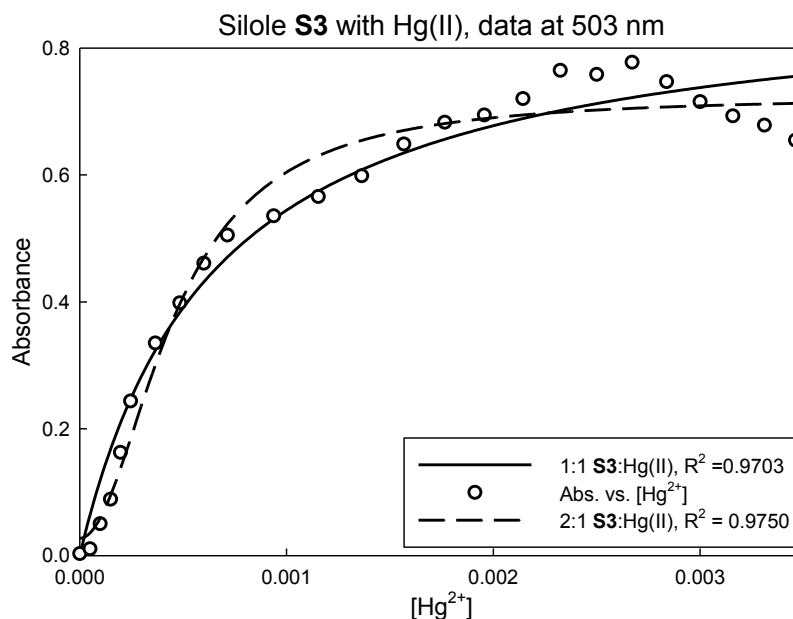


Figure 3-15. The absorbance versus mercury(II) concentration, along with the 1:1 and 2:1 Hg(II):S3 fit curves, for the titration in dichloromethane/methanol. Statistical data is provided Figure A-93 after in the appendix (Section 5.4.2).

Our initial titrations simulated the solvent conditions of the qualitative spectra obtained for S3 and Hg(II) (Section 3.5.1), where a solution of Hg(II) perchlorate in

methanol (1.5×10^{-2} M) was titrated into a solution of **S3** in dichloromethane (1.0×10^{-4} M, 3 mL). All of the spectra collected for this run are displayed in Figure A-92 in the appendix. From this data, we extracted the absorbance values at one wavelength (503 nm), and plotted these values against their respective values of [Hg(II)]. This graph, along with the fit curves employed (using Equation 3 above), is displayed in Figure 3-15.

Our initial assumption was that the mercury would bind to either one or both of the dimethylamino moieties on **S3**, so we wanted to model both one-cation binding and two-cation binding with **S3**, and to determine which would more accurately model the data observed. Equation 3 above could also give us some idea for the binding affinity by calculating K_n from the experimental data.

The data in Figure 3-15 initially provides for smooth changes that are especially agreeable with a two-cation binding event, but on larger concentrations of Hg(II), the data begins to have large deviations from any fit curve. The R^2 value for a two-cation event (0.9750) are slightly better than for the single cation binding event (0.9703), but this deviation makes the model for the fit curves unreliable. Nevertheless, rough estimates for the binding (see Figure A-93 and subsequent statistical data for details) based on the assumed model show a K_1 of $(1.5 \pm 0.3) \times 10^3 \text{ M}^{-1}$ (if one-cation binding is assumed), and a K_2 of $(4.8 \pm 0.8) \times 10^6 \text{ M}^{-2}$ (if two-cation binding is assumed). Two-cation binding, according to Equation 3 above, is dependent on the square of the metal concentration; that K_2 is approximately double the squared value of K_1 at least suggests a similar binding “strength” for each system.

Though the binding constants could be approximated, the quality of the data, particularly at higher [Hg(II)], makes the model potentially unreliable. It was then

hypothesized that the mixed solvent system could be a contributing factor for this unreliable data. As the methanol solution of Hg(II) was added, the solvent polarity was changing due to the added methanol. This could be alleviated by using a solvent system in which both **S3** and Hg(II) were soluble. Ultimately, THF was able to satisfy this requirement. In addition, THF is a much more coordinating solvent than dichloromethane, so the added competition for binding may help shed light on the coordinative environment of the metal at **S3**.

Several titrations were attempted at varied concentrations, with the goal of having most of the low energy absorption (*ca.* 500 nm) within the Beer-Lambert region of absorbance (i.e., between 0.2 and 0.8); a concentration of 1.5×10^{-4} M for the **S3** ultimately had the best absorption response during titration. The raw spectral data is shown in Figure A-94. Upon increasing the concentration of Hg(II), the initial silole absorption at 415 nm decreases in intensity rapidly. This is replaced with an absorption band at *ca.* 355 nm, at 70% intensity of the original silole peak. Further increasing the concentration of Hg(II) causes this band to slowly reduce in intensity, while the low-energy band slowly begins to increase in intensity, approaching a maximum intensity of approximately 20% of the original silole band; the intensity is much lower in THF than in dichloromethane/methanol, and the proposed reason for the decreased intensity is discussed in Section 3.5.1.

The data at 503 nm was again extracted for in order to attempt to model the interaction of Hg(II). This is shown in Figure 3-16, along with the fit curves representing a one-cation and a two-cation binding model. The data obtained for this titration appears much less variable than the data obtained for the titration performed in dichloromethane

/methanol. There is some significant difference apparent in the fit curves used, as well. The R^2 value for the one-cation binding system (0.9618) is much lower than that of the two-cation binding system (0.9903). This could suggest that at least two metals are binding on the silole molecule. The one-cation fit curve does not seem to fit the data at all, but the two-cation fit curve seems to fit the data enough to give a reasonable estimate of the binding constant, which was calculated in SigmaPlot to be $(1.4 \pm 0.1) \times 10^6 \text{ M}^{-2}$. The standard of deviation for this result is much lower, representative of the better quality data obtained. The value of the binding constant is also 3.5 times lower than the system in dichloromethane/methanol; this agrees well with the much reduced intensity of the lower energy band in THF.

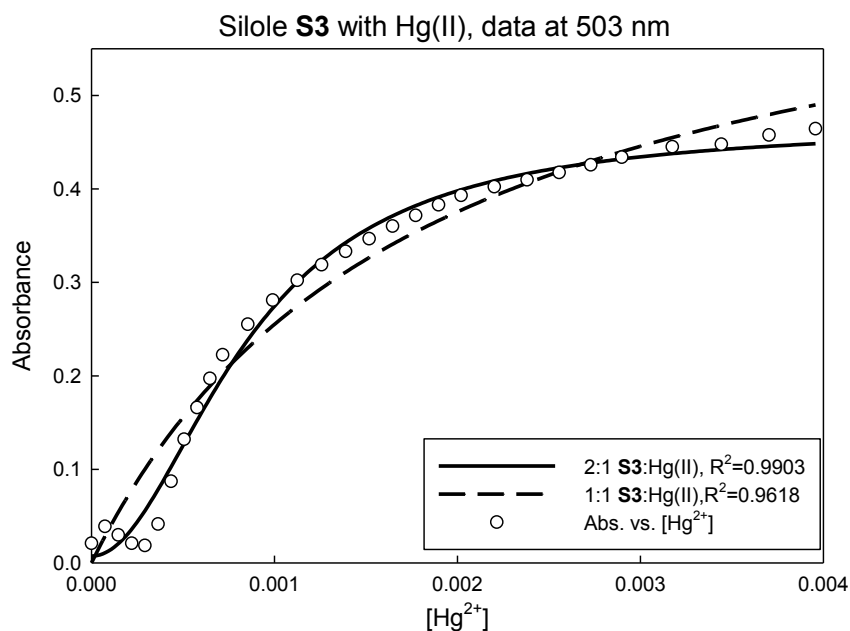


Figure 3-16. The titration data extract from the raw data (Figure A-94) at 503 nm. The total $[\text{Hg}^{2+}]$ was calculated from the initial volume of **S3** (3 mL), plus the volume added by the titrant (i.e., Hg(II) perchlorate in THF). The fit curves for one-cation and two-cation binding are displayed, along with their R^2 values in the legend.

However, the explanation offered above might not fully address the binding effects occurring with **S3**, as the Equation 3 listed above only really addresses a concurrent binding event with metal centers.⁵⁰ From the titration experiment conducted in THF (Figure A-94), it is clearly apparent that there are two separate species of coordinated **S3**. The higher-energy band at 355 nm appears *before* the lower-energy band at 500 nm, and the higher-energy band also decreases in intensity as it increases for the lower-energy band. Figure 3-17 displays the data extracted at 355 nm to show this increase, and then decrease, in intensity.

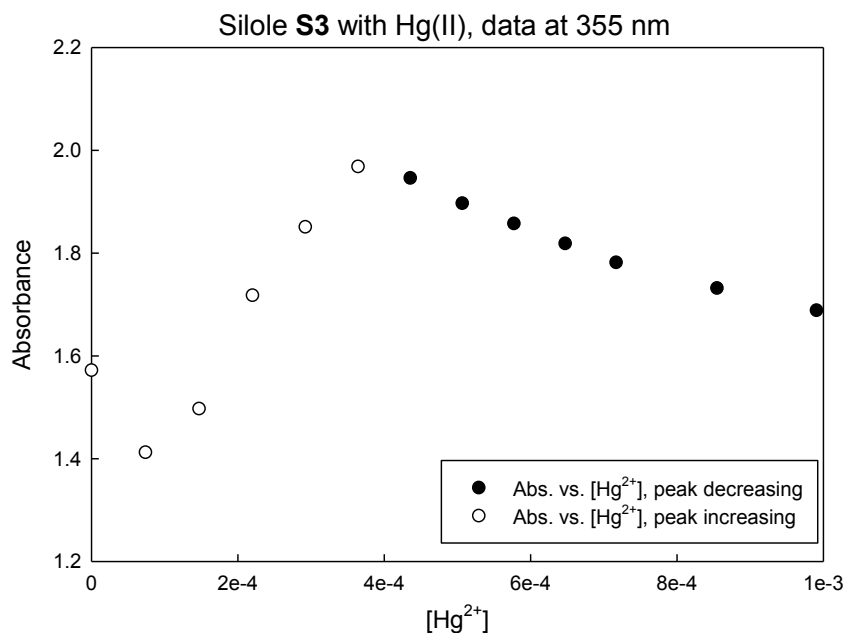


Figure 3-17. The titration data extract from the raw data (Figure A-94) at 355 nm. The total [Hg²⁺] was calculated from the initial volume of **S3** (3 mL), plus the volume added by the titrant (i.e., Hg(II) perchlorate in THF).

The portion of the titration where the higher-energy band is increasing appears essentially linear (except for the initial, “pure silole” data point), and is followed by a sharp turnaround to decreasing intensity. This transition also occurs at around 4×10^{-4}

M, which is roughly double the concentration of the silole (1.5×10^{-4} M). The linearity of the increase, the hypsochromic shift and lower intensity,⁴⁸ and the concentration at which the intensity is decreasing all suggest very strong binding to the dimethylamino-substituents, which behaves as a “ π -donor” in free **S3**. After this, a much weaker binding event occurs, and due to the bathochromic shift, it is believed to be somewhere along the silole ring or the arene substituents.

Therefore, the binding after 4×10^{-4} M must be analyzed separately, as if the strongly coordinated dimercury-**S3** was now behaving itself as a ligand. This would effectively remove the same amount of mercury from solution, causing each measurement to have less free cation in solution. The “corrected” graph is displayed in Figure 3-18, statistical data is posted subsequent to this same graph as Figure A-97.

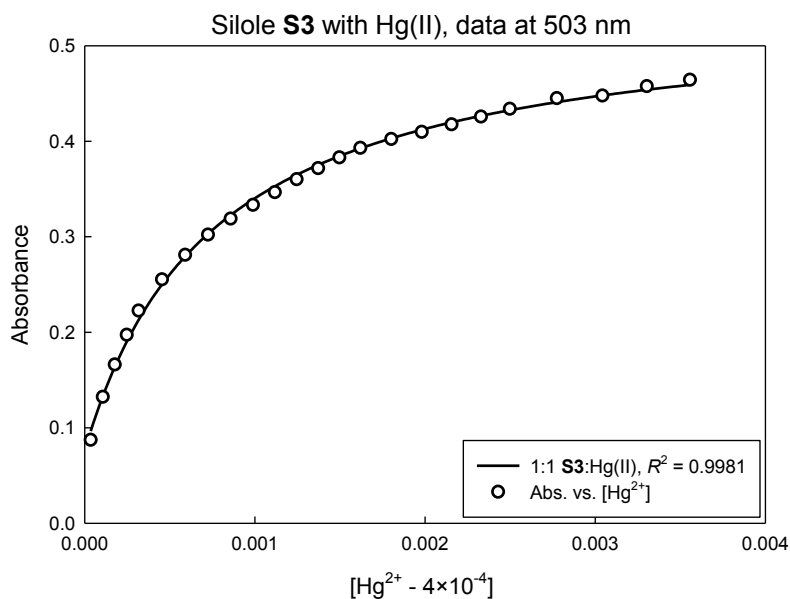
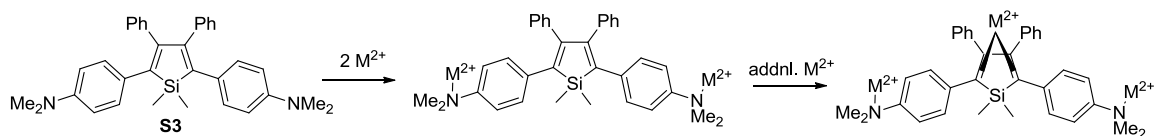


Figure 3-18. The plot of absorbance versus the concentration of Hg(II), after subtracting 4×10^{-4} M to account for the previously coordinated Hg(II) (see text).

The R^2 value obtained by this corrected graph (0.9981) suggests that the coordination of Hg(II) (and likely the other metals studied in Section 3.5.1) are modeled very well using the one-cation binding event. The fit curve generated from data in this graph shows a binding constant of $1320 \pm 58 \text{ M}^{-1}$, which surprisingly matches closely with the one-cation binding constant for the dichloromethane/methanol system above, though the binding constant shown here has a significantly smaller standard of deviation (again due to the better data obtained).

The coordination study in THF demonstrated that the binding of metal cations to **S3** occurs in two steps: first, the metals bind to the dimethylamino-substituents on **S3**, and second, a third cation binds to the π -system of the silole itself, possibly through the butadiene moiety of the silole ring, as it is generally the more “ π -accepting” moiety on the molecule. This stepwise binding is described pictorially in Scheme 3-4. This also could potentially help to explain the strong intensity in dichloromethane/methanol in the initial study using different equivalents with the same volume (Section 3.5.1). Because, for example, the solution containing ten equiv of the metal was much more concentrated, more of the trimetal-coordinated **S3** species would form because of the higher probability of three metal centers being close enough to form the complex nearly simultaneously.



Scheme 3-4. A representation of the metal binding sites as suggested through the spectrophotometric titration studies.

3.6. Preliminary calculations of **S3** with varying stoichiometries of metal coordination.

Section 3.5.2 outlined the likely modes of binding of **S3** with mercury(II), with the metal center coordinating first to the two nitrogen atoms, inducing a hypsochromic shift in absorbance, followed by coordination to the acceptor portion of the silole (i.e., the diene of the silole ring), which causes a bathochromic shift in absorbance. All of the metals exhibited similar optical changes upon addition to **S3** (Section 3.5.1); therefore, the mode of binding for **S3** to metal centers is likely general, with most of the electronic changes occurring within the silole itself. The change to both lower and higher energies are indicative that photoinduced charge transfer (PCT, Section 1.4)⁴⁸ occurs in free **S3** and is adjusted upon binding to the donor end (dimethylamino-substituent) or the acceptor moiety (silole ring). In order to investigate the electronics of this transition further, some initial calculations were performed using Wavefunction's Spartan '04 package. Copper(II) was chosen as the metal center employed in order to ease the calculation, as very heavy atoms such as mercury require both pseudopotential corrections, as well as relativistic corrections. The free compound **S3**, as well as the donor-bound dicopper complex **S3+2Cu**, and the acceptor-bound tricopper complex **S3+3Cu**, were all minimized to equilibrium geometry using DFT (B3LYP functional and 6-31G* basis set), which has been used successfully for other siloles.⁵¹ The complex **S3+3Cu** initially had problems obtaining SCF convergence, so to aid calculation several options in the program were flagged to increase tolerance such that the model would finish. These were also set for the other compounds studied, in order to try to limit as many variables as possible. Solvents had to be omitted due to memory constraints, so the

results obtained thus far are more for comparative, or relative results, not absolute. The results of the calculation are shown in Table 3-4. The free silole exhibits HOMO and LUMO in the range of other siloles studied,^{51,52} but are slightly destabilized, which is as expected for the strongly π -donating dimethylamino-substituent.¹ As metal coordination increases on **S3+2Cu** and **S3+3Cu**, a large stabilization of the HOMO and LUMO values is calculated.

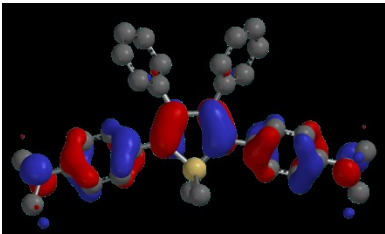
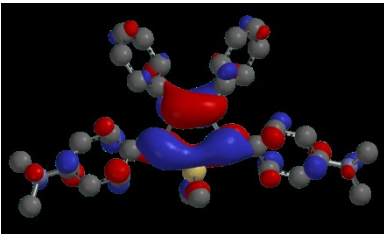
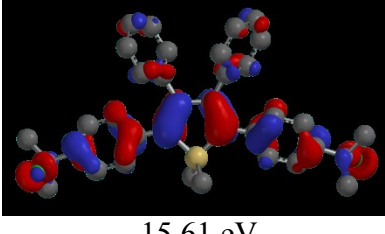
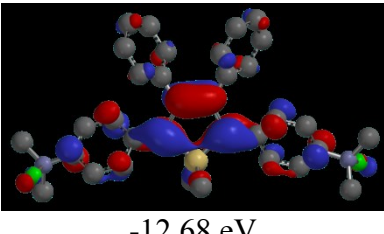
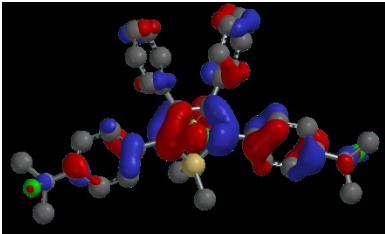
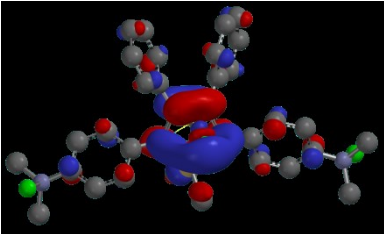
Cmpd.	HOMO	LUMO	E_g
S3	 -4.38 eV	 -1.22 eV	3.16 eV
S3+2Cu	 -15.61 eV	 -12.68 eV	2.93 eV
S3+3Cu	 -20.81 eV	 -18.04 eV	2.77 eV

Table 3-4. The probability densities of the HOMO and LUMO orbitals for **S3**, **S3+2Cu**, and **S3+3Cu**. Calculation details are outlined in the text. Hydrogen atoms have been omitted for clarity.

For compound **S3+2Cu**, the HOMO probability density looks very much unchanged, qualitatively; most of the density is still within the 2,5-aryl groups and the butadiene of the silole ring. The only difference noticeable, besides the largely stabilized energy, is that there is some probability density present on the copper atoms, indicative of the interaction with nitrogen lone pairs, which helps to justify the initial hypsochromic shift in the titration experiment (PCT effects). Additionally, the LUMO of the compound shows a significant removal of probability density away from the silicon center. As the silylene σ^* molecular orbital is necessary for the bathochromic shift in the silole optical spectra,⁵³ its noticeable absence in the contribution to the LUMO may also help to explain the hypsochromic shift. Surprisingly, the bandgap (E_g) is calculated to be slightly lower for this complex than free **S3**. While this may indicate that the model predicts a lower energy absorption band for the complex, these are ground state calculations; PCT, which is invoked to explain this model, also relies on interactions or lack thereof in the excited state. To this end, UV-vis simulations were attempted as they can account for excited states more thoroughly, but unfortunately could not be completed due to memory constraints on our hardware.

Complex **S3+3Cu** also minimized such that much of the probability density remained on the silole core. The added copper at the silole ring, however, also has significant amounts of density, indicative of an appreciable interaction between the silole ring and the copper. In comparison to the HOMO in **S3+2Cu**, **S3+3Cu** has much less density at the copper centers coordinated at nitrogen, which suggests that the binding of copper to the silole ring directly alters the energy such that orbital interaction of the other two copper centers is limited. The LUMO of the complex shows an even more dramatic

shift to the copper center at the silole ring, which is predicted as a part of PCT,⁴⁸ as interactions with accepting portions of the fluorophore should show a larger charge separation by including the di-positive cation in the total.

3.7. Summary

Several known and new siloles were synthesized for their potential as ligands to metal centers, or as intermediates to form other systems, and were characterized by multinuclear NMR, UV-vis and fluorescence spectroscopies, elemental analysis, and/or X-ray crystallography. The optical spectra of **S1-S4** were studied with 1-10 equiv of Ni(II), Cu(II), and Hg(II) solutions, and changes were monitored. Compound **S1** showed very slight changes mainly to the relatively weak binding ability of the cyano-substituent towards the metal centers studied. Compound **S2** showed very small changes, but the fluorescence of the molecule was selectively quenched when in the presence of ten equiv of the mercury(II), demonstrating some modest selectivity. Compound **S3** showed the most dramatic changes in spectra on metal binding, as two new bands appeared that were indicative of their binding positions; the changes were similar with all metals studied, suggesting that the optoelectronic modifications were more affected on the silole itself. Compound **S4** showed some hypsochromic shifts in absorption upon binding likely due to the increased torsional angle caused by coordination of the metal ion with the bipyridine moieties, and showed efficient quenching of fluorescence upon coordination with all the metals studied.

Compounds **S5** and **S6** were synthesized with hopes of converting them to a α -bromotolylspecies that could be reacted with phenoxides to form “off-on” metal detecting molecules through interrupting photoinduced charge transfer. Multiple bromination

conditions were attempted with **S6**, but all conditions that were attempted could not cleanly convert this silole. Alkyl-methoxy substituents, such as those on **S5**, have been known to react with BBr_3 to form brominated products; however, action of this brominating reagent on **S5** yielded a butadiene compound through silole ring cleavage caused by the aggressive BBr_3 reagent. An alternative route was developed, using the bromobenzyl-quinolate substituted compound **SP2** to attempt direct formation of the targeted silole by the Tamao procedure, but isolation of the material has not yet been achieved.

The successful synthesis of the 2,5-dihalo- unsymmetric silole **AP1** was carried out in order to attempt a cross-coupling reaction with synthesized terminal acetylenes **AP2** to **AP4**, under Sonogashira conditions. All precursors were successfully synthesized, but the reaction to couple them together in hopes of generating unsymmetric siloles that could bind to metals proved to be troublesome. Part of the reason was an inaccurately reported experimental by other researchers that made synthesis impossible. Later attempts showed a palladium byproduct that suggested that the compound could react with the active palladium(0) species.

The crystal structures of **S1**, **S2**, and **S5** were obtained and generally refined with low residual electron densities. Compound **S2** had an arrangement of its methylthio-substituents that suggested some C-H/ π interactions were assisting and/or directing crystallization; analysis of the geometry shows that this could be reasonable, even though the distance measured is larger than many of those interactions.

Further study was pursued in the binding environment of **S3** with metals, *via* spectrophotometric titration of the silole with a mercury(II) solution. Initially the

procedure was performed using dichloromethane/methanol for the silole and mercury(II) solutions, respectively; however, using THF for both of these compounds gave better data. The THF-based titration revealed that the two bands observed, at ca. 355 and 503 nm, are in fact different species. The higher energy band is likely due to metals binding to the “donor” ends of the silole ($-NMe_2$ groups), while the lower energy band seems to be caused by weak coordination of a third metal center to the π -system of the silole itself. Preliminary computational studies performed on **S3** with varying coordinations of copper also suggest, through the manipulations of the probability densities of the **HOMO** and **LUMO**, that the electronics are altered upon coordination in a way that is indicative of a charge transfer process.

3.8. References

-
- (1) Zhan, X.; Barlow, S.; Marder, S. R. *Chem. Comm.* **2009**, 1948–1955.
 - (2) Yamaguchi, S.; Endo, T.; Uchida, M.; Izumizawa, T.; Furukawa, K.; Tamao, K. *Chem. Eur. J.* **2000**, *6*, 1683–1692.
 - (3) See for example: (a) McMahon, R.J. *Coord. Chem. Rev.* **1982**, *47*, 1-14; (b) Carré, F.; Colomer, E.; Corey, J.Y.; Corriu, R.J.P.; Guérin, C.; Henner, B.J.L.; Kolani, B.; Man, W.W.C.W.C. *Organometallics* **1986**, *5*, 910-917; (c) Ohshita, J.; Hamaguchi, T.; Toyoda, E.; Kunai, A.; Komaguchi, K.; Shiotani, M. *Organometallics* **1999**, *18*, 1717-1723; (d) Dysard, J.M.; Tilley, T.D. *J. Am. Chem. Soc.* **2000**, *122*, 3097-3105.
 - (4) Lee, J.; Liu, Q.-D.; Motala, M.; Dane, J.; Gao, J.; Kang, Y.; Wang, S. *Chem. Mater.* **2004**, *16*, 1869-1877.
 - (5) Aubouy, L.; Huby, N.; Wantz, G.; Vignau, L.; Hirsch, L.; Guérin, C.; Gerbier, P. *C. R. Chimie* **2005**, *8*, 1262-1267.
 - (6) Yin, S.; Zhang, J.; Feng, H.; Zhao, Z.; Xu, L.; Qiu, H.; Tang, B.Z. *Dyes and Pigments* **2012**, *95*, 174-179.
 - (7) (a) Braddock-Wilking, J.; Gao, L.-B.; Rath, N.P. *Organometallics* **2010**, *29*, 1612-1621; (b) Braddock-Wilking, J.; Gao, L.-B.; Rath, N.P. *Dalton Trans.* **2010**, *39*, 9321-9328.
 - (8) Tamao, K.; Yamaguchi, S.; Shiro, M. *J. Am. Chem. Soc.* **1994**, *116*, 11715–11722.

-
- (9) Morra, N. A.; Pagenkopf, B. L. In *Organic Syntheses*; John Wiley & Sons, Inc.; Daisuke, T.; Mita, T.; Shibasaki, M., Eds.; John Wiley & Sons, Inc.: Hoboken, NJ, USA, 2008; pp. 53–63.
- (10) King, A. O.; Okukado, N.; Negishi, E. *J. Chem. Soc., Chem. Commun.* **1977**, 0, 683–684.
- (11) Liu, Q.; Lan, Y.; Liu, J.; Li, G.; Wu, Y.-D.; Lei, A. *J. Am. Chem. Soc.* **2009**, *131*, 10201–10210.
- (12) Chau, N. T. T.; Meyer, M.; Komagawa, S.; Chevallier, F.; Fort, Y.; Uchiyama, M.; Mongin, F.; Gros, P. C. *Chem. Eur. J.* **2010**, *16*, 12425–12433.
- (13) Dötze, M.; Klar, G. *Phosphorus Sulfur* **1993**, *84*, 95–106.
- (14) (a) Uchida, M.; Izumizawa, T.; Nakano, T.; Yamaguchi, S.; Tamao, K.; Furukawa, K. *Chem. Mater.* **2001**, *13*, 2680–2683; (b) Mäkinen, A. J.; Uchida, M.; Kafafi, Z. H. *Applied Physics Letters* **2003**, *82*, 3889; (c) Son, H.-J.; Han, W.-S.; Wee, K. R.; Lee, S.-H.; Hwang, A.-R.; Kwon, S.; Cho, D. W.; Suh, I.-H.; Kang, S. O. *J. Mater. Chem.* **2009**, *19*, 8964–8973.
- (15) Carroll, J. B.; Braddock-Wilking, J. *Organometallics* **2013**, *32*, 1905–1912.
- (16) Kienle, M.; Knochel, P. *Org. Lett.* **2010**, *12*, 2702–2705.
- (17) Hayashi, T.; Konishi, M.; Kobori, Y.; Kumada, M.; Higuchi, T.; Hirotsu, K. *J. Am. Chem. Soc.* **1984**, *106*, 158–163.
- (18) Yu, G.; Yin, S.; Liu, Y.; Chen, J.; Xu, X.; Sun, X.; Ma, D.; Zhan, X.; Peng, Q.; Shuai, Z.; Tang, B.Z.; Zhu, D.; Fang, W.; Luo, Y. *J. Am. Chem. Soc.* **2005**, *127*, 6335–6346.
- (19) Mei, J.; Wang, J.; Sun, J.Z.; Zhao, H.; Yuan, W.; Deng, C.; Chen, S.; Sung, H.H.Y.; Lu, P.; Qin, A.; Kwok, H.S.; Ma, Y.; Williams, I.D.; Tang, B.Z. *Chem. Sci.* **2012**, *3*, 549–558.
- (20) Boydston, A.J.; Pagenkopf, B.L. *Angew. Chem.* **2004**, *116*, 6496–6498.
- (21) Nishio, M. *Phys. Chem. Chem. Phys.* **2011**, *13*, 13873–13900.
- (22) Jung, H. S.; Ko, K. C.; Lee, J. H.; Kim, S. H.; Bhuniya, S.; Lee, J. Y.; Kim, Y.; Kim, S. J.; Kim, J. S. *Inorg. Chem.* **2010**, *49*, 8552–8557.
- (23) Lin, W.; Yuan, L.; Cao, Z.; Feng, J.; Feng, Y. *Dyes Pigments* **2009**, *83*, 14–20.
- (24) (a) Nordvik, T.; Brinker, U. H. *J. Org. Chem.* **2003**, *68*, 9394–9399; (b) Doyagüez, E. G. *Synlett* **2005**, *10*, 1636–1637.
- (25) Djerassi, C. *Chem. Rev.* **1948**, *43*, 271–317.
- (26) Bedel, S.; Ulrich, G.; Picard, C. *Tetrahedron Lett.* **2002**, *43*, 1697–1700.
- (27) Mestres, R.; Palenzuela, J. *Green Chem.* **2002**, *4*, 314–316.
- (28) Podgoršek, A.; Stavber, S.; Zupan, M.; Iskra, J. *Tetrahedron Lett.* **2006**, *47*, 7245–7247.
- (29) Chen, H.; Shen, L.; Lin, Y. *Synth. Comm.* **2010**, *40*, 998–1003.
- (30) Podgoršek, A.; Stavber, S.; Zupan, M.; Iskra, J. *Tetrahedron* **2009**, *65*, 4429–4439.
- (31) Amijs, C. H. M.; van Klink, G. P. M.; van Koten, G. *Green Chem.* **2003**, *5*, 470.
- (32) Yamaguchi, S.; Jin, R.-Z.; Tamao, K. *J. Organomet. Chem.* **1998**, *559*, 73–80.

-
- (33) Boydston, A. J.; Yin, Y.; Pagenkopf, B. L. *J. Am. Chem. Soc.* **2004**, *126*, 3724–3725.
- (34) Boydston, A. J.; Yin, Y.; Pagenkopf, B. L. *J. Am. Chem. Soc.* **2004**, *126*, 10350–10354.
- (35) Hrobáriková, V.; Hrobárik, P.; Gajdoš, P.; Fitolis, I.; Fakis, M.; Persephonis, P.; Zahradník, P. *The Journal of Organic Chemistry* **2010**, *75*, 3053–3068.
- (36) Vrábek, M.; Hocek, M.; Havran, L.; Fojta, M.; Votruba, I.; Klepetářová, B.; Pohl, R.; Rulišek, L.; Zendlová, L.; Hobza, P.; Shih, I.; Mabery, E.; Mackman, R. *Eur. J. Inorg. Chem.* **2007**, 1752–1769.
- (37) Takahashi, S.; Kuroyama, Y.; Sonogashira, K.; Hagihara, N. *Synthesis* **15**, 1980, 627–630.
- (38) Chinchilla, R.; Nájera, C. *Chem. Rev.* **2007**, *107*, 874–922.
- (39) Xiao-Chun, T.; Yue-Ping, Z.; Tian-Xiong, H.; Dong, S. *Chin. J. Chem.* **2007**, *25*, 1326.
- (40) Luo, J.; Xie, Z.; Lam, J. W. Y.; Cheng, L.; Tang, B. Z.; Chen, H.; Qiu, C.; Kwok, H. S.; Zhan, X.; Liu, Y.; Zhu, D. *Chem. Comm.* **2001**, 1740–1741.
- (41) Theissmann, T.; Bolte, M. *Acta. Cryst.* **2006**, *E62*, m1056–m1058.
- (42) Linschitz, H.; Pekkarinen, L. *J. Am. Chem. Soc.* **1960**, *82*, 2411–2416.
- (43) Nolan, E.M.; Lippard, S.J. *Chem. Rev.* **2008**, *108*, 3343–3380.
- (44) Berlman, I.B. *J. Phys. Chem.* **1973**, *77*, 562–567.
- (45) Rurack, K. *Spectrochim. Acta, Part A* **2001**, *57*, 2161–2195. Relevant information is contained in Section 4.1.2.
- (46) Behrens, U.; Berges, P.; Bieganowski, R.; Hinrichs, W.; Schiffling, C.; Klar, G. *J. Chem. Res. (S)* **1986**, *9*, 326–327.
- (47) Pearson, R.G. *J. Am. Chem. Soc.* **1963**, *85*, 3533–3539.
- (48) Valeur, B.; Leray, I. *Coord. Chem. Rev.* **2000**, *205*, 3–40. Relevant information on PCT is contained in Section 3.
- (49) Helm, H.; Merbach, A.E. *Chem. Rev.* **2005**, *105*, 1923–1959.
- (50) Valeur, B.; Pouget, J.; Bourson, J.; Kaschke, M.; Ernsting, N. P. *J. Phys. Chem.* **1992**, *96*, 6545–6549.
- (51) (a) Zhan, X.; Risko, C.; Amy, F.; Chan, C.; Zhao, W.; Barlow, S.; Kahn, A.; Brédas, J.-L.; Marder, S. R. *Journal of the American Chemical Society* **2005**, *127*, 9021–9029; (b) Zhan, X.; Risko, C.; Korlyukov, A.; Sena, F.; Timofeeva, T. V.; Antipin, M. Y.; Barlow, S.; Brédas, J.-L.; Marder, S. R. *Journal of Materials Chemistry* **2006**, *16*, 3814; (c) Zhan, X.; Haldi, A.; Risko, C.; Chan, C. K.; Zhao, W.; Timofeeva, T. V.; Korlyukov, A.; Antipin, M. Y.; Montgomery, S.; Thompson, E.; An, Z.; Domercq, B.; Barlow, S.; Kahn, A.; Kippelen, B.; Brédas, J.-L.; Marder, S. R. *Journal of Materials Chemistry* **2008**, *18*, 3157.
- (52) Bozeman, T. C.; Edwards, K. A.; Fecteau, K. M.; Verde, M. G.; Blanchard, A.; Woodall, D. L.; Benfaremo, N.; Ford, J. R.; Mullin, J. L.; Prudente, C. K.; Tracy, H. J. *J. Inorg. Orgnomet. P.* **2011**, *21*, 316–326.
- (53) Yamaguchi, S.; Tamao, K. *Bull. Chem. Soc. Jpn.* **1996**, *69*, 2327–2334.

Chapter 4. Experimental Section

General Remarks. Unless otherwise indicated, synthetic reactions were performed under an inert atmosphere of argon with flame-dried glassware, using standard Schlenk techniques. The solvents; dichloromethane, ethyl acetate, diethyl ether, hexanes, chloroform, THF, methanol, and toluene were purchased from Fisher Chemical or Sigma-Aldrich, and were used as received unless noted below. For air- and moisture-sensitive reactions, THF and diethyl ether were dried over activated 4 Å sieves over several hours and then freshly distilled from Na/9-fluorenone under argon prior to use. Chloroform-*d* and was purchased from Cambridge Isotope Labs and dried over sieves prior to use. The compounds 3-ethynylpyridine, 2-ethynylpyridine, 6-bromo-2,2'-bipyridine, trimethylsilylacetylene, lithium metal (wire, in oil), *n*-butyllithium in hexanes (1.6 and 2.5 M), 4-bromo-*N,N*-dimethylaniline, (4-bromobenzyl)methyl ether, diphenylacetylene, *N*-chlorophthalimide, germanium(IV) chloride, 4-bromobenzyl bromide, ethynylmagnesium bromide (0.5 M, THF), 8-hydroxyquinoline, 4-bromobenzonitrile, 4-iodotoluene, 1-iodo-4-nitrobenzene, 1-bromo-4-(methoxymethyl)benzene, copper(I) iodide were purchased from Sigma-Aldrich and used as received. Phenylacetylene was purchased from GFS Chemicals and was used as received. Triethylamine (Acros Organics), diisopropylamine (Acros Organics), and *N,N,N',N'*-tetramethylethylenediamine (TMEDA, Sigma-Aldrich) were dried over potassium hydroxide, distilled, and stored over potassium hydroxide for moisture-sensitive reactions. Dichlorodimethylsilane was purchased from Sigma-Aldrich, distilled over anhydrous potassium carbonate under argon, and stored under argon prior to use. Lithium

metal (pellets, 0.5-1% sodium content) was purchased from Sigma-Aldrich and introduced into the drybox, where it was weighed into vials for individual reactions. Zinc(II) chloride for air/moisture-sensitive reactions was purchased from Sigma-Aldrich and was flame-dried under vacuum until completely melted, then introduced to the glovebox, where it was ground with a mortar and stored; for individual reactions, the material was weighed in the glovebox into a suitable container. Naphthalene (Fisher) was recrystallized from ethanol. Silica gel (Premium Rf, 200-400 mesh, 60 Å porosity) was purchased from Sorbent Technologies, Inc. Methanol for optical spectra experiments (spectrophotometric grade) was purchased from Sigma-Aldrich and used as received. Dichloromethane for optical spectra experiments (spectrophotometric grade) was purchased from Acros Organics and used as received. Dichloro(1,5-cyclooctadienyl)palladium(II) ((COD)PdCl₂) was generously donated from Professor Gordon Anderson's laboratory.

Many precursor compounds were synthesized from standard literature procedures, including 1,1'-bis(diphenylphosphino)ferrocene (dppf),¹ ethynyldiphenylphosphine,² 1,1-dichloro-2,3,4,5-tetraphenylgermole,³ bis(phenylethynyl)dimethylsilane,⁴ 4-bromo-1,2-bis(methylthio)benzene,⁵ dichlorobis(triphenylphosphine)palladium(II),⁶ ZnCl₂(TMEDA),⁷ and 4-iodo-N,N-dimethylaniline.⁸

NMR spectra were recorded on a Bruker Avance-300 MHz or Bruker ARX-500 MHz instrument at ambient temperature. Spectroscopic data were recorded at 300 MHz or 500 MHz, respectively for ¹H, 75 MHz or 125 MHz, respectively for ¹³C, 121 or 202 MHz, respectively for ³¹P, and 99 MHz for ²⁹Si. Chloroform-*d* is the NMR solvent used, unless otherwise indicated, and all ¹H and ¹³C NMR spectra were referenced to residual

protic solvent. $^{29}\text{Si}\{^1\text{H}\}$ (DEPT) spectra are externally referenced to tetramethylsilane. $^{31}\text{P}\{^1\text{H}\}$ spectra are referenced to external phosphoric acid. Chemical shifts are reported in parts per million (ppm), with coupling constants reported in Hertz (Hz). Gas chromatography experiments were performed using a Shimadzu GC-14A gas chromatograph; GC-MS analyses employed a Hewlett Packard Model 5988A GC-MS instrument. Melting points were determined on a Mel-Temp capillary melting point apparatus and are uncorrected. UV-visible spectroscopic data were collected on a Cary (Varian) 50 Bio UV-visible spectrometer. Fluorescence spectra were recorded on a Cary (Varian) Eclipse fluorescence spectrometer. Quartz cuvettes were used for optical spectra data collection. SEM images were acquired on a JEOL JSM-6320F instrument. Elemental analysis determinations were performed by Atlantic Microlabs, Inc., Norcross, GA.

X-ray determination of compounds. Crystals with appropriate dimensions were mounted on a glass capillary in a random orientation. Preliminary examination and data collection were performed using a Bruker Kappa Apex II charge coupled device (CCD) detector system single-crystal X-ray diffractometer using an Oxford Cryostream LT device; data were collected at 100 K unless otherwise stated, using graphite-monochromated Mo $K\alpha$ radiation ($\lambda = 0.71073 \text{ \AA}$) from a fine focus sealed X-ray tube source. Preliminary unit cell constants were determined using a set of 36 narrow frame scans. Data sets consist of combinations of φ scan frames with a typical scan width of 0.5° and an exposure time of 5-15 s/frame at a crystal to detector distance of 4.0 cm. The collected frames were integrated using an orientation matrix determined from the narrow frame scans. Apex II and SAINT software packages were used for data collection and

integration. Systematic errors in the data were corrected using the SADABS, based on the Laue symmetry using equivalent reflections.

Structure solutions were typically carried out using SHELXS⁹ or the solution software provided in OLEX2,¹⁰ and refinement was performed against the reduced data using SHELXL,⁹ using the OLEX2 graphical interface software.¹⁰ The structures were refined with full matrix least-squares refinement by minimizing $\sum w(F_o^2 - F_c^2)^2$. All non-hydrogen atoms were refined to convergence. Detailed crystallographic data and structural refinement details for individual structures are provided in Chapter 5, Section 5.3, Table A-1 and Table A-2.

4.1. Synthesis and reactivity of several 1,1-disubstituted germoles.

Preparation of 1,1-dichloro-2,3,4,5-tetraphenylgermole, G1. The title compound was prepared according to a modified literature procedure.³ To desiccate diphenylacetylene (7.0 g, 39 mmol) in dry diethyl ether (16 mL) was added lithium wire (0.27 g, 6.0 cm, 39 mmol) under a steady flow of argon gas. Within thirty minutes, the reaction mixture changed from yellow to reddish brown to a dark brown color. Aliquots of the reaction mixture were quenched into vials containing water and hexanes at every hour, with the organic layer isolated and filtered for GC monitoring of the conversion to 1,4-dilithio-1,2,3,4-tetraphenylbuta-1,3-diene. The reaction was stirred for a total of 6.5 h, at which time the reaction contained a dark brown solution with a yellow precipitate. This suspension was cannulated into a solution of germanium(IV) chloride (4.2 g, 19.5 mmol) in dry diethyl ether (167 mL), and the solution immediately turned bright yellow, with mild refluxing. This solution was allowed to stir overnight. The diethyl ether was removed by vacuum, and the contents were redissolved in dichloromethane (100 mL).

The suspension was filtered to remove lithium salts, and the filtrate was concentrated to half the original volume using rotary evaporation. On cooling at -20 °C overnight, large yellow crystals of the title compound precipitated. The solid was filtered, washed with cold diethyl ether, and air dried. Subsequent crystallizations of the filtrate yielded several crops of **G1** (7.4 g, 15 mmol, 75%). Mp: 198–201 °C (lit.³ 197–199 °C). The reaction was repeated up to scales of 20 g theoretical yield, with yields ranging from 50–75%. ¹H NMR (500 MHz): δ 7.23–7.09 (m, 16H), 6.90–6.88 (m, 4H). ¹³C{¹H} NMR (126 MHz): δ 150.1, 136.7, 134.8, 132.9, 129.7, 129.6, 128.5, 128.2, 127.8, 127.6. ¹H (Figure A-1) and ¹³C{¹H} (Figure A-2) spectra are included in the appendix (Chapter 5).

Preparation of 1,1-bis(3-pyridinylethynyl)-2,3,4,5-tetraphenylgermole, G2.¹¹ To a flame dried Schlenk flask containing 3-ethynylpyridine (0.20 g, 1.9 mmol) in dry THF (6 mL) was added *n*-butyllithium (0.73 mL, 1.8 mmol, 2.5 M) dropwise at -78 °C, and the solution was stirred for 15 min to generate the lithiated alkyne. This suspension was syringed into a solution of **G1** (0.48 g, 0.96 mmol) in dry THF (9 mL) at once with quick stirring. The solution darkened very slightly, and a salt was formed almost immediately. The solution was stirred overnight.

The solvents were removed by rotary evaporation, and the resulting mixture was purified on a silica gel column (2:1 diethyl ether/hexanes, followed by dichloromethane rinse). Initial fractions contained mostly 3-ethynylpyridine and **G1**. After the dichloromethane rinse, the fractions were mainly the target product. In these fractions, solvents were removed by rotary evaporation, and the material was isolated as the target compound after being crystallized by a slow diffusion of hexane into dichloromethane solution to give large yellow crystals of **G2** (0.36 g, 0.57 mmol, 59%). The reaction was

repeated several times on a similar scale, and yields typically were around 60%. Mp: 220–221.5 °C. ^1H NMR (300 MHz): δ 8.76 (dd, $J = 2, 0.7$ Hz, 2H), 8.56 (dd, $J = 5, 1.7$ Hz, 2H), 7.81 (dt, $J = 8, 1.9$ Hz, 2H), 7.29–7.03 (m, 16H), 6.91–6.86 (m, 4H). $^{13}\text{C}\{^1\text{H}\}$ NMR (125 MHz): δ 153.5, 153.1, 149.5, 139.3, 138.5, 137.7, 135.5, 129.9, 129.8, 128.3, 128.0, 127.0, 126.9, 123.1, 119.7, 104.0, 89.7. Anal. Calcd for $\text{C}_{42}\text{H}_{28}\text{GeN}_2$: C, 79.65; H, 4.46. Found: C, 79.18; H, 4.36. ^1H (Figure A-3) and $^{13}\text{C}\{^1\text{H}\}$ (Figure A-4) spectra are included in the appendix (Chapter 5).

Preparation of 1,1-bis(2-pyridinylethynyl)-2,3,4,5-tetraphenylgermole, G3.¹¹ To a 25 mL Schlenk flask was added 2-ethynylpyridine (0.22 g, 2.1 mmol) in dry THF (2 mL). To this solution was added *n*-butyllithium (0.85 mL, 2.1 mmol, 2.5 M) dropwise at -78 °C, and the solution was stirred for 15 min to generate the lithiated alkyne. This suspension was syringed into a solution of **G1** (0.50 g, 1.0 mmol) in dry THF (6 mL) at once with quick stirring. The solution darkened very slightly, and after 30 minutes became light, opaque, and yellow. The lithium chloride precipitate was filtered off, and the solution was concentrated giving a yellow solid. The solid was purified on a silica gel column (methanol), and the solvents were removed to yield a crystalline yellow solid of **G3** (0.45 g, 0.71 mmol, 66 %). X-ray quality crystals were grown from a slow diffusion of hexanes into a dichloromethane solution of **G3**. Mp: 260 °C (dec). ^1H NMR (300 MHz): δ 8.59 (ddd, $J = 4.9, 1.7, 0.9$ Hz, 2H), 7.66 (td, $J = 7.7, 1.8$ Hz, 2H), 7.54 (dt, $J = 7.8, 1.1$ Hz, 2H), 7.29–7.19 (m, 6H), 7.15–7.02 (m, 10H), 6.90–6.84 (m, 4H). $^{13}\text{C}\{^1\text{H}\}$ NMR (75 MHz): δ 153.8, 150.4, 142.9, 138.9, 137.9, 136.6, 135.7, 130.2, 130.2, 128.5, 128.4, 128.2, 127.1, 127.0, 124.0, 105.9, 86.6. Anal. Calcd for $\text{C}_{42}\text{H}_{28}\text{GeN}_2$: C,

79.65; H, 4.46. Found: C, 79.39; H, 4.91. ^1H (Figure A-5) and $^{13}\text{C}\{^1\text{H}\}$ (Figure A-6) spectra are included in the appendix (Chapter 5).

Preparation of 1,1-bis((diphenylphosphino)ethynyl)-2,3,4,5-tetraphenylgermole, G4.¹¹ A solution of ethynyldiphenylphosphine (0.51 g, 2.4 mmol) in THF (5 mL) was cooled to 0 °C. To this solution was added *n*-butyllithium (3 mL, 7.50 mmol, 2.5 M) dropwise. The solution turned deep brown and was allowed to stir for 30 min at 0 °C. A solution of **G1** (604 mg, 1.21 mmol) in dry THF (10 mL) was added to the first solution dropwise at 0 °C, and was allowed to come to room temperature. The solvents were removed by rotary evaporation, and the viscous residue was subjected to silica column chromatography (2:1 hexanes/toluene). After removal of solvents, the yellow viscous residue solidified on standing to give the title compound (0.45 g, 0.53 mmol, 44%) as a yellow solid. X-ray quality crystals were grown by slow evaporation of a diethyl ether solution. Mp: 154.5–156 °C. ^1H NMR (500 MHz): δ 7.58–7.53 (m, 8H), 7.34–7.24 (m, 14H), 7.23–7.19 (m, 4H), 7.16–7.13 (m, 6H), 7.10–7.05 (m, 6H), 6.89 (dd, $J = 8, 1.7$ Hz, 4H). $^{13}\text{C}\{^1\text{H}\}$ NMR (125 MHz): δ 153.4, 138.5, 137.6, 135.7, 135.5 (d, $J_{\text{PC}} = 6$ Hz), 132.7 (d, $J_{\text{PC}} = 21$ Hz), 130.0, 129.9, 129.2, 128.8 (d, $J_{\text{PC}} = 8$ Hz), 128.2, 127.9, 126.9, 126.8, 107.2 (d, $J_{\text{PC}} = 18$ Hz), 106.5 (d, $J_{\text{PC}} = 3$ Hz). $^{31}\text{P}\{^1\text{H}\}$ NMR (202 MHz): δ -32.2. Anal. Calcd for $\text{C}_{56}\text{H}_{40}\text{GeP}_2$: C, 79.36; H, 4.76. Found: C, 79.69; H, 5.06. ^1H (Figure A-7), $^{13}\text{C}\{^1\text{H}\}$ (Figure A-8), and $^{31}\text{P}\{^1\text{H}\}$ (Figure A-9) NMR spectra are included in the appendix (Chapter 5).

Preparation of 1,1-bis(ethynyl)-2,3,4,5-tetraphenylgermole, G5.¹² A solution of ethynylmagnesium bromide (5.8 mL, 2.7 mmol, 0.47 M) was added to a solution of **G1** (0.68 g, 1.4 mmol) in dry THF (20 mL). The solution was allowed to stir for 2 hours,

before being checked by TLC. The solution was quenched by adding 2 drops of water, and the solvent was evaporated. The residue was subjected to silica column chromatography (toluene/hexanes), the product was isolated as 1,1-diethynyl-2,3,4,5-tetraphenylgermole (0.45 g, 0.95 mmol, 70% yield). ^1H NMR (300 MHz): δ 7.23–7.03 (m, 16H), 6.90–6.84 (m, 4H), 2.63 (s, 2H). $^{13}\text{C}\{^1\text{H}\}$ NMR (126 MHz): δ 153.6, 138.4, 137.4, 134.9, 129.8, 129.7, 128.2, 127.9, 127.0, 126.9, 95.9, 81.4. ^1H (Figure A-10) and $^{13}\text{C}\{^1\text{H}\}$ (Figure A-11) spectra are included in the appendix (Chapter 5).

Reaction of G4 with (1,5-cyclooctadienyl)PtCl₂. The compound G4 (59 mg, 0.070 mmol) was dissolved in dichloromethane (5 mL), and sparged for 5 minutes with argon. To this stirring solution was added (1,5-cyclooctadienyl)platinum(II) chloride (26 mg, 0.070 mmol) in dichloromethane (5 mL). The solution was stirred for 17 h under argon. The solvents were evaporated, yielding a pale yellow solid that was poorly soluble in chloroform, diethyl ether, and THF. ^1H NMR (500 MHz): δ 7.48–7.43 (m, 6H), 7.24–7.17 (m, 6H), 7.09–6.92 (m, 26H), 6.78–6.73 (m, 4H). $^{31}\text{P}\{^1\text{H}\}$ NMR (202 MHz): δ –9.2 (s, with satellites, $^1J_{\text{PtP}} = 3673$ Hz). The NMR data is indicative of a *cis*-P-Pt-P species. The $^{31}\text{P}\{^1\text{H}\}$ (Figure A-12) NMR spectrum is included in the appendix (Chapter 5).

4.2. Synthesis of symmetrical 2,5 substituted siloles.

4.2.1. Synthesis of precursors and starting materials to symmetrical 2,5 substituted siloles.

Synthesis of [1,1'-bis(diphenylphosphino)ferrocene]palladium(II) chloride, CH₂Cl₂ adduct, SP1.¹³ To a solution of (COD)PdCl₂ (3.1 g, 5.6 mmol) in CH₂Cl₂ (150 mL) was added a solution of 1,1'-bis(diphenylphosphino)ferrocene (1.6 g, 5.6 mmol) in CH₂Cl₂ (50 mL) dropwise over the course of 10 min, under air. The solvents were

evaporated, and the solid was triturated with diethyl ether to yield a red micro-crystalline solid of the title compound (4.2 g, 5.1 mmol, 91% assuming a 1:1 CH₂Cl₂ adduct). ¹H NMR (300 MHz): δ 7.96–7.84 (m, 8H), 7.53–7.35 (m, 12H), 5.30 (s, CH₂Cl₂), 4.39 (s, 4H), 4.19 (s, 4H). ³¹P{¹H} NMR (121 MHz): δ 34.0 (lit. 34.5^{13b}). ¹H (Figure A-13) and ³¹P{¹H} (Figure A-14) NMR spectra are included in the appendix (Chapter 5).

Synthesis of 8-((4-bromobenzyl)oxy)quinoline, SP2. Potassium carbonate (1.5 g, 11 mmol) and 8-hydroxyquinoline (1.5 g, 10 mmol) were combined in methanol (75 mL) and sonicated (in an ultrasonic bath) and heated several times to ensure full dissolution of the solids, yielding a yellow solution. To this stirring solution was added 4-bromobenzyl bromide (2.7 g, 11 mmol) in CH₂Cl₂ (20 mL) at once. The solution darkened to red over a period of 30 min. After stirring overnight, the solvents were evaporated, and the residue was redissolved in ethyl acetate, filtered to remove potassium bromide salts, and the solvents were evaporated yielding a purple residue. This residue was recrystallized from hot methanol (70 mL), and filtered to yield purple/white crystals of the target compound (1.9 g, 6.1 mmol, 59%). Mp. 124–126 °C. ¹H NMR (300 MHz): δ 8.88 (dd, *J* = 4.2, 1.8 Hz, 1H), 8.05 (dd, *J* = 8.3, 1.8 Hz, 1H), 7.42–7.25 (m, 7H), 6.89 (dd, *J* = 6.5, 2.4 Hz, 1H), 5.30 (s, 2H). ¹³C{¹H} NMR (75 MHz) δ 154.1, 149.6, 140.5, 136.1, 131.9, 129.6, 128.9, 126.6, 121.8, 120.3, 109.9, 70.1. ¹H (Figure A-15) and ¹³C{¹H} (Figure A-16) NMR spectra are included in the appendix (Chapter 5).

4.2.2. Synthesis of some symmetric siloles.

Preparation of 2,5-bis(*p*-cyanophenyl)-1,1-dimethyl-3,4-diphenylphenylsilole, S1.¹⁴ Lithium pellets (55 mg, 7.9 mmol), naphthalene (1.1 g, 8.6 mmol) and dry THF (12 mL) were combined and sonicated⁴ for 2 h to form a deep-green solution of lithium

naphthalenide. A solution of bis(phenylethynyl)dimethylsilane (0.50 g, 1.9 mmol) in dry THF (8 mL) was added dropwise to the solution over 15 min by an addition funnel. This mixture was stirred for 20 min and cooled to 0 °C. Then, ZnCl₂(TMEDA) (2.1 g, 8.3 mmol) was added as a solid at once, followed by additional dry THF (15 mL). If gelation occurred (*vide supra*), the contents were sonicated for several seconds in a sonicating bath. After stirring for 1.5 h, 4-bromobenzonitrile (0.73 g, 4.0 mmol) and Pd(PPh₃)₂Cl₂ (60 mg, 0.085 mmol) were successively added, and the mixture was refluxed overnight. The solution was quenched with 1 M HCl. The aqueous layers were combined, extracted with Et₂O (2 x 20 mL), and the organics were combined, washed with water, sodium bicarbonate solution, brine, and dried with MgSO₄. The solution was filtered, the solvents were removed by rotary evaporation, and the crude mixture was subjected to silica gel column chromatography (hexanes then hexanes/Et₂O, 10:1) to obtain compound **1** as yellow powder (0.35 g, 40% yield). Mp: 229–230 °C. X-ray quality crystals were obtained by slow evaporation of an Et₂O solution of **1** at room temperature. ¹H NMR (500 MHz): δ 7.43–7.39 (m, 4H, ArH), 7.09–6.98 (m, 10H, ArH), 6.75–6.73 (m, 4H, ArH), 0.48 (s, 6H, SiMe). ¹³C{¹H} NMR (125 MHz): δ 156.2, 144.9, 141.7, 137.4, 132.1, 129.8, 129.3, 127.9, 127.2, 119.3, 109.3, –4.0. ²⁹Si{¹H} NMR (99 MHz): δ 9.3. Anal. Calcd for C₃₂H₂₄N₂Si: C, 82.72; H, 5.21. Found: C, 82.51; H, 5.14. ¹H (Figure A-17), ¹³C{¹H} (Figure A-18), and ²⁹Si{¹H} (Figure A-19) NMR spectra are included in the appendix (Chapter 5).

Preparation of 2,5-bis(3,4-di(methylthio)phenyl)-1,1-dimethyl-3,4-diphenylsilole, S2.¹⁴ Lithium pellets (55 mg, 7.9 mmol), naphthalene (1.1 g, 8.6 mmol) and dry THF (8 mL) were combined and sonicated⁴ for 1 h, then stirred overnight, to

form a deep-green solution of lithium naphthalenide. A solution of bis(phenylethynyl)dimethylsilane (0.51 g, 1.9 mmol) in dry THF (12 mL) was added dropwise to the solution over 15 min by an addition funnel. This mixture was stirred for 10 min and cooled to 0 °C. Then, ZnCl₂(TMEDA) (2.1 g, 8.3 mmol) was added as a solid at once, followed by additional dry THF (15 mL). After stirring for 1.5 h, Pd(PPh₃)₂Cl₂ (77 mg, 0.11 mmol) was added as a solid, followed by 4-bromo-1,2-bis(methylthio)benzene (0.99 g, 4.0 mmol) as a neat liquid, under an argon flow. The mixture was refluxed overnight, and then quenched with degassed 1 M HCl solution. The phases were separated, and the aqueous layer was extracted with ethyl acetate (2 x 30 mL). The organic solutions were combined, washed with brine, dried with MgSO₄, filtered, and the solvents were evaporated.

The material was dry-loaded onto a silica gel column (hexane/ethyl acetate 3:1). The target compound solidified on the column; after removing other byproducts, ethyl acetate was run on the column to remove the target compound, which was isolated as a yellow powder. Slow diffusion of methanol into a CH₂Cl₂ solution yielded X-ray quality needles of the target compound (0.58 g, 51% yield). Mp: 187–189 °C. ¹H NMR (500 MHz): δ 7.05–7.03 (m, 8H), 6.86 (dd, *J* = 6.86, 1.85 Hz, 2H), 6.84–6.81 (m, 4H), 6.64 (d, *J* = 1.85 Hz, 2H), 2.44 (s, 6H), 1.97 (s, 6H), 0.51 (s, 6H). ¹³C{¹H} NMR (125 MHz): δ 154.4, 140.6, 139.2, 137.4, 137.2, 134.0, 130.1, 128.1, 126.67, 126.64, 126.60, 126.58, 16.5, 15.7, –3.1. ²⁹Si{¹H} NMR (99 MHz): δ 7.9. Anal. Calcd for C₃₄H₃₄S₄Si: C, 68.18; H, 5.72. Found: C, 68.10; H, 5.67. ¹H (Figure A-20), ¹³C{¹H} (Figure A-21), and ²⁹Si{¹H} (Figure A-22) NMR spectra are included in the appendix (Chapter 5).

Preparation of 1,1-dimethyl-2,5-bis[*p*-(*N,N*-dimethylamino)phenyl]-3,4-diphenylphenylsilole, S3.¹⁵ Lithium pellets (53 mg, 7.6 mmol), naphthalene (1.2 g, 9.2 mmol) and dry THF (9 mL) were combined and sonicated⁴ for 2 h to form a deep-green solution of lithium naphthalenide. A solution of bis(phenylethynyl)dimethylsilane (0.49 g, 1.9 mmol) in dry THF (8 mL) was added dropwise to the solution over 30 min by an addition funnel. This mixture was stirred for 20 min and cooled to 0 °C. Then, ZnCl₂(TMEDA) (2.2 g, 8.5 mmol) was added as a solid at once, followed by additional dry THF (15 mL). After stirring for 1.5 h, 4-bromo-*N,N*-dimethylaniline (0.80 g, 4.0 mmol) and Pd(PPh₃)₂Cl₂ (83 mg, 0.12 mmol) were successively added under a flow of argon, and the mixture was refluxed overnight.

The reaction was quenched with 1 M HCl solution. The products were first extracted with ethyl acetate (2 x 20 mL). Plate-like crystals began to precipitate from the aqueous layer; to test for possible product protonation, 2 M NaOH was added. A yellow solid precipitated, which was extracted with dichloromethane (3 x 30 mL), and the organics were combined. The solvents were evaporated, and the residue was dry-loaded onto a silica gel column (hexanes then hexanes/ethyl acetate 1:1). The solvents were evaporated, and the residue was triturated with diethyl ether in small batches, and centrifuged to compact the yellow powder, which was separated from the brown-red supernate. This yellow powder was identified by NMR to be the target compound (0.50 g, 1.0 mmol, 51%). ¹H NMR (500 MHz): δ 7.06–7.01 (m, 6H), 6.89–6.81 (m, 8H), 6.52–6.48 (m, 4H), 2.89 (s, 12 H), 0.51 (s, 6H). ¹³C{¹H} NMR (125 MHz): δ 151.8, 148.4, 140.5, 139.2, 130.3, 130.2, 128.0, 127.7, 125.9, 112.1, 40.5, –2.6. ¹H (Figure A-23) and ¹³C{¹H} (Figure A-24) NMR spectra are included in the appendix (Chapter 5).

Alternative preparation of S3. Lithium (55 mg, 7.9 mmol), naphthalene (1.1 g, 8.9 mmol) and dry THF (9 mL) were combined and sonicated⁴ for 3 h, and stirred overnight, to form a deep-green solution of lithium naphthalenide. A solution of bis(phenylethynyl)dimethylsilane (0.50 g, 1.9 mmol) in dry THF (6 mL) was added dropwise to the solution over 30 min by an addition funnel. This mixture was stirred for 20 min and cooled to 0 °C. Then, ZnCl₂(TMEDA) (2.1 g, 8.2 mmol) was added as a solid at once, followed by additional dry THF (15 mL). After stirring for 1.5 h at rt, degassed 2-iodopropane¹⁶ (0.4 mL, 4.0 mmol) was added, and the solution changed from black to deep red. The vessel was wrapped in foil, and 4-bromo-*N,N*-dimethylaniline (0.81 g, 4.0 mmol) and Pd(PPh₃)₂Cl₂ (67 mg, 0.10 mmol) were successively added under a flow of argon. Upon addition of the catalyst, the solution changed from deep red to dark brown/black over the course of 5 minutes. The solution was then refluxed overnight.

The black (with deep yellow overtones) mixture was quenched with 50 mL of 1 M HCl, extracted with ethyl acetate (2 x 20 mL). The aqueous layer was basified as above for **S3**, extracted with additional ethyl acetate (2 x 20 mL), and the organics were combined, washed with brine, and then dried over MgSO₄, filtered, and the solvents were evaporated. The residue was subjected to silica gel chromatography (hexanes then hexanes/ethyl acetate 1:1). The solvents were evaporated, and the residue was triturated with diethyl ether in small batches, and centrifuged to compact the yellow powder, which was separated from the brown-red supernate. NMR analysis indicated synthesis of the target compound (0.52 g, 1.0 mmol, 54%).

Preparation of 1,1-dimethyl-2,5-bis[2,2'-bipyridin-6-yl]-3,4-diphenylphenylsilole, S4.¹⁷ Lithium wire (28 mg, 7.9 mmol), naphthalene (0.68 g, 5.3 mmol) and dry THF (5 mL) were combined and sonicated⁴ for overnight, and stirred for 30 minutes, to form a deep-green solution of lithium naphthalenide. A solution of bis(phenylethynyl)dimethylsilane (0.25 g, 0.97 mmol) in dry THF (6 mL) was added dropwise to the solution over 30 min by an addition funnel. This mixture was stirred for 30 min and cooled to 0 °C. Then, ZnCl₂(TMEDA) (1.2 g, 4.6 mmol) was added as a solid at once, followed by additional dry THF (7 mL). After stirring for 1.5 h at rt, 6-bromo-2,2'-bipyridine (0.46 g, 0.039 mmol) and Pd(PPh₃)₂Cl₂ (27 mg, 0.039 mmol) were successively added under a flow of argon. The mixture was refluxed overnight. The solvents were then evaporated, and the residue was dry-loaded onto a column (hexanes/ethyl acetate 9:1). The fractions containing the target were combined, and the silole was crystallized from the eluent by slow-evaporation yielding the title compound (0.22 g, 39%). ¹H NMR (500 MHz): δ 8.67 (ddd, *J* = 4.65, 1.83, 0.91 Hz, 2H), 8.42 (dt, *J* = 7.85, 1.36 Hz, 2H), 8.10 (dd, *J* = 7.85, 0.91 Hz, 2H), 7.85 (td, *J* = 7.85, 1.83 Hz, 2H), 7.39 (t, *J* = 7.85 Hz, 2H), 7.30 (ddd, *J* = 7.45, 4.67, 0.91 Hz, 2H), 7.17–7.14 (m, 6H), 7.00–6.97 (m, 4H), 6.58 (dd, *J* = 8.11, 0.86, 2H), 0.80 (s, 6H). ¹³C{¹H} NMR (125 MHz): δ 157.7, 156.9, 156.1, 155.4, 149.2, 144.3, 139.8, 137.0, 136.5, 129.4, 128.4, 126.9, 123.6, 123.2, 121.2, 118.1, -2.2. ¹H (Figure A-25) and ¹³C{¹H} (Figure A-26) NMR spectra are included in the appendix (Chapter 5).

Preparation of 1,1-dimethyl-3,4-diphenyl-2,5-bis[*p*-(methoxymethyl)phenyl]silole, S5. Lithium pellets (53 mg, 7.6 mmol), naphthalene (1.2 g, 9.0 mmol) and dry THF (9 mL) were combined and sonicated⁴ for 2 h to form a deep-

green solution of lithium naphthalenide. A solution of bis(phenylethynyl)dimethylsilane (0.50 g, 1.9 mmol) in dry THF (10 mL) was added dropwise to the solution over 30 min by an addition funnel. This mixture was stirred for 20 min and cooled to 0 °C. Then, ZnCl₂(TMEDA) (2.2 g, 8.5 mmol) was added as a solid at once, followed by additional dry THF (15 mL). After stirring for 1.5 h, 1-bromo-4-(methoxymethyl)benzene (0.82 g, 4.1 mmol) and Pd(PPh₃)₂Cl₂ (81 mg, 0.12 mmol) were successively added under a flow of argon. The mixture was refluxed overnight. The solvents were removed and the material was dry-loaded onto a silica gel column (hexanes/ether 10:1 to 1:1) to isolate the target compound (0.48 g, 0.96 mmol, 50%) as a crystalline solid. X-ray quality crystals were grown from slow evaporation of a diethyl ether solution of **S5**. Mp: 134–135 °C. ¹H NMR (500 MHz): δ 7.11–7.08 (m, 4H), 7.02–6.97 (m, 6H), 6.92–6.89 (m, 4H), 6.82–6.78 (m, 4H), 4.35 (s, 4H), 3.37 (s, 6H), 0.46 (s, 6H). ¹³C{¹H} NMR (125 MHz): δ 154.1, 141.6, 138.9, 135.4, 130.1, 130.0, 127.7, 127.6, 126.3, 74.8, 58.4, –3.7. ²⁹Si{¹H} NMR (99 MHz): δ 5.4. ¹H (Figure A-27), ¹³C{¹H} (Figure A-28), and ²⁹Si{¹H} (Figure A-29) NMR spectra are included in the appendix (Chapter 5).

Preparation of 1,1-dimethyl-3,4-diphenyl-2,5-(*p*-tolyl)silole, **S6.**¹⁵ Lithium pellets (55 mg, 7.9 mmol), naphthalene (1.2 g, 9.3 mmol) and dry THF (10 mL) were combined and sonicated⁴ for 2 h to form a deep-green solution of lithium naphthalenide. A solution of bis(phenylethynyl)dimethylsilane (0.50 g, 1.9 mmol) in dry THF (7 mL) was added dropwise to the solution over 30 min by an addition funnel. This mixture was stirred for 40 min and cooled to 0 °C. Then, ZnCl₂(TMEDA) (2.1 g, 8.3 mmol) was added as a solid at once, followed by additional dry THF (15 mL). After stirring for 1.5 h, 4-iodotoluene (0.86 g, 4.0 mmol) and Pd(PPh₃)₂Cl₂ (70 mg, 0.10 mmol) were successively

added under a flow of argon. The mixture was refluxed overnight. The reaction was quenched with 1 M HCl, and the aqueous layer was separated and washed with diethyl ether (2 x 20 mL). The organic layers were combined and washed with water, sodium bicarbonate solution, brine, and dried with MgSO₄. After filtration, the solvents were evaporated and the residue was subjected to silica gel column chromatography (hexanes, then hexanes/ether 10:1) to isolate the target compound as a yellow solid. The solid was further purified by recrystallization by a slow evaporation of a diethyl ether solution of **S6**. ¹H NMR (300 MHz): δ 7.04–6.98 (m, 6H), 6.95–6.90 (m, 4H) 6.84–6.78 (m, 8H), 2.25 (s, 6H), 0.47 (s, 6H). GC–MS m/z (% relative intensity, ion): 442 (100, M⁺), 443 (39, M+1). The ¹H (Figure A-30) NMR spectrum and the MS chromatogram (Figure A-39) are included in the appendix (Chapter 5).

4.3. Synthesis of unsymmetrical silole precursors.

Formation of 2-chloro-5-iodo-1,1-dimethyl-3,4-diphenylsilole, AP1. The compound was synthesized according to a modified literature procedure.¹⁸ Lithium pellets (34 mg, 4.9 mmol), naphthalene (0.62 g, 4.8 mmol) and dry THF (7 mL) were combined and sonicated⁴ for 2 h, and stirred for 20 min, to form a deep-green solution of lithium naphthalenide. A solution of bis(phenylethynyl)dimethylsilane (0.25 g, 0.97 mmol) in dry THF (10 mL) was added dropwise to the solution over 30 min by an addition funnel. This mixture was stirred for 30 min. At this point, the flask was wrapped in foil, and the room lights were switched off for the remainder of the reaction and workup. The vessel was brought to –78 °C using a dry ice/acetone bath, and *N*-chlorophthalimide (0.20 g, 1.1 mmol) in dry THF (25 mL) was added slowly dropwise over the course of 45 min by an addition funnel. Stirring was continued for an additional

30 min, and then iodine (0.46 g, 1.8 mmol) was added as a solid to the solution at $-78\text{ }^{\circ}\text{C}$ under an argon flow. The solution was stirred for 1 h at $-78\text{ }^{\circ}\text{C}$, and then poured cold into a rapidly stirring half-saturated NH_4Cl solution (25 mL). The aqueous layer was separated, extracted with diethyl ether (2 x 30 mL), and the organics were washed in half-saturated sodium thiosulfate solution (25 mL), brine (2 x 25 mL), and dried with MgSO_4 (the flask was wrapped in foil during drying). The pale yellow solution was filtered through a silica plug (ethyl acetate), and the solvents were removed by rotary evaporation with the flask covered in foil (using a tepid water bath).

The yellow-orange solid was redissolved in 20% CH_2Cl_2 /hexanes, and the off-white suspension of phthalimide was filtered off using a silica plug. Additional 20% CH_2Cl_2 /hexanes (50 mL) was run on the plug to ensure removal of the product. The solvents were removed by rotary evaporation with the flask covered in foil, and the pale yellow solids were analyzed by NMR for conversion, with yields of the target compound ranging from 40–75% based on the naphthalene integration. The NMR spectra reported below are for the mixture, as the compound's general light sensitivity precludes its further isolation, and the main byproduct (naphthalene) is innocuous in further reactions. ^1H NMR (300 MHz): δ 7.90–7.82 (m, naphthalene), 7.53–7.46 (m, naphthalene), 7.20–7.13 (m, 6H), 6.99–6.93 (m, 4H), 0.45 (s, 6H). $^{13}\text{C}\{^1\text{H}\}$ NMR (75 MHz): δ 161.0, 153.8, 140.0, 136.0, 135.6, 134.1, 133.5 (naphthalene), 129.3, 128.8, 128.0 (naphthalene), 127.7, 127.6, 125.9 (naphthalene), 123.4, 95.2, -6.15 . GC–MS m/z (% relative intensity, ion): 424 (8, $M + 2$), 422 (21, M^+), 93 (100, SiClMe_2^+ , decomp). ^1H (Figure A-31) and $^{13}\text{C}\{^1\text{H}\}$ (Figure A-32) NMR spectra, and the MS chromatogram (Figure A-46) are included in the appendix (Chapter 5).

Preparation of 4-ethynyl-*N,N*-dimethylaniline, AP2.¹⁹ In a Schlenk flask were combined 4-iodo-*N,N*-dimethylaniline (2.0 g, 8.1 mmol), (dppf)PdCl₂•CH₂Cl₂ (0.26 g, 0.32 mmol), copper iodide (0.12 g, 0.65 mmol), and the flask was purged with a positive flow of argon for 20 min. Degassed diisopropylamine (16 mL) was added, and the solution turned yellow. Degassed trimethylsilylacetylene (1.6 g, 16 mmol) was added by syringe at once. The solution turned blue, and then brown; a precipitate formed within 10 minutes at rt. Dry THF (8 mL) was added, and the solution was stirred at rt for 2 hours prior to being refluxed overnight. Hexanes (20 mL) were added to the mixture at rt, then the contents were filtered through a short silica gel plug, and rinsed through with ethyl acetate (30 mL). The solvents were evaporated to yield a dark brown crystalline solid that was confirmed by NMR to be the TMS-protected precursor of **AP2** (1.6 g, 7.4 mmol, 91%). ¹H NMR (300 MHz): δ 7.39–7.30 (m, 2H), 6.63–6.52 (m, 2H), 2.96 (s, 6H), 0.23 (s, 9H). ¹³C{¹H} NMR (75 MHz): δ 150.3, 133.3, 111.7, 110.0, 106.7, 91.3, 40.3, 0.4. GC–MS m/z (% relative intensity, ion): 217 (56, M⁺), 202 (100, M – CH₃), 101 (35, M – N(CH₃)₂ – TMS). ¹H (Figure A-33) and ¹³C{¹H} (Figure A-34) NMR spectra, and the MS chromatogram (Figure A-47) are included in the appendix (Chapter 5).

The product containing mostly the protected target was dissolved in THF (30 mL) and MeOH (30 mL), and KF (3.0 g, 51.6 mmol) was added under air. The solution was stirred for 2 d at rt, and the solvents were evaporated, and the mixture was redissolved in ethyl acetate (100 mL) and filtered through a silica plug. The solvents were evaporated to yield a dark brown crystalline solid that was confirmed by GC-MS to be the target compound **AP2**. GC–MS m/z (% relative intensity, ion): 145 (94, M⁺), 144 (100, M – H),

129 (25, M – H – CH₃), 101 (35, M – N(CH₃)₂). The MS chromatogram (Figure A-48) is included in the appendix (Chapter 5).

Preparation of 6-ethynyl-2,2'-bipyridine, AP3.²⁰ In a Schlenk flask were combined 6-bromo-2,2'-bipyridine (1.0 g, 4.3 mmol), (dppf)PdCl₂•CH₂Cl₂ (0.14 g, 0.17 mmol), copper iodide (0.049 g, 0.26 mmol), and the flask was purged with a positive flow of argon for 20 min. Degassed diisopropylamine (18 mL) was added, followed by degassed trimethylsilylacetylene (0.84 g, 8.5 mmol), and the solution changed from orange-yellow to dark brown. On heating to *ca.* 60 °C, a precipitate began to form, and the reaction was stirred for 2 d. The solvents were afterwards evaporated, and redissolved in hexanes/diethyl ether 1:1, and filtered on a silica plug. The solvents were again evaporated to yield a crystalline material, confirmed by NMR to be the TMS-protected precursor of **AP3** (0.75 g, 3.0 mmol, 70%). ¹H NMR (300 MHz): δ 8.67 (d, *J* = 4.1 Hz, 1H), 8.48 (d, *J* = 8.0 Hz, 1H), 8.37 (d, *J* = 8.0 Hz, 1H), 7.82 (td, *J* = 8.0, 1.7 Hz, 1H), 7.79 (t, *J* = 8.0 Hz, 1H), 7.50 (d, *J* = 8.0 Hz, 1H), 7.33 (dd, *J* = 6.6, 5.0 Hz, 1H), 0.29 (s, 9H). ¹³C{¹H} NMR (75 MHz): δ 156.5, 155.4, 149.2, 142.6, 137.1, 137.1, 127.8, 124.2, 121.8, 120.7, 111.4, 104.1, 94.8, –0.1. ¹H (Figure A-35) and ¹³C{¹H} (Figure A-36) NMR spectra are included in the appendix (Chapter 5).

The product containing the protected target was dissolved in THF (38 mL) and MeOH (38 mL), and KF (0.26 g, 4.5 mmol) was added under air. The solution was stirred for 2 d at rt, and the solvents were evaporated, and the mixture was redissolved in ethyl acetate (120 mL) and filtered through a silica plug. Evaporation of the solvents yielded light-brown crystalline material that was confirmed by NMR to be the target product **AP3**. ¹H NMR (300 MHz): δ 8.67 (d, *J* = 4.7 Hz, 1H), 8.48 (d, *J* = 8.0 Hz, 1H), 8.41 (d, *J*

= 8.0 Hz, 1H), 7.82 (td, $J = 8.0, 1.6$ Hz, 1H), 7.80 (t, $J = 7.6$ Hz, 1H), 7.51 (d, $J = 7.6$ Hz, 1H), 7.32 (dd, $J = 6.8, 4.9$ Hz, 1H), 3.19 (s, 1H). ^1H (Figure A-35) and $^{13}\text{C}\{^1\text{H}\}$ (Figure A-36) NMR spectra are included in the appendix (Chapter 5).

Preparation of 1-ethynyl-4-nitrobenzene, AP4.²¹ In a Schlenk flask were combined 1-iodo-4-nitrobenzene (2.0 g, 8.0 mmol), (dppf)PdCl₂•CH₂Cl₂ (0.20 g, 0.17 mmol) and copper iodide (0.061 g, 0.32 mmol), and the flask was purged with a positive flow of argon for 10 min. Degassed diisopropylamine (20 mL) was added, followed by degassed trimethylsilylacetylene (1.6 g, 8.5 mmol). The reaction developed heavy precipitate and was noticeably exothermic within 2 min. The solution was sonicated briefly to break up the solids and aid stirring. The mixture was stirred at rt over 2 d. The solvents were evaporated, and run through a short silica plug (hexanes/ethyl acetate 1:1). The solvents were evaporated to yield a dark brown oil that solidified to large crystals on standing. The solids were redissolved in MeOH (40 mL) and THF (40 mL), and KF (0.72 g, 12 mmol) was added. The solution was stirred overnight, and the solvents were evaporated. The residue was filtered through a silica plug (hexanes/ethyl acetate 2:1), and the solvents were evaporated from the filtrate to yield an orange powder that was confirmed by NMR as the target compound **AP4**. ^1H NMR (300 MHz): δ 8.23 – 8.17 (m, 2H), 7.67 – 7.61 (m, 2H), 3.36 (s, 1H). The ^1H (Figure A-38) NMR spectrum is included in the appendix (Chapter 5).

4.4. References

-
- (1) Butler, I. R. In *Inorganic Experiments*; Wooll'ams, J. D., Ed.; Wiley-VCH: Weinheim, 1994; pp. 88–94.
 - (2) Huc, V.; Balueva, A.; Sebastian, R.-M.; Caminade, A.-M.; Majoral, J.-P. *Synthesis* **2000**, 726–730.
 - (3) Curtis, M. D. *J. Am. Chem. Soc.* **1969**, *91*, 6011–6018.
 - (4) Morra, N. A.; Pagenkopf, B. L. In *Organic Syntheses*; John Wiley & Sons, Inc.; Daisuke, T.; Mita, T.; Shibasaki, M., Eds.; John Wiley & Sons, Inc.: Hoboken, NJ, USA, 2008; pp. 53–63.
 - (5) Dötze, M.; Klar, G. *Phosphorus Sulfur* **1993**, *84*, 95–106.
 - (6) Boag, N. M. In *Inorganic Experiments*; Wooll'ams, J. D., Ed.; Wiley-VCH: Weinheim, 1994; pp. 80–82.
 - (7) Chau, N. T. T.; Meyer, M.; Komagawa, S.; Chevallier, F.; Fort, Y.; Uchiyama, M.; Mongin, F.; Gros, P. C. *Chem. Eur. J.* **2010**, *16*, 12425–12433.
 - (8) Slocum, D. W.; Tekin, K. C.; Nguyen, Q.; Whitley, P. E.; Reinscheld, T. K.; Fouzia, B. *Tetrahedron Lett.* **2011**, *52*, 7141–7145.
 - (9) Sheldrick, G.M. *Acta Cryst.* **2008**, *A64*, 112–122.
 - (10) Dolomanov, O.V.; Bourhis, L.J.; Gildea, R.J.; Howard, J.A.K.; Puschmann, H. *J. Appl. Cryst.* **2009**, *42*, 339–341.
 - (11) Bandrowsky, T. L.; Carroll, J. B.; Braddock-Wilking, J. *Organometallics* **2011**, *30*, 3559–3569.
 - (12) Meier-Brocks, F.; Weiss, E. *J. Organomet. Chem.* **1993**, *453*, 33 – 45.
 - (13) (a) Hayashi, T.; Konishi, M.; Kobori, Y.; Kumada, M.; Higuchi, T.; Hirotsu, K. *J. Am. Chem. Soc.* **1984**, *106*, 158–163; (b) Colacot, T. J.; Qian, H.; Cea-Olivares, R.; Hernandez-Ortega, S. *J. Organomet. Chem.* **2001**, *637-639*, 691–697.
 - (14) Carroll, J. B.; Braddock-Wilking, J. *Organometallics* **2013**, *32*, 1905–1912.
 - (15) Yamaguchi, S.; Endo, T.; Uchida, M.; Izumizawa, T.; Furukawa, K.; Tamao, K. *Chem. Eur J.* **2000**, *6*, 1683–1692.
 - (16) Kienle, M.; Knochel, P. *Org. Lett.* **2010**, *12*, 2702–2705.
 - (17) Son, H.-J.; Han, W.-S.; Wee, K. R.; Lee, S.-H.; Hwang, A.-R.; Kwon, S.; Cho, D. W.; Suh, I.-H.; Kang, S. O. *J. Mater. Chem.* **2009**, *19*, 8964–8973.
 - (18) Boydston, A. J.; Yin, Y.; Pagenkopf, B. L. *J. Am. Chem. Soc.* **2004**, *126*, 3724–3725.
 - (19) Hrobáriková, V.; Hrobárik, P.; Gajdoš, P.; Fitolis, I.; Fakis, M.; Persephonis, P.; Zahradník, P. *The Journal of Organic Chemistry* **2010**, *75*, 3053–3068.
 - (20) Vrábel, M.; Hocek, M.; Havran, L.; Fojta, M.; Votruba, I.; Klepetářová, B.; Pohl, R.; Rulíšek, L.; Zendlová, L.; Hobza, P.; Shih, I.; Mabery, E.; Mackman, R. *Eur. J. Inorg. Chem.* **2007**, *2007*, 1752–1769.
 - (21) Takahashi, S.; Kuroyama, Y.; Sonogashira, K.; Hagihara, N. *Synthesis* **15**, 1980, 627–630.

Chapter 5. Appendices

Table of Figures

Figure A-1. ^1H NMR spectrum of G1.	150
Figure A-2. $^{13}\text{C}\{^1\text{H}\}$ NMR of G1.	151
Figure A-3. ^1H NMR spectrum of G2.	152
Figure A-4. $^{13}\text{C}\{^1\text{H}\}$ NMR of G2.	153
Figure A-5. ^1H NMR spectrum of G3.	154
Figure A-6. $^{13}\text{C}\{^1\text{H}\}$ NMR of G3.	155
Figure A-7. ^1H NMR spectrum of G4.	156
Figure A-8. $^{13}\text{C}\{^1\text{H}\}$ NMR of G4.	157
Figure A-9. $^{31}\text{P}\{^1\text{H}\}$ NMR of G4.	158
Figure A-10. ^1H NMR spectrum of G5.	159
Figure A-11. $^{13}\text{C}\{^1\text{H}\}$ NMR of G5.	160
Figure A-12. $^{31}\text{P}\{^1\text{H}\}$ NMR of the reaction of G4 with (COD)PtCl ₂	161
Figure A-13. ^1H NMR of SP1.	162
Figure A-14. $^{31}\text{P}\{^1\text{H}\}$ NMR of SP1.	163
Figure A-15. ^1H NMR of SP2.	164
Figure A-16. $^{13}\text{C}\{^1\text{H}\}$ NMR of SP2.	165
Figure A-17. ^1H NMR of S1.	166
Figure A-18. $^{13}\text{C}\{^1\text{H}\}$ NMR of S1.	167
Figure A-19. $^{29}\text{Si}\{^1\text{H}\}$ NMR of S1.	168
Figure A-20. ^1H NMR of S2. Spinning sidebands are present ± 20 Hz of each peak.	169

Figure A-21. $^{13}\text{C}\{^1\text{H}\}$ NMR of S2.....	170
Figure A-22. $^{29}\text{Si}\{^1\text{H}\}$ NMR of S2.....	171
Figure A-23. ^1H NMR of S3.....	172
Figure A-24. $^{13}\text{C}\{^1\text{H}\}$ NMR of S3.....	173
Figure A-25. ^1H NMR of S4.....	174
Figure A-26. $^{13}\text{C}\{^1\text{H}\}$ NMR of S4.....	175
Figure A-27. ^1H NMR of S5.....	176
Figure A-28. $^{13}\text{C}\{^1\text{H}\}$ NMR of S5.....	177
Figure A-29. $^{29}\text{Si}\{^1\text{H}\}$ NMR of S5.....	178
Figure A-30. ^1H NMR of S6.....	179
Figure A-31. ^1H NMR of the crude material of AP1.....	180
Figure A-32. $^{13}\text{C}\{^1\text{H}\}$ NMR of the crude material of AP1.	181
Figure A-33. ^1H NMR spectrum of the TMS-protected precursor of AP2.	182
Figure A-34. $^{13}\text{C}\{^1\text{H}\}$ NMR spectrum of the TMS-protected precursor of AP2. ...	183
Figure A-35. ^1H NMR spectrum of the TMS-protected precursor of AP3.	184
Figure A-36. $^{13}\text{C}\{^1\text{H}\}$ NMR spectrum of the TMS-protected precursor of AP3. ...	185
Figure A-37. ^1H NMR spectrum of AP3.	186
Figure A-38. ^1H NMR of AP4.....	187
Figure A-39. MS Chromatogram of S6.	188
Figure A-40. A GC-MS chromatogram of the crude mixture in a reaction to synthesize S6; the assigned structure is inset. Retention time for the species is 4.54 min.	189

Figure A-41. A GC-MS chromatogram of the crude mixture in a reaction to synthesize S6; the assigned structure (“homocoupled”) is inset. Retention time for the species is 7.57 min.	190
Figure A-42. A GC-MS chromatogram of the crude mixture in a reaction to synthesize S6; the assigned structure (“partially reduced”) is inset. Retention time for the species is 9.08 min.	191
Figure A-43. A GC-MS chromatogram of the crude mixture in a reaction to synthesize S6; the assigned structure (“partially reduced + 18”) is inset. Retention time for the species is 9.93 min.	192
Figure A-44. A GC-MS chromatogram of the crude mixture in a reaction to synthesize S6; the assigned structure (“partially coupled”) is inset. Retention time for the species is 12.01 min.	193
Figure A-45. A GC-MS chromatogram of the crude mixture in a reaction to synthesize S6; the assigned structure (target compound, S6) is inset. Retention time for the species is 14.00 min.	194
Figure A-46. MS Chromatogram of AP1.	195
Figure A-47. MS Chromatogram for TMS-protected precursor of AP2.	196
Figure A-48. MS Chromatogram of AP2.	197
Figure A-49. Molecular structure of G2 (with ellipsoids shown at the 50% probability level).	198
Figure A-50. Molecular structure of G3 (with ellipsoids shown at the 50% probability level).	199

Figure A-51. Molecular structure of G4 (with ellipsoids shown at the 50% probability level).....	200
Figure A-52. Molecular structure of G6 (with ellipsoids shown at the 50% probability level).....	201
Figure A-53. Molecular structure of G7 (with ellipsoids shown at the 50% probability level).....	202
Figure A-54. Molecular structure of G8 (with ellipsoids shown at the 50% probability level).....	203
Figure A-55. Molecular structure of G9 (with ellipsoids shown at the 50% probability level).....	204
Figure A-56. Molecular structure of G10 (with ellipsoids shown at the 50% probability level).....	205
Figure A-57. Molecular structure of G11 (with ellipsoids shown at the 50% probability level).....	206
Figure A-58. Molecular structure of G12 (with ellipsoids shown at the 50% probability level).....	207
Figure A-59. Molecular structure of G13 (with ellipsoids shown at the 50% probability level).....	208
Figure A-60. Molecular structure of G14 (with ellipsoids shown at the 50% probability level).....	209
Figure A-61. Molecular structure of G15 (with ellipsoids shown at the 50% probability level).....	212

Figure A-62. Molecular structure of G16 (with ellipsoids shown at the 50% probability level).....	213
Figure A-63. Molecular structure of G17 (with ellipsoids shown at the 50% probability level).....	214
Figure A-64. Molecular structure of G18 (with ellipsoids shown at the 50% probability level).....	215
Figure A-65. Molecular structure of S1. Hydrogen atoms have been removed for clarity. Thermal ellipsoids are drawn at the 50% probability level.	217
Figure A-66. Molecular structure of S2. Hydrogen atoms and solvent molecules have been removed for clarity, and the full molecule was symmetrically generated from the asymmetric unit. Thermal ellipsoids are drawn at the 50% probability level.	218
Figure A-67. Molecular structure of S5. Hydrogen atoms have been removed for clarity. Thermal ellipsoids are drawn at the 50% probability level.	219
Figure A-68. UV-vis spectra of silole S1 with 1-10 equiv of Ni(II) perchlorate, 1:1 dichloromethane/methanol mixture, and total silole concentration is 5×10^{-5} M.	221
Figure A-69. UV-vis spectra of silole S1 with 1-10 equiv of Cu(II) perchlorate, 1:1 dichloromethane/methanol mixture, and total silole concentration is 5×10^{-5} M.	221
Figure A-70. UV-vis spectra of silole S1 with 1-10 equiv of Hg(II) perchlorate, 1:1 dichloromethane/methanol mixture, and total silole concentration is 5×10^{-5} M.	222
Figure A-71. Fluorescence spectra of silole S1 with 1-10 equiv of Ni(II) perchlorate, 1:1 dichloromethane/methanol mixture, and total silole concentration is 5×10^{-5} M. Excitation at 365 nm.	222

Figure A-72. Fluorescence spectra of silole S1 with 1-10 equiv of Cu(II) perchlorate, 1:1 dichloromethane/methanol mixture, and total silole concentration is 5×10^{-5} M. Excitation at 365 nm.	223
Figure A-73. Fluorescence spectra of silole S1 with 1-10 equiv of Hg(II) perchlorate, 1:1 dichloromethane/methanol mixture, and total silole concentration is 5×10^{-5} M. Excitation at 365 nm.	223
Figure A-74. UV-vis spectra of silole S2 with 1-10 equiv of Ni(II) perchlorate, 1:1 dichloromethane/methanol mixture, and total silole concentration is 5×10^{-5} M.	224
Figure A-75. UV-vis spectra of silole S2 with 1-10 equiv of Cu(II) perchlorate, 1:1 dichloromethane/methanol mixture, and total silole concentration is 5×10^{-5} M.	224
Figure A-76. UV-vis spectra of silole S2 with 1-10 equiv of Hg(II) perchlorate, 1:1 dichloromethane/methanol mixture, and total silole concentration is 5×10^{-5} M.	225
Figure A-77. Fluorescence spectra of silole S2 with 1-10 equiv of Ni(II) perchlorate, 1:1 dichloromethane/methanol mixture, and total silole concentration is 5×10^{-5} M. Excitation at 390 nm.	225
Figure A-78. Fluorescence spectra of silole S2 with 1-10 equiv of Cu(II) perchlorate, 1:1 dichloromethane/methanol mixture, and total silole concentration is 5×10^{-5} M. Excitation at 390 nm.	226
Figure A-79. Fluorescence spectra of silole S2 with 1-10 equiv of Hg(II) perchlorate, 1:1 dichloromethane/methanol mixture, and total silole concentration is 5×10^{-5} M. Excitation at 390 nm.	226
Figure A-80. UV-vis spectra of silole S3 with 1-10 equiv of Ni(II) perchlorate, 1:1 dichloromethane/methanol mixture, and total silole concentration is 5×10^{-5} M.	227

Figure A-81. UV-vis spectra of silole S3 with 1-10 equiv of Cu(II) perchlorate, 1:1 dichloromethane/methanol mixture, and total silole concentration is 5×10^{-5} M.	227
Figure A-82. UV-vis spectra of silole S3 with 1-10 equiv of Hg(II) perchlorate, 1:1 dichloromethane/methanol mixture, and total silole concentration is 5×10^{-5} M.	228
Figure A-83. Fluorescence spectra of silole S3 with 1-10 equiv of Ni(II) perchlorate, 1:1 dichloromethane/methanol mixture, and total silole concentration is 5×10^{-5} M. Excitation at 415 nm.	228
Figure A-84. Fluorescence spectra of silole S3 with 1-10 equiv of Cu(II) perchlorate, 1:1 dichloromethane/methanol mixture, and total silole concentration is 5×10^{-5} M. Excitation at 415 nm.	229
Figure A-85. Fluorescence spectra of silole S3 with 1-10 equiv of Hg(II) perchlorate, 1:1 dichloromethane/methanol mixture, and total silole concentration is 5×10^{-5} M. Excitation at 415 nm.	229
Figure A-86. UV-vis spectra of silole S4 with 1-10 equiv of Ni(II) perchlorate, 1:1 dichloromethane/methanol mixture, and total silole concentration is 5×10^{-5} M.	230
Figure A-87. UV-vis spectra of silole S4 with 1-10 equiv of Cu(II) perchlorate, 1:1 dichloromethane/methanol mixture, and total silole concentration is 5×10^{-5} M.	230
Figure A-88. UV-vis spectra of silole S4 with 1-10 equiv of Hg(II) perchlorate, 1:1 dichloromethane/methanol mixture, and total silole concentration is 5×10^{-5} M.	231
Figure A-89. Fluorescence spectra of silole S4 with 1-10 equiv of Ni(II) perchlorate, 1:1 dichloromethane/methanol mixture, and total silole concentration is 5×10^{-5} M. Excitation at 383 nm.	231

Figure A-90. Fluorescence spectra of silole S4 with 1-10 equiv of Cu(II) perchlorate, 1:1 dichloromethane/methanol mixture, and total silole concentration is 5×10^{-5} M.

Excitation at 383 nm. 232

Figure A-91. Fluorescence spectra of silole S4 with 1-10 equiv of Hg(II) perchlorate, 1:1 dichloromethane/methanol mixture, and total silole concentration is 5×10^{-5} M.

Excitation at 383 nm. 232

Figure A-92. The raw spectral data of titration of 1×10^{-4} M S3 in dichloromethane with 1.5×10^{-2} M Hg(II) perchlorate solution. Annotations are added to indicate the appearance or disappearance of absorption bands. The legend to the right lists the volume of Hg(II) solution added that corresponds to the line in the graph. 233

Figure A-93. The titration data extracted from the raw data (Figure A-92) at 503 nm. The total $[\text{Hg}^{2+}]$ was calculated from the initial volume of S3 (3 mL), plus the volume added by the titrant (i.e., Hg(II) perchlorate in MeOH). 233

Figure A-94. The raw spectral data of titration of 1.5×10^{-4} M S3 in THF with 1.5×10^{-2} M Hg(II) perchlorate solution (also in THF). Annotations are added to indicate the appearance or disappearance of absorption bands. The legend to the right lists the volume of Hg(II) solution added that corresponds to the line in the graph. 236

Figure A-95. The titration data extracted from the raw data (Figure A-94) at 503 nm. The total $[\text{Hg}^{2+}]$ was calculated from the initial volume of S3 (3 mL), plus the volume added by the titrant (i.e., Hg(II) perchlorate in THF). 237

Figure A-96. The titration data extracted from the raw data (Figure A-94) at 355 nm. The total $[\text{Hg}^{2+}]$ was calculated from the initial volume of S3 (3 mL), plus the volume added by the titrant (i.e., Hg(II) perchlorate in THF). 237

Figure A-97. The plot of absorbance versus the concentration of Hg(II), after subtracting 4×10^{-4} M to account for the previously coordinated Hg(II) (see Section 3.5.2). 240

Table of Tables

Table A-1. Crystallographic data and structure refinement details for the 2,3,4,5-tetraphenylgermoles in this study. 210

Table A-2. Crystallographic data and structure refinement details for the substituted germafluorenes in this study. 216

Table A-3. Crystallographic data and structure refinement details for the symmetric siloles in this study. 220

5.1. NMR Spectra of compounds.

5.1.1. NMR spectra of several 1,1-disubstituted germoles.

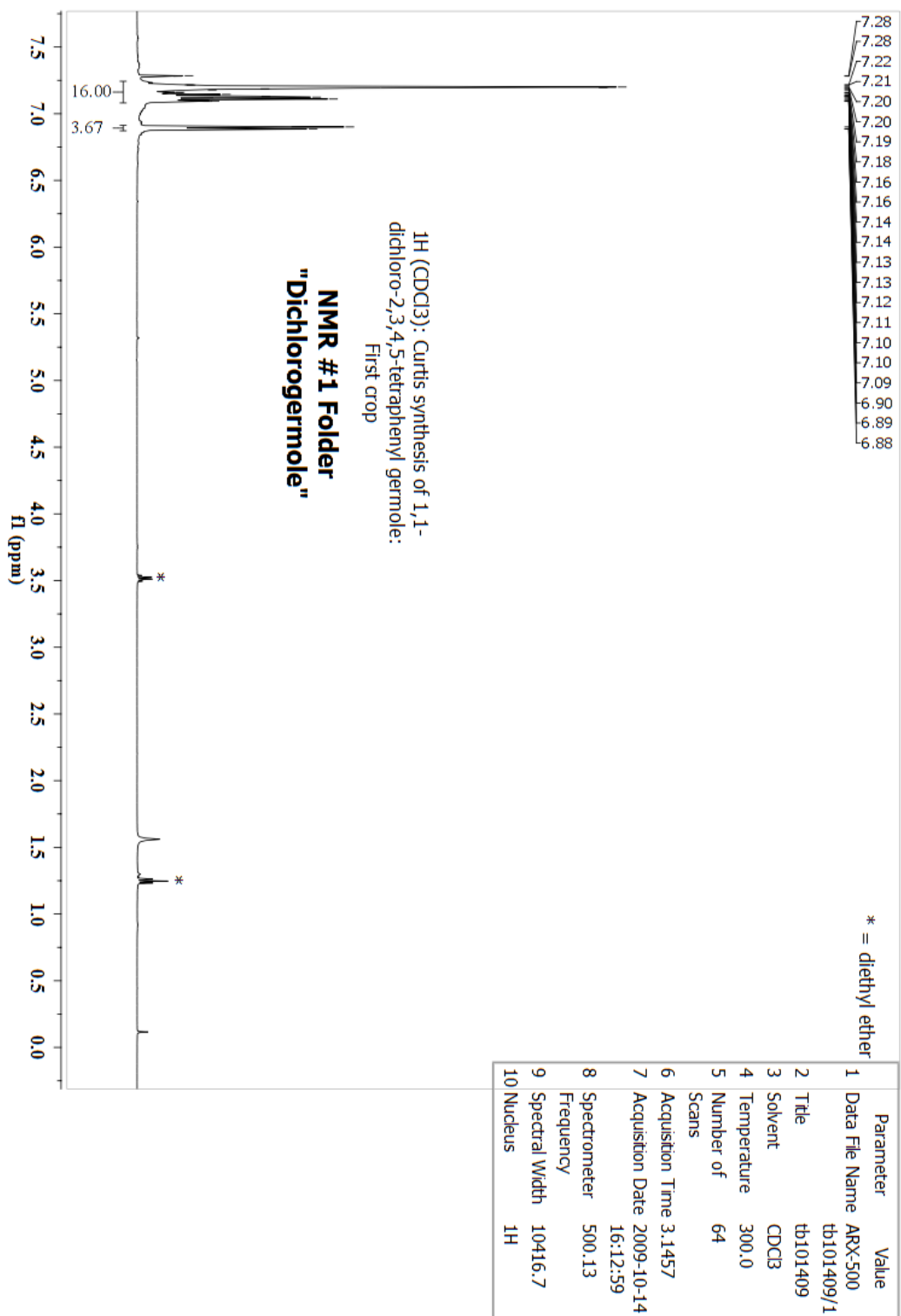


Figure A-1. ¹H NMR spectrum of G1.

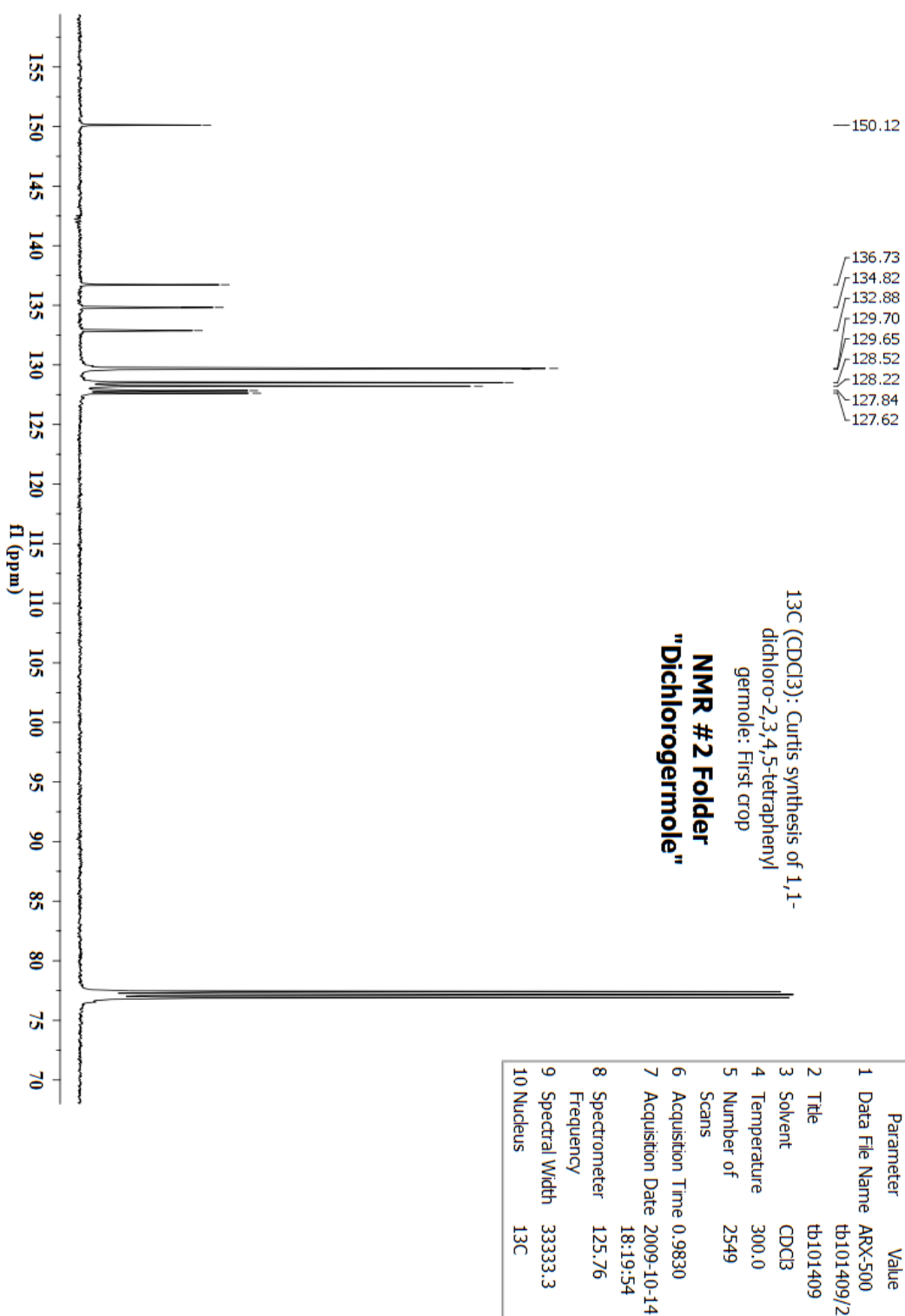


Figure A-2. $^{13}\text{C}\{^1\text{H}\}$ NMR of G1.

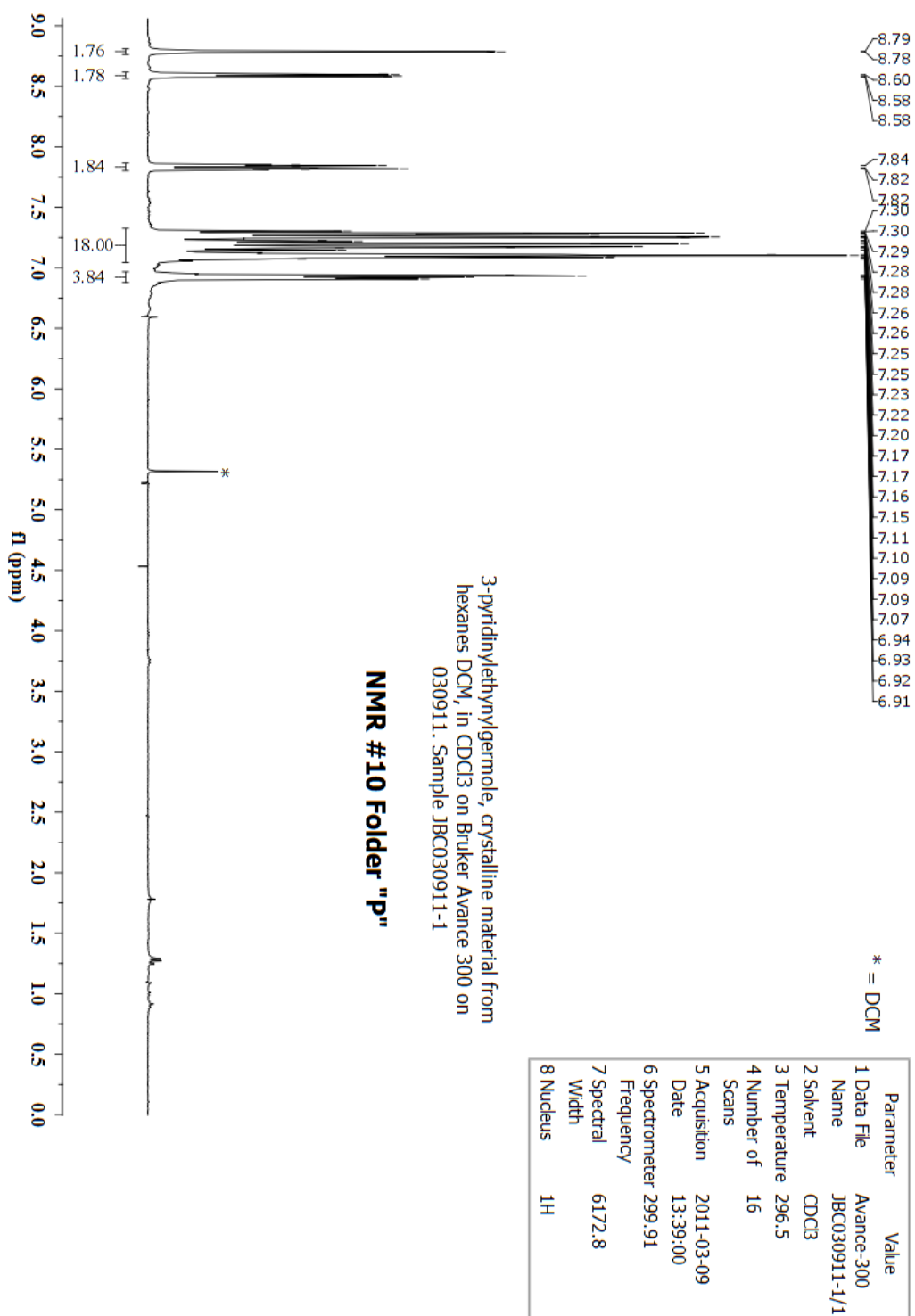


Figure A-3. ¹H NMR spectrum of G2.

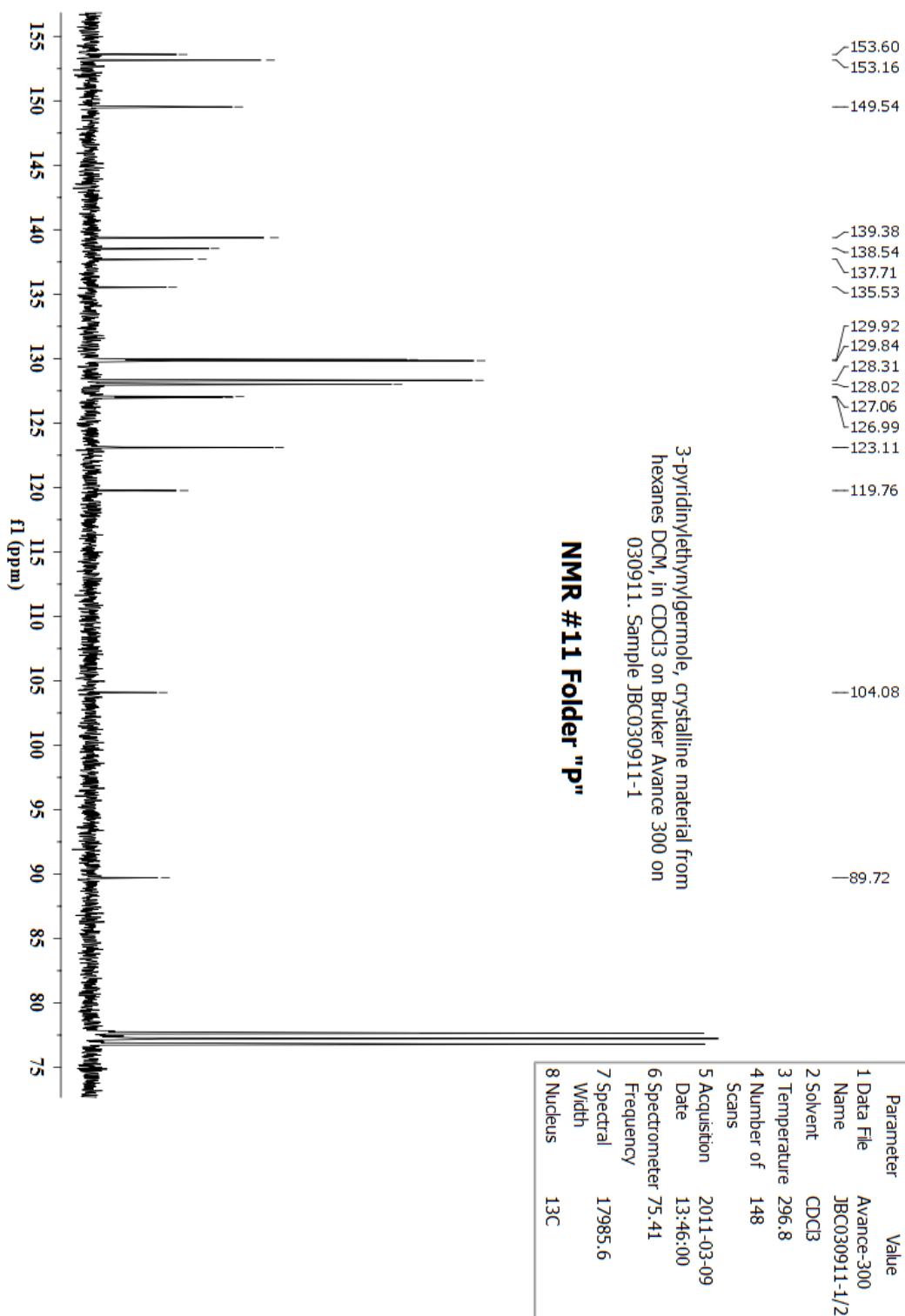
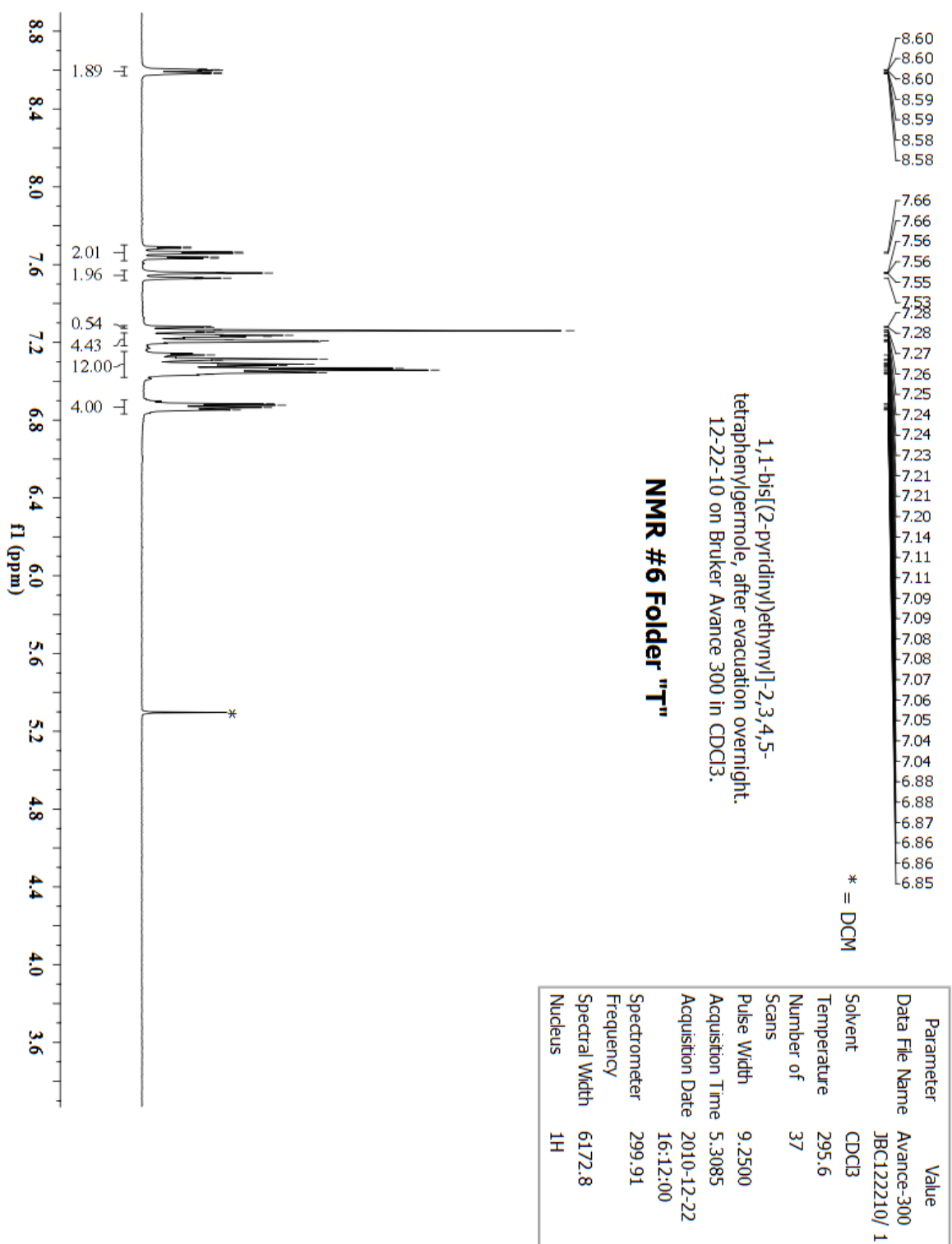


Figure A-4. ¹³C {¹H} NMR of G2.

Figure A-5. ¹H NMR spectrum of G3.

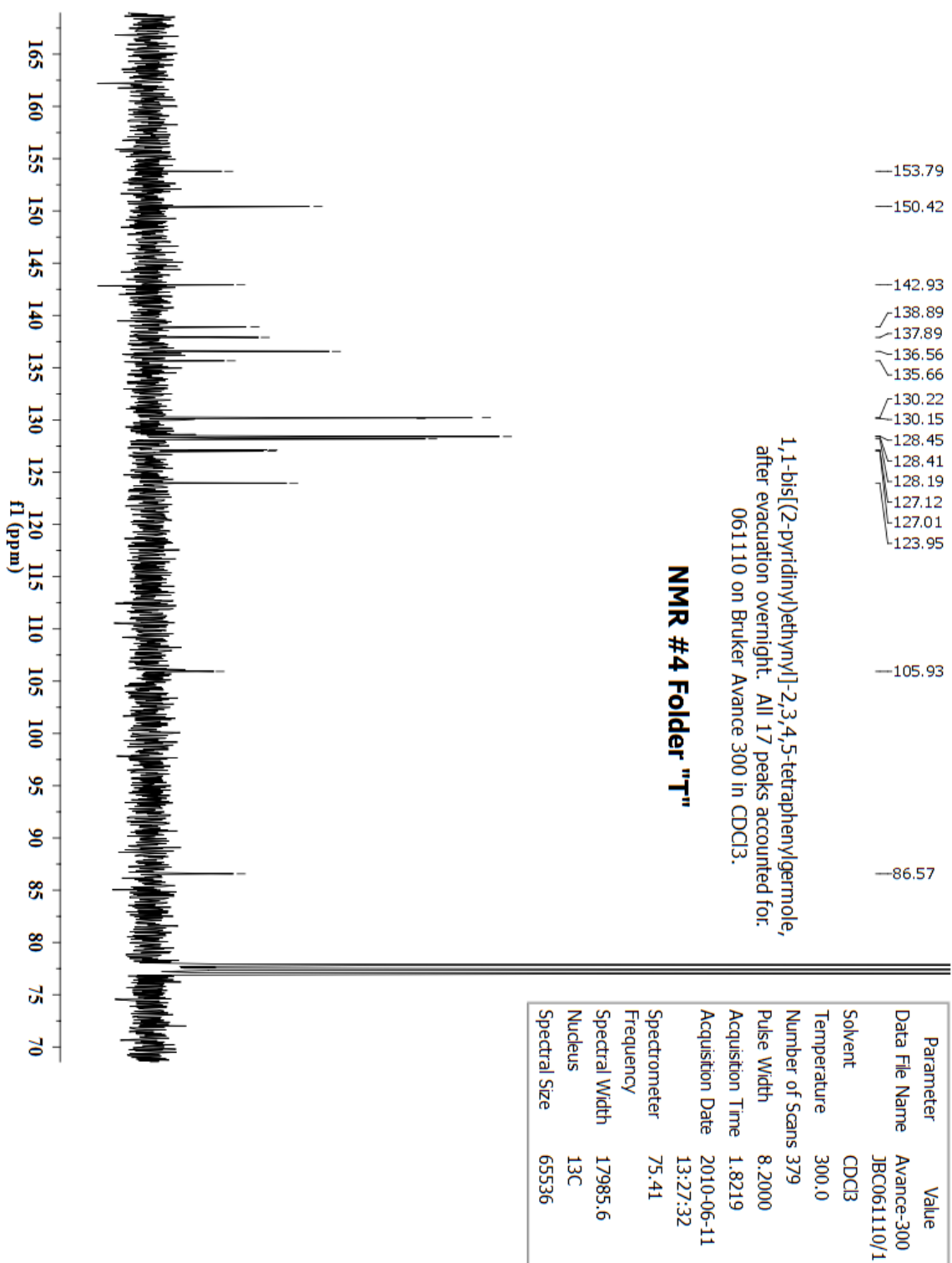


Figure A-6. ¹³C {¹H} NMR of G3.

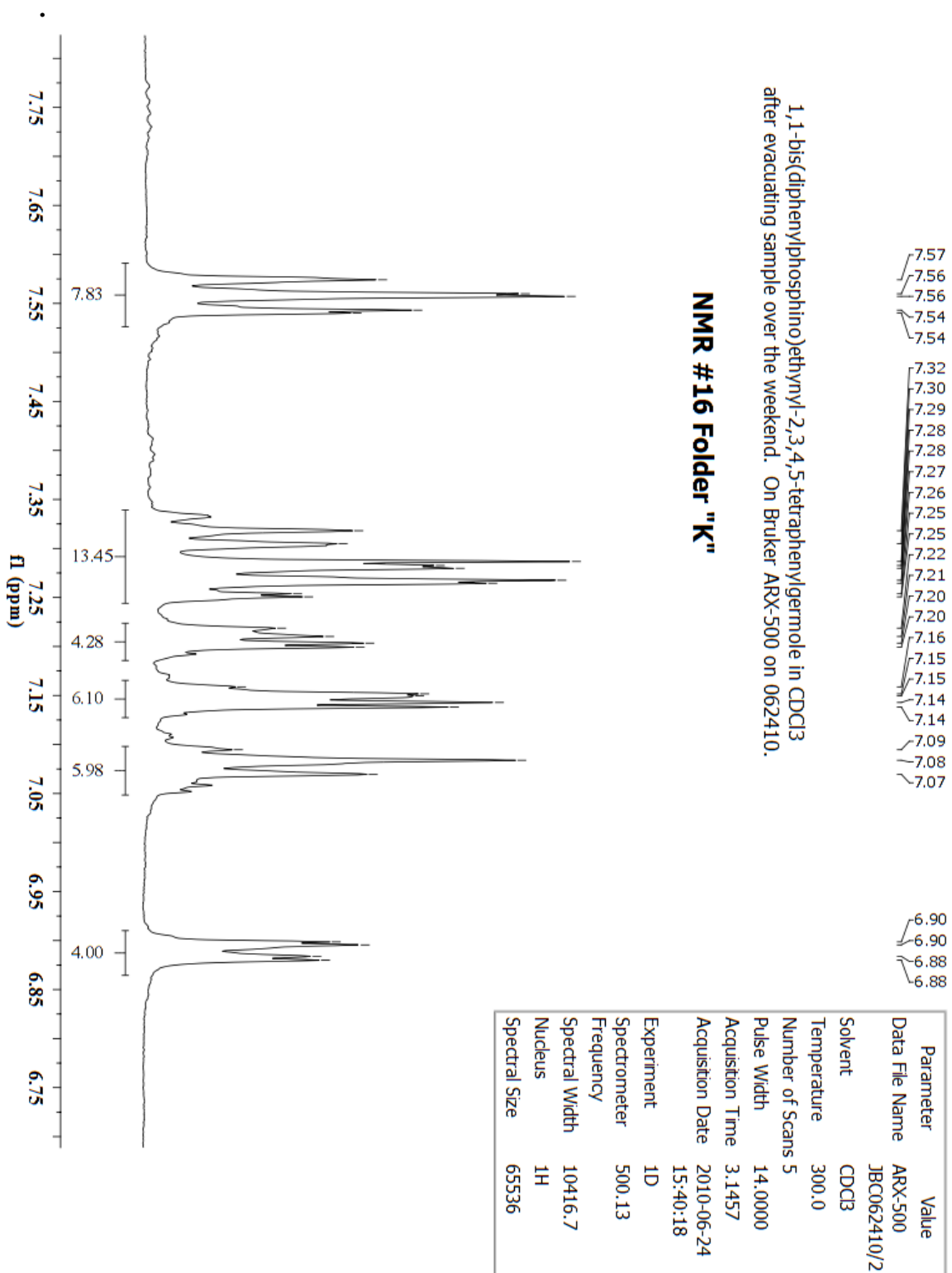


Figure A-7. ¹H NMR spectrum of G4.

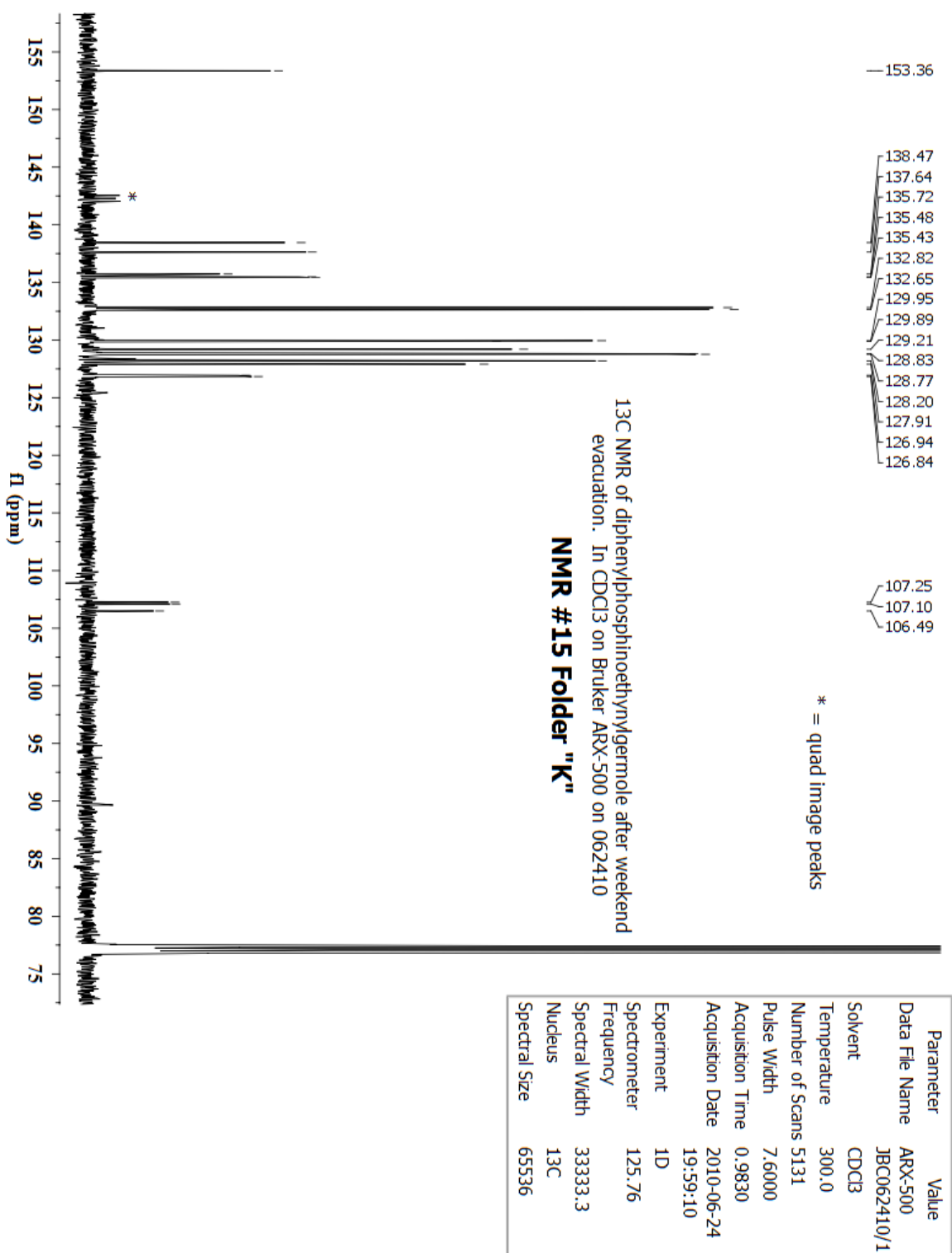


Figure A-8. $^{13}\text{C}\{^1\text{H}\}$ NMR of G4.

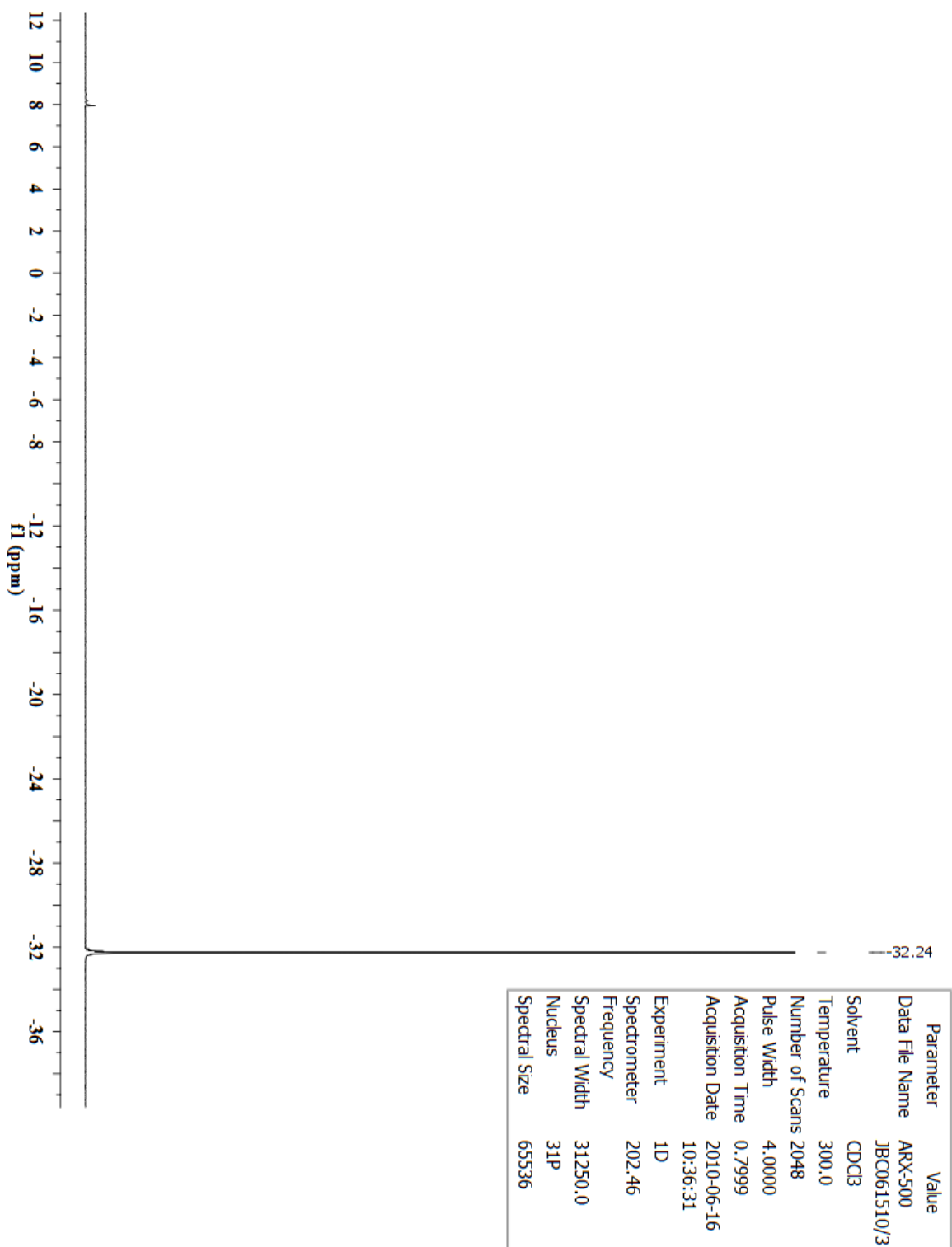


Figure A-9. $^{31}\text{P}\{^1\text{H}\}$ NMR of G4.

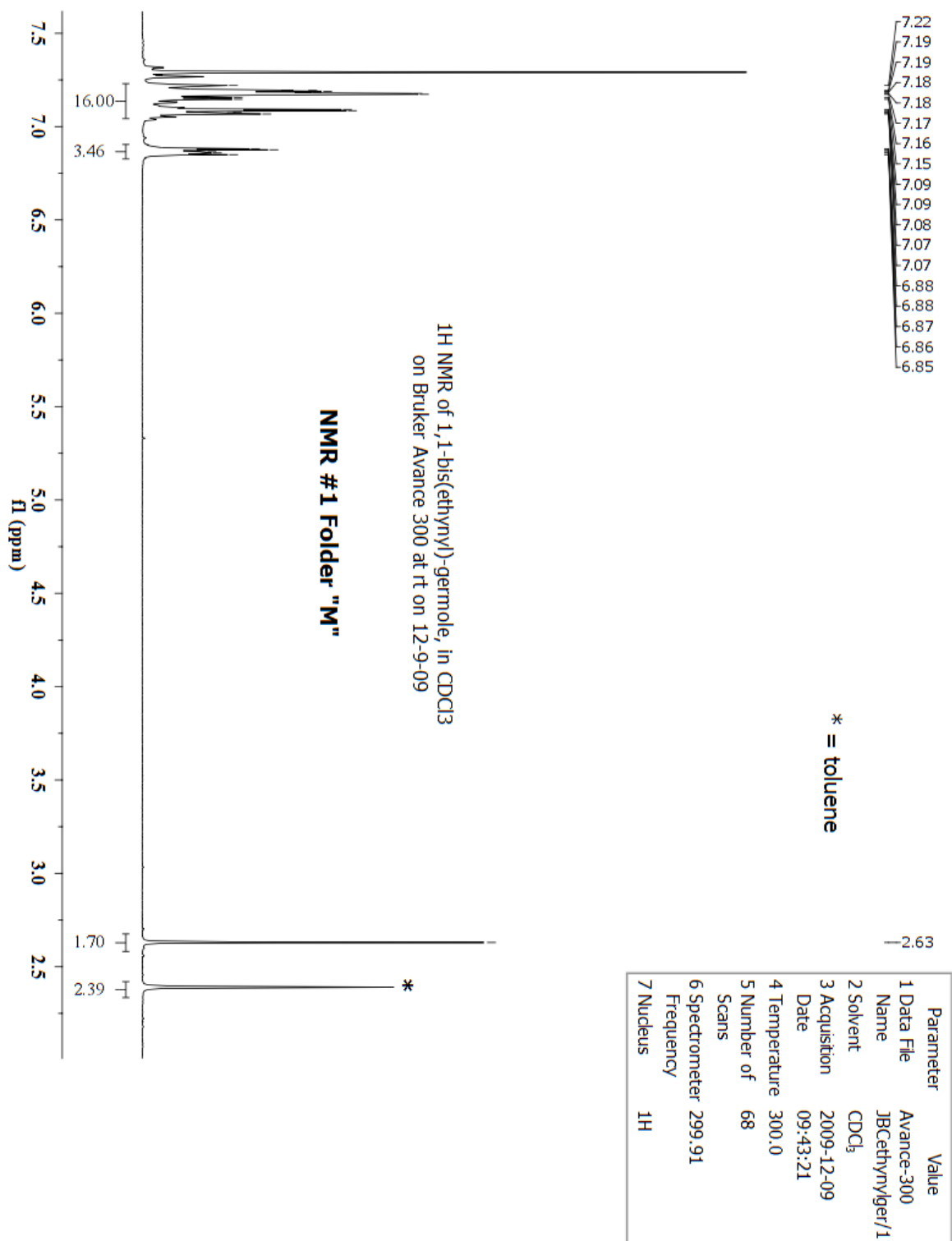
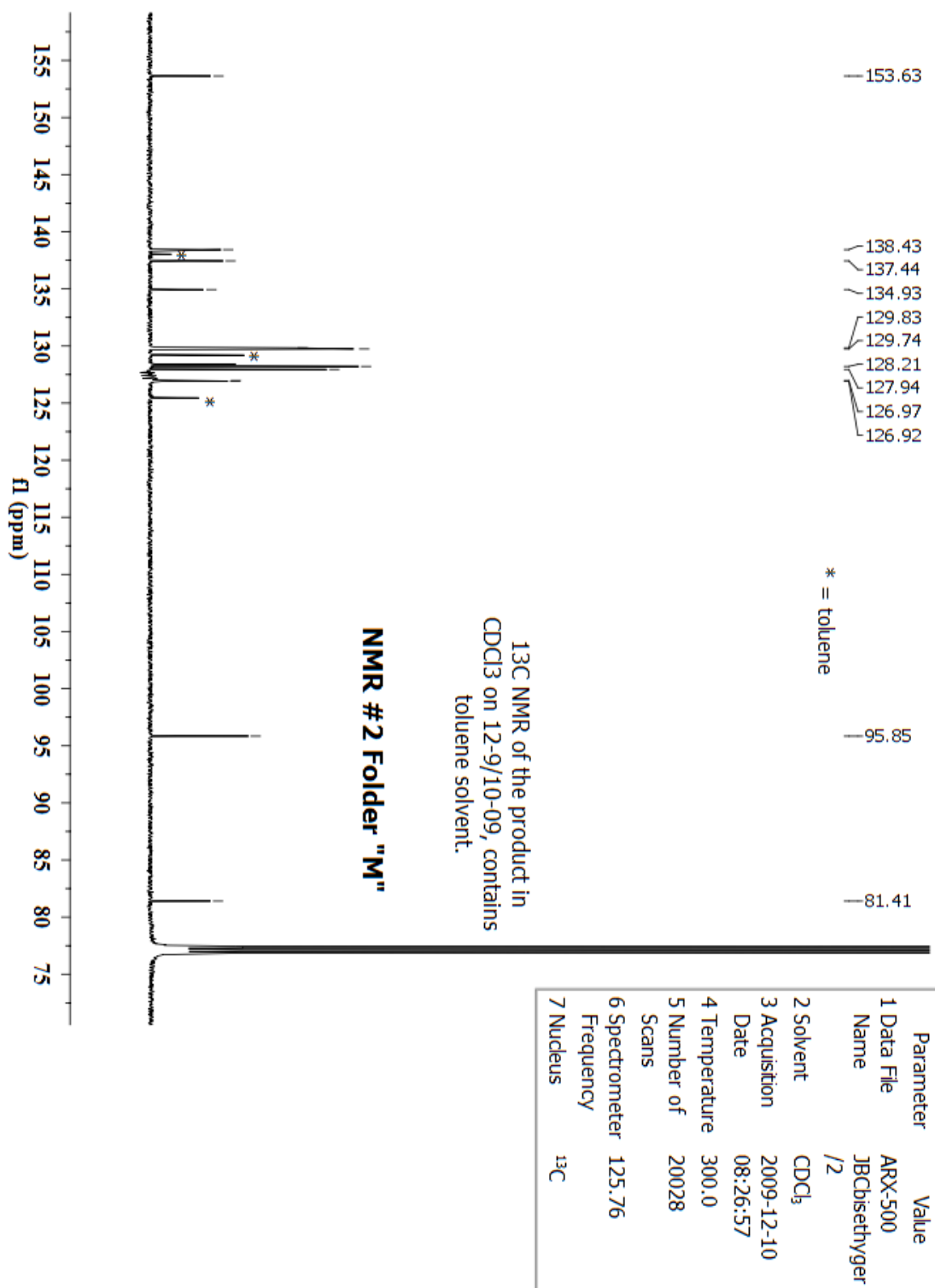


Figure A-10. ¹H NMR spectrum of G5.

Figure A-11. $^{13}\text{C}\{^1\text{H}\}$ NMR of G5.

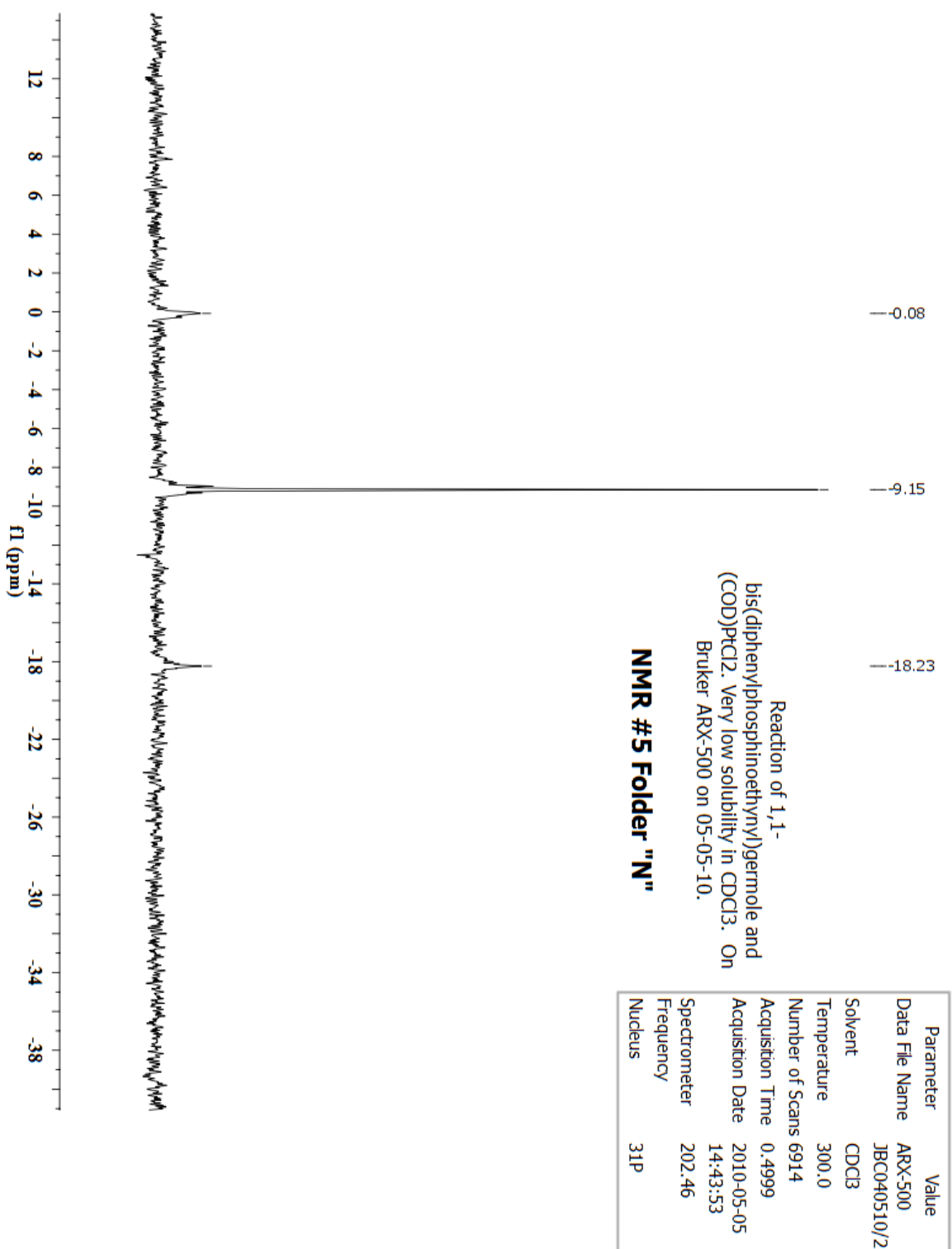


Figure A-12. ³¹P{¹H} NMR of the reaction of G4 with (COD)PtCl₂.

5.1.2. NMR spectra of symmetrical silole precursors.

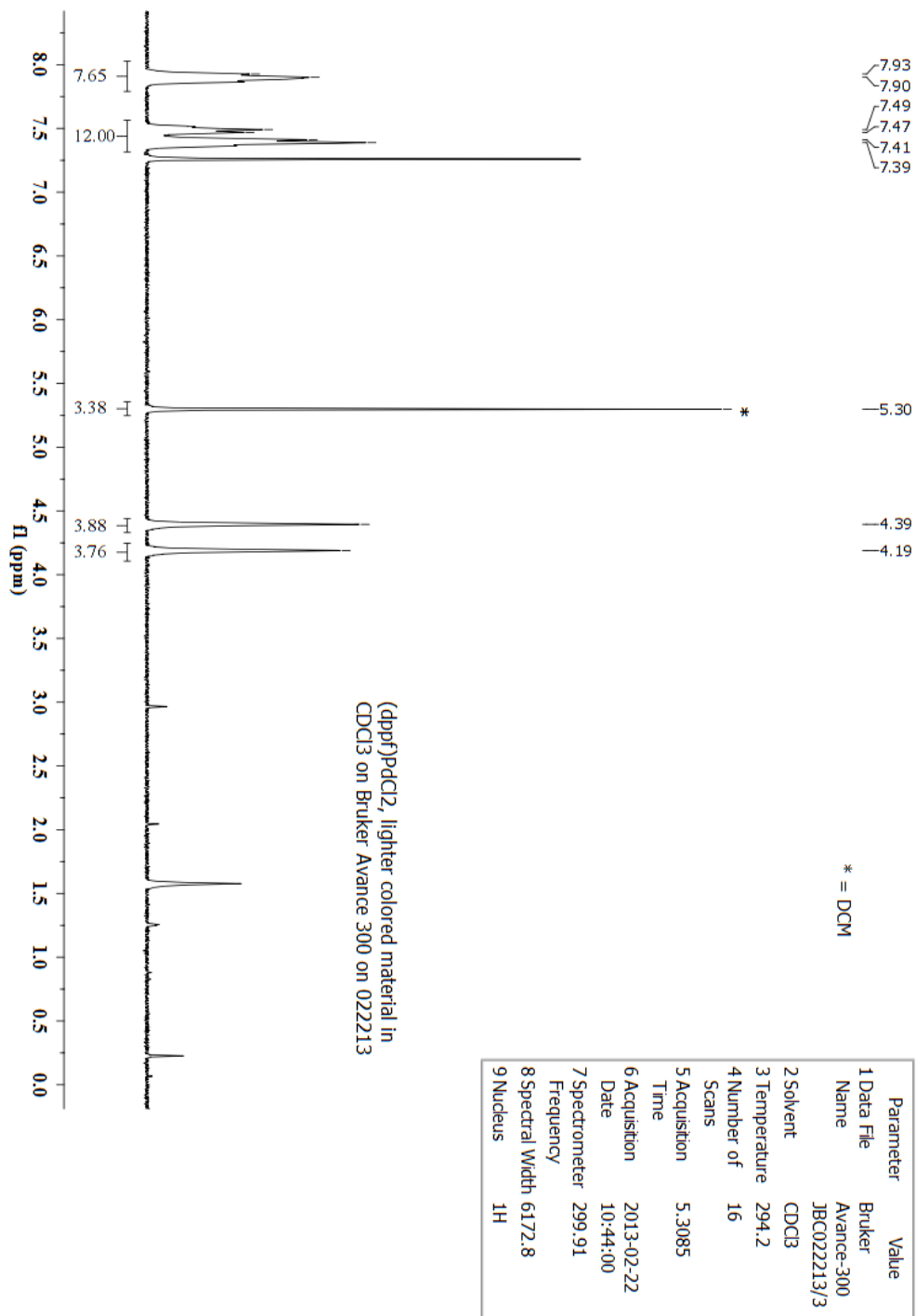


Figure A-13. ¹H NMR of SP1.

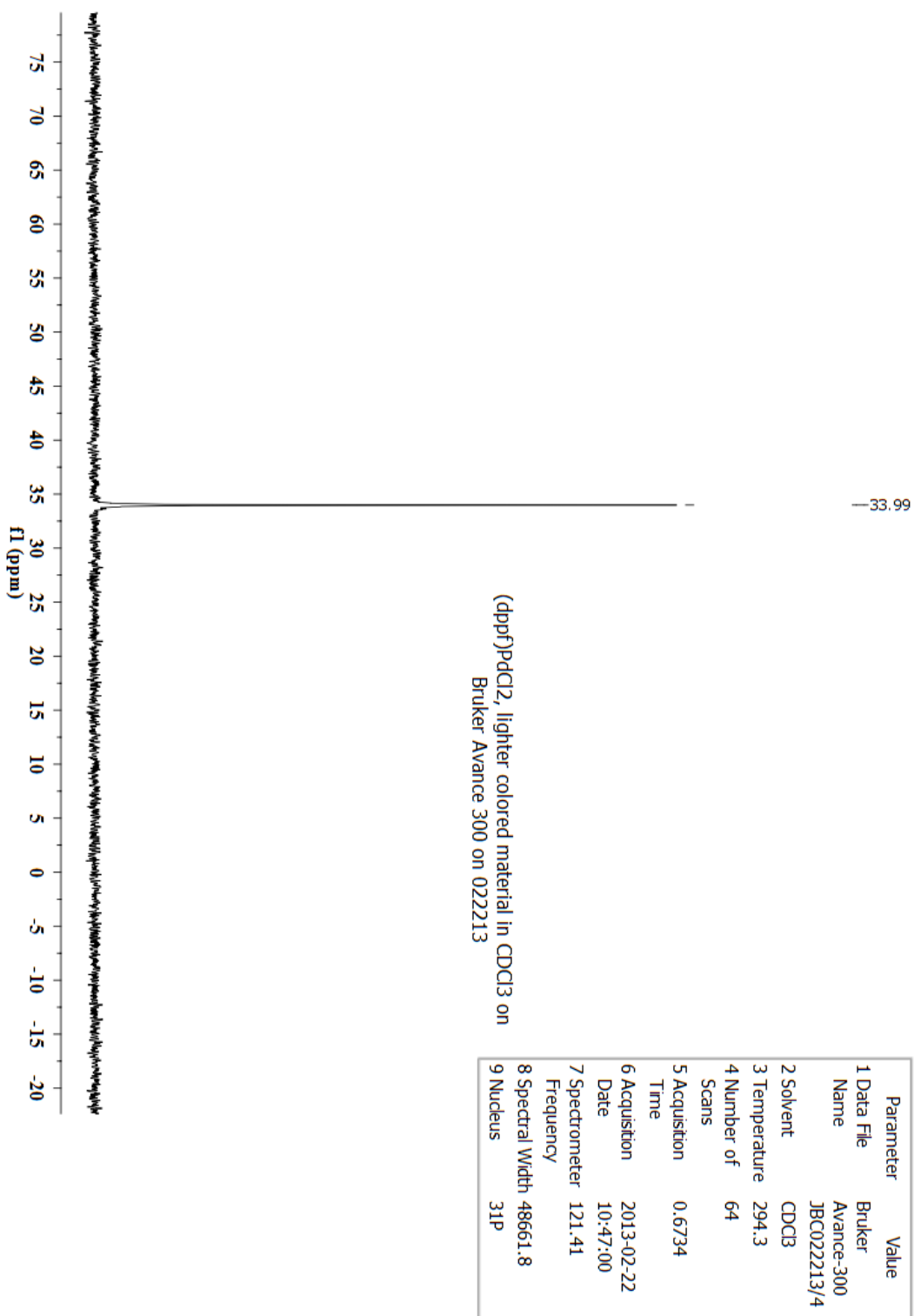
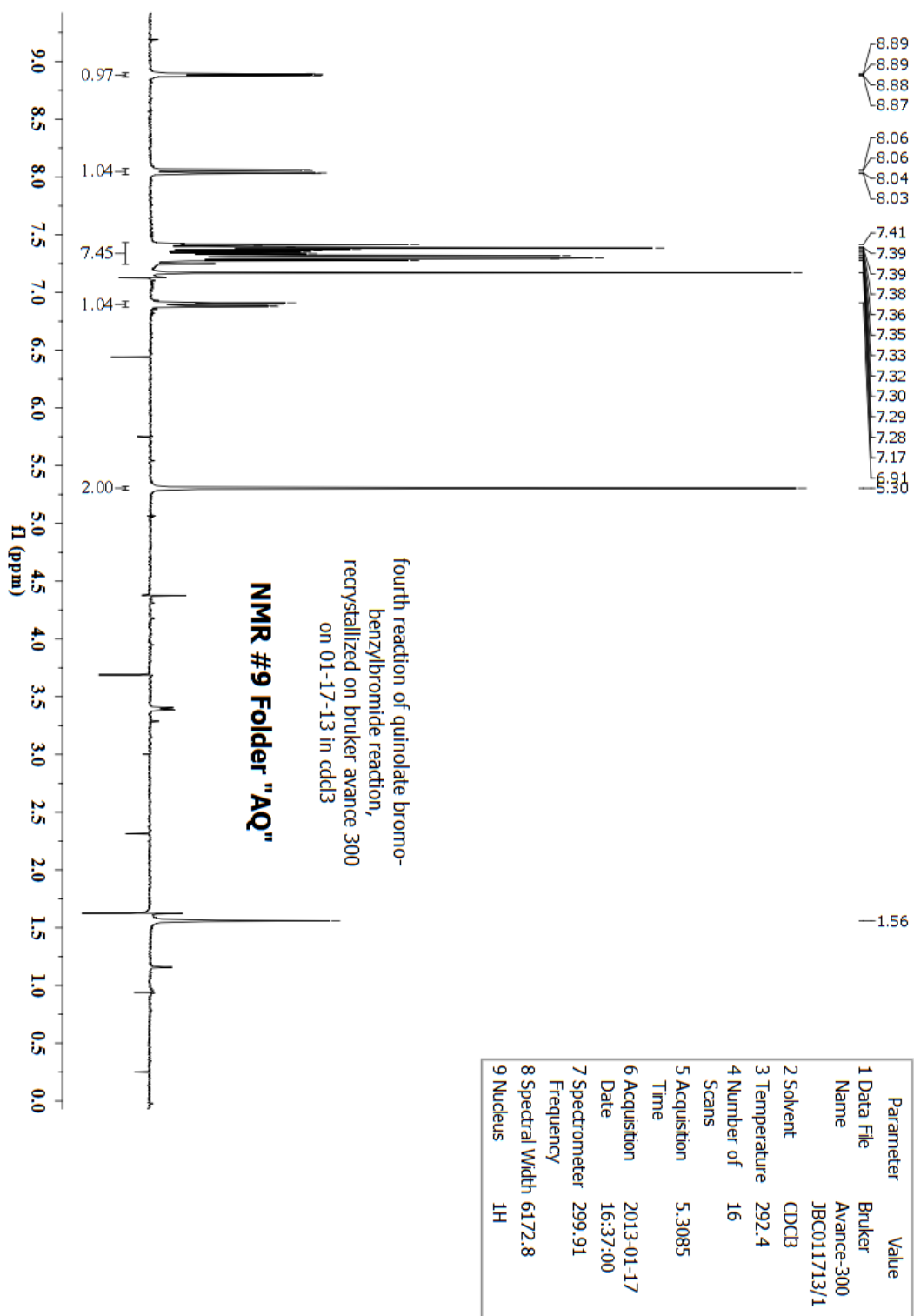
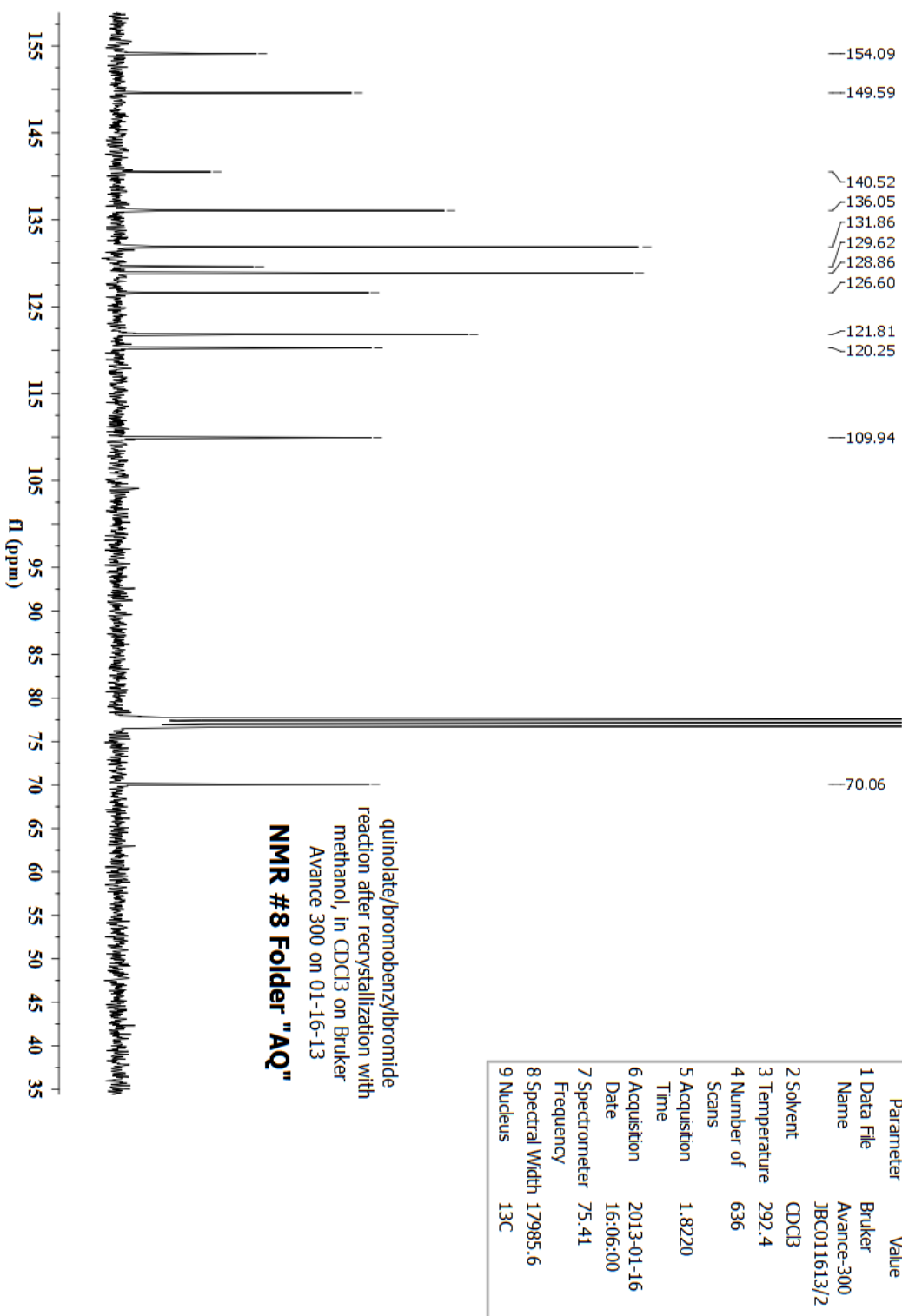
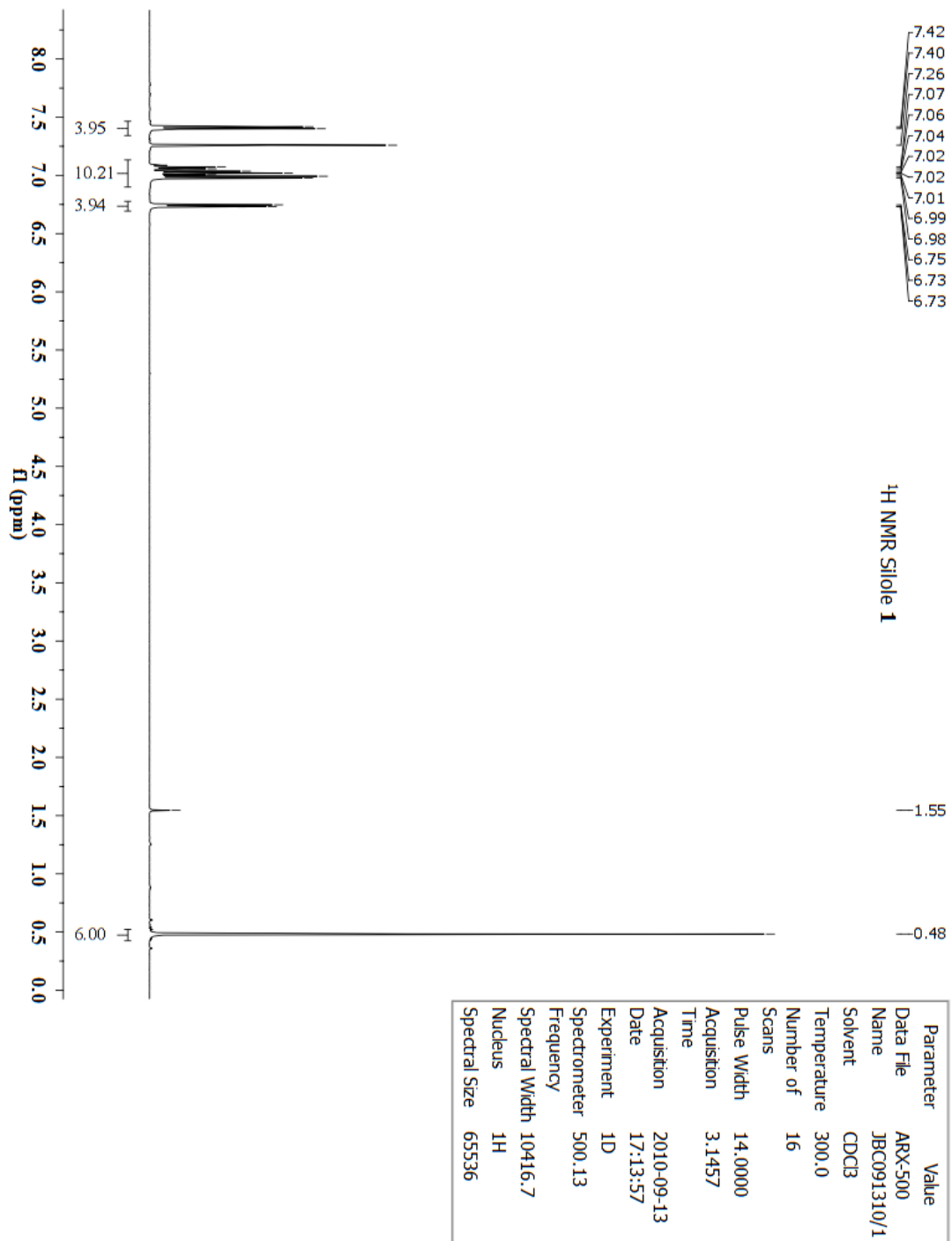


Figure A-14. $^{31}\text{P}\{^1\text{H}\}$ NMR of SPI.

Figure A-15. ^1H NMR of SP2.

Figure A- 16. ¹³C{¹H} NMR of SP2.

5.1.3. NMR spectra of symmetrical siloles.

Figure A-17. ¹H NMR of S1.

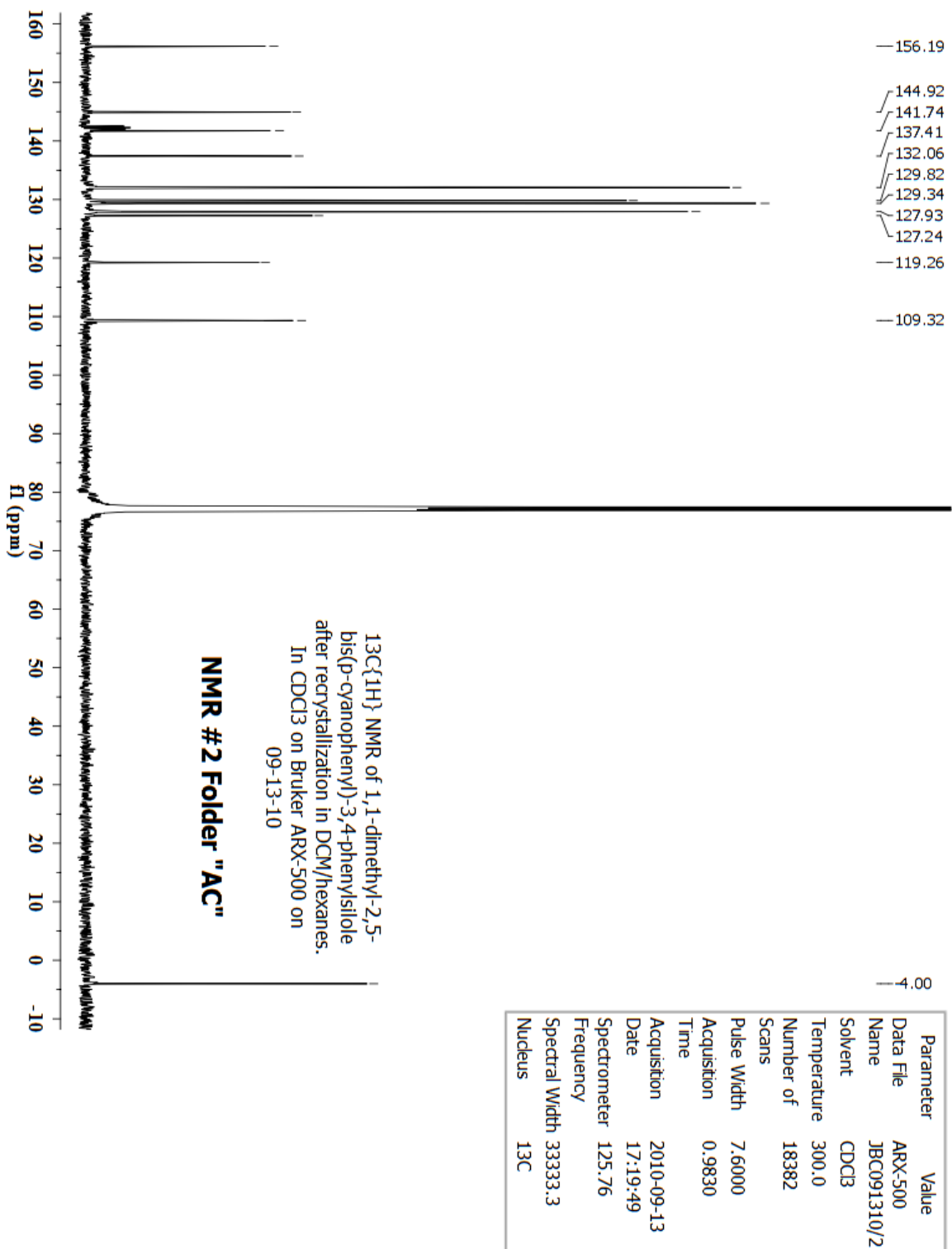


Figure A-18. $^{13}\text{C}\{^1\text{H}\}$ NMR of S1.

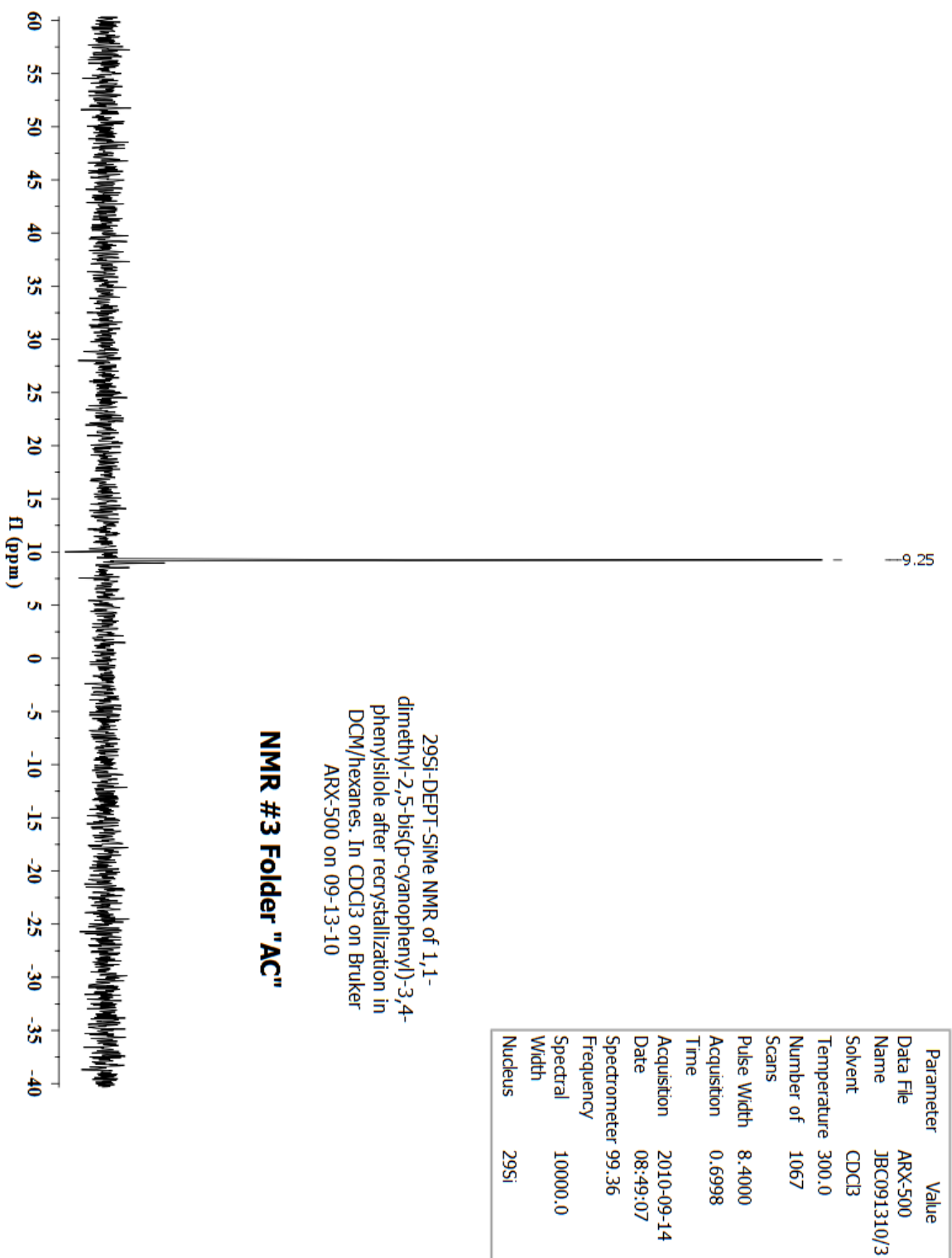


Figure A-19. $^{29}\text{Si}\{^1\text{H}\}$ NMR of S1.

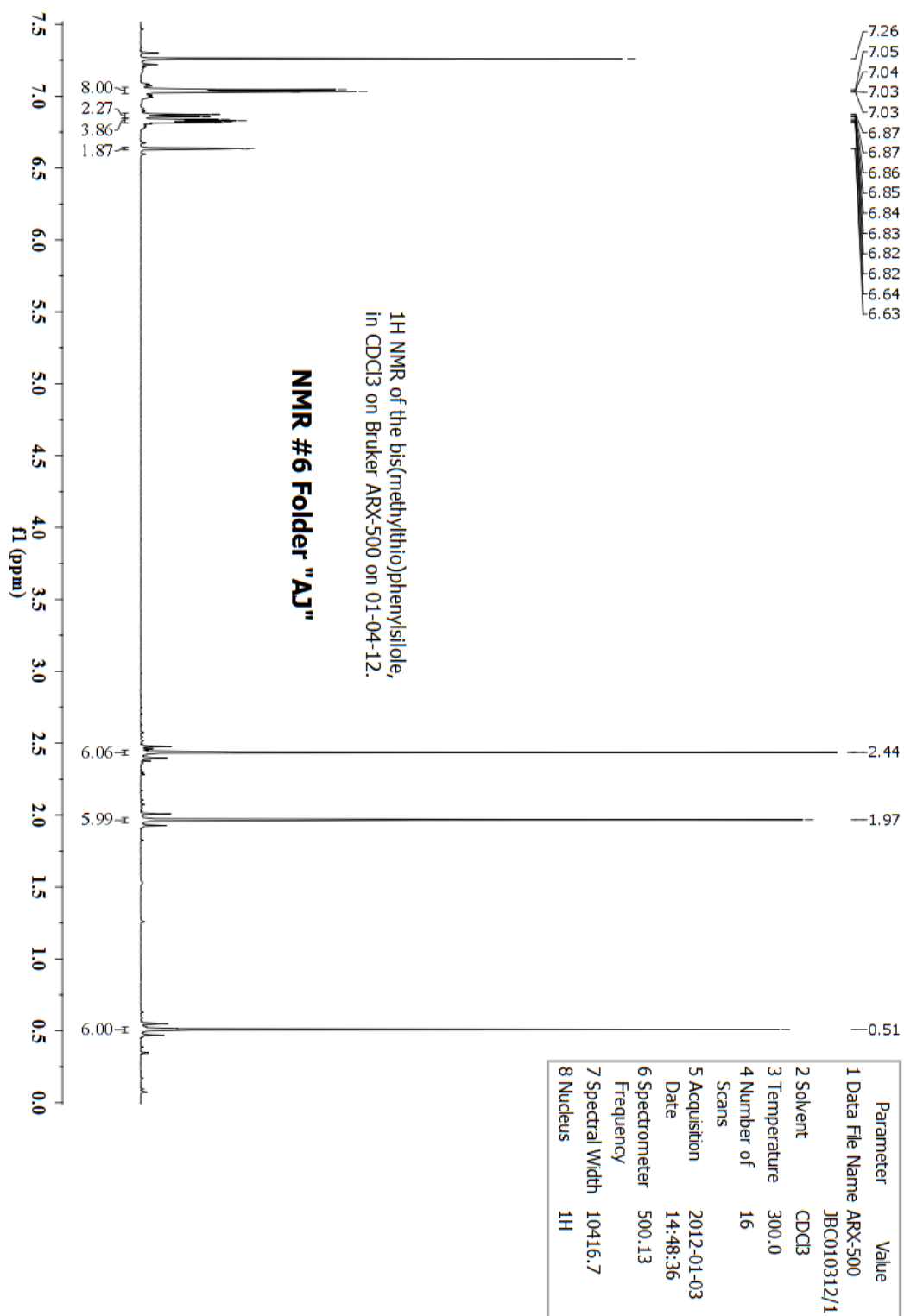
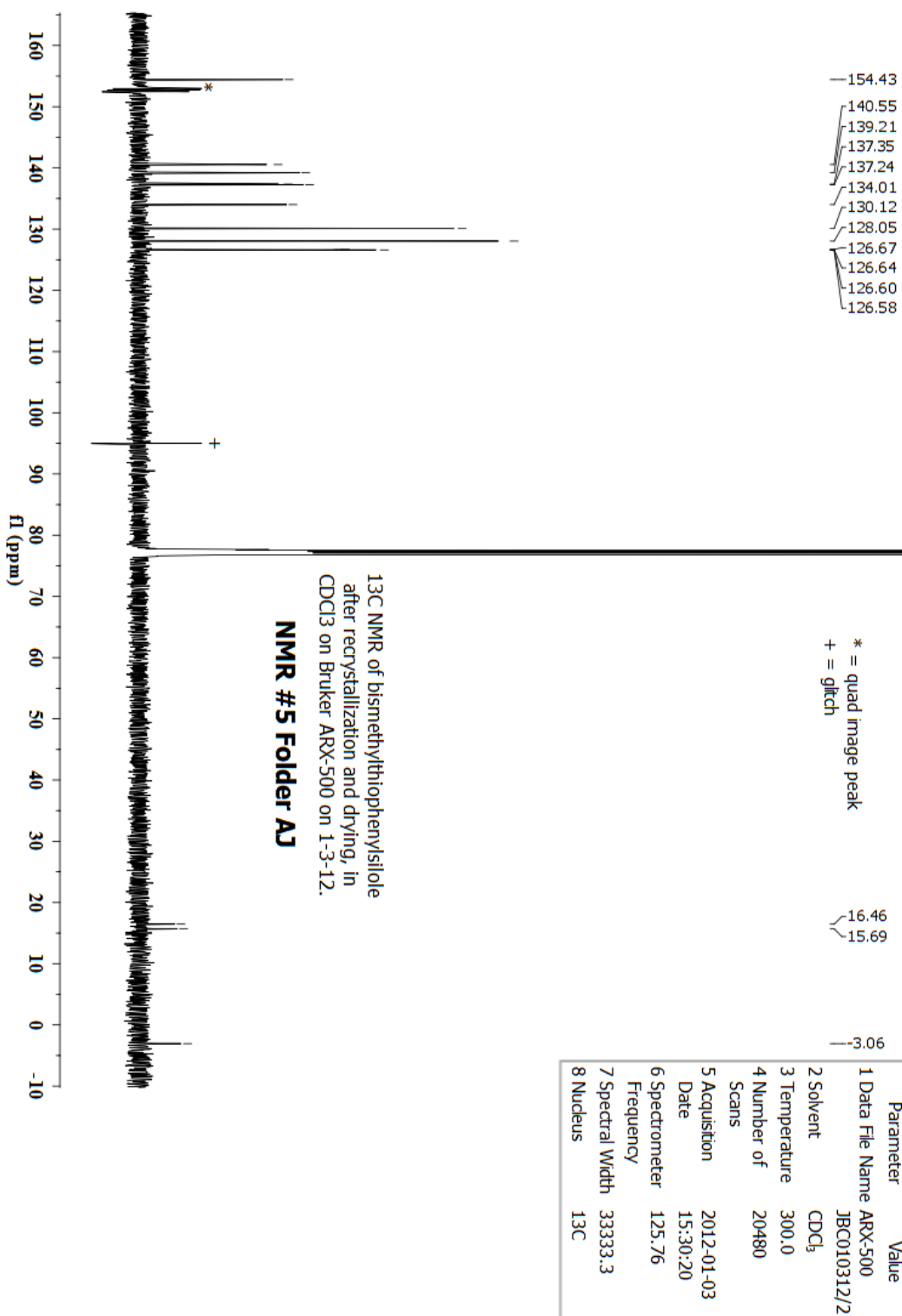


Figure A-20. ¹H NMR of S2. Spinning sidebands are present ± 20 Hz of each peak.

Figure A-21. ¹³C{¹H} NMR of S2.

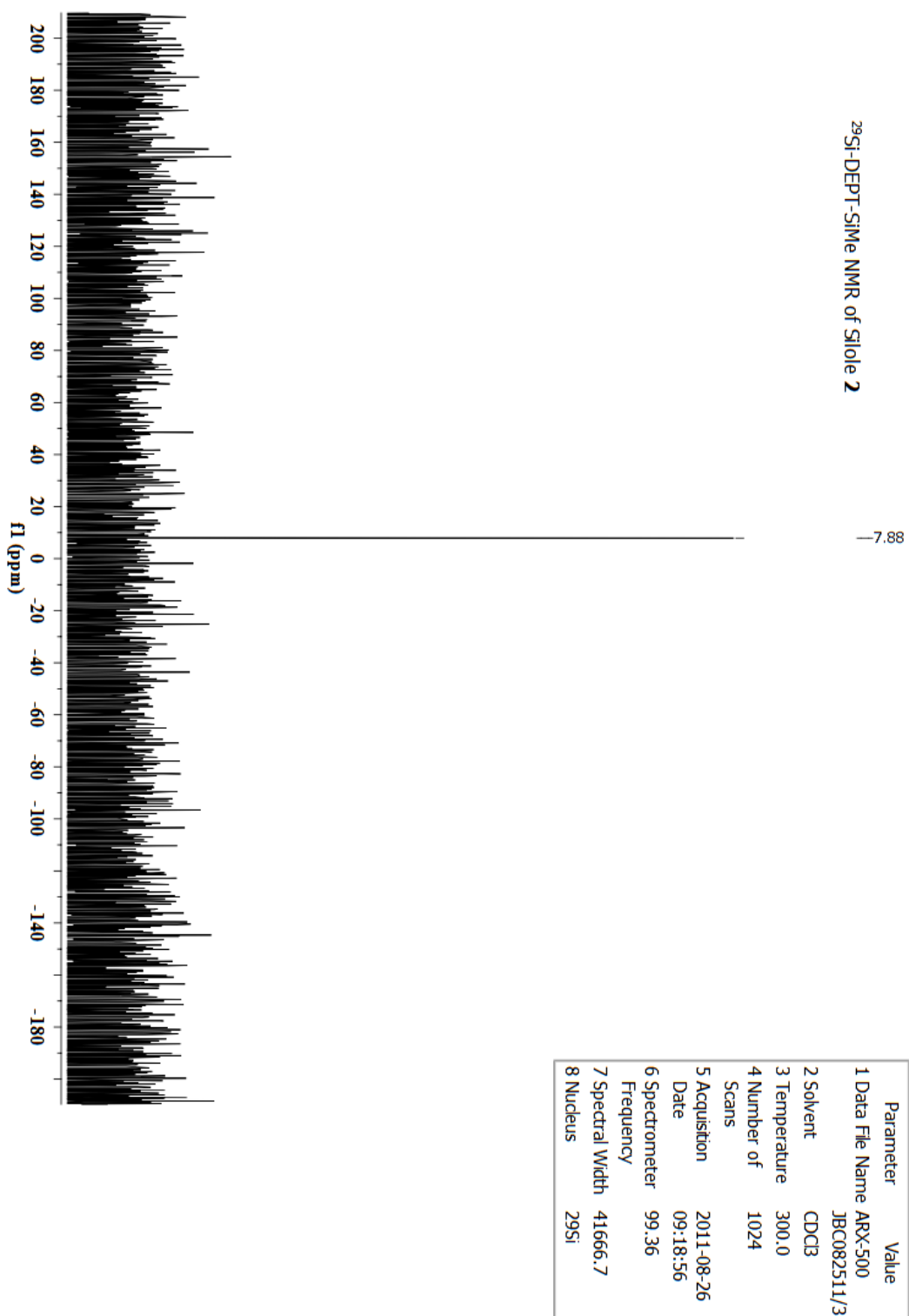
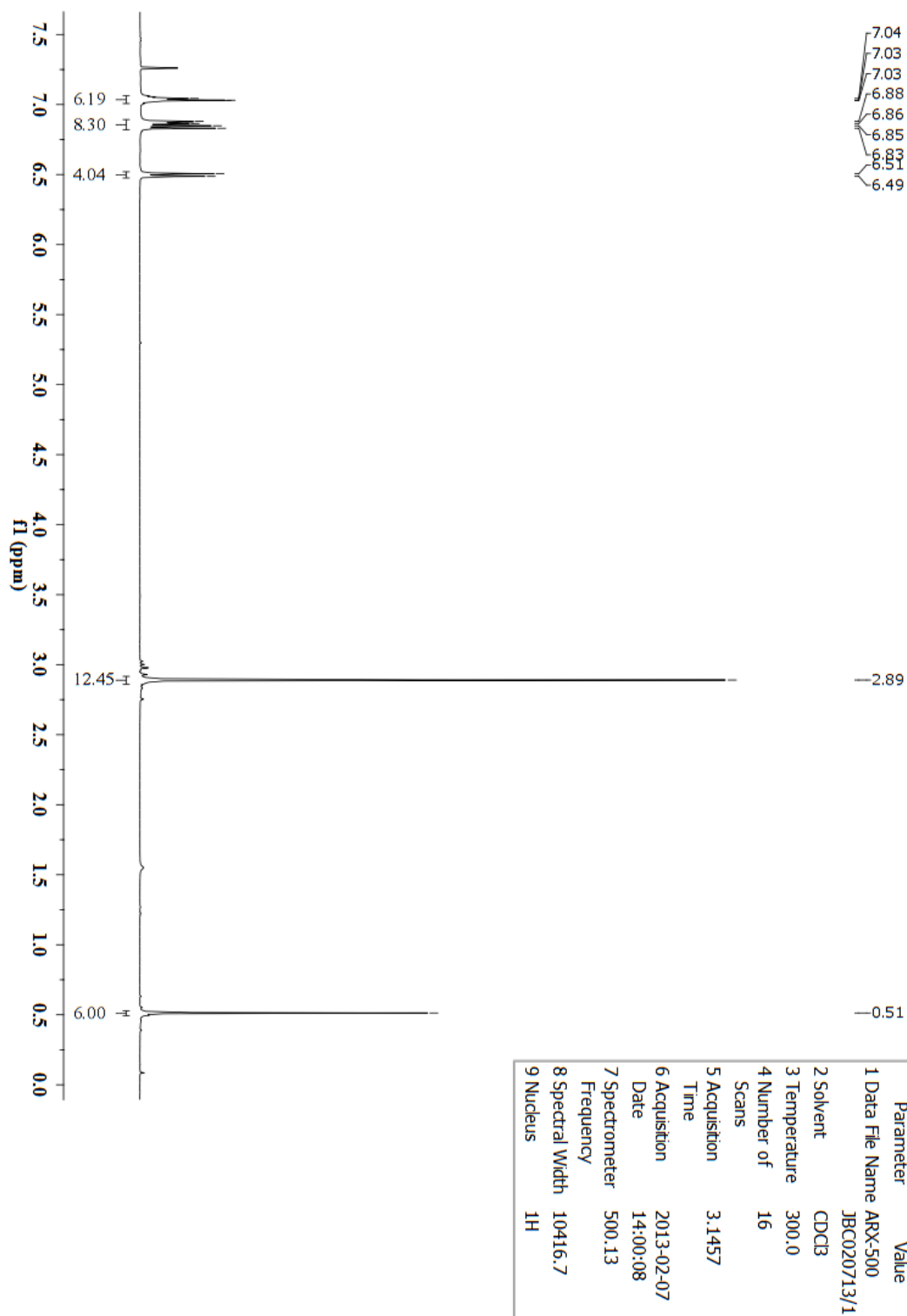


Figure A-22. ²⁹Si{¹H} NMR of **S2**.

Figure A-23. ^1H NMR of S3.

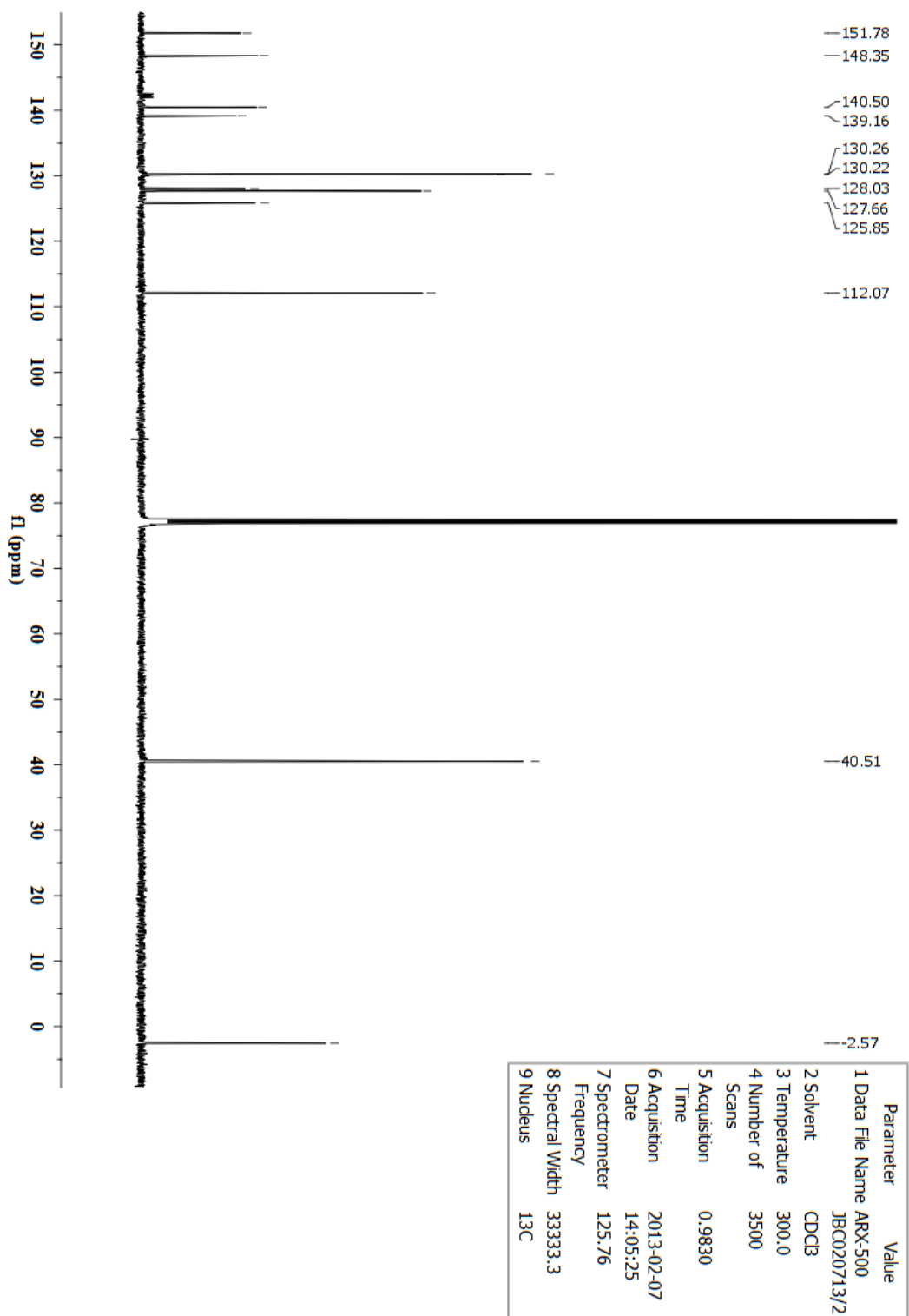
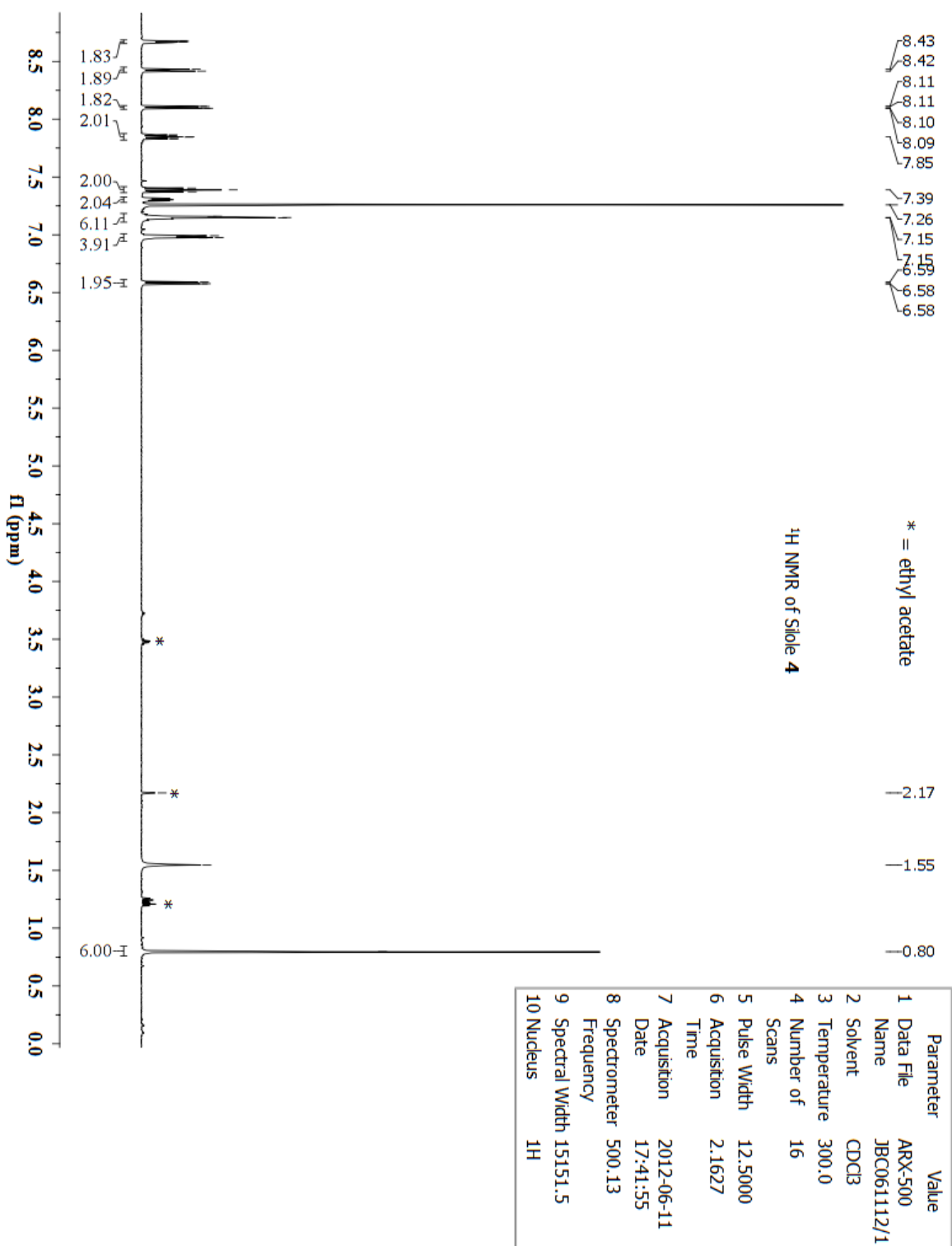


Figure A-24. $^{13}\text{C}\{^1\text{H}\}$ NMR of S3.

Figure A-25. ¹H NMR of S4.

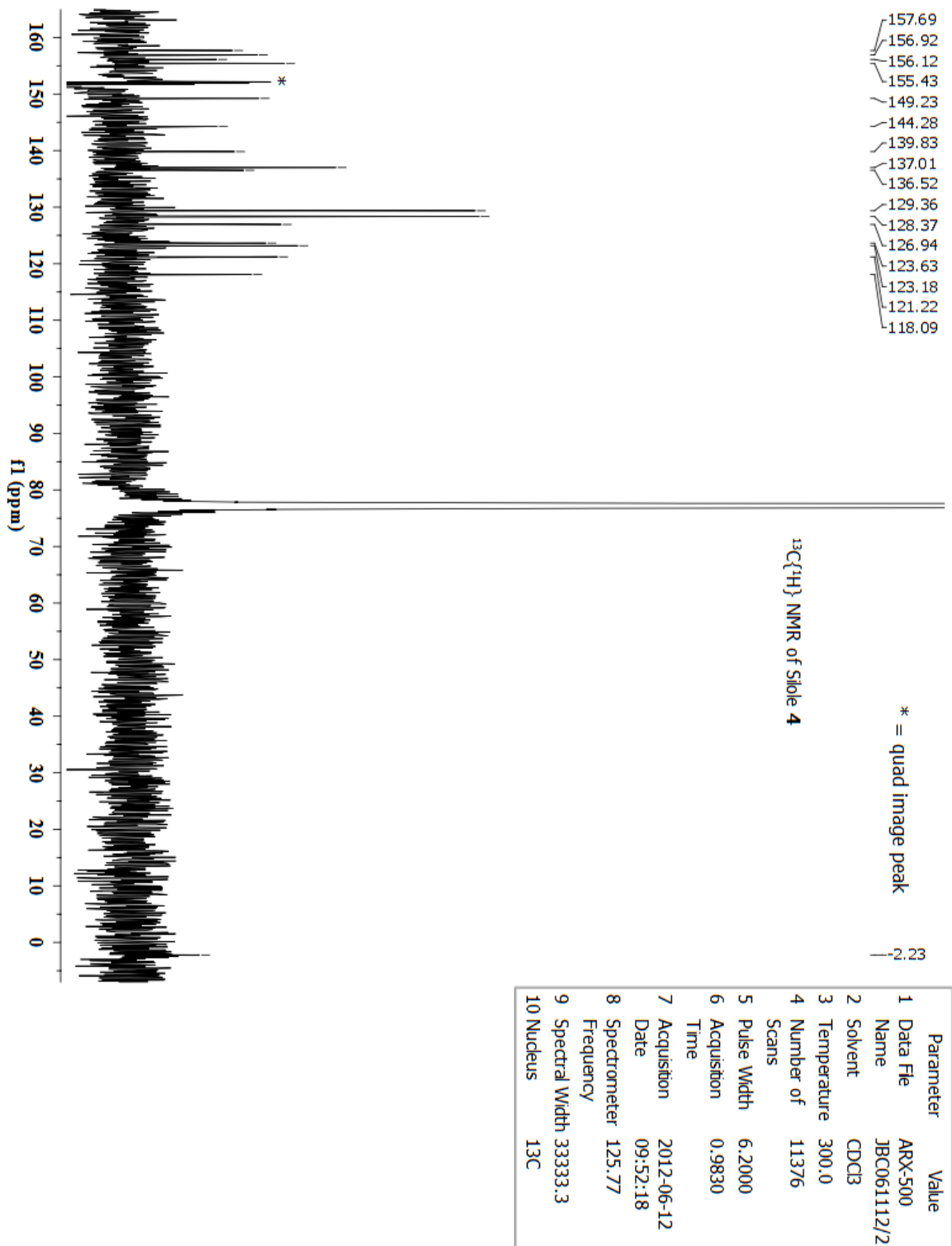
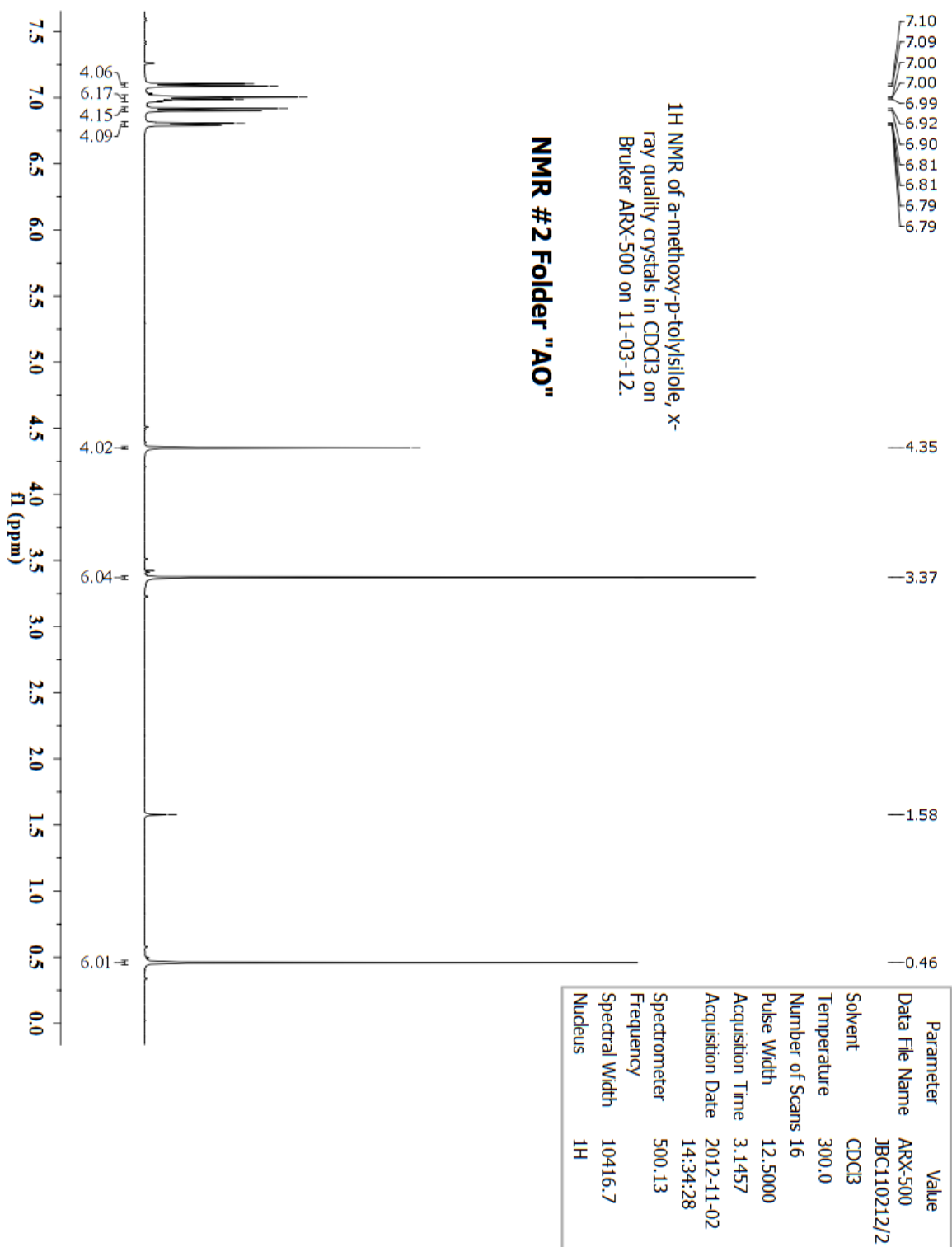


Figure A-26. $^{13}\text{C}\{^1\text{H}\}$ NMR of S4.

Figure A-27. ¹H NMR of S5.

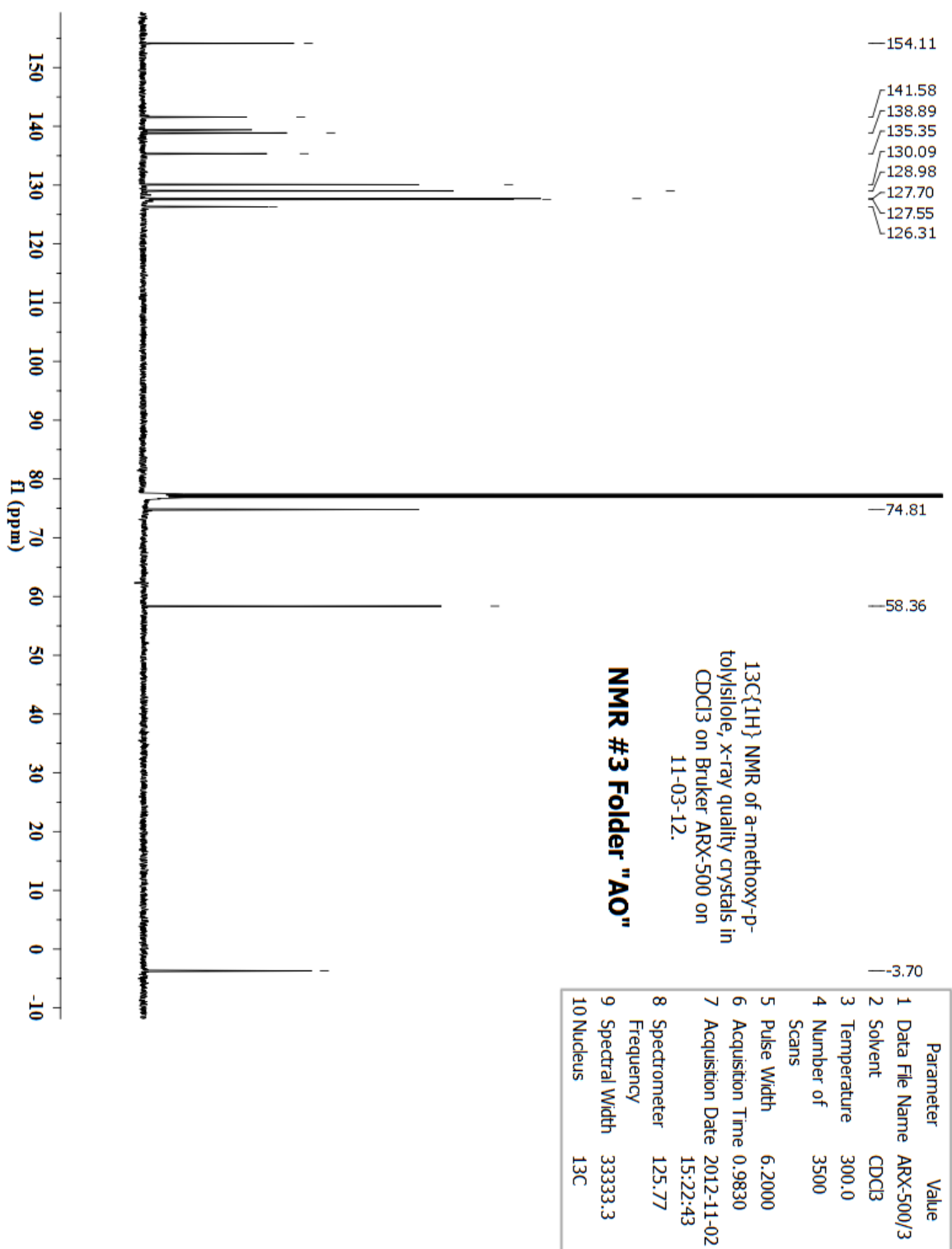


Figure A-28. $^{13}\text{C}\{^1\text{H}\}$ NMR of S5.

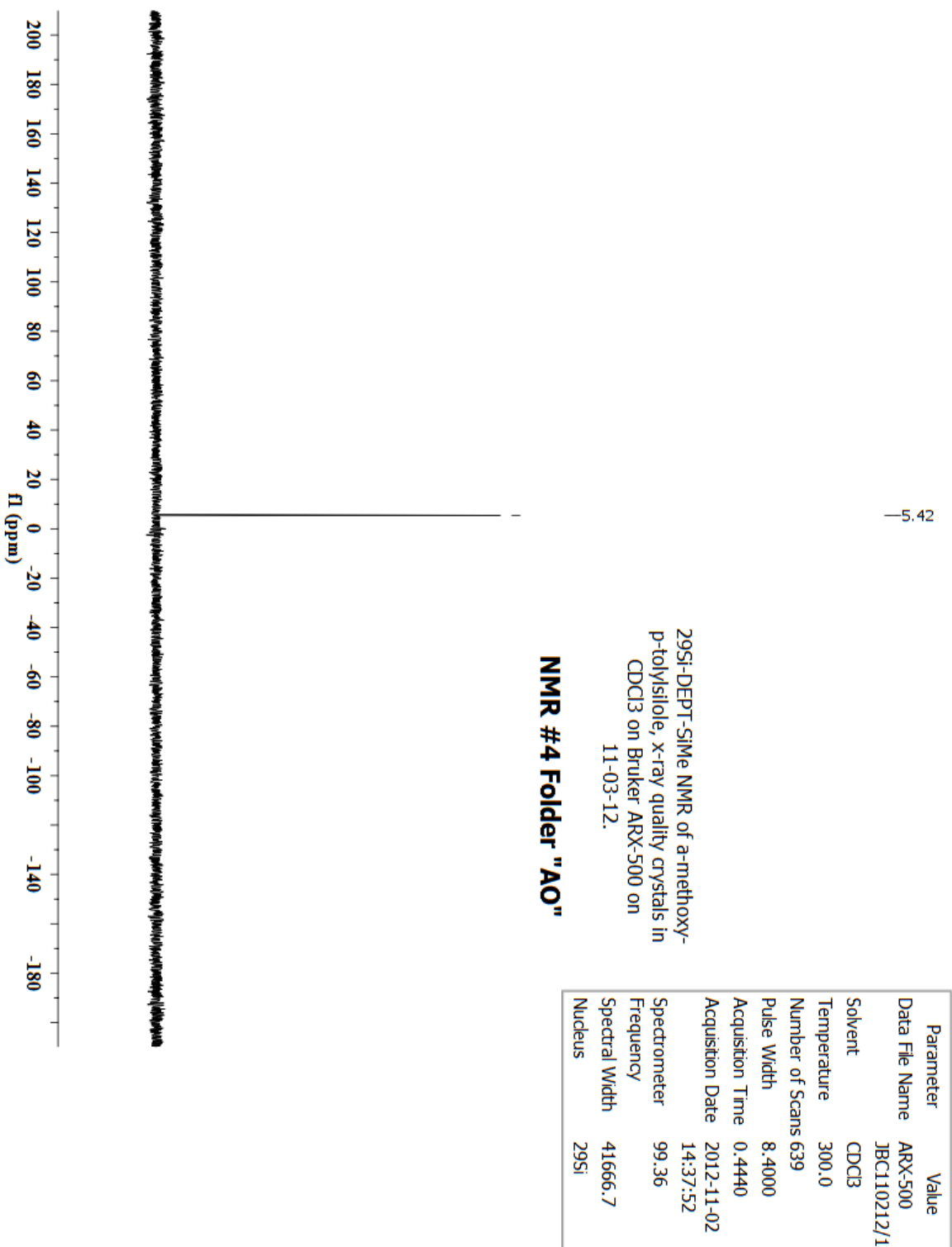
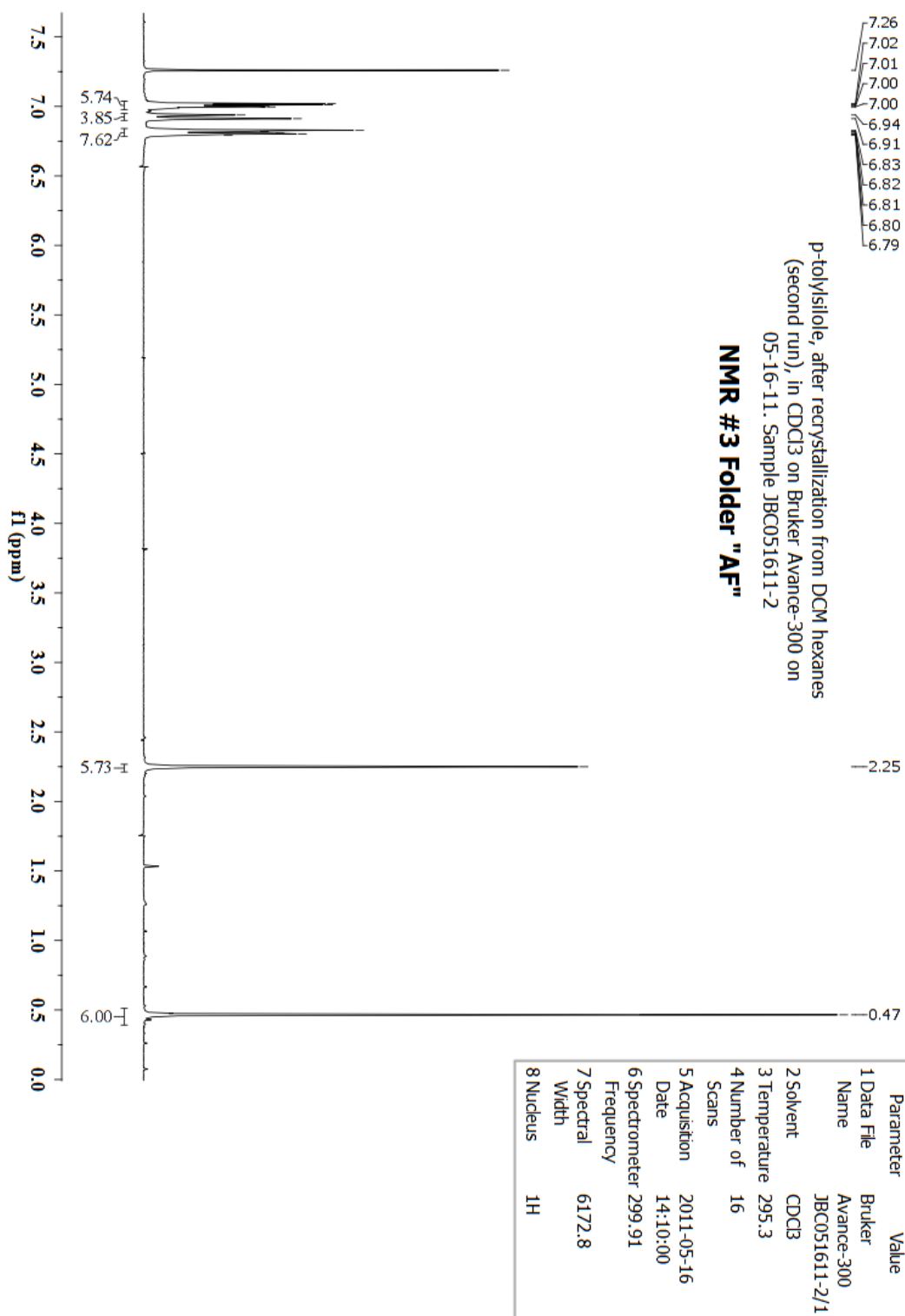


Figure A-29. $^{29}\text{Si}\{^1\text{H}\}$ NMR of S5.

Figure A-30. ¹H NMR of S6.

5.1.4. NMR spectra of unsymmetrical silole precursors.

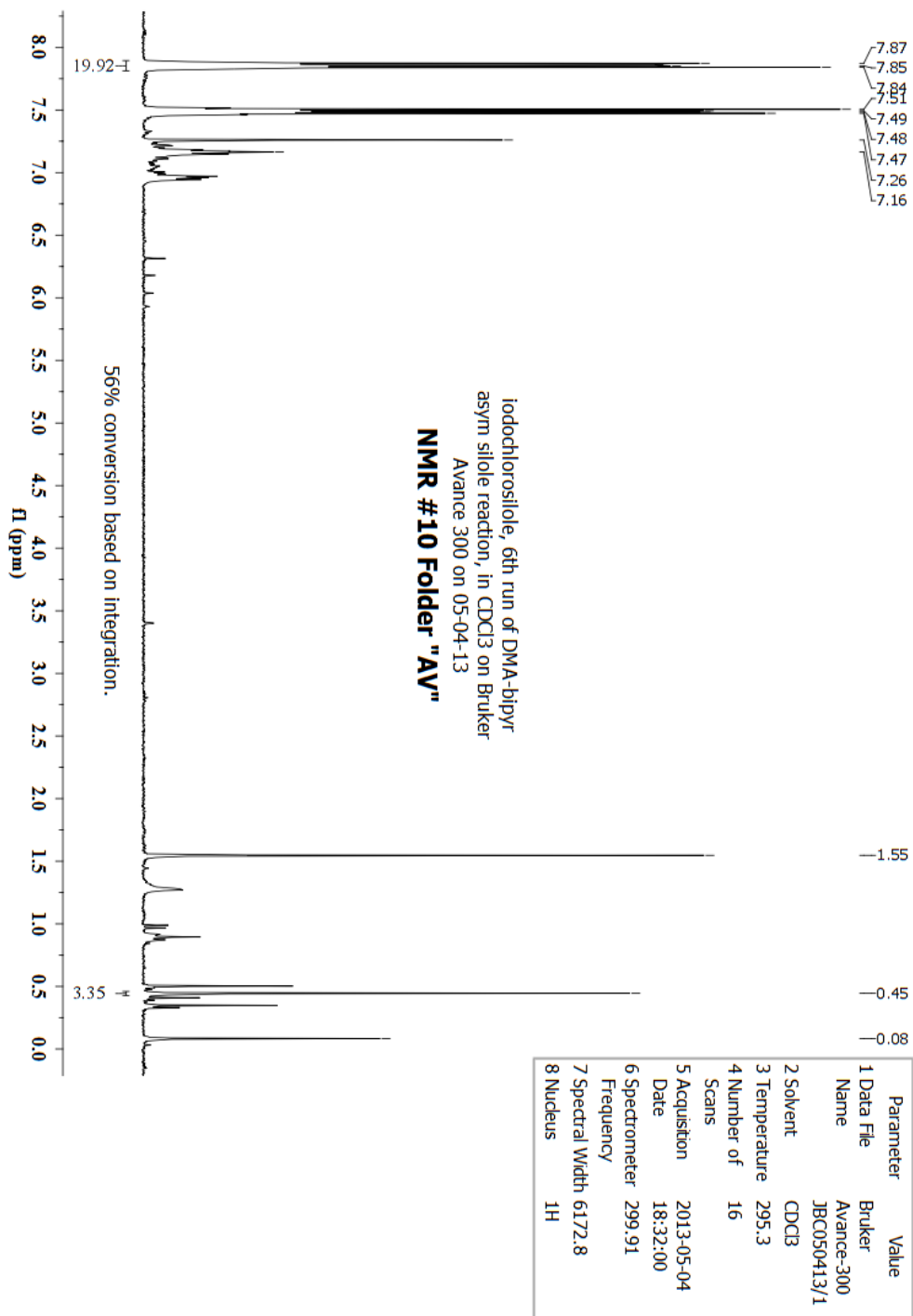


Figure A-31. ¹H NMR of the crude material of AP1.

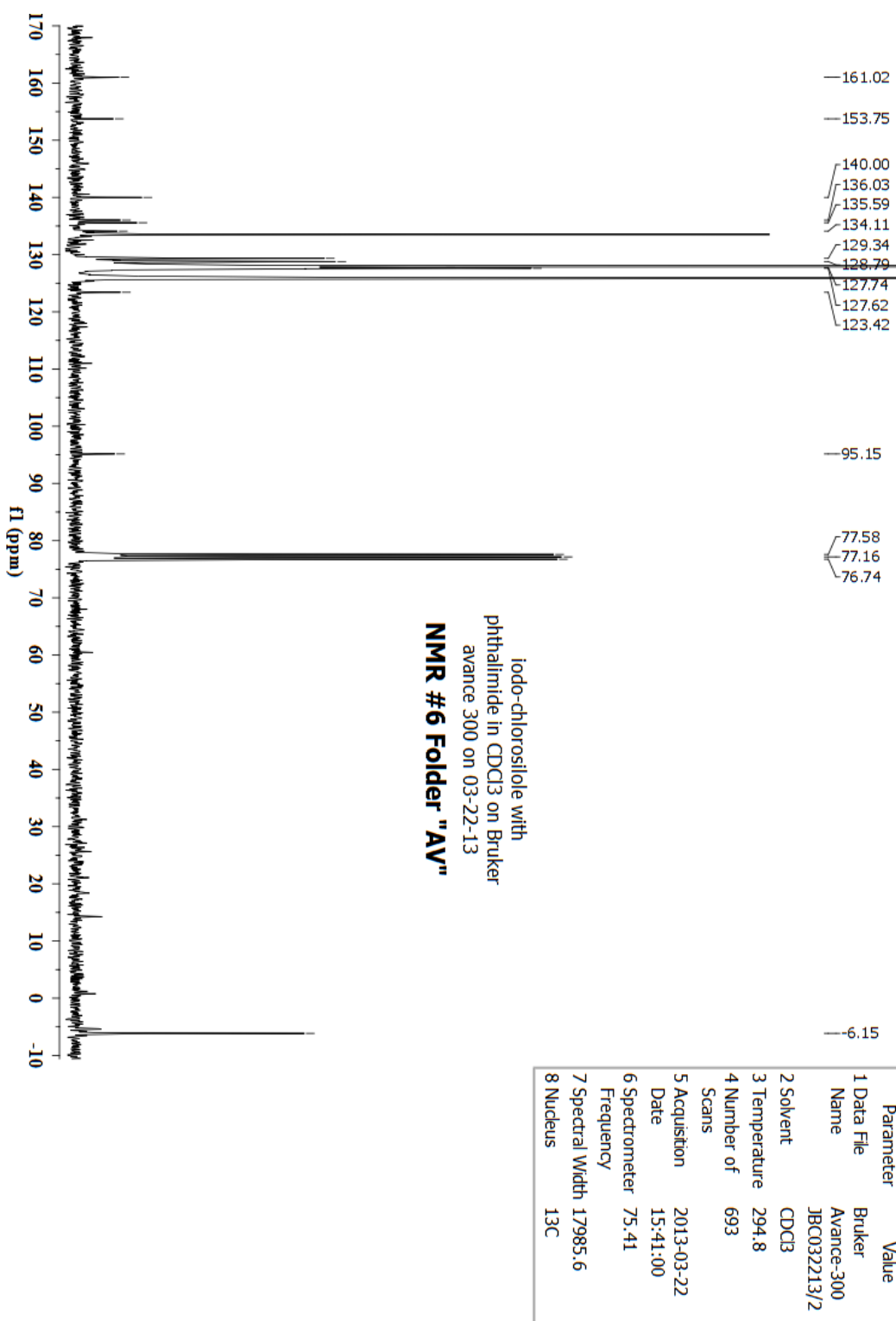


Figure A-32. ¹³C{¹H} NMR of the crude material of AP1.

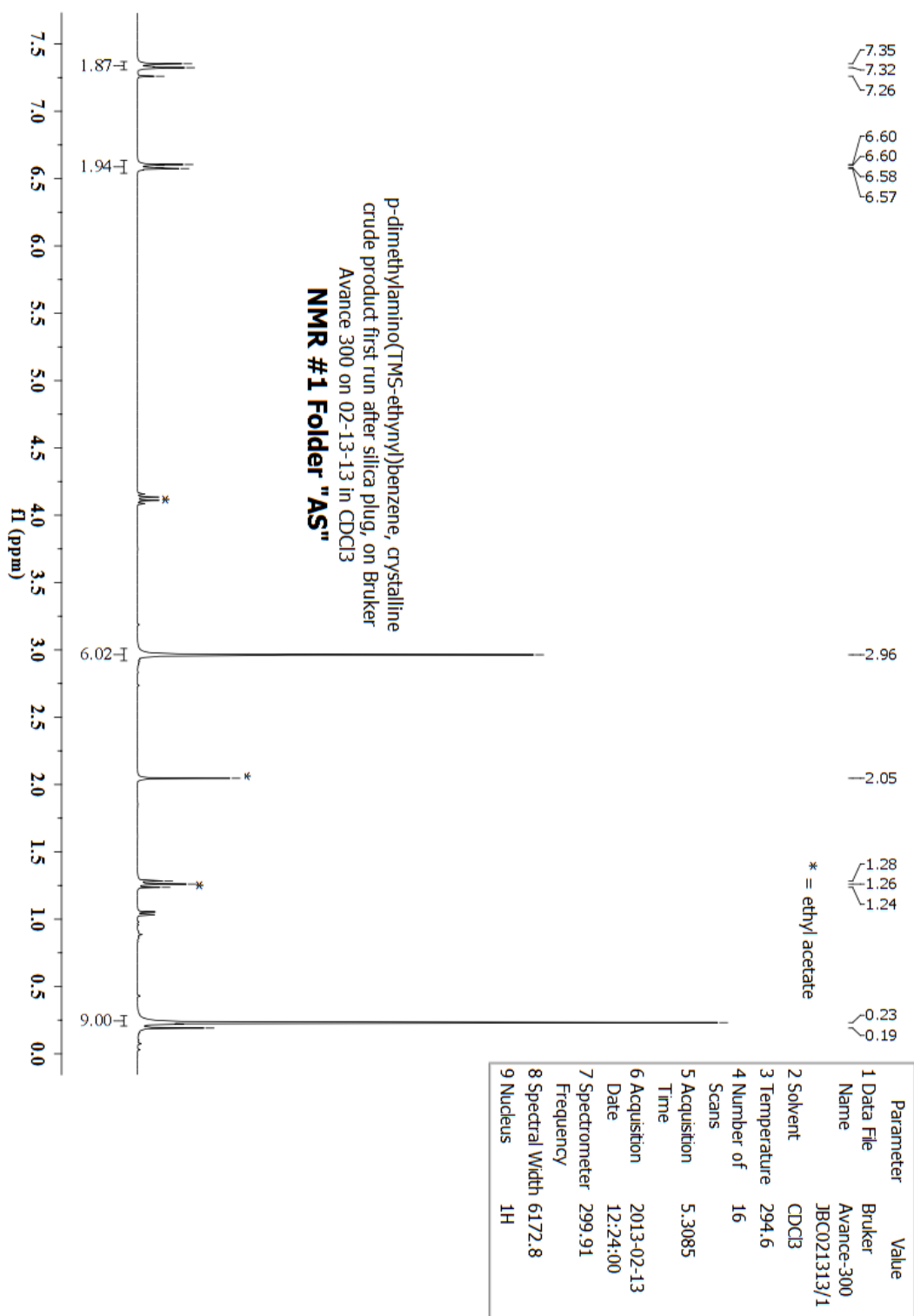


Figure A-33. ¹H NMR spectrum of the TMS-protected precursor of AP2.

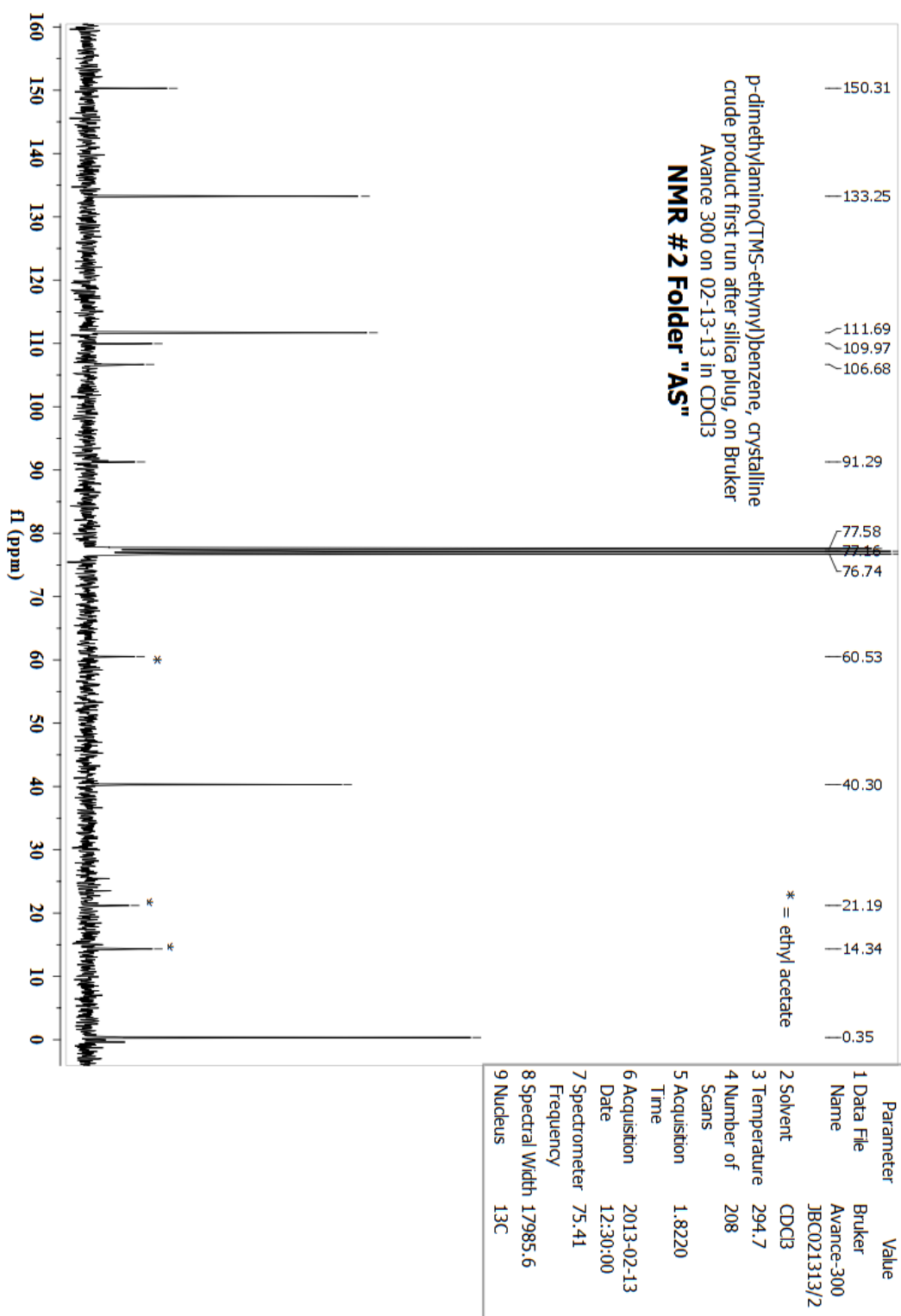


Figure A-34. ¹³C{¹H} NMR spectrum of the TMS-protected precursor of AP2.

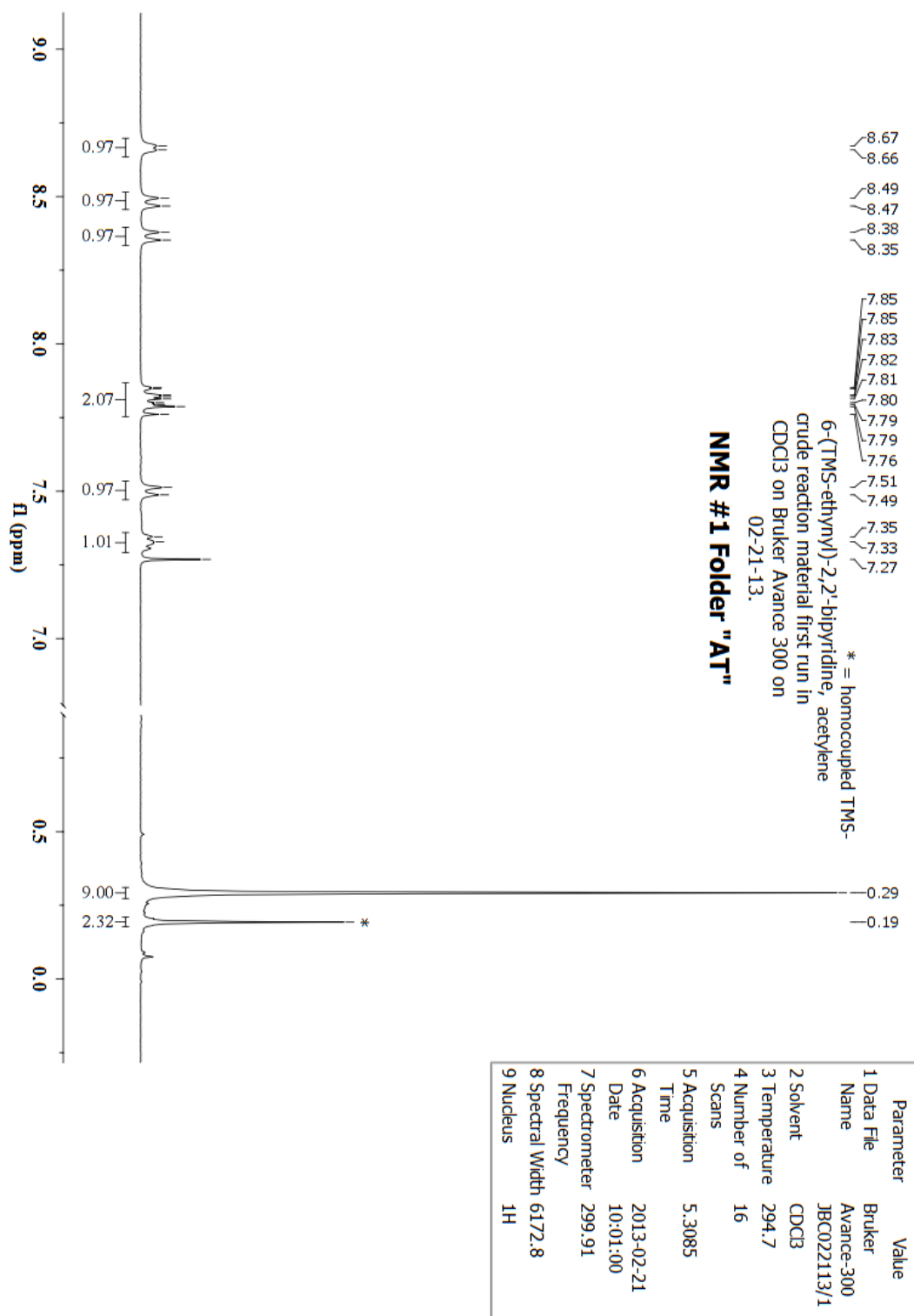


Figure A-35. ¹H NMR spectrum of the TMS-protected precursor of AP3.

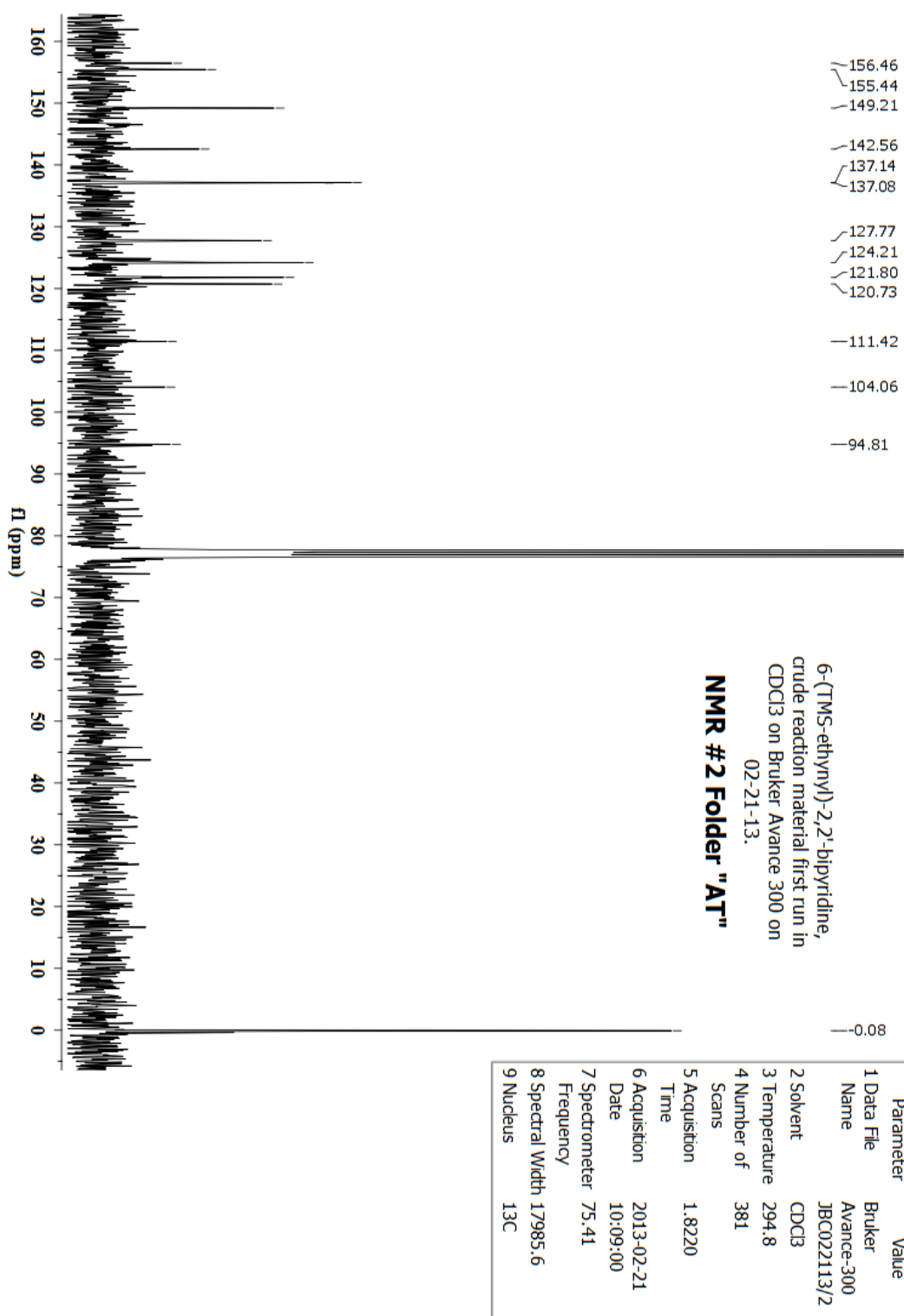


Figure A-36. $^{13}\text{C}\{^1\text{H}\}$ NMR spectrum of the TMS-protected precursor of AP3.

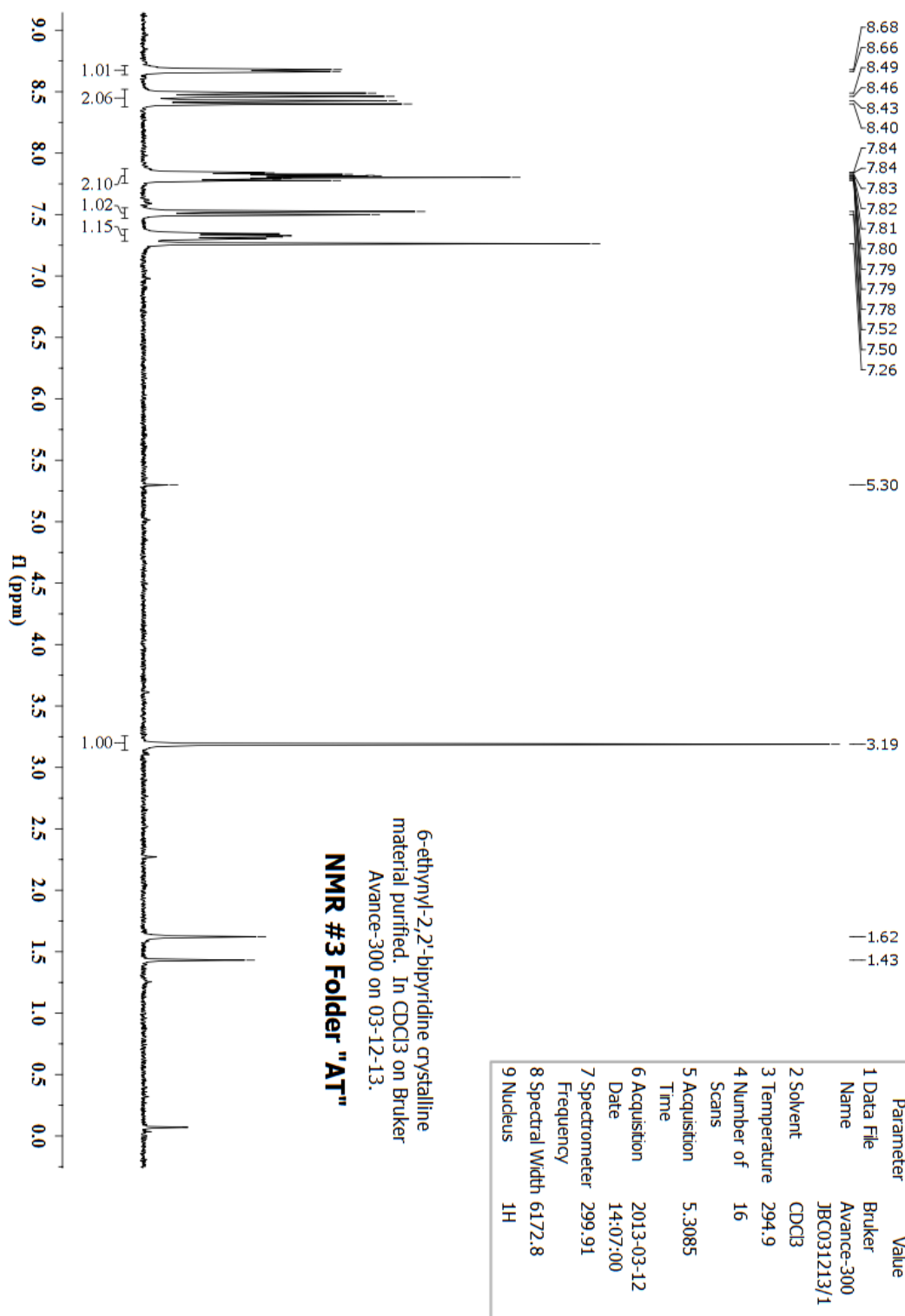
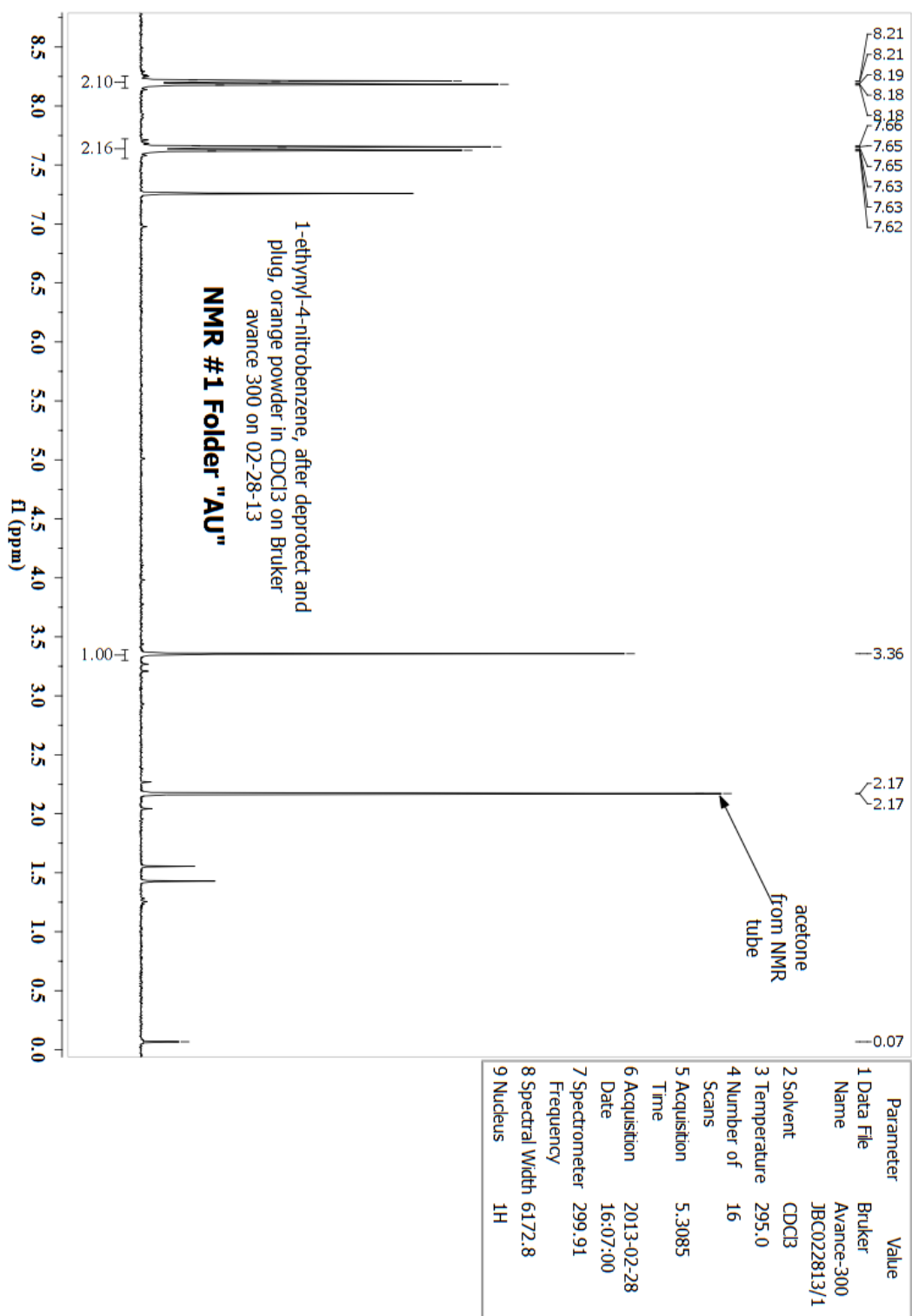


Figure A-37. ¹H NMR spectrum of AP3.

Figure A-38. ¹H NMR of AP4.

5.2. MS Spectra and Chromatograms of compounds.

5.2.1. MS of symmetrical siloles.

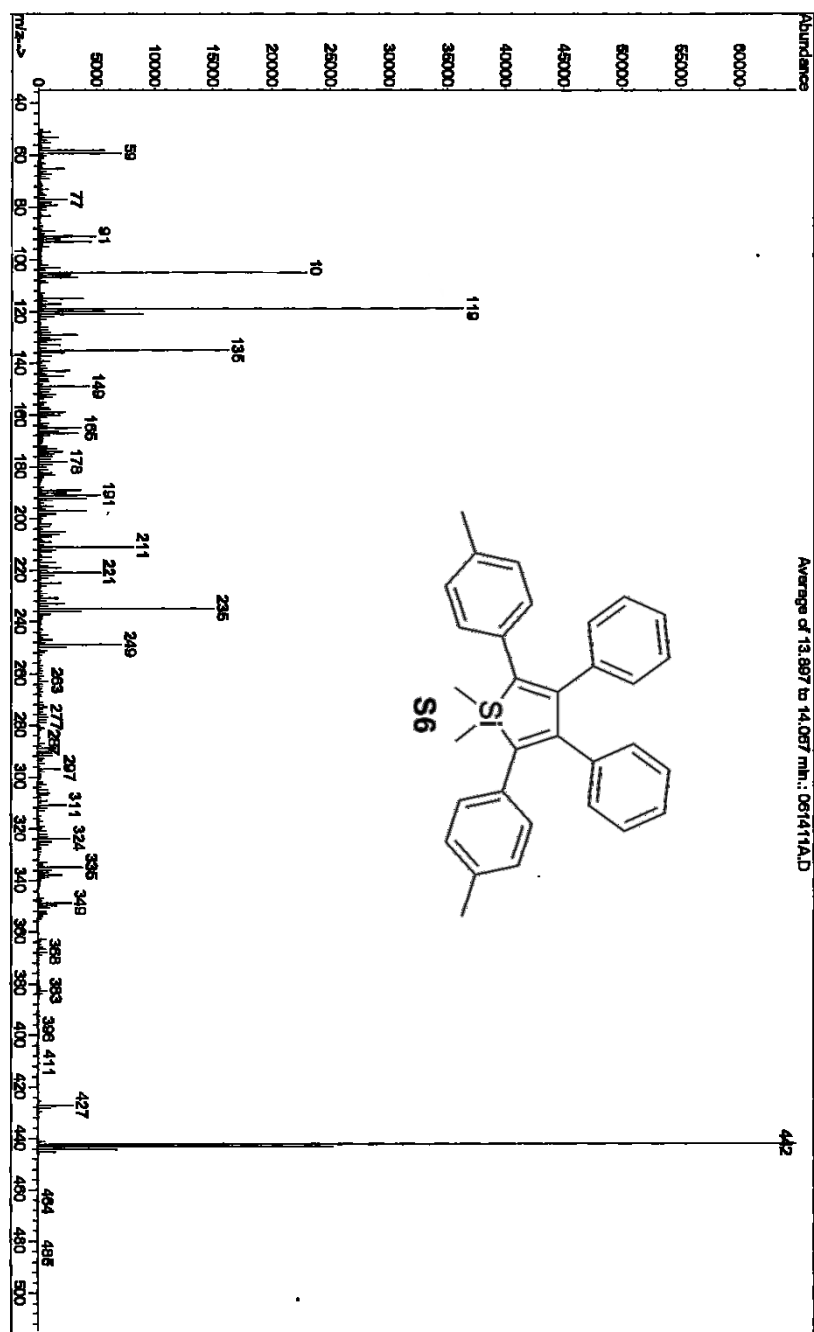


Figure A-39. MS Chromatogram of S6.

File : C:\HPCHEM\1\DATA\JB\021312.D
Operator : JB
Acquired : 13 Feb 2012 14:18 using AcqMethod JB
Instrument : CSS Instr
Sample Name : p-tolylsilole
Misc Info : using CaH2 dried THF, still gelled
Vial Number: 1

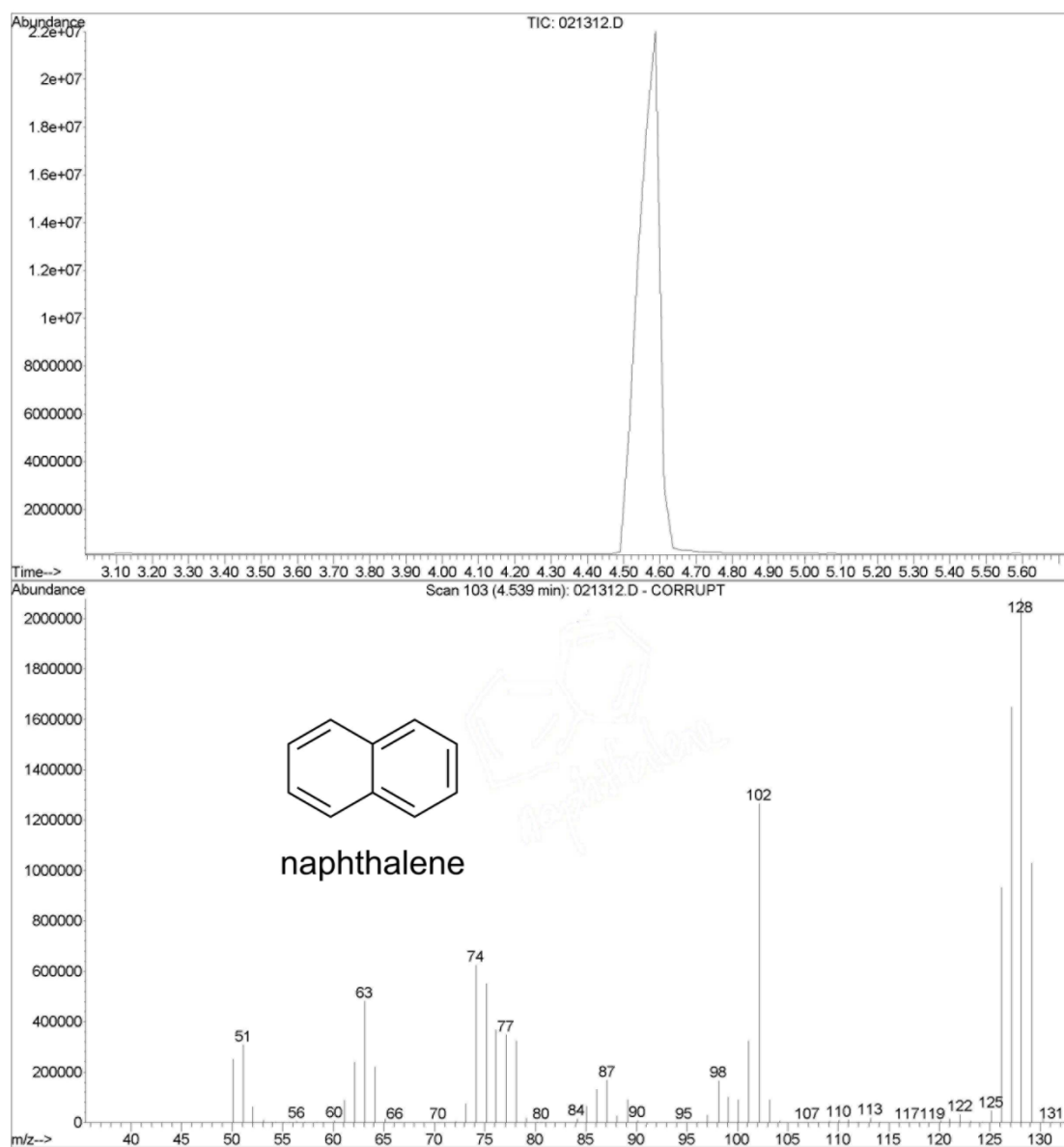


Figure A-40. A GC-MS chromatogram of the crude mixture in a reaction to synthesize **S6**; the assigned structure is inset. Retention time for the species is 4.54 min.

File : C:\HPCHEM1\DATA\JB\021312.D
Operator : JB
Acquired : 13 Feb 2012 14:18 using AcqMethod JB
Instrument : CSS Instr
Sample Name: p-tolylsilole
Misc Info : using CaH2 dried THF, still gelled
Vial Number: 1

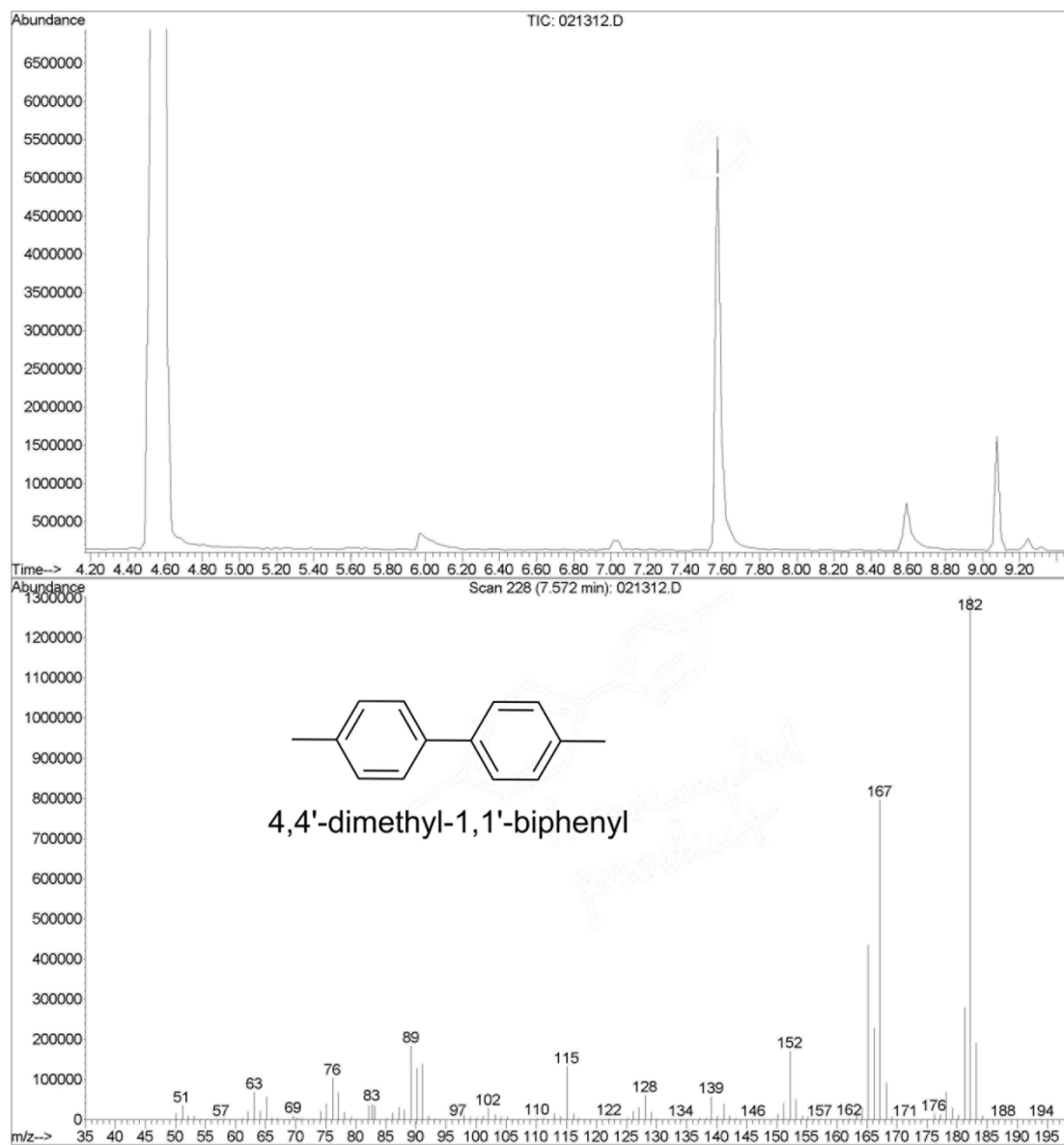


Figure A-41. A GC-MS chromatogram of the crude mixture in a reaction to synthesize **S6**; the assigned structure (“homocoupled”) is inset. Retention time for the species is 7.57 min.

File : C:\HPCHEM1\DATA\JB\021312.D
Operator : JB
Acquired : 13 Feb 2012 14:18 using AcqMethod JB
Instrument : CSS Instr
Sample Name: p-tolylsilole
Misc Info : using CaH2 dried THF, still gelled
Vial Number: 1

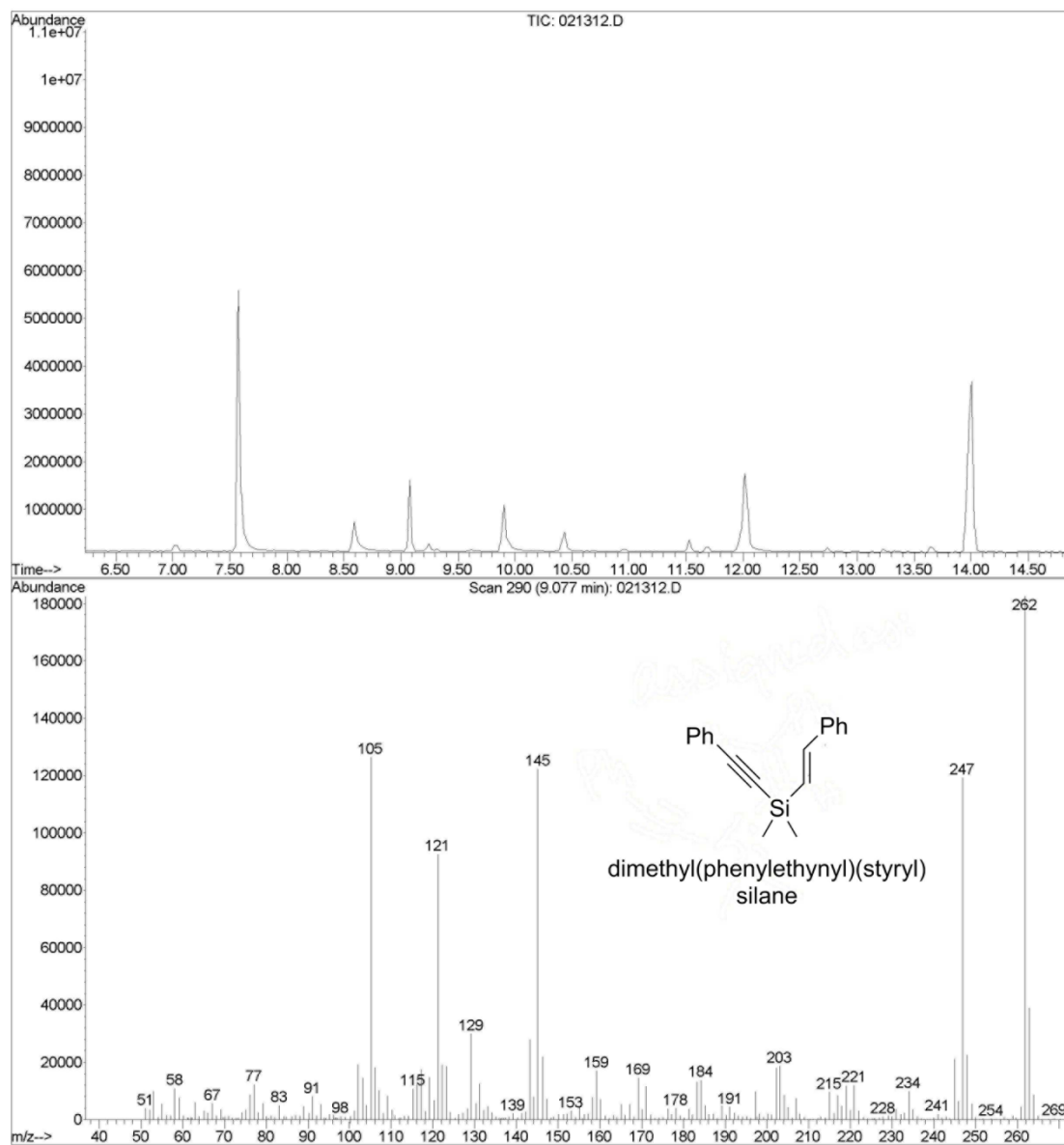


Figure A-42. A GC-MS chromatogram of the crude mixture in a reaction to synthesize **S6**; the assigned structure (“partially reduced”) is inset. Retention time for the species is 9.08 min.

File : C:\HPCHEM1\DATA\JB\021312.D
Operator : JB
Acquired : 13 Feb 2012 14:18 using AcqMethod JB
Instrument : CSS Instr
Sample Name: p-tolylsilole
Misc Info : using CaH2 dried THF, still gelled
Vial Number: 1

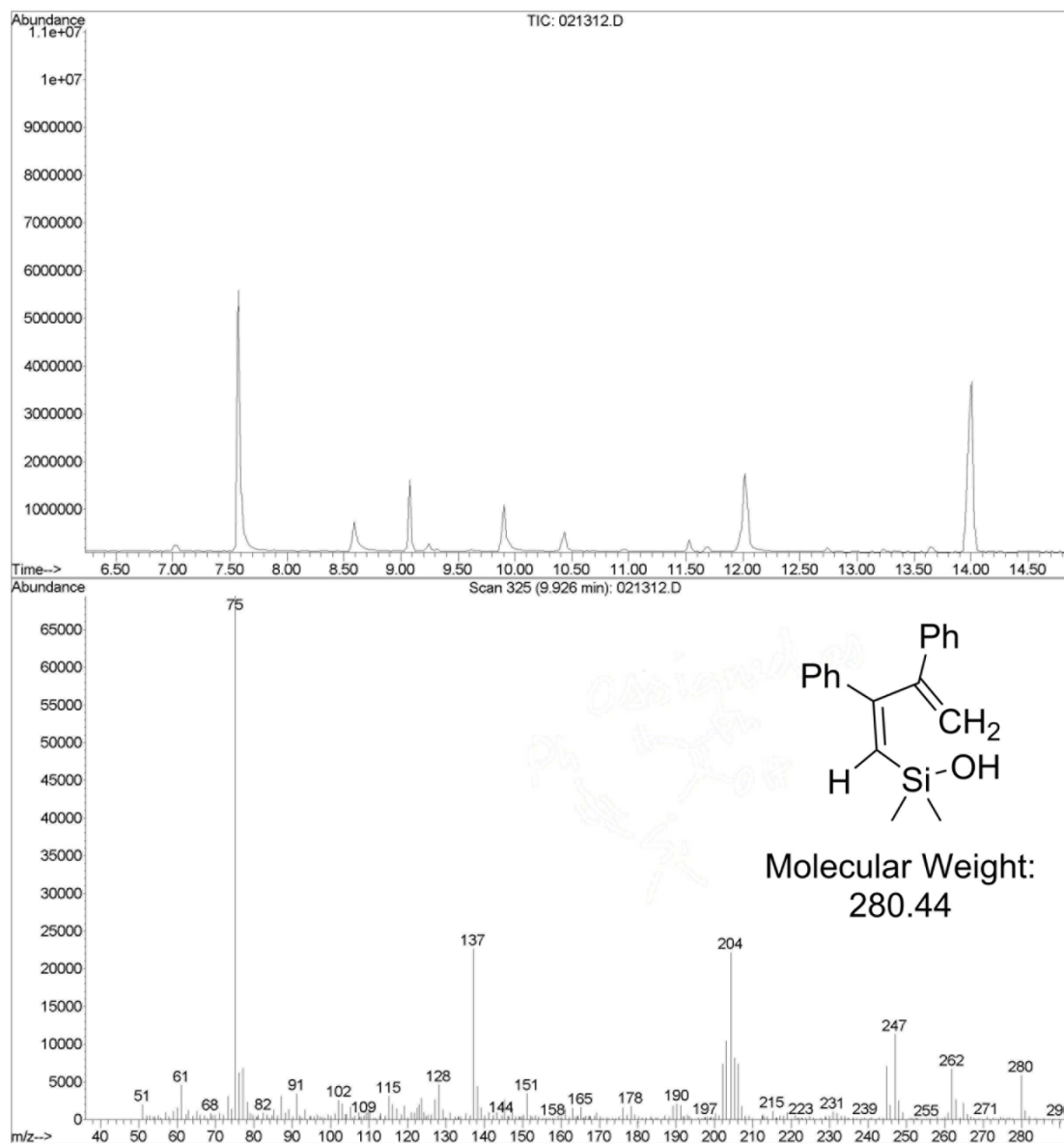


Figure A-43. A GC-MS chromatogram of the crude mixture in a reaction to synthesize **S6**; the assigned structure (“partially reduced + 18”) is inset. Retention time for the species is 9.93 min.

File : C:\HPCHEM1\DATA\JB\021312.D
Operator : JB
Acquired : 13 Feb 2012 14:18 using AcqMethod JB
Instrument : CSS Instr
Sample Name: p-tolylsilole
Misc Info : using CaH2 dried THF, still gelled
Vial Number: 1

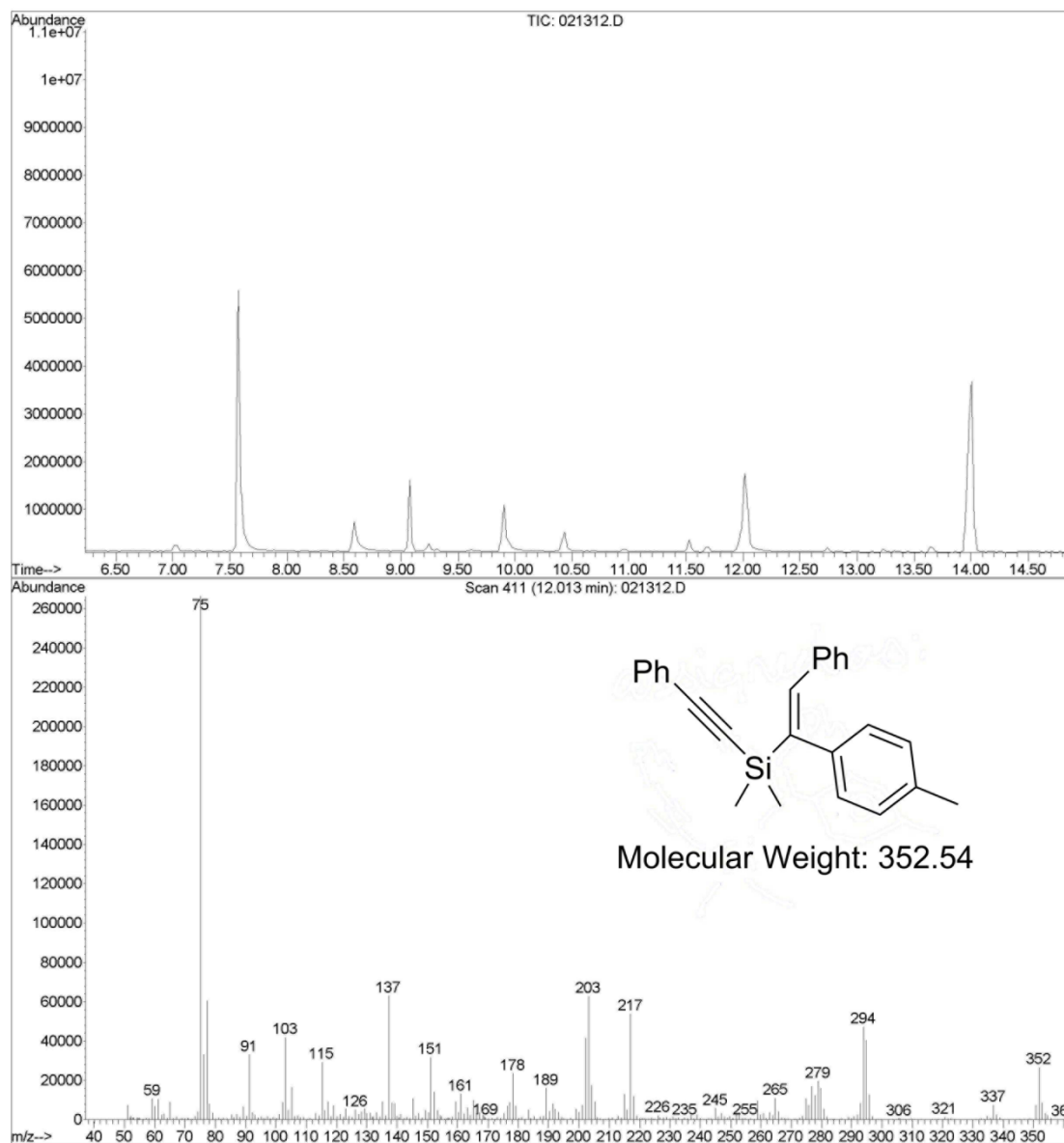


Figure A-44. A GC-MS chromatogram of the crude mixture in a reaction to synthesize **S6**; the assigned structure (“partially coupled”) is inset. Retention time for the species is 12.01 min.

File : C:\HPCHEM1\DATA\JB\021312.D
Operator : JB
Acquired : 13 Feb 2012 14:18 using AcqMethod JB
Instrument : CSS Instr
Sample Name: p-tolylsilole
Misc Info : using CaH2 dried THF, still gelled
Vial Number: 1

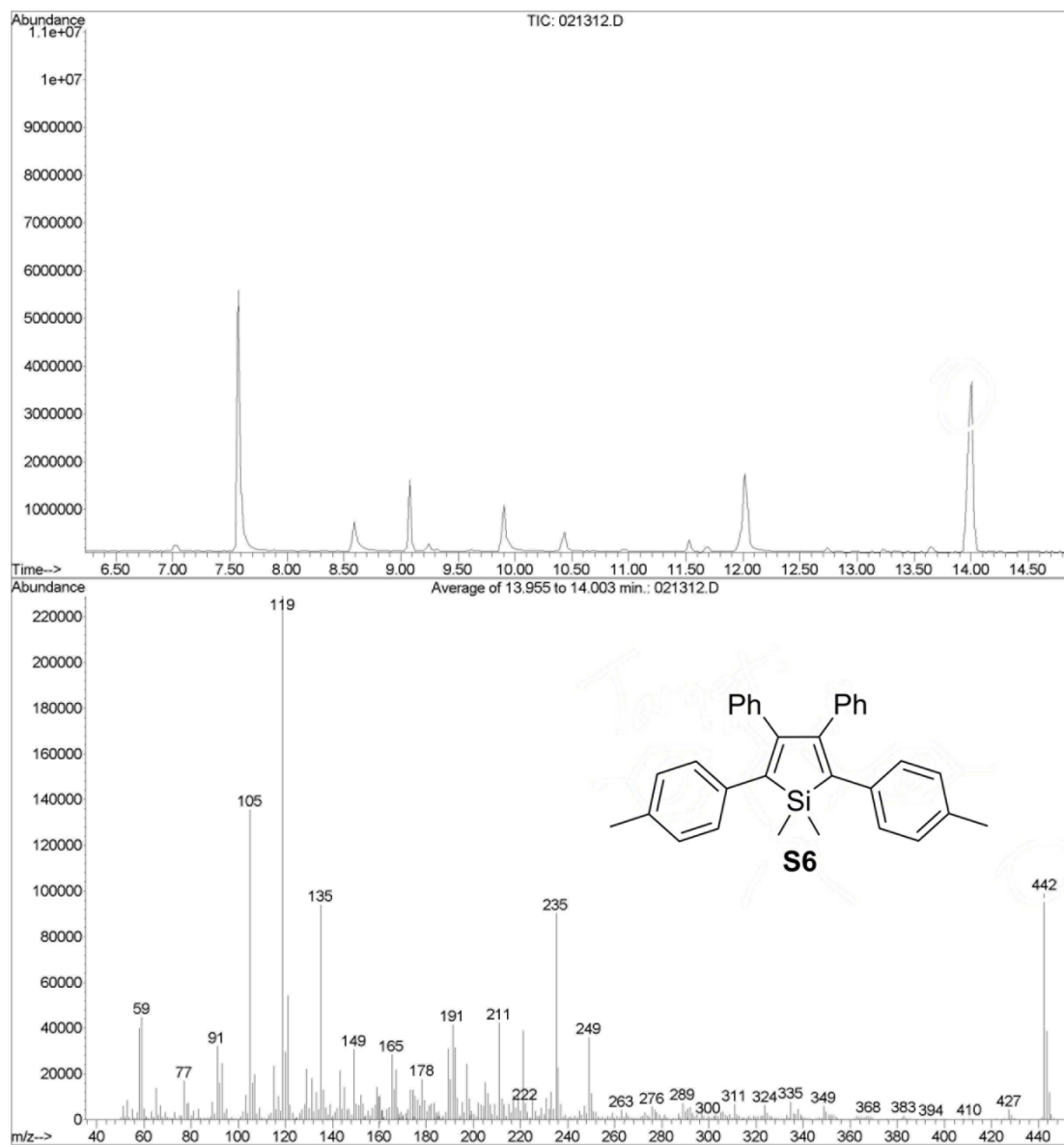


Figure A-45. A GC-MS chromatogram of the crude mixture in a reaction to synthesize **S6**; the assigned structure (target compound, **S6**) is inset. Retention time for the species is 14.00 min.

5.2.2. MS of unsymmetrical siloles and precursors.

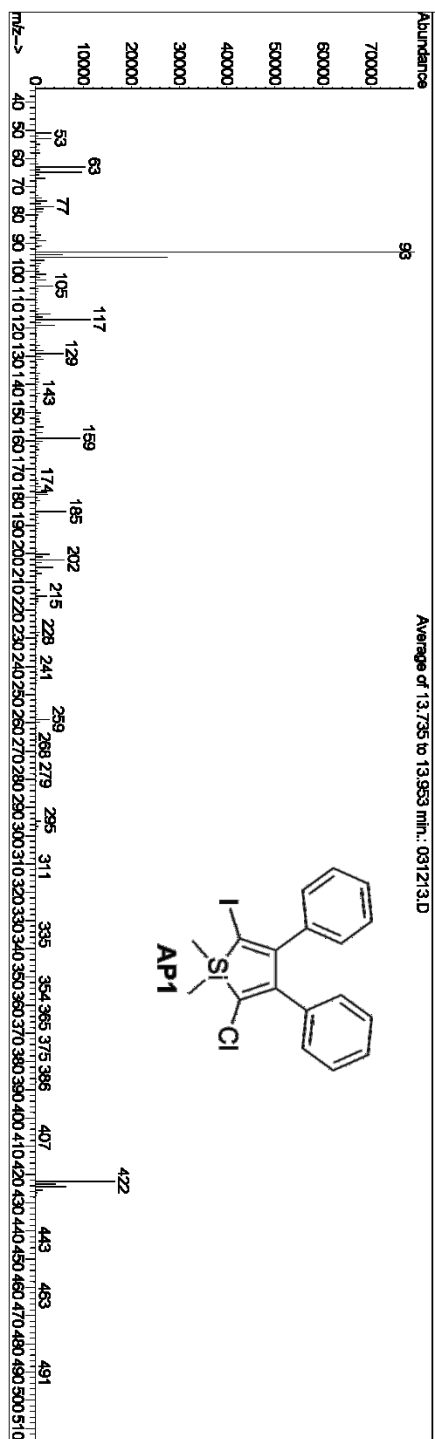


Figure A-46. MS Chromatogram of AP1.

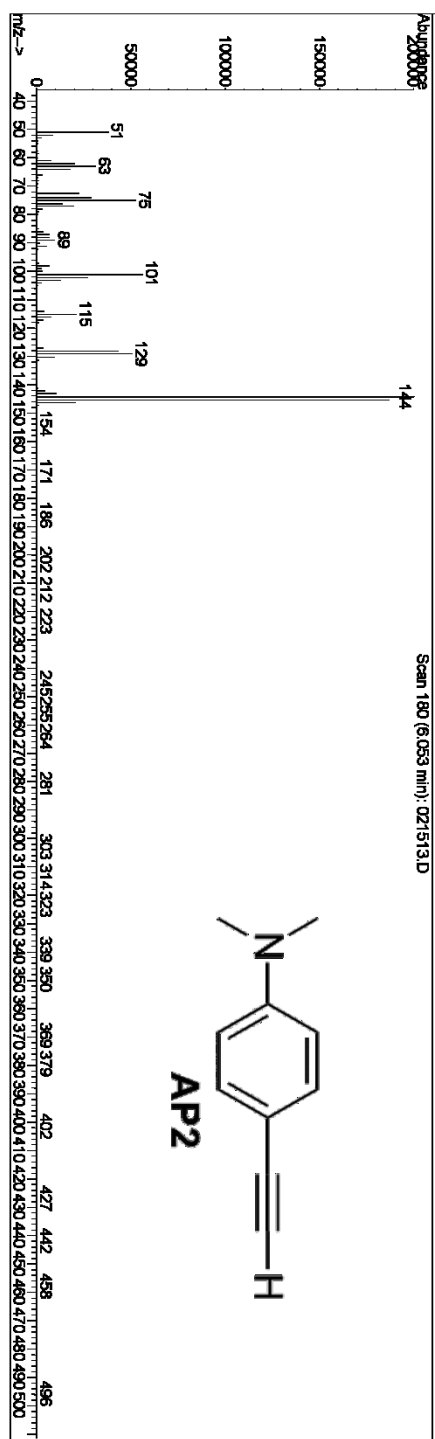


Figure A-47. MS Chromatogram for TMS-protected precursor of AP2.



Figure A-48. MS Chromatogram of AP2.

5.3. X-ray crystal structures of compounds.

5.3.1. X-ray crystallography of 2,3,4,5-tetraphenyl-1,1-disubstituted-germoles.

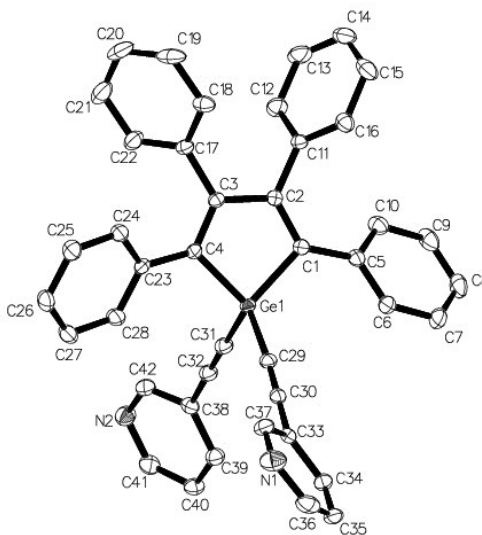


Figure A-49. Molecular structure of **G2** (with ellipsoids shown at the 50% probability level).

Hydrogen atoms have been removed for clarity. Selected bond distances (Å), angles (deg), and torsions (deg): Ge1–C1 = 1.940(1), Ge1–C4 = 1.930(2), C4–C3 = 1.361(2), C3–C2 = 1.507(2), Ge1–C31 = 1.904(1), Ge1–C29 = 1.892(2), C31–C32 = 1.202(2), C29–C30 = 1.203(2); C1–Ge1–C4 = 91.50(6), C29–Ge1–C31 = 105.54(6), Ge1–C1–C2 = 106.1(1), Ge1–C4–C3 = 106.5(1); Ge1–C4–C23–C28 = -30.4(2), Ge1–C1–C5–C6 = -39.0(2), C1–C2–C11–C16 = -67.2(2), C4–C3–C17–C22 = -56.6(2).

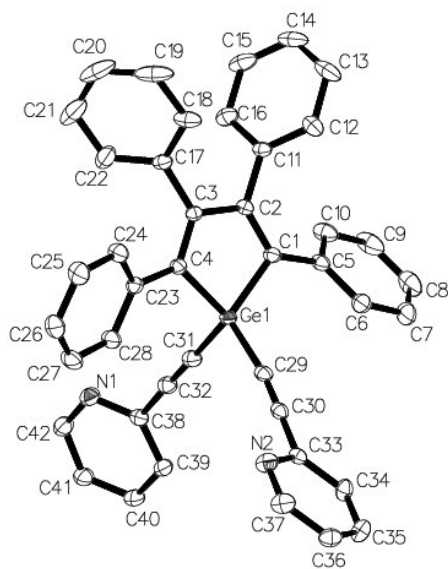


Figure A-50. Molecular structure of **G3** (with ellipsoids shown at the 50% probability level).

Hydrogen atoms have been removed for clarity. Selected bond distances (Å), angles (deg), and torsions (deg): Ge1–C1 = 1.9318(9), Ge1–C4 = 1.926(1), C4–C3 = 1.355(1), C3–C2 = 1.355(1), Ge1–C31 = 1.9003(9), Ge1–C29 = 1.895(1), C31–C32 = 1.198(1), C29–C30 = 1.188(1); C1–Ge1–C4 = 91.57(4), C29–Ge1–C31 = 104.95(4), Ge1–C1–C2 = 106.33(6), Ge1–C4–C3 = 106.37(7); Ge1–C4–C23–C28 = -27.4(1), Ge1–C1–C5–C6 = -46.6(1), C1–C2–C11–C16 = -67.0(1), C4–C3–C17–C22 = -59.0(1).

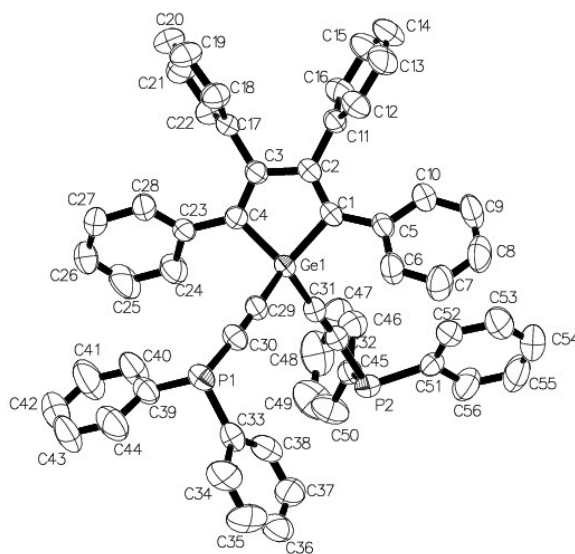


Figure A-51. Molecular structure of **G4** (with ellipsoids shown at the 50% probability level).

Hydrogen atoms and disorder at one diphenylphosphine moiety have been removed for clarity. Selected bond distances (Å), angles (deg), and torsions (deg): Ge1–C1 = 1.940(3), Ge1–C4 = 1.929(3), C4–C3 = 1.349(4), C3–C2 = 1.517(4), Ge1–C31 = 1.897(3), Ge1–C29 = 1.904(3), C31–C32 = 1.202(4), C29–C30 = 1.194(4); C1–Ge1–C4 = 91.48(12), C29–Ge1–C31 = 105.52(12), Ge1–C1–C2 = 106.5(2), Ge1–C4–C3 = 106.52(2); Ge1–C4–C23–C24 = -48.6(6), Ge1–C1–C5–C6 = -35.7(3), C1–C2–C11–C12 = -56.7(2), C4–C3–C17–C22 = -63.4(3).

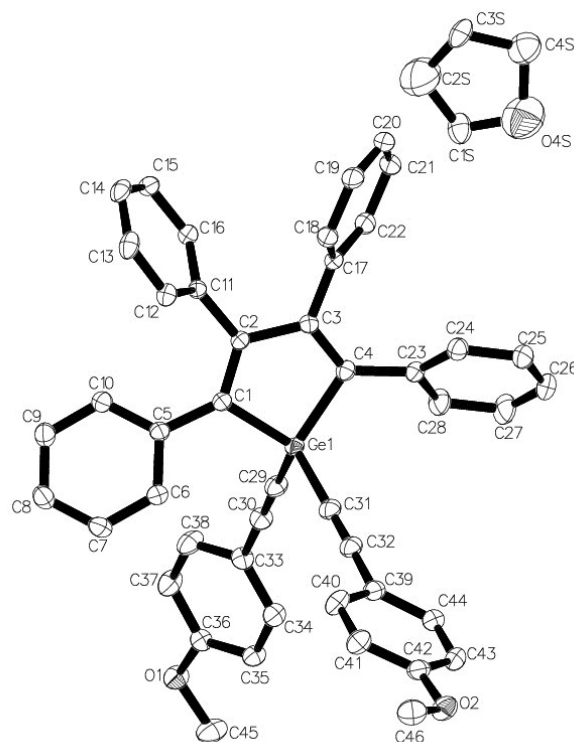


Figure A-52. Molecular structure of **G6** (with ellipsoids shown at the 50% probability level).

Hydrogen atoms and disordered atoms about the THF molecule have been removed for clarity. Selected bond distances (Å), angles (deg), and torsions (deg): Ge1–C1 = 1.941(2), Ge1–C4 = 1.932(2), C4–C3 = 1.362(3), C3–C2 = 1.519(3), Ge1–C31 = 1.892(2), Ge1–C29 = 1.890(2), C31–C32 = 1.208(3), C29–C30 = 1.210(3); C1–Ge1–C4 = 91.31(9), C29–Ge1–C31 = 106.9(1), Ge1–C1–C2 = 106.9(1), Ge1–C4–C3 = 107.0(1), C36–O1–C45 = 118.2(2), C42–O2–C46 = 116.7(2); Ge1–C4–C23–C28 = 51.8(3), Ge1–C1–C5–C6 = 39.2(3), C1–C2–C11–C12 = 57.4(3), C4–C3–C17–C22 = 54.8(3).

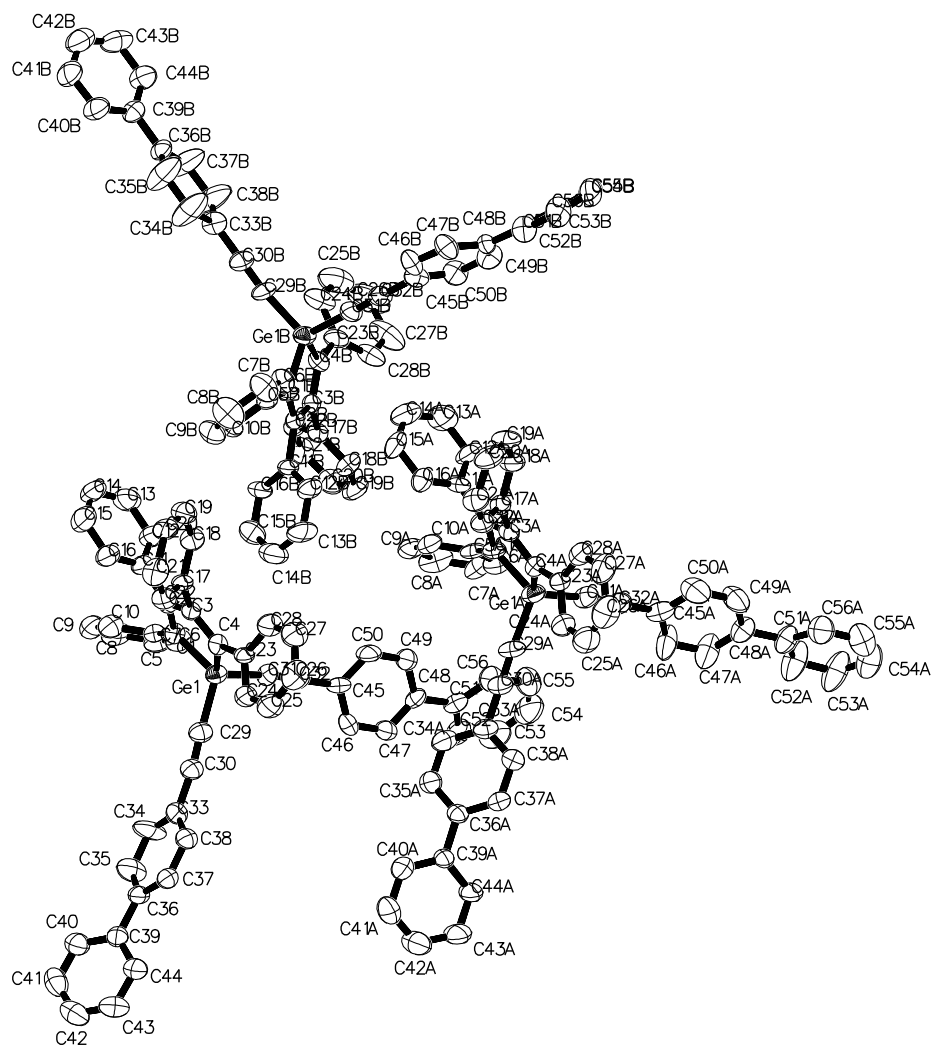


Figure A-53. Molecular structure of **G7** (with ellipsoids shown at the 50% probability level).

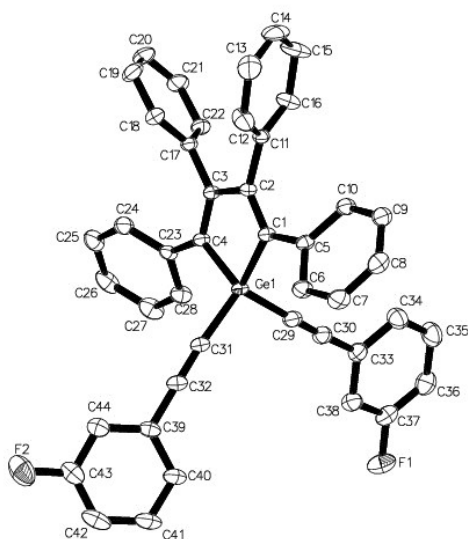


Figure A-54. Molecular structure of **G8** (with ellipsoids shown at the 50% probability level).

Hydrogen atoms have been removed for clarity. Selected bond distances (Å), angles (deg), and torsions (deg): Ge1–C1 = 2.071(2), Ge1–C4 = 1.952(2), C4–C3 = 1.430(2), C3–C2 = 1.589(2), Ge1–C31 = 1.919(2), Ge1–C29 = 1.891(2), C31–C32 = 1.229(2), C29–C30 = 1.220(3); C1–Ge1–C4 = 93.78(6), C29–Ge1–C31 = 104.85(7), Ge1–C1–C2 = 105.3(1), Ge1–C4–C3 = 103.1(1); Ge1–C4–C23–C28 = -30.2(2), Ge1–C1–C5–C6 = -35.8(2), C1–C2–C11–C12 = -71.3(2), C4–C3–C17–C22 = -61.1(2).

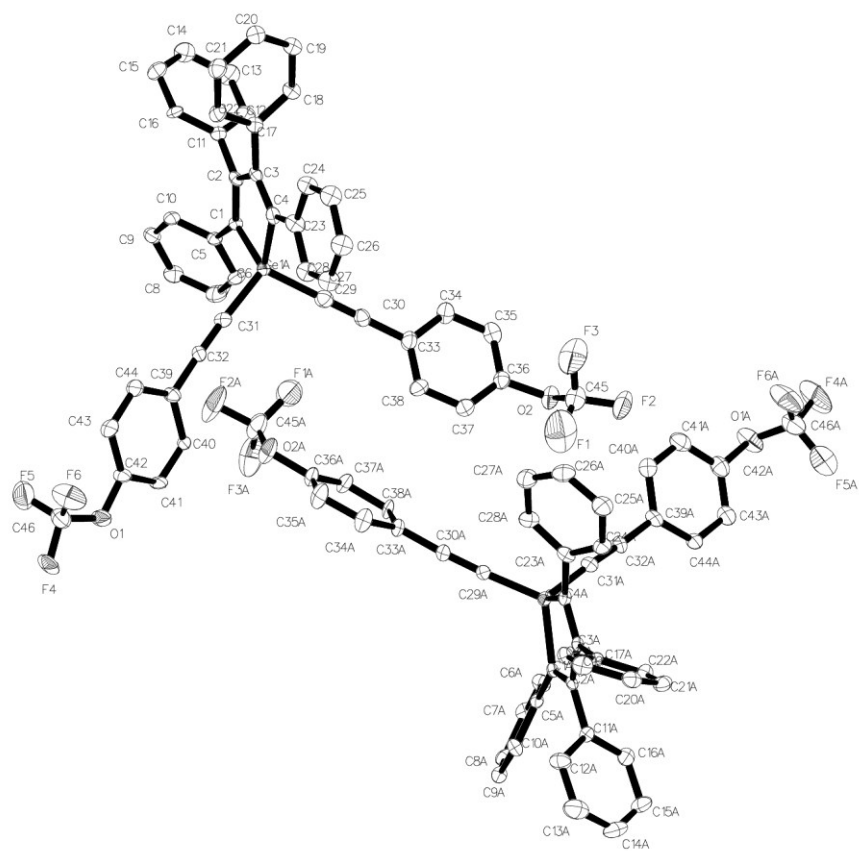


Figure A-55. Molecular structure of **G9** (with ellipsoids shown at the 50% probability level).

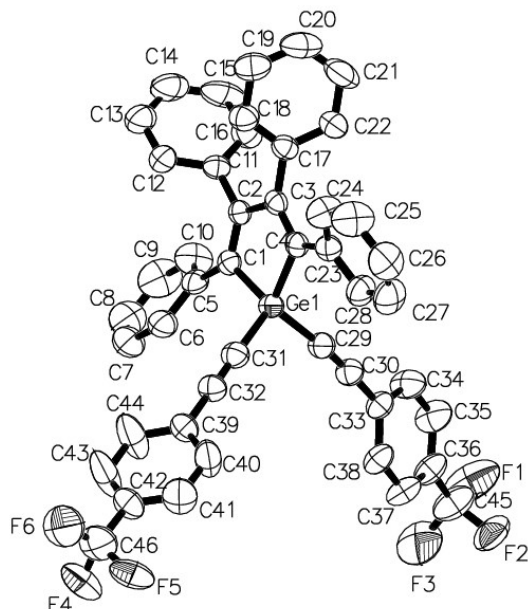


Figure A-56. Molecular structure of **G10** (with ellipsoids shown at the 50% probability level).

Hydrogen atoms and disorder at $-\text{CF}_3$ groups have been removed for clarity.

Selected bond distances (\AA), angles (deg), and torsions (deg): $\text{Ge1}-\text{C1} = 1.945(3)$, $\text{Ge1}-\text{C4} = 1.944(3)$, $\text{C4}-\text{C3} = 1.354(5)$, $\text{C3}-\text{C2} = 1.520(5)$, $\text{Ge1}-\text{C31} = 1.898(4)$, $\text{Ge1}-\text{C29} = 1.898(4)$, $\text{C31}-\text{C32} = 1.198(6)$, $\text{C29}-\text{C30} = 1.199(6)$; $\text{C1}-\text{Ge1}-\text{C4} = 91.2(1)$, $\text{C29}-\text{Ge1}-\text{C31} = 105.4(2)$, $\text{Ge1}-\text{C1}-\text{C2} = 106.6(2)$, $\text{Ge1}-\text{C4}-\text{C3} = 106.7(2)$; $\text{Ge1}-\text{C4}-\text{C23}-\text{C28} = 29.7(5)$, $\text{Ge1}-\text{C1}-\text{C5}-\text{C6} = 45.0(5)$, $\text{C1}-\text{C2}-\text{C11}-\text{C12} = 64.4(5)$, $\text{C4}-\text{C3}-\text{C17}-\text{C22} = 66.5(5)$.

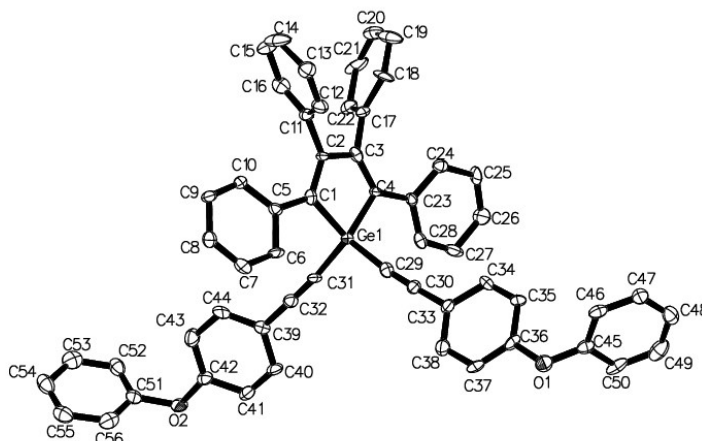


Figure A-57. Molecular structure of **G11** (with ellipsoids shown at the 50% probability level).

Hydrogen atoms have been removed for clarity. Selected bond distances (Å), angles (deg), and torsions (deg): Ge1–C1 = 1.923(5), Ge1–C4 = 1.955(5), C4–C3 = 1.343(7), C3–C2 = 1.512(8), Ge1–C31 = 1.894(4), Ge1–C29 = 1.896(5), C31–C32 = 1.217(6), C29–C30 = 1.190(7); C1–Ge1–C4 = 91.5(2), C29–Ge1–C31 = 109.4(2), Ge1–C1–C2 = 107.1(3), Ge1–C4–C3 = 105.6(3), C36–O1–C45 = 117.6(4), C42–O2–C51 = 116.9(4); Ge1–C4–C23–C28 = 15.2(7), Ge1–C1–C5–C6 = 16.1(6), C1–C2–C11–C12 = 66.6(7), C4–C3–C17–C22 = 64.1(7).

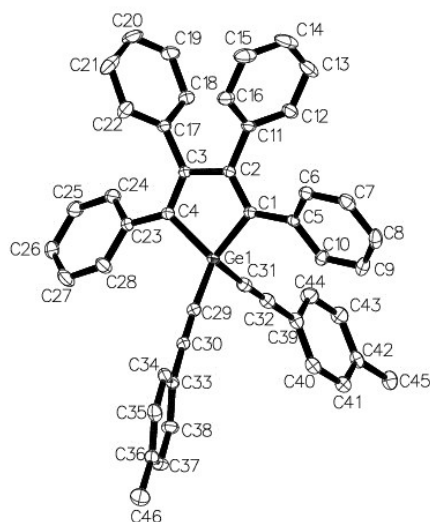


Figure A-58. Molecular structure of **G12** (with ellipsoids shown at the 50% probability level).

Hydrogen atoms have been removed for clarity. Selected bond distances (Å), angles (deg), and torsions (deg): Ge1–C1 = 1.943(1), Ge1–C4 = 1.944(1), C4–C3 = 1.356(2), C3–C2 = 1.511(2), Ge1–C31 = 1.892(2), Ge1–C29 = 1.893(1), C31–C32 = 1.208(2), C29–C30 = 1.208(2); C1–Ge1–C4 = 91.78(6), C29–Ge1–C31 = 106.03(6), Ge1–C1–C2 = 105.6(1), Ge1–C4–C3 = 106.1(1); Ge1–C4–C23–C28 = 39.8(2), Ge1–C1–C5–C10 = 29.4(2), C1–C2–C11–C12 = 64.6(2), C4–C3–C17–C22 = 76.2(2).

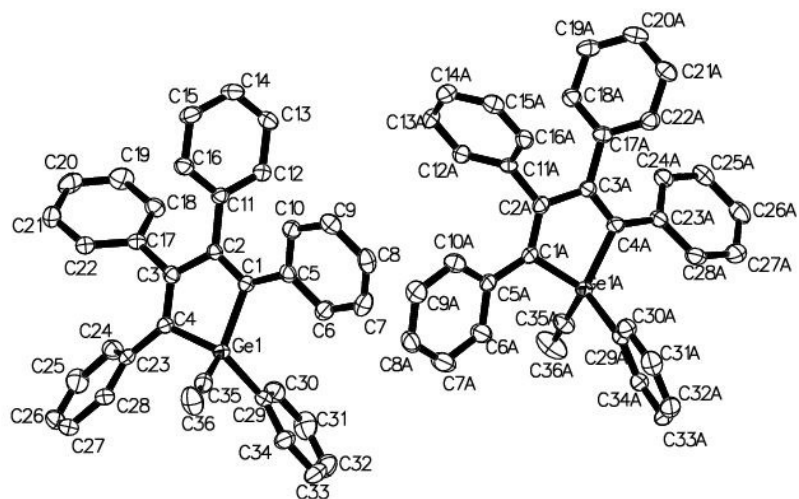


Figure A-59. Molecular structure of **G13** (with ellipsoids shown at the 50% probability level).

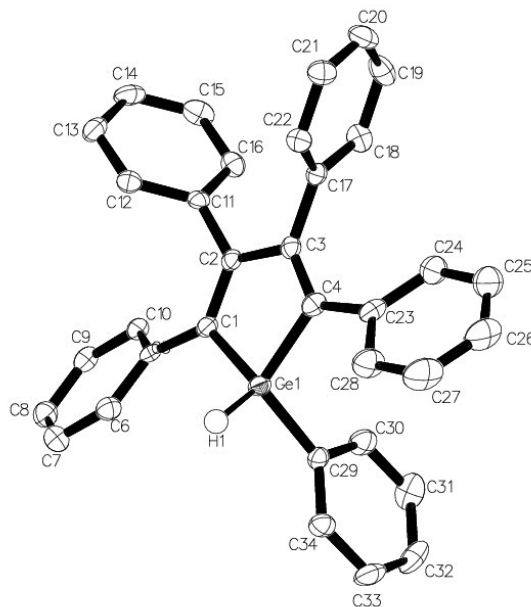


Figure A-60. Molecular structure of **G14** (with ellipsoids shown at the 50% probability level).

Hydrogen atoms have been removed for clarity. Selected bond distances (Å), angles (deg), and torsions (deg): Ge1–C1 = 1.945(2), Ge1–C4 = 1.944(2), C4–C3 = 1.355(3), C3–C2 = 1.512(3), Ge1–C29 = 1.931(2); C1–Ge1–C4 = 89.9(1), C29–Ge1–H1 = 106.1(9), Ge1–C1–C2 = 107.5(2), Ge1–C4–C3 = 108.3(2); Ge1–C4–C23–C28 = -30.4(3), Ge1–C1–C5–C6 = 32.4(3), C1–C2–C11–C12 = 64.3(3), C4–C3–C17–C22 = -68.5(3).

	G2	G3	G4	G6•THF	G7	G8	G9
formula	C ₄₂ H ₂₈ N ₂ Ge	C ₄₂ H ₂₈ N ₂ Ge	C ₅₆ H ₄₀ GeP ₂	C ₅₀ H ₄₂ GeO ₃	C ₅₆ H ₃₈ Ge	C ₄₄ H ₂₈ F ₂ Ge	C ₄₆ H ₂₈ F ₆ GeO ₂
fw	633.25	633.25	847.41	854.07	783.45	667.25	799.27
cryst size/mm	0.327 × 0.26 × 0.221	0.251 × 0.201 × 0.198	0.8 × 0.6 × 0.4	0.344 × 0.295 × 0.238	0.264 × 0.243 × 0.127	0.463 × 0.342 × 0.312	0.429 × 0.311 × 0.092
cryst syst	monoclinic	monoclinic	triclinic	monoclinic	monoclinic	triclinic	monoclinic
space group	P2 ₁ /n	P2 ₁ /n	P-1	P2 ₁ /n	P2 ₁ /c	P-1	Pc
a/Å	9.5710(6)	9.6922(6)	11.4828(14)	13.24330(10)	10.8646(18)	10.555(2)	10.6743(4)
b/Å	18.1502(10)	18.3316(13)	12.9012(13)	18.0730(2)	30.674(5)	11.095(2)	30.4150(13)
c/Å	18.6543(10)	18.3392(13)	18.022(2)	16.1476(2)	37.520(6)	16.680(3)	11.7480(5)
α/deg	90.00	90.00	71.258(3)	90.00	90.00	92.23(3)	90.00
β/deg	103.101(3)	102.975(3)	77.857(4)	92.4250(10)	98.665(9)	104.77(3)	98.169(2)
γ/deg	90.00	90.00	64.911(4)	90.00	90.00	113.52(3)	90.00
V/Å ³	3156.2(3)	3175.2(4)	2281.2(4)	3861.41(7)	12361(3)	1710.0(6)	3775.4(3)
D _{calcd} /g cm ⁻³	1.333	1.325	1.234	1.469	1.263	1.296	1.406
Z	4	4	2	4	12	2	4
abs coeff/mm ⁻¹	1.004	0.998	0.778	1.035	0.781	0.936	0.879
2θ range/deg	3.18 to 64.48°	3.18 to 73.5°	2.4 to 49.98°	3.38 to 64.58°	3.44 to 34.34°	2.56 to 68.04°	1.34 to 52.82°
reflins collected/indep reflins	59967/11119 [R(int) = 0.0447]	214206/15640 [R(int) = 0.0601]	22480/7943 [R(int) = 0.0410]	97250/13676 [R(int) = 0.0427]	65145/7196 [R(int) = 0.0873]	50264/12224 [R(int) = 0.0274]	41754/7577 [R(int) = 0.0707]
abs correct	multi-scan	multi-scan	multi-scan	multi-scan	multi-scan	multi-scan	multi-scan
max. and min. transm	0.7464 and 0.6820	0.7471 and 0.6782	1.0000 and 0.8625	0.7464 and 0.6416	0.7441 and 0.4804	0.7467 and 0.6576	0.7454 and 0.5909
final R indices [I>2σ(I)]	0.0365	0.0318	0.0390	0.0392	0.0307	0.0392	0.0849
wR ₂	0.0801	0.0803	0.1056	0.1479	0.0615	0.1094	0.2161
largest diff peak and hole/e Å ⁻³	0.51 and -0.45	0.56 and -0.49	0.68 and -0.31	0.65 and -0.65	0.22 and -0.18	1.21 and -0.72	3.59 and -0.86

Table A-1. Crystallographic data and structure refinement details for the 2,3,4,5-tetraphenylgermoles in this study.

	G10	G11	G12	G13	G14
formula	C ₄₆ H ₂₈ F ₆ Ge	C ₅₆ H ₃₈ O ₂ Ge	C ₄₆ H ₃₄ Ge	C ₃₆ H ₂₆ Ge	C ₃₄ H ₂₆ Ge
fw	767.27	815.45	659.32	531.16	507.14
cryst size/mm	0.7 × 0.5 × 0.4	0.207 × 0.189 × 0.174	0.239 × 0.179 × 0.178	0.357 × 0.235 × 0.144	1.0 × 0.41 × 0.14
cryst syst	monoclinic	monoclinic	triclinic	monoclinic	monoclinic
space group	C _{2/h}	Cc	P-1	P ₂ /c	P ₂ /c
a/Å	28.3368(18)	24.2228(2)	11.16560(10)	12.1631(15)	16.4694(15)
b/Å	11.1159(9)	10.21630(10)	11.16690(10)	19.192(2)	6.1919(6)
c/Å	24.7585(18)	16.7527(2)	16.1687(2)	23.219(3)	24.528(2)
α/deg	90.00	90.00	93.0420(10)	90.00	90.00
β/deg	94.008(3)	98.9710(10)	108.8100(10)	92.084(7)	91.644(3)
γ/deg	90.00	90.00	111.5560(10)	90.00	90.00
V/Å ³	7779.6(10)	4095.03(7)	1740.84(3)	5416.7(11)	2500.3(4)
D _{calc} /g cm ⁻³	1.310	1.323	1.258	1.303	1.347
Z	8	4	2	8	4
abs coeff/mm ⁻¹	0.847	0.792	0.911	1.154	1.246
2θ range/deg	2.88 to 50.04°	3.4 to 59.36°	2.72 to 67.94°	2.76 to 50.28°	3.32 to 51.84°
reflns collected/indep reflns	24891/6807 [R(int) = 0.0451]	43667/11266 [R(int) = 0.0424]	45433/13173 [R(int) = 0.0365]	79186/9660 [R(int) = 0.0777]	20143/4829 [R(int) = 0.0702]
abs correct	multi-scan	multi-scan	multi-scan	multi-scan	multi-scan
max. and min. transm	1.0000 and 0.8490	0.7459 and 0.6711	0.7467 and 0.6829	0.7452 and 0.5340	0.7453 and 0.5297
final R indices [I>2σ(I)]	0.0451	0.0346	0.0354	0.0326	0.0349
wR ₂	0.1206	0.0762	0.0823	0.0767	0.0738
largest diff peak and hole/e Å ⁻³	0.47/-0.47	0.45/-0.34	0.68/-0.40	0.48/-0.69	0.44/-0.46

Table A-1 (cont'd).

5.3.2 X-ray crystallography of differently substituted germafluorenes.

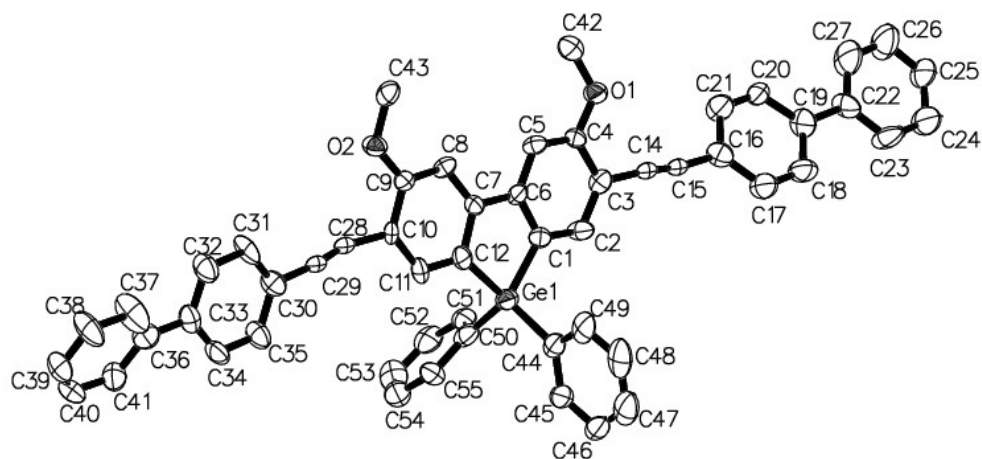


Figure A-61. Molecular structure of **G15** (with ellipsoids shown at the 50% probability level).

Hydrogen atoms have been removed for clarity. Selected bond distances (Å), angles (deg), and torsions (deg): Ge1–C1 = 1.93(1), Ge1–C12 = 1.93(1), Ge1–C44 = 1.95(1), Ge1–C50 = 1.92(1); C12–Ge1–C1 = 88.8(5), C50–Ge1–C44 = 111.8(5), C4–O1–C42 = 116.0(8), C9–O2–C43 = 117.5(8); C8–C9–O2–C43 = -2(1), C5–C4–O1–C42 = -3(2), C12–Ge1–C50–C51 = 102(1), C1–Ge1–C44–C49 = 53(1).

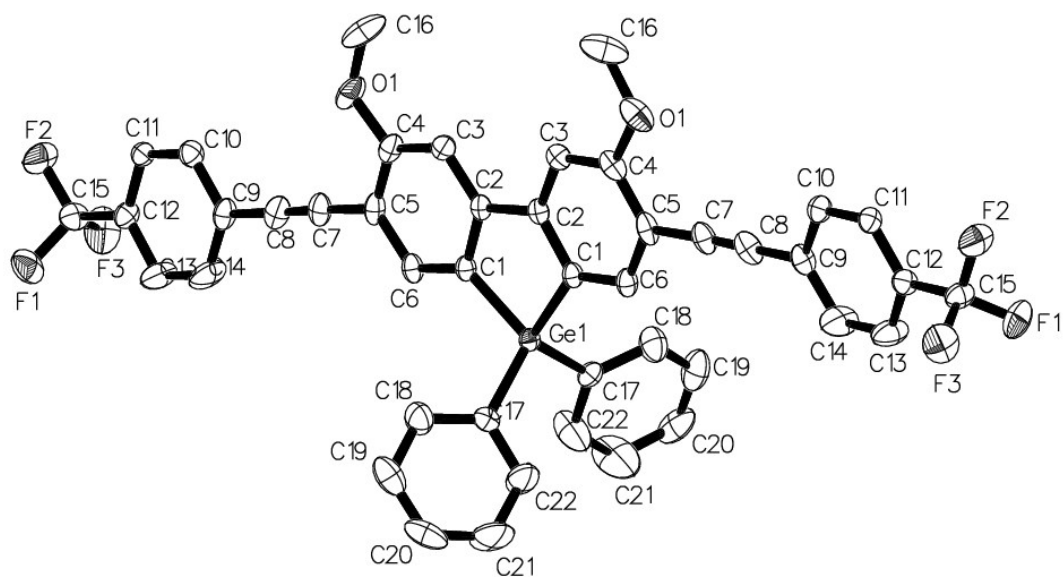


Figure A-62. Molecular structure of **G16** (with ellipsoids shown at the 50% probability level).

Hydrogen atoms have been removed for clarity. Selected bond distances (Å), angles (deg), and torsions (deg): Ge1–C1 = 1.941(2), Ge1–C17 = 1.943(2); C1–Ge1–C1 = 89.18(8), C17–Ge1–C17 = 106.61(9), C4–O1–C16 = 117.3(2); C1–Ge1–C17–C18 = -13.2(2), C3–C4–O1–C16 = -0.5(3), C4–C5–C9–C10 = 5.8(2).

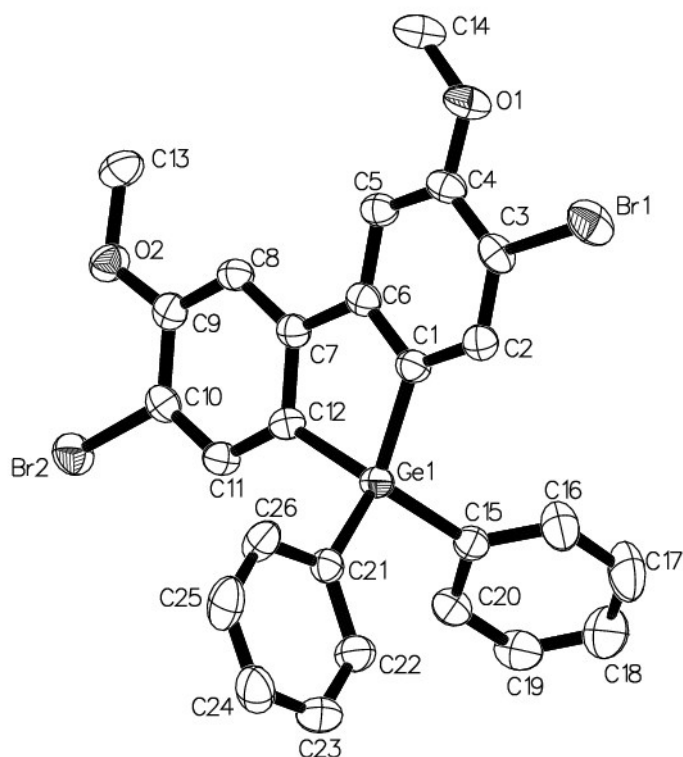


Figure A-63. Molecular structure of **G17** (with ellipsoids shown at the 50% probability level).

Hydrogen atoms have been removed for clarity. Selected bond distances (Å), angles (deg), and torsions (deg): Ge1–C1 = 1.941(2), Ge1–C12 = 1.948(3), Ge1–C15 = 1.951(3), Ge1–C21 = 1.947(3), C3–Br1 = 1.887(2), C10–Br2 = 1.892(2); C1–Ge1–C12 = 88.5(1), C15–Ge1–C21 = 107.7(1), C4–O1–C14 = 117.8(2), C9–O2–C13 = 118.0(2); C5–C4–O1–C14 = -2.7(4), C8–C9–O2–C13 = 9.8(4), C1–Ge1–C15–C16 = 28.2(3), C12–Ge1–C21–C26 = -53.9(3).

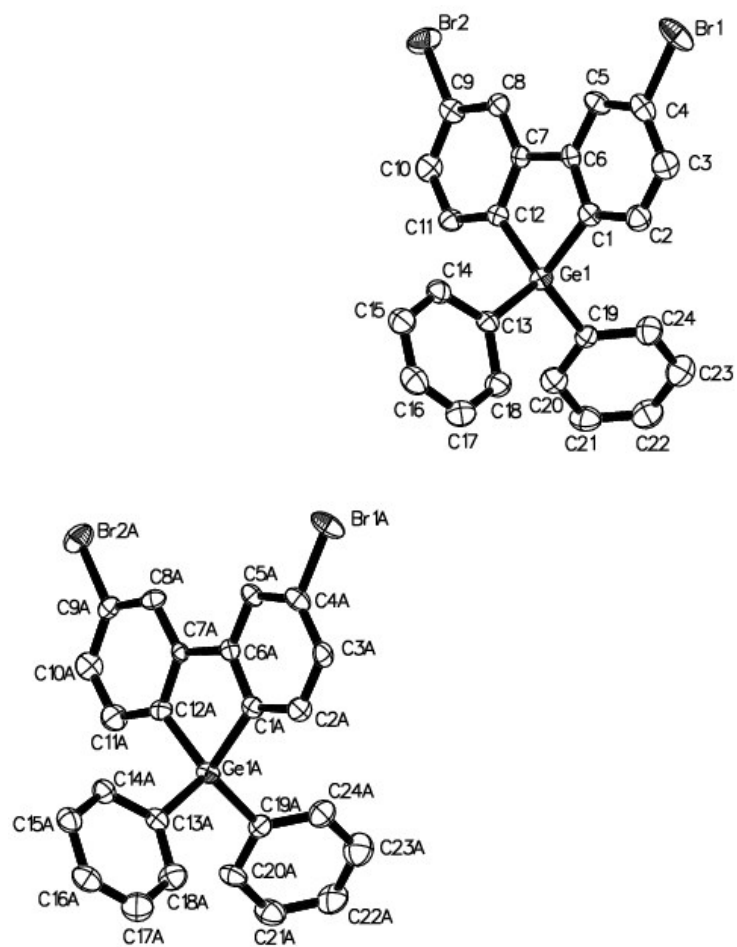


Figure A-64. Molecular structure of **G18** (with ellipsoids shown at the 50% probability level).

	G15	G16	G17	G18
formula	C ₅₄ H ₃₈ O ₂ Ge	C ₄₄ H ₂₈ GeO ₂ F ₆	C ₂₆ H ₂₀ O ₂ GeBr ₂	C ₂₄ H ₁₆ Br ₂ Ge
fw	791.43	775.25	596.83	536.78
cryst size/mm	0.163 × 0.161 × 0.036	0.269 × 0.121 × 0.082	0.36 × 0.346 × 0.328	0.417 × 0.238 × 0.167
cryst syst	monoclinic	monoclinic	monoclinic	monoclinic
space group	<i>P2₁/c</i>	<i>C2/c</i>	<i>P2₁/c</i>	<i>P2₁/c</i>
<i>a</i> /Å	11.293(2)	25.7576(9)	9.2118(2)	6.2877(4)
<i>b</i> /Å	11.867(3)	11.1305(4)	22.2149(4)	41.708(3)
<i>c</i> /Å	29.487(6)	13.6310(5)	11.4542(2)	16.1732(10)
α /deg	90.00	90.00	90.00	90.00
β /deg	91.754(7)	114.1283(19)	98.4790(10)	103.459(4)
γ /deg	90.00	90.00	90.00	90.00
<i>V</i> /Å ³	3949.7(14)	3566.5(2)	2318.36(8)	4124.9(5)
<i>D</i> _{calcd} /g cm ⁻³	1.331	1.444	1.710	1.729
<i>Z</i>	4	4	4	8
abs coeff/mm ⁻¹	0.819	0.928	4.789	5.366
<i>2θ</i> range/deg	3.6 to 50.14°	3.46 to 52.76°	3.66 to 56.62°	1.96 to 51°
reflns collected/indep reflns	29136/7006 [R(int) = 0.2036]	29612/3653 [R(int) = 0.0442]	38857/5681 [R(int) = 0.0469]	87640/7557 [R(int) = 0.0971]
abs correct	multi-scan	multi-scan	multi-scan	multi-scan
max. and min. transm	0.7452 and 0.6342	0.7454 and 0.6681	0.7457 and 0.5290	0.7452 and 0.4742
final <i>R</i> indices [<i>I</i> > 2σ(<i>I</i>)]	0.1082	0.0323	0.0294	0.0973
<i>wR</i> ₂	0.2519	0.0782	0.0660	0.1683
largest diff peak and hole/e Å ⁻³	2.61 and -1.05	0.60 and -0.50	0.92 and -0.48	2.20 and -1.68

Table A-2. Crystallographic data and structure refinement details for the substituted germafluorenes in this study.

5.3.3. X-ray crystallography of symmetric 2,5-substituted siloles

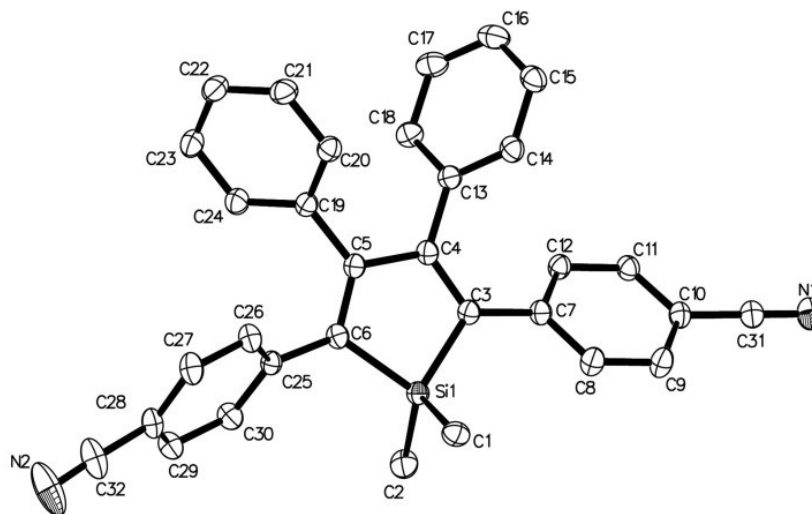


Figure A-65. Molecular structure of **S1**. Hydrogen atoms have been removed for clarity. Thermal ellipsoids are drawn at the 50% probability level.

Selected bond distances (Å), angles (deg), and torsions (deg) for **S1**: Si1–C1 = 1.873(1), Si1–C2 = 1.859(1), Si–C3 = 1.883(1), Si–C6 = 1.880(1), C3–C4 = 1.366(1), C5–C6 = 1.361(1), C31–N2 = 1.146(2), C32–N1 = 1.150(2); C3–Si1–C6 = 91.54(4), C2–Si1–C1 = 110.09(5), C10–C32–N1 = 179.4(1), C28–C31–N2 = 177.3(2); C12–C7–C3–C4 = -36.5(2), C3–C4–C13–C14 = -58.2(1), C6–C5–C19–C24 = -56.5(1), C5–C6–C25–C26 = -53.7(1).

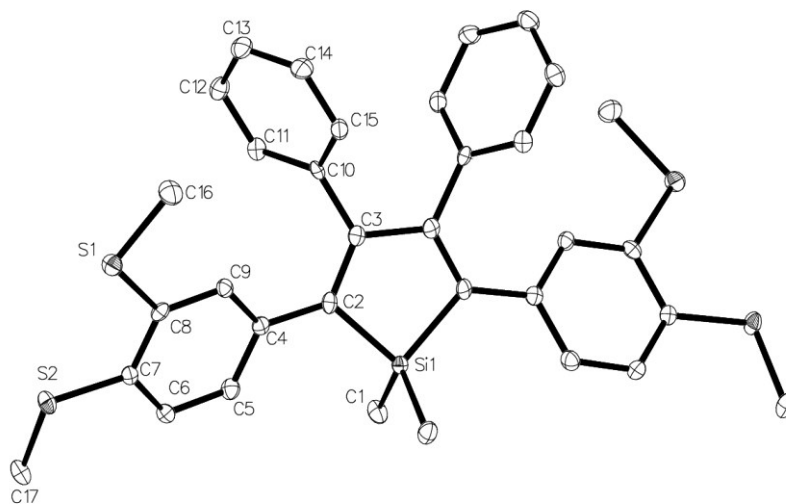


Figure A-66. Molecular structure of **S2**. Hydrogen atoms and solvent molecules have been removed for clarity, and the full molecule was symmetrically generated from the asymmetric unit. Thermal ellipsoids are drawn at the 50% probability level.

Selected bond distances (Å), angles (deg), and torsions (deg) for **S2**: Si1–C1 = 1.873(4), Si1–C2 = 1.887(3), C2–C3 = 1.362(4), C3–C3 = 1.500(5), C8–S1 = 1.768(3), S1–C16 = 1.798(4); C1–Si1–C1 = 108.7(2), C2–Si1–C2 = 92.1(1), Si1–C2–C3 = 107.4(2), C8–S1–C16 = 103.1(2), C7–S2–C17 = 102.4(2); Si1–C2–C4–C5 = -28.0(4), C2–C3–C10–C11 = -64.0(4), C9–C8–S2–C17 = -11.5(3).

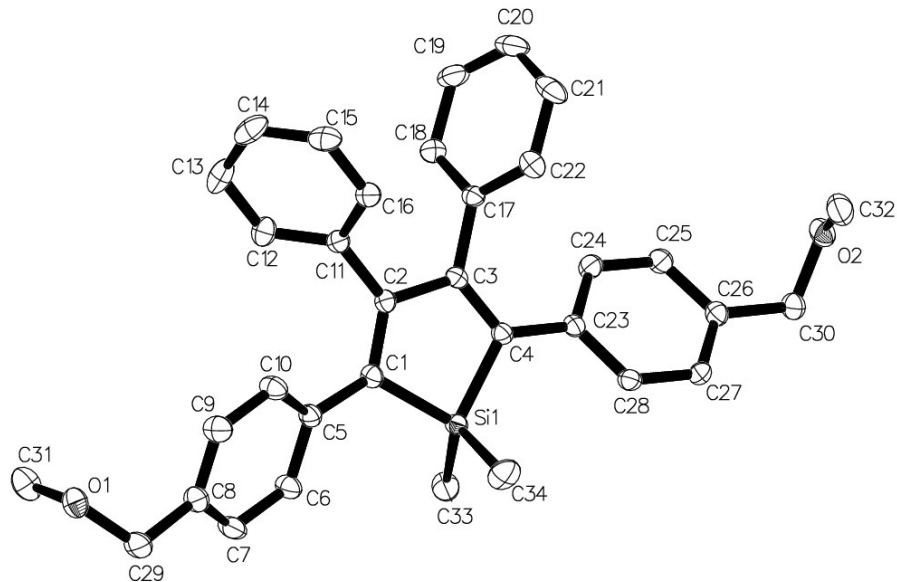


Figure A-67. Molecular structure of **S5**. Hydrogen atoms have been removed for clarity. Thermal ellipsoids are drawn at the 50% probability level.

Selected bond distances (Å), angles (deg), and torsions (deg) for **S5**: Si1–C1 = 1.872(1), Si1–C4 = 1.876(2), Si1–C33 = 1.858(2), Si1–C34 = 1.858(2), C4–C3 = 1.361(2), C3–C2 = 1.510(2); C1–Si1–C4 = 92.53(7), C33–Si1–C34 = 110.84(9), Si1–C1–C2 = 107.5(1), C29–O1–C31 = 112.7(1), C30–O2–C32 = 112.1(1); C2–C1–C5–C10 = -31.6(2), C1–C2–C11–C12 = -68.2(2), C4–C3–C17–C22 = -60.2(2), C3–C4–C23–C24 = -27.1(3)

	S1	S2	S5
formula	C ₃₂ H ₂₄ N ₂ Si	C ₃₇ H ₄₀ Cl ₆ S ₄ Si	C ₃₄ H ₃₄ SiO ₂
fw	464.62	853.72	502.70
cryst size/mm	0.54 × 0.56 × 0.59	0.095 × 0.100 × 0.558	0.468 × 0.412 × 0.326
cryst syst	orthorhombic	orthorhombic	monoclinic
space group	<i>Pbca</i>	<i>Pbcn</i>	<i>Pn</i>
<i>a</i> /Å	18.8812(4)	27.5566(19)	6.7424(6)
<i>b</i> /Å	13.8509(3)	14.5109(9)	21.6480(17)
<i>c</i> /Å	19.7703(4)	9.9159(6)	9.8503(9)
α /deg	90	90	90.00
β /deg	90	90	107.869(4)
γ /deg	90	90	90.00
<i>V</i> /Å ³	5170.36(19)	3965.1(4)	1368.4(2)
<i>D</i> _{calcd} /g cm ⁻³	1.1937	1.430	1.220
<i>Z</i>	8	4	2
abs coeff/mm ⁻¹	0.113	0.702	0.115
2 θ range/deg	4.12 to 63.0	5.20 to 53.74	3.76 to 56.72°
reflns collected/indep reflns	88966/8602 [R(int) = 0.0967]	13225/2520 [R(int) = 0.1905]	25826/3411 [R(int) = 0.0247]
abs correct	multi-scan	multi-scan	multi-scan
max. and min. transm	0.7462 and 0.6701	0.9363 and 0.6955	0.7457 and 0.7076
final <i>R</i> indices [I>2 σ (I)]	0.0413	0.0606	0.0265
<i>wR</i> ₂	0.1081	0.1428	0.0698
largest diff peak and hole/e Å ⁻³	0.49 and -0.18	1.06 and -0.73	0.20 and -0.17

Table A-3. Crystallographic data and structure refinement details for the symmetric siloles in this study.

5.4. UV-vis and fluorescence spectra with Ni(II), Cu(II), and Hg(II).

5.4.1. Interactions of metal salts with the siloles listed.

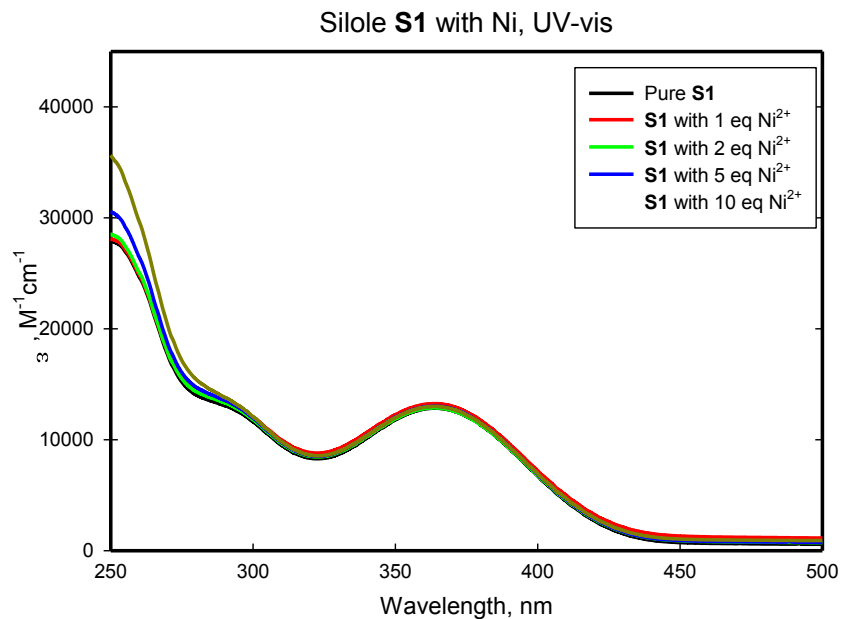


Figure A-68. UV-vis spectra of silole **S1** with 1-10 equiv of Ni(II) perchlorate, 1:1 dichloromethane/methanol mixture, and total silole concentration is 5×10^{-5} M.

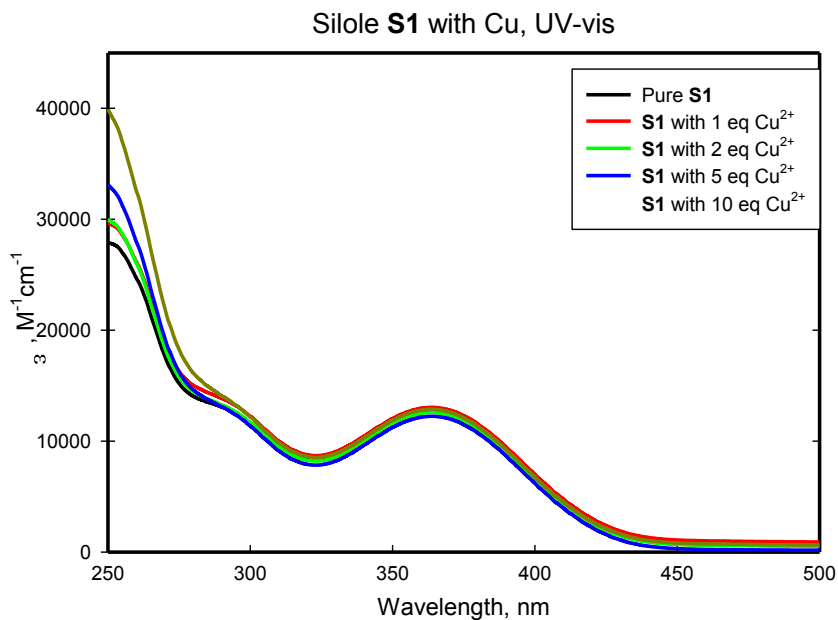


Figure A-69. UV-vis spectra of silole **S1** with 1-10 equiv of Cu(II) perchlorate, 1:1 dichloromethane/methanol mixture, and total silole concentration is 5×10^{-5} M.

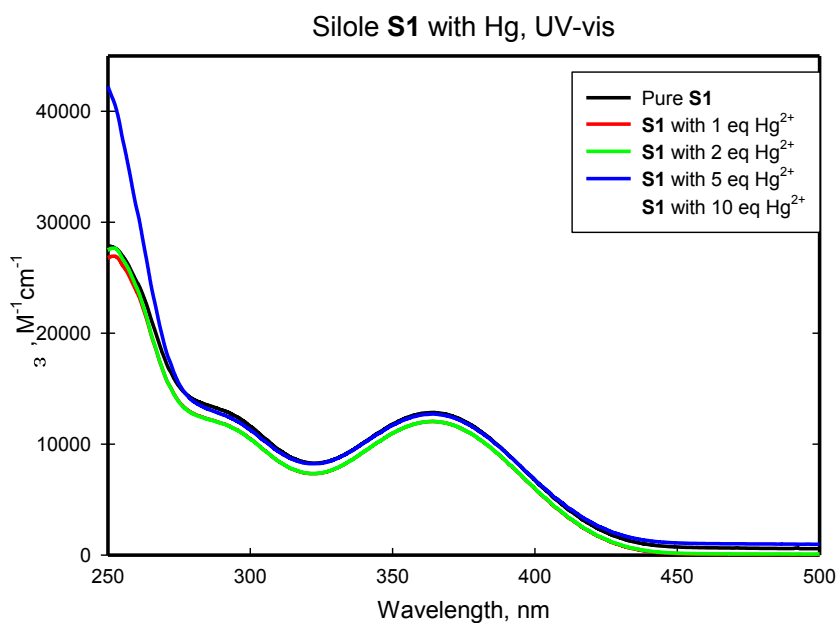


Figure A-70. UV-vis spectra of silole **S1** with 1-10 equiv of Hg(II) perchlorate, 1:1 dichloromethane/methanol mixture, and total silole concentration is 5×10^{-5} M.

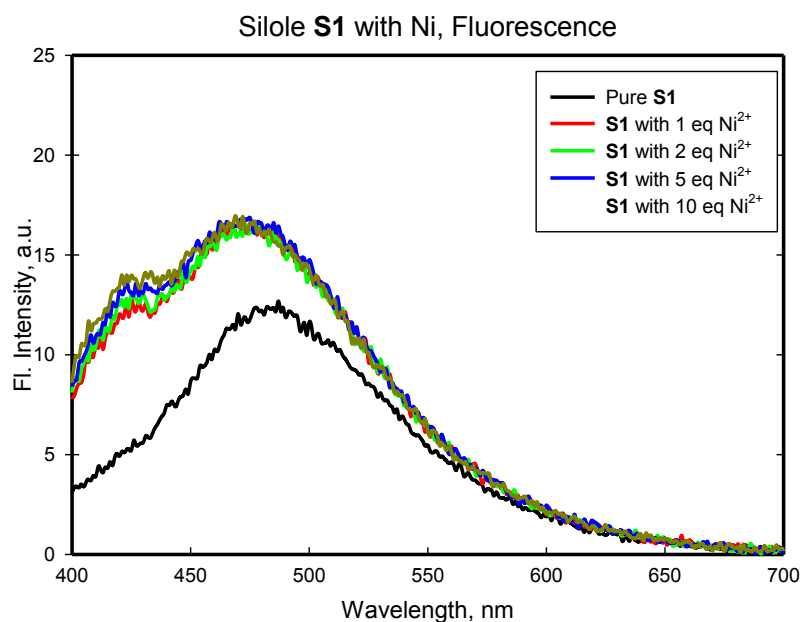


Figure A-71. Fluorescence spectra of silole **S1** with 1-10 equiv of Ni(II) perchlorate, 1:1 dichloromethane/methanol mixture, and total silole concentration is 5×10^{-5} M. Excitation at 365 nm.

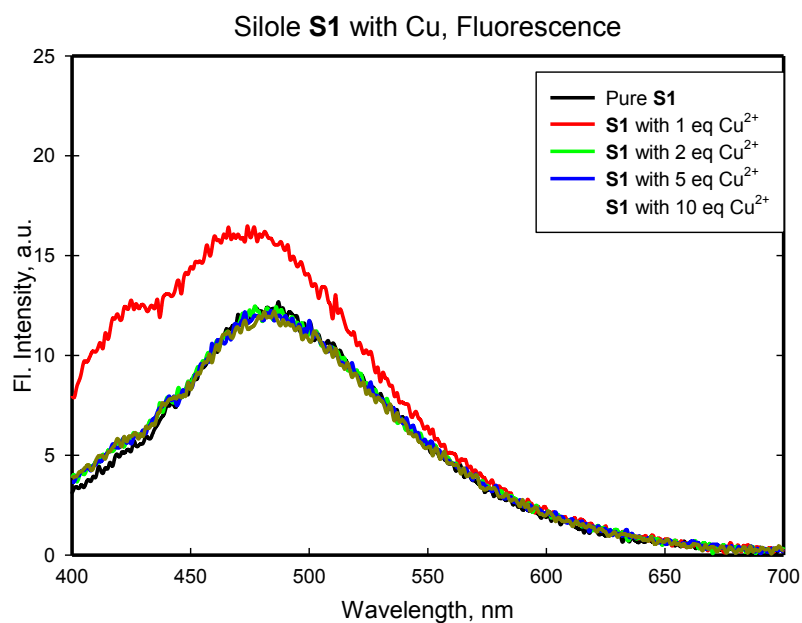


Figure A-72. Fluorescence spectra of silole **S1** with 1-10 equiv of Cu(II) perchlorate, 1:1 dichloromethane/methanol mixture, and total silole concentration is 5×10^{-5} M. Excitation at 365 nm.

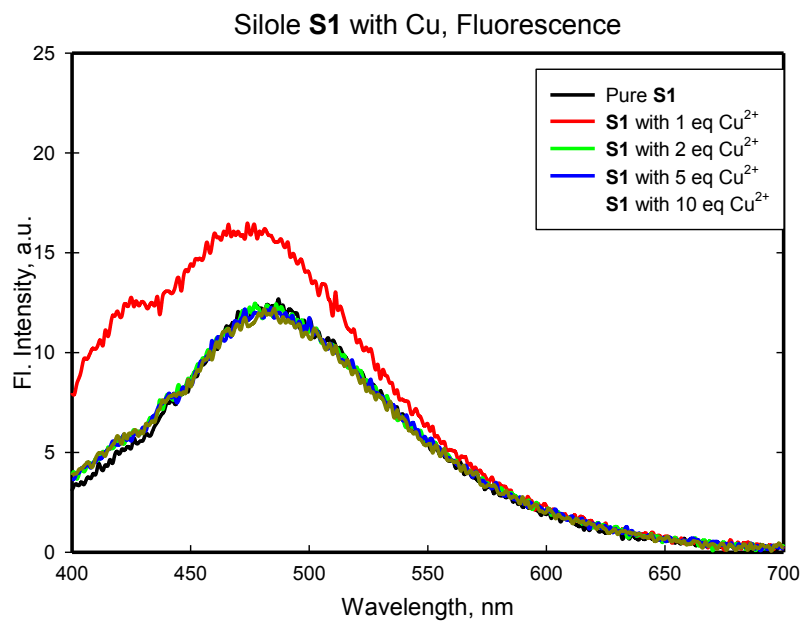


Figure A-73. Fluorescence spectra of silole **S1** with 1-10 equiv of Hg(II) perchlorate, 1:1 dichloromethane/methanol mixture, and total silole concentration is 5×10^{-5} M. Excitation at 365 nm.

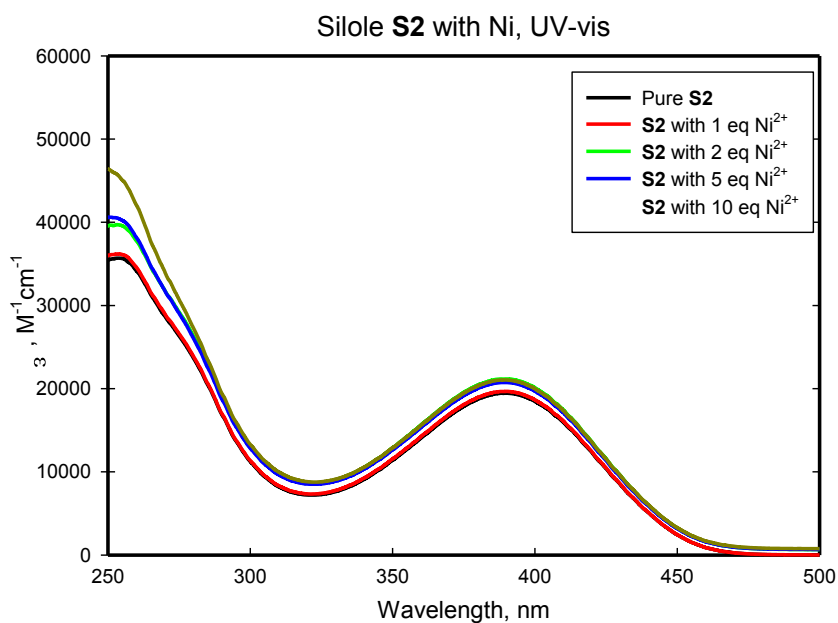


Figure A-74. UV-vis spectra of silole **S2** with 1-10 equiv of Ni(II) perchlorate, 1:1 dichloromethane/methanol mixture, and total silole concentration is 5×10^{-5} M.

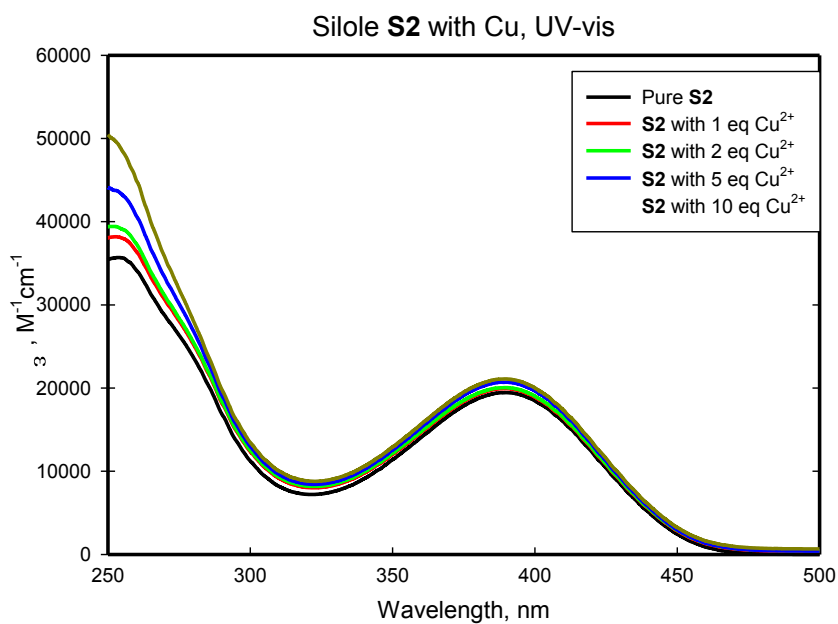


Figure A-75. UV-vis spectra of silole **S2** with 1-10 equiv of Cu(II) perchlorate, 1:1 dichloromethane/methanol mixture, and total silole concentration is 5×10^{-5} M.

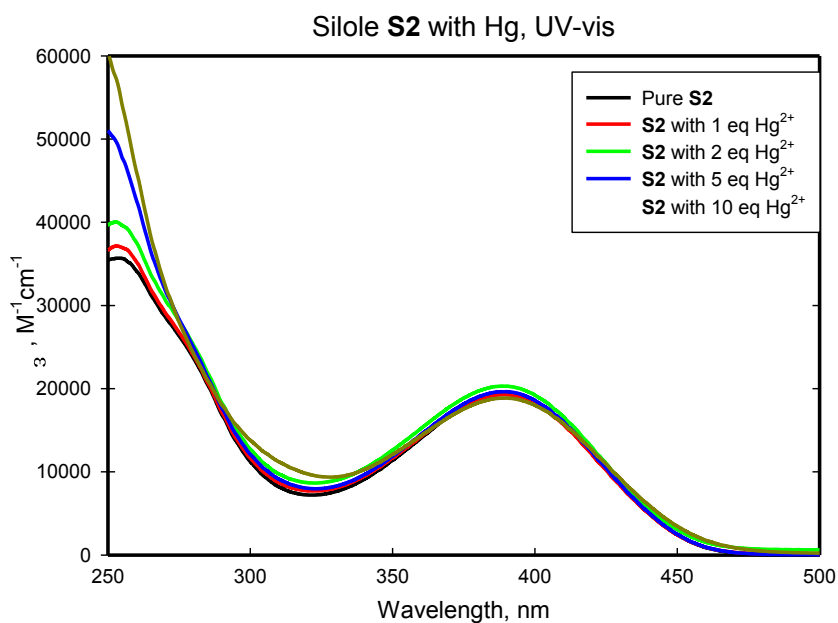


Figure A-76. UV-vis spectra of silole **S2** with 1-10 equiv of Hg(II) perchlorate, 1:1 dichloromethane/methanol mixture, and total silole concentration is 5×10^{-5} M.

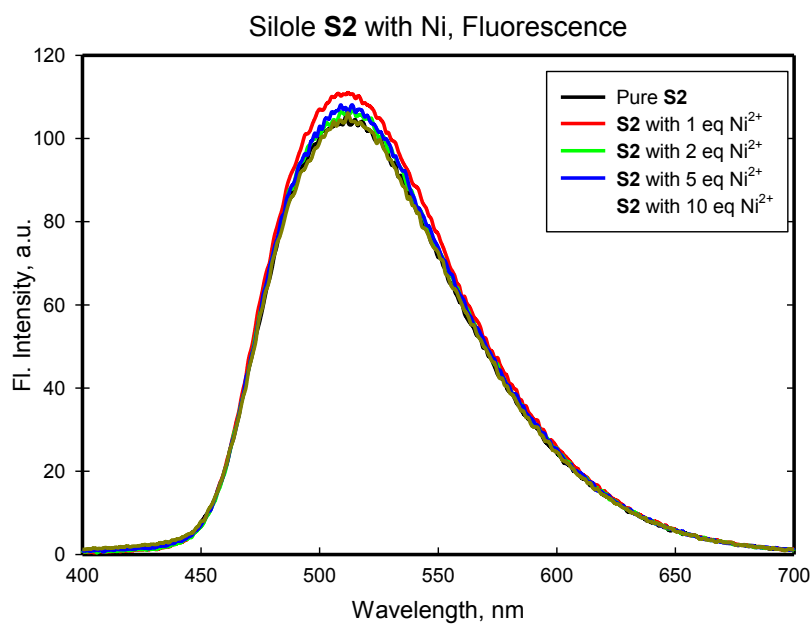


Figure A-77. Fluorescence spectra of silole **S2** with 1-10 equiv of Ni(II) perchlorate, 1:1 dichloromethane/methanol mixture, and total silole concentration is 5×10^{-5} M. Excitation at 390 nm.

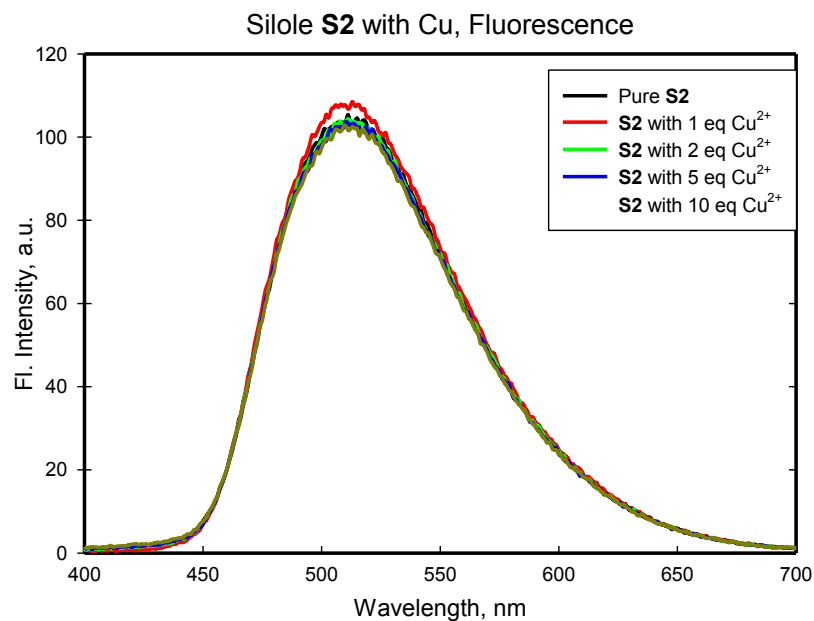


Figure A-78. Fluorescence spectra of silole **S2** with 1-10 equiv of Cu(II) perchlorate, 1:1 dichloromethane/methanol mixture, and total silole concentration is 5×10^{-5} M. Excitation at 390 nm.

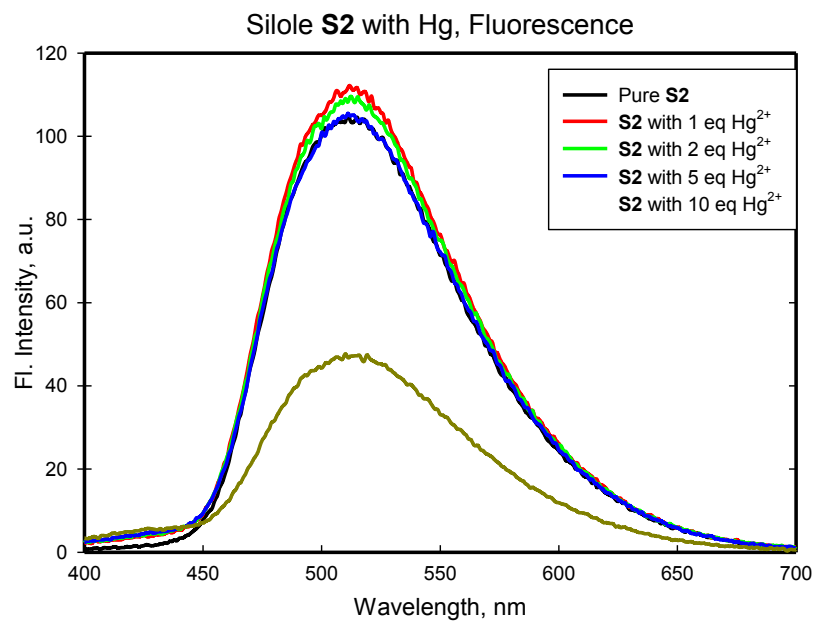


Figure A-79. Fluorescence spectra of silole **S2** with 1-10 equiv of Hg(II) perchlorate, 1:1 dichloromethane/methanol mixture, and total silole concentration is 5×10^{-5} M. Excitation at 390 nm.

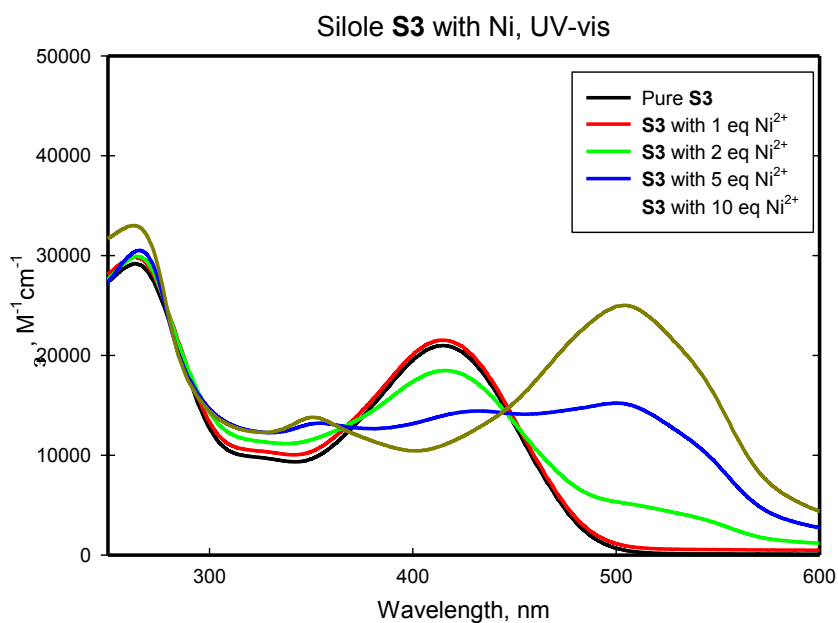


Figure A-80. UV-vis spectra of silole **S3** with 1-10 equiv of Ni(II) perchlorate, 1:1 dichloromethane/methanol mixture, and total silole concentration is 5×10^{-5} M.

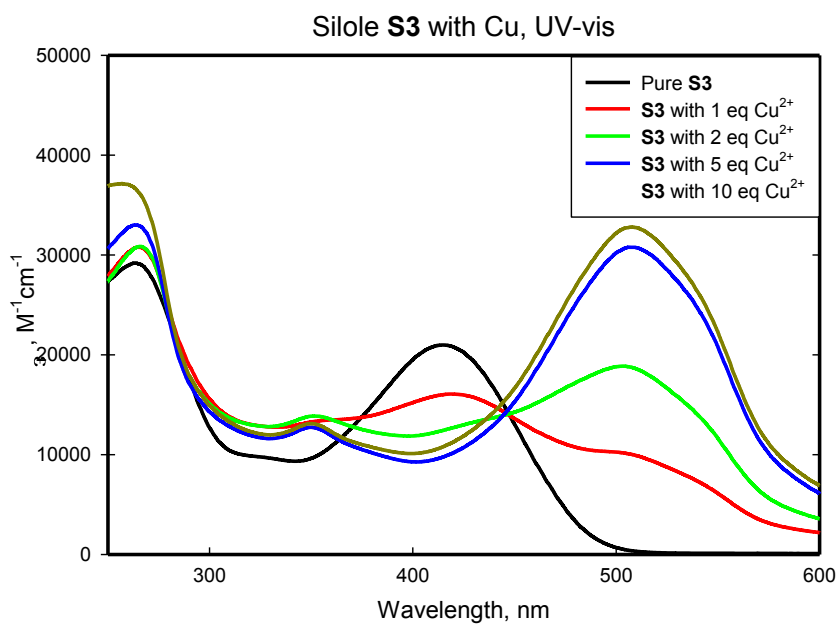


Figure A-81. UV-vis spectra of silole **S3** with 1-10 equiv of Cu(II) perchlorate, 1:1 dichloromethane/methanol mixture, and total silole concentration is 5×10^{-5} M.

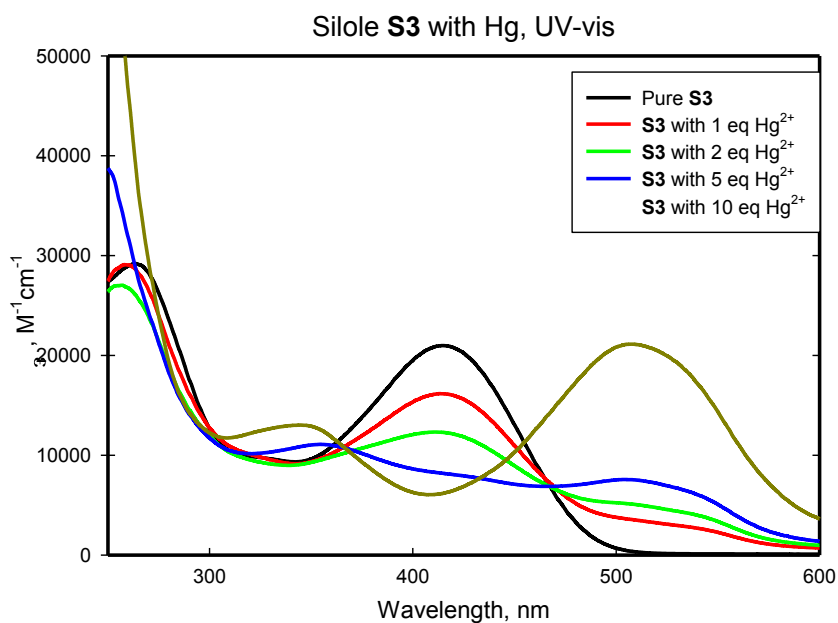


Figure A-82. UV-vis spectra of silole **S3** with 1-10 equiv of Hg(II) perchlorate, 1:1 dichloromethane/methanol mixture, and total silole concentration is 5×10^{-5} M.

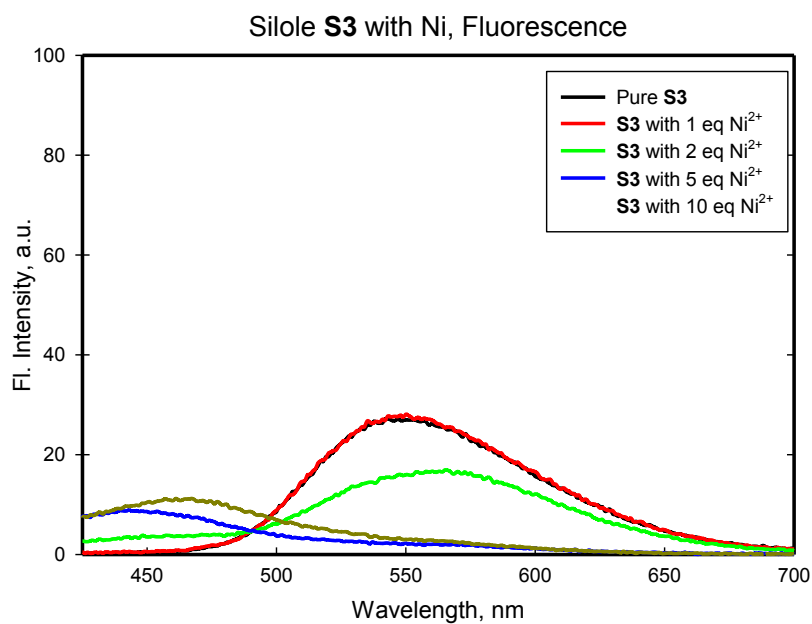


Figure A-83. Fluorescence spectra of silole **S3** with 1-10 equiv of Ni(II) perchlorate, 1:1 dichloromethane/methanol mixture, and total silole concentration is 5×10^{-5} M. Excitation at 415 nm.

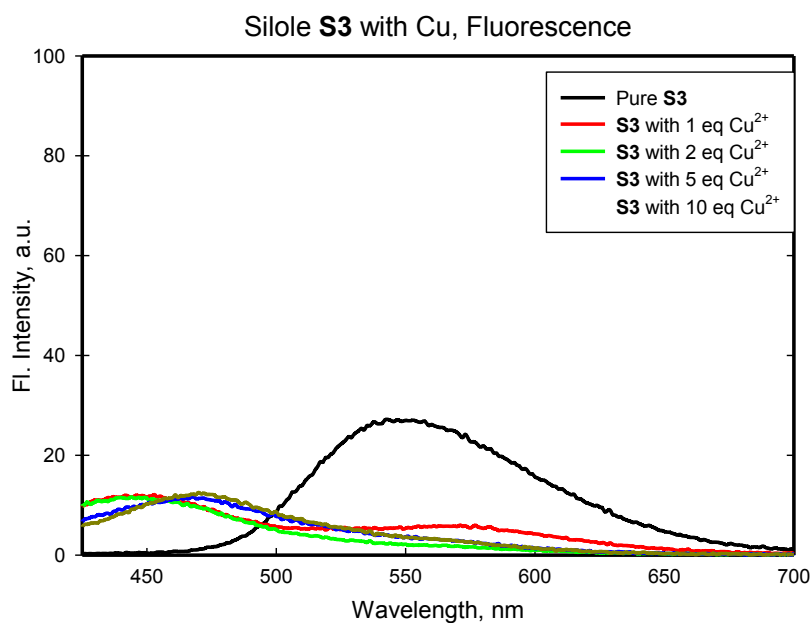


Figure A-84. Fluorescence spectra of silole **S3** with 1-10 equiv of Cu(II) perchlorate, 1:1 dichloromethane/methanol mixture, and total silole concentration is 5×10^{-5} M. Excitation at 415 nm.

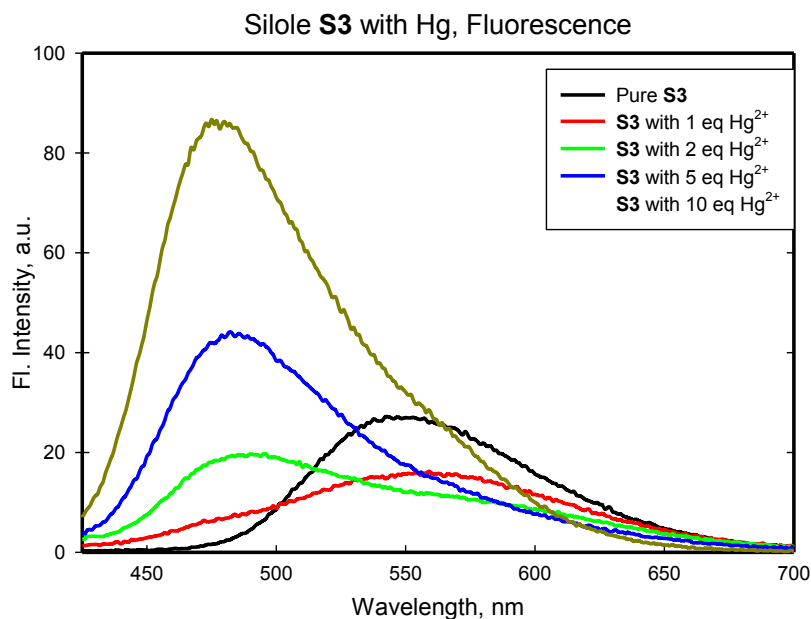


Figure A-85. Fluorescence spectra of silole **S3** with 1-10 equiv of Hg(II) perchlorate, 1:1 dichloromethane/methanol mixture, and total silole concentration is 5×10^{-5} M. Excitation at 415 nm.

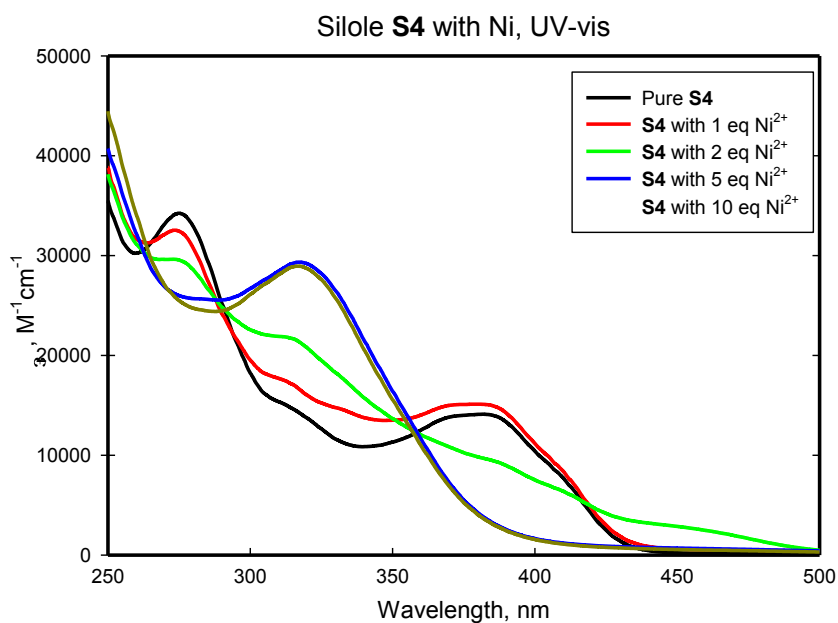


Figure A-86. UV-vis spectra of silole **S4** with 1-10 equiv of Ni(II) perchlorate, 1:1 dichloromethane/methanol mixture, and total silole concentration is 5×10^{-5} M.

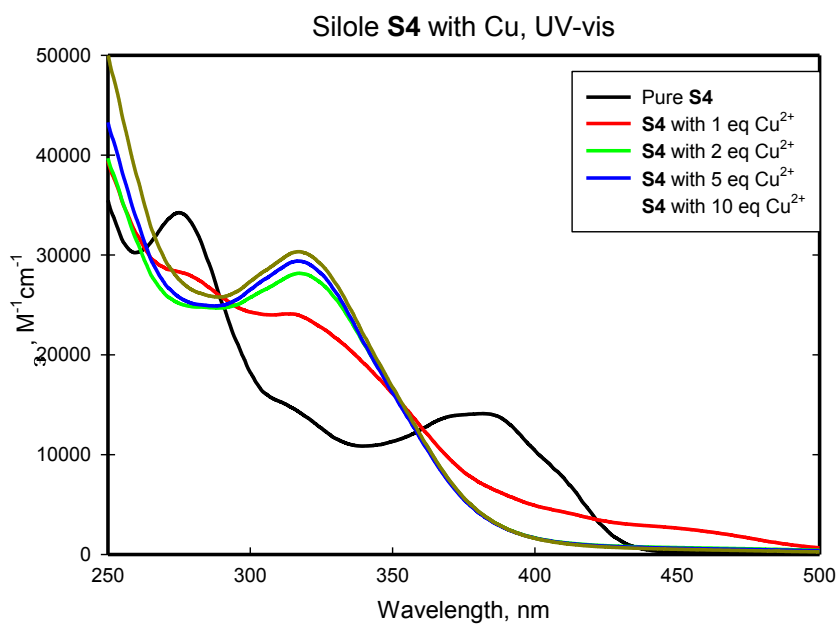


Figure A-87. UV-vis spectra of silole **S4** with 1-10 equiv of Cu(II) perchlorate, 1:1 dichloromethane/methanol mixture, and total silole concentration is 5×10^{-5} M.

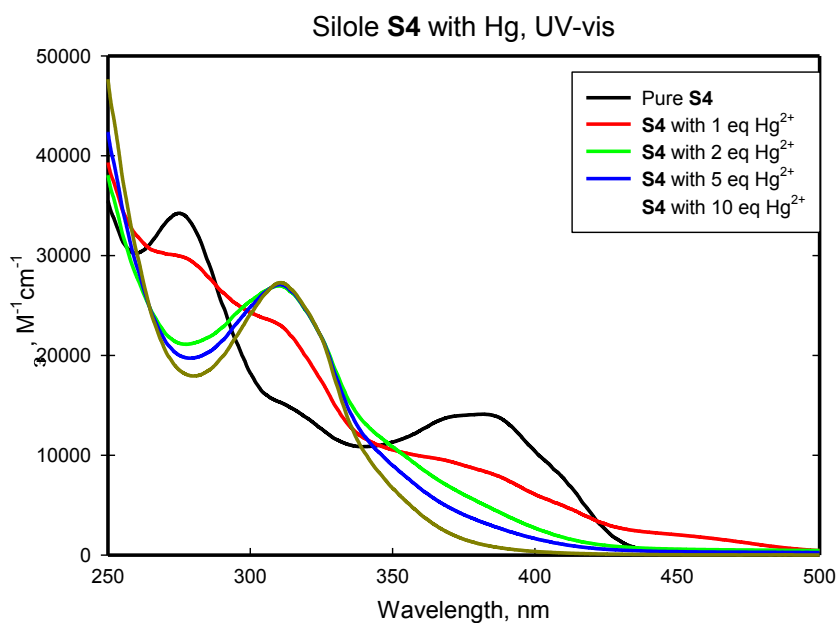


Figure A-88. UV-vis spectra of silole **S4** with 1-10 equiv of Hg(II) perchlorate, 1:1 dichloromethane/methanol mixture, and total silole concentration is 5×10^{-5} M.

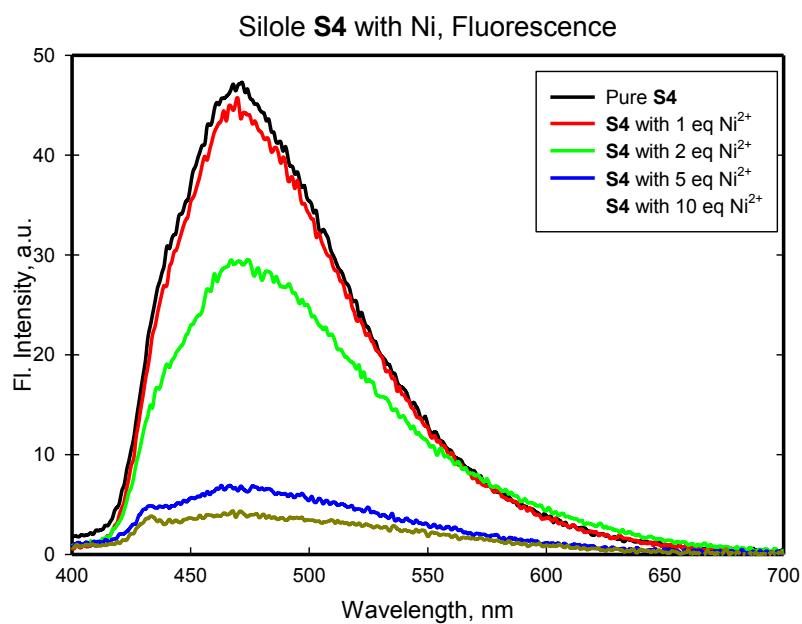


Figure A-89. Fluorescence spectra of silole **S4** with 1-10 equiv of Ni(II) perchlorate, 1:1 dichloromethane/methanol mixture, and total silole concentration is 5×10^{-5} M. Excitation at 383 nm.

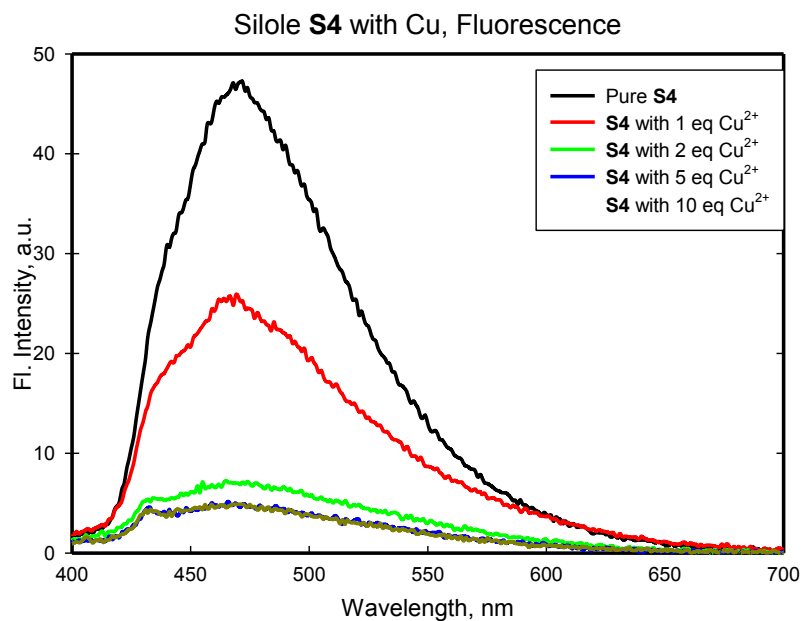


Figure A-90. Fluorescence spectra of silole **S4** with 1-10 equiv of Cu(II) perchlorate, 1:1 dichloromethane/methanol mixture, and total silole concentration is 5×10^{-5} M. Excitation at 383 nm.

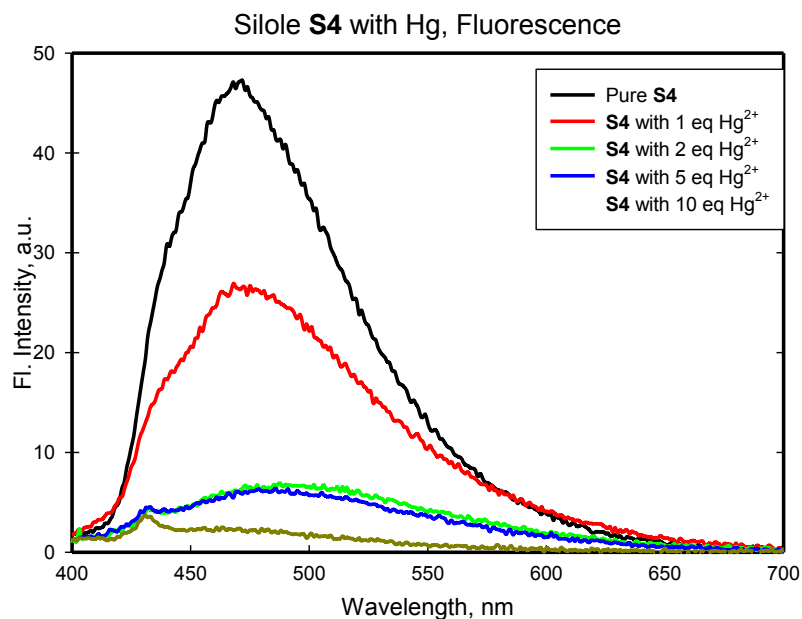


Figure A-91. Fluorescence spectra of silole **S4** with 1-10 equiv of Hg(II) perchlorate, 1:1 dichloromethane/methanol mixture, and total silole concentration is 5×10^{-5} M. Excitation at 383 nm.

5.4.2. Titration spectra and related calculations.

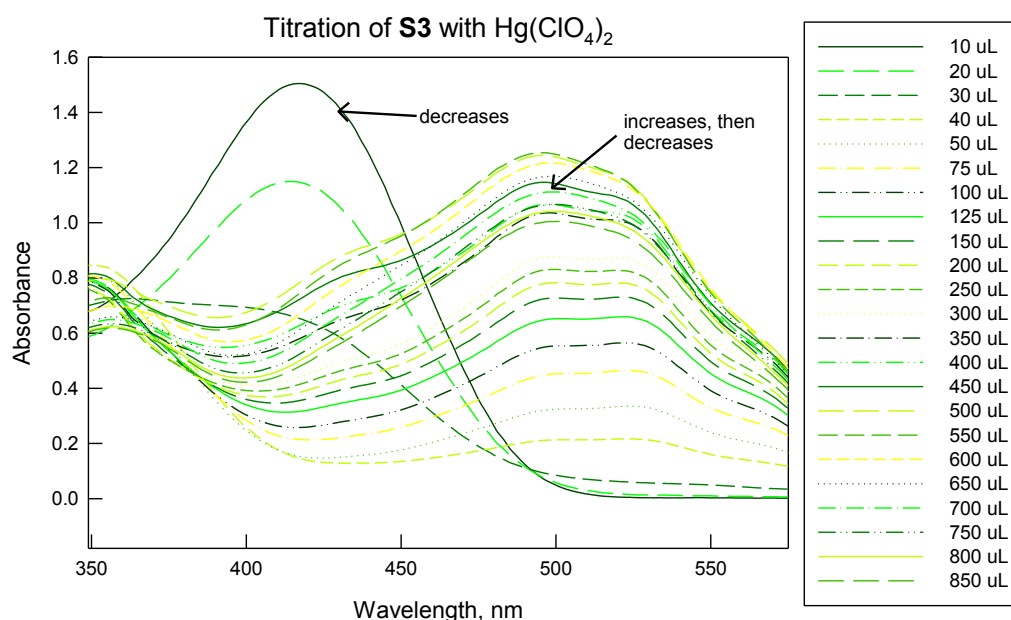


Figure A-92. The raw spectral data of titration of 1×10^{-4} M **S3** in dichloromethane with 1.5×10^{-2} M Hg(II) perchlorate solution. Annotations are added to indicate the appearance or disappearance of absorption bands. The legend to the right lists the volume of Hg(II) solution added that corresponds to the line in the graph.

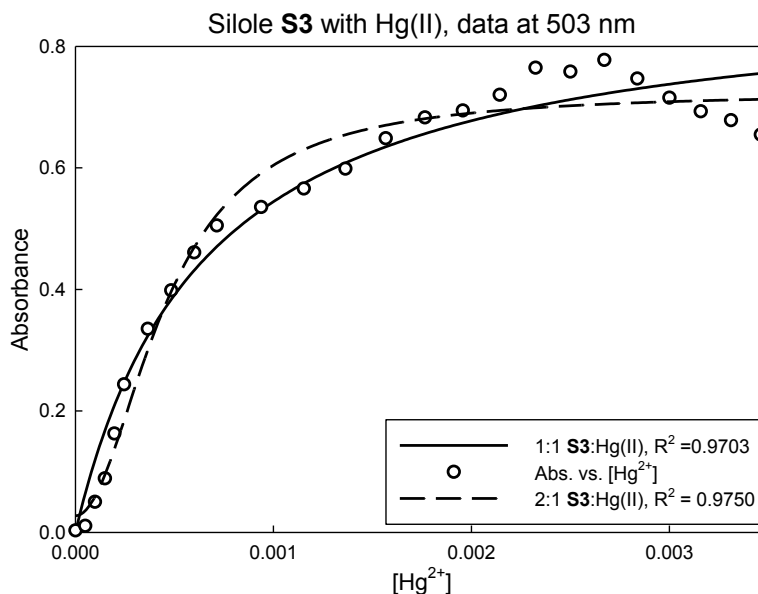


Figure A-93. The titration data extracted from the raw data (Figure A-92) at 503 nm. The total $[\text{Hg}^{2+}]$ was calculated from the initial volume of **S3** (3 mL), plus the volume added by the titrant (i.e., Hg(II) perchlorate in MeOH).

Data Source: Data 2 in Titration spectra by Hg amount

Equation: User-Defined, 1 metal fit curve 2

$$f=(a+b*c*x)/(c*x+1)$$

R	Rsqr	Adj Rsqr	Standard Error of Estimate
0.9850	0.9703	0.9676	0.0471

	Coefficient	Std. Error	t	P
a	3.2205E-014	0.0309	1.0424E-012	1.0000
b	0.8971	0.0380	23.6260	<0.0001
c	1543.0784	285.6500	5.4020	<0.0001

Analysis of Variance:

Analysis of Variance:

	DF	SS	MS
Regression	3	7.8398	2.6133
Residual	22	0.0489	0.0022
Total	25	7.8887	0.3155

Corrected for the mean of the observations:

	DF	SS	MS	F	P
Regression	2	1.5986	0.7993	359.5946	<0.0001
Residual	22	0.0489	0.0022		
Total	24	1.6475	0.0686		

Statistical Tests:

Normality Test (Shapiro-Wilk) Passed (P = 0.1669)

W Statistic= 0.9423 Significance Level = 0.0500

Constant Variance Test Passed (P = 0.1632)

The statistical data for 1:1 S3:Hg(II) for **Figure A-93**.

Data Source: Data 2 in Titration spectra by Hg amount

Equation: User-Defined, 2:1 metal silole

$$f=(a+b*c*x^2)/(c*x^2+1)$$

R	Rsqr	Adj Rsqr	Standard Error of Estimate
0.9885	0.9771	0.9750	0.0414

	Coefficient	Std. Error	t	P
a	0.0274	0.0219	1.2534	0.2232
b	0.7248	0.0135	53.6986	<0.0001
c	4790953.0698753618.8449		6.3573	<0.0001

Analysis of Variance:

Analysis of Variance:

	DF	SS	MS
Regression	3	7.8510	2.6170
Residual	22	0.0378	0.0017
Total	25	7.8887	0.3155

Corrected for the mean of the observations:

	DF	SS	MS	F	P
Regression	2	1.6097	0.8049	468.6913	<0.0001
Residual	22	0.0378	0.0017		
Total	24	1.6475	0.0686		

Statistical Tests:

Normality Test (Shapiro-Wilk) Passed (P = 0.4004)

W Statistic= 0.9593 Significance Level = 0.0500

Constant Variance Test Passed (P = 0.1891)

The statistical data for 2:1 S3:Hg(II) for **Figure A-93**.

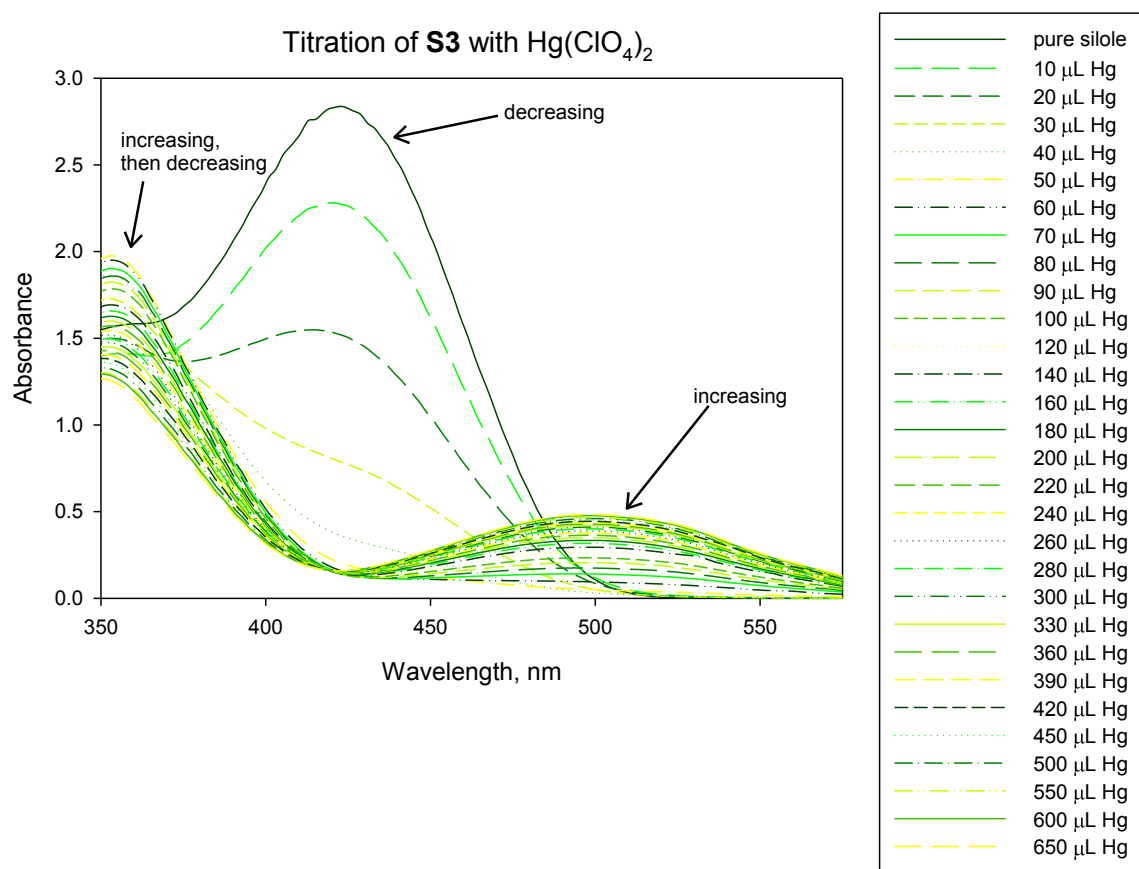


Figure A-94. The raw spectral data of titration of 1.5×10^{-4} M **S3** in THF with 1.5×10^{-2} M $\text{Hg}(\text{II})$ perchlorate solution (also in THF). Annotations are added to indicate the appearance or disappearance of absorption bands. The legend to the right lists the volume of $\text{Hg}(\text{II})$ solution added that corresponds to the line in the graph.

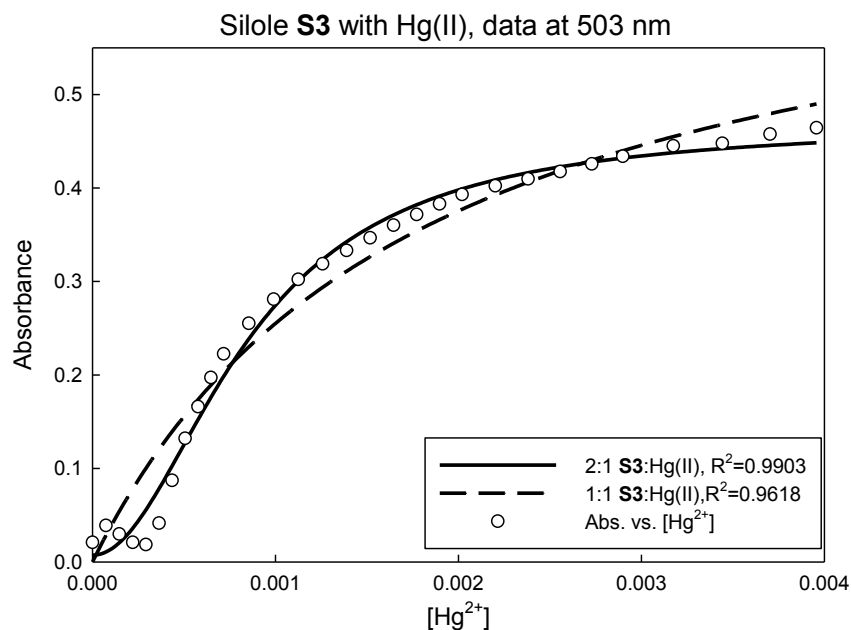


Figure A-95. The titration data extracted from the raw data (Figure A-94) at 503 nm. The total [Hg²⁺] was calculated from the initial volume of **S3** (3 mL), plus the volume added by the titrant (i.e., Hg(II) perchlorate in THF).

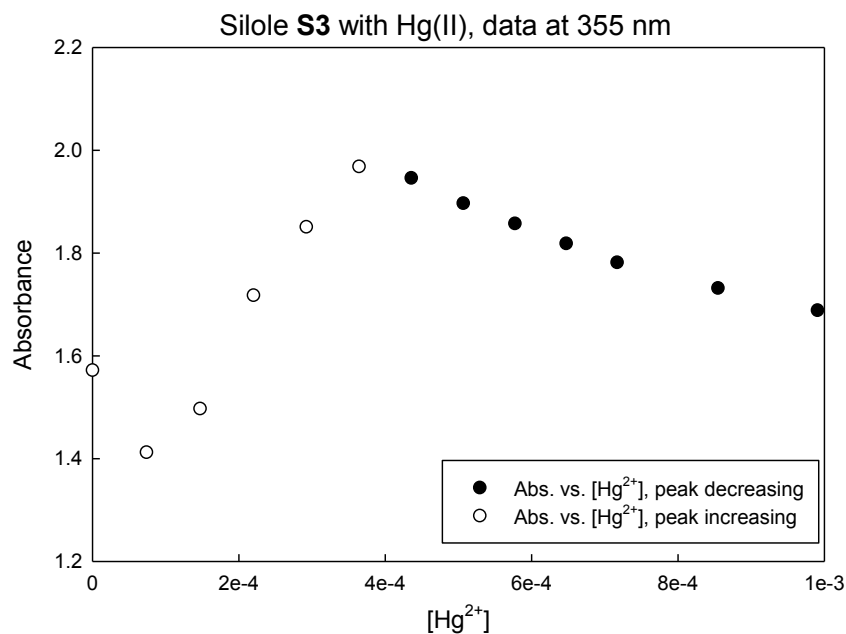


Figure A-96. The titration data extracted from the raw data (Figure A-94) at 355 nm. The total [Hg²⁺] was calculated from the initial volume of **S3** (3 mL), plus the volume added by the titrant (i.e., Hg(II) perchlorate in THF).

Data Source: Data 4 in titration data.JNB

Equation: User-Defined, 1:1 metal silole

$$f=(a+b*c*x)/(c*x+1)$$

R	Rsqr	Adj Rsqr	Standard Error of Estimate
0.9807	0.9618	0.9590	0.0320

	Coefficient	Std. Error	t	P
a	4.6791E-014	0.0191	2.4483E-012	1.0000
b	0.7111	0.0624	11.4026	<0.0001
c	559.4521	128.7124	4.3465	0.0002

Analysis of Variance:

Analysis of Variance:

	DF	SS	MS
Regression	3	2.9543	0.9848
Residual	27	0.0277	0.0010
Total	30	2.9820	0.0994

Corrected for the mean of the observations:

	DF	SS	MS	F	P
Regression	2	0.6981	0.3490	340.1205	<0.0001
Residual	27	0.0277	0.0010		
Total	29	0.7258	0.0250		

Statistical Tests:

Normality Test (Shapiro-Wilk) Failed (P = 0.0009)

W Statistic= 0.8572 Significance Level = 0.0500

Constant Variance Test Failed (P = 0.0142)

The statistical data for 1:1 **S3**:Hg(II) for **Figure A-95**.

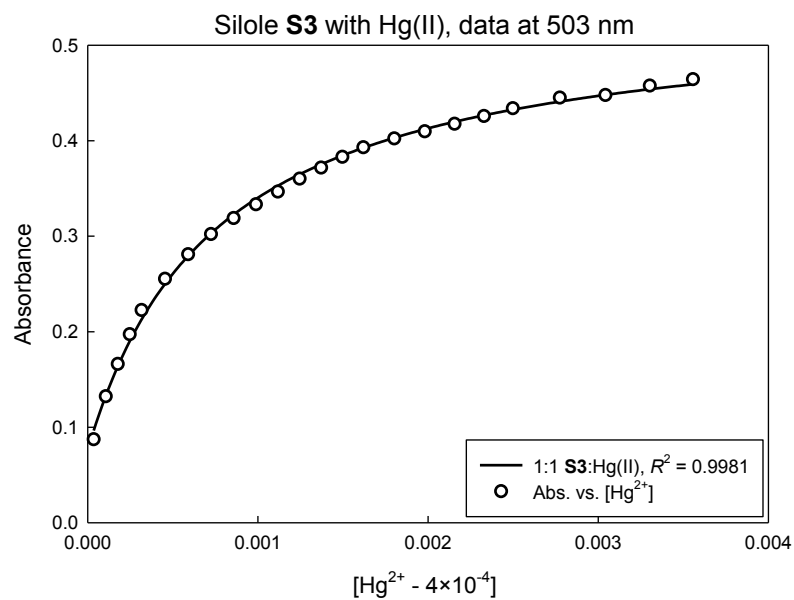
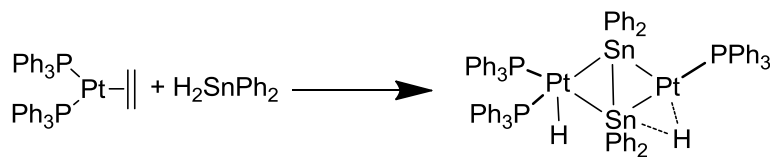


Figure A-97. The plot of absorbance versus the concentration of Hg(II), after subtracting 4×10^{-4} M to account for the previously coordinated Hg(II) (see Section 3.5.2).

Chapter 6. Addendum: Platinum and Palladium complexes for use as Precursors for M-Sn nanoparticles.

6.1. Background

Prior to our interest in the coordinative abilities of siloles, our group desired to make preformed complexes containing platinum and tin, with the intention to thermolyze these complexes, which would remove the light atoms from the ligands, and thus leaving behind PtSn nanoparticles that would have the exact Pt:Sn stoichiometry of the complex prior to thermolysis. These nanoparticles, with ideally a more homogenous distribution than standard syntheses, were then to be tested as a material for use in a methanol fuel cell, as tin added to platinum helps to mitigate the poisoning of the fuel cell, compared to just using platinum.¹ Some initial studies of the reaction of a platinum(0) complex with diphenylstannane yielded a complex similar to silicon-platinum dimers studied by our group and others (Scheme 6-1).²



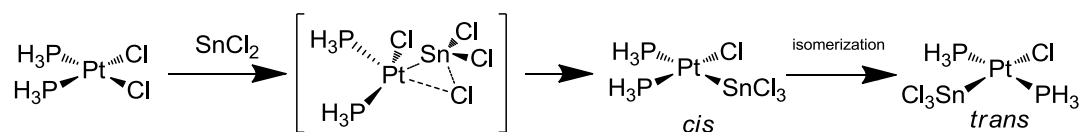
Scheme 6-1. The complex synthesized for preliminary thermolysis studies.

Thermolysis of the preformed catalyst showed the formation of PtSn nanoparticles, but the particles were only part of a non-homogenous distribution. Therefore, we desired to make platinum or palladium complexes containing tin in multiple geometries, in order to assess the performance of these complexes or clusters for homogeneity on thermolysis. Several different routes are described in this section, with an informal description of their synthesis, isolation and characterization of any products formed.

6.2. Insertion of tin chloride into a platinum or palladium-chloride bond

6.2.1. Introduction

One of the most facile ways to generate platinum-tin precursors is through the insertion of tin(II) chloride into a platinum-chloride bond. Interest in this reaction extends back many years, ever since the discovery that tin(II) chloride greatly accelerated the carbonylation of aryl- and alkyl-platinum chloride complexes.³ Holt *et al.* published a comprehensive review of transition metal-tin chemistry, of which insertion of tin(II) chloride into many types of bonds is discussed at length.⁴ The mechanism for insertion of tin into platinum-chloride bonds in particular was not elucidated until several years later, with Rocha and De Almeida performing an *ab initio* study of tin(II) chloride insertion into the *cis*-Pt(PH₃)₂Cl₂. They found that the transition was a 3-membered intermediate of the tin, platinum,⁵ and chloride bonds, with the chloride bonds of the tin(II) pointed away from the platinum in the transition state. As others have noted,⁴ the theoretical investigation revealed the resultant trichlorostannyl- ligand to be a strong *trans*-director, more so than even the phosphine, as the molecule was found to easily isomerize into the *trans*-isomer.⁵ A depiction of this process is shown in Scheme 6-2.

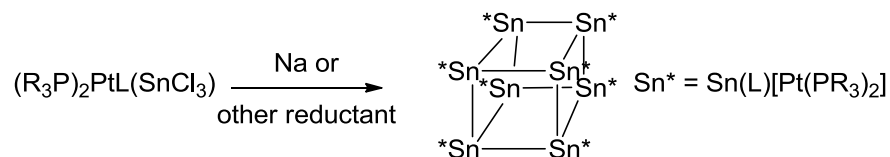


Scheme 6-2. The mechanism of insertion of tin(II) chloride into the Pt-Cl bond.⁵

6.2.2. Synthetic efforts with tin(II) chloride insertion.

Our own efforts into research on insertion reactions to generate trichlorostannyl-ligated metal centers began with preformed platinum chloride complexes, generously donated by Anderson's group. We desired to synthesis trichlorostannyl-platinum

complexes as a potential precursor for generation of stannacubane structures (Scheme 6-3), via a Wurtz-type coupling reaction with sodium or other reductant.



Scheme 6-3. Our planned reaction sequence upon isolation of a trichlorostannyl-platinum complex.

One of the first reactions attempted was with *trans*-bis(tricyclohexylphosphine)-platinum(II) chloride. Initially, we attempted the reaction with two equivalents of tin(II) chloride per equivalent of metal complex (i.e., one tin chloride for each Pt-Cl bond). $^{31}P\{^1H\}$ NMR analysis of this mixture indicated only trace amounts of the product may have formed, with the vast majority being starting material. Momeni *et al.* reported that the insertion of tin(II) chloride is actually *reversible*; even at up to five equivalents of tin(II) chloride to $(Ph_3P)_2PtCl_2$, some evidence of the platinum complex starting material is apparent in solution.⁶ Use of acetone or other oxygen containing solvent caused even further dissociation.^{6b}

Later attempts at this insertion reaction involved use of *trans*- $(Ph_3P)_2Pt(H)Cl$. It was initially thought that having only one chloride in the complex might make identification of products easier, as well as make the reaction kinetics more straightforward. Another advantage of this system was the platinum hydride; being the only environment upfield in the 1H NMR, it provided a rather isolated handle to monitor reaction progress. Though several equivalents were again needed to ensure complete conversion, the hydride signal showed both the $^2J_{P-H}$ and $^1J_{Pt-H}$. Though there are two NMR active nuclei for tin (^{117}Sn

and ^{119}Sn , 7.68% and 8.59% abundance, respectively), the coupling constant was too small at two bonds to measure. Figure 6-1 shows the ^1H NMR of the trichlorostannyl product in the hydride region, exhibiting the satellites explained above.

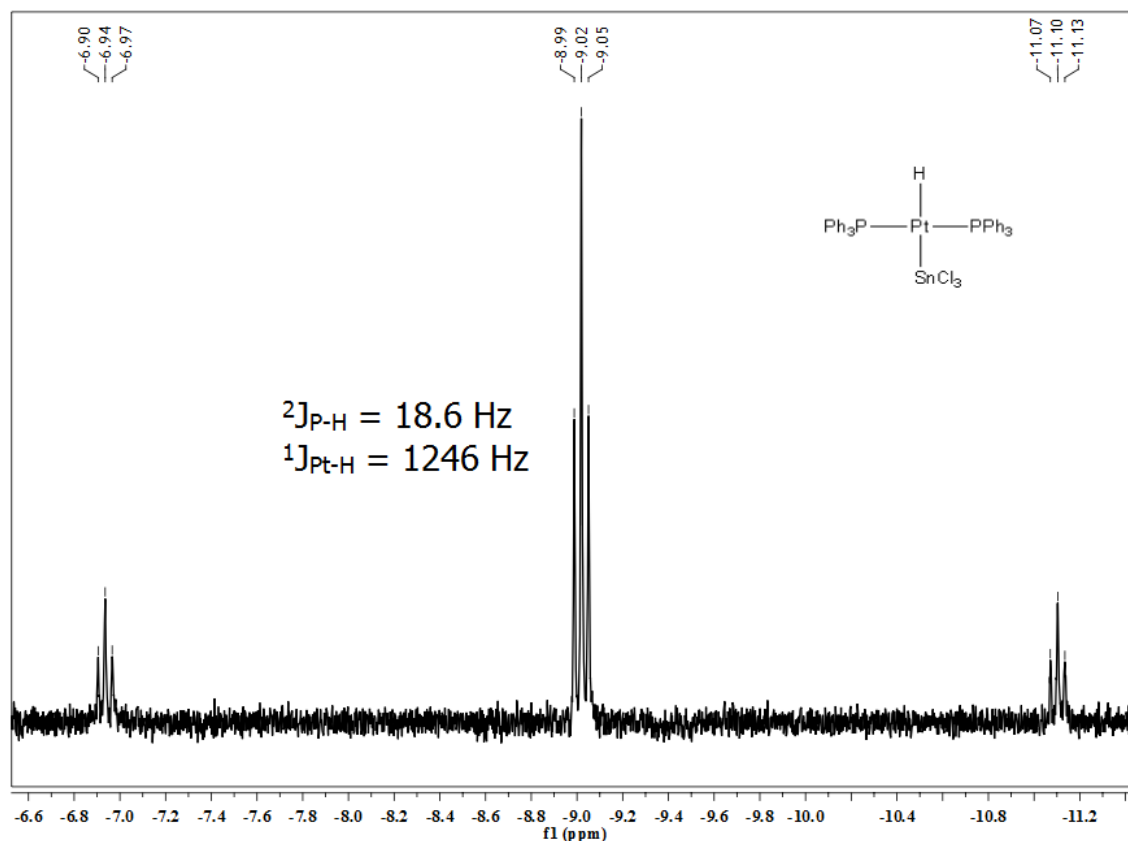


Figure 6-1. The hydride region of the product of $\text{trans}-(\text{Ph}_3\text{P})_2\text{Pt}(\text{H})\text{Cl}$ and tin(II) chloride. The structure and coupling constants are inset.

The prior reactions both needed significant excesses of tin(II) chloride in order to ensure full conversion to the trichlorostannyl complex. This would obviously complicate subsequent Wurtz type reactions, but attempts to purify the complexes from the excess tin(II) chloride by, e.g., recrystallization failed; generally the only crystalline product obtained was the starting material, possibility due to the reversibility of the insertion.

Therefore, we decided to try a new system. Desirable properties of this system would include: only one equivalent of tin(II) chloride, the insertion reaction would be relatively irreversible, other ligands at the metal center would make the overall complex neutral (for subsequent Wurtz reactions), and a good yield, if possible. The system that was then investigated was (Fmes)Pd(COD)Cl,⁷ where Fmes = 2,4,6-tris(trifluoromethyl)phenyl-. The Fmes ligand was found to have significant hypercoordinate stabilizing ability, via the pendant fluorides, for a series of group 14 halide complexes.⁸ Indeed, the authors of the Fmes-palladium paper also indicate such effects through crystal structures obtained.⁷ It was thought that these assisting properties of the ancillary fluorides might help to strengthen the Pd-Sn bond through an inductive effect. The authors also report the syntheses of Fmes-Pd complexes with (phosphine)PdCl₂ complexes; however, the synthesis usually have both Fmes and bis(Fmes) palladium complexes as products, which are difficult to separate. On the other hand, the (Fmes)Pd(COD)Cl species could be synthesized as only the mono-Fmes species, due to the relative bulkiness of cyclooctadiene.⁷ An additional benefit of this system is the fluorine atoms on the Fmes, which provide an isolated environment to monitor products by ¹⁹F{¹H} NMR spectroscopy.

The generation of the requisite lithiated Fmes species is straightforward: to one equivalent of 1,3,5-tris(trifluoromethyl)benzene in dry diethyl ether is added slightly less than one equivalent of *n*-BuLi at -78 °C. It is important to use an excess of FmesH, as using an excess of BuLi might cause explosive formation of LiF.⁹ The resulting lithiated Fmes is combined with 0.5 equivalents of (COD)PdCl₂, reacted for 2 h, and the solvents were removed under reduced pressure. The residue was extracted with dichloromethane,

and hexanes were added. Cooling in a $-20\text{ }^{\circ}\text{C}$ freezer gave a light yellow solid in low yield (20 %).

Once the (FMes)Pd(COD)Cl product was confirmed by ^1H and $^{19}\text{F}\{^1\text{H}\}$ NMR spectroscopy, it was then reacted with 2 equivalents of tin(II) chloride. A $^{19}\text{F}\{^1\text{H}\}$ NMR spectrum of the resulting solid shows both the *ortho* and *para* trifluoromethyl positions, with the *ortho* positions exhibiting $^5\text{J}_{\text{Sn-F}}$ coupling at 80 Hz (Figure 6-2).

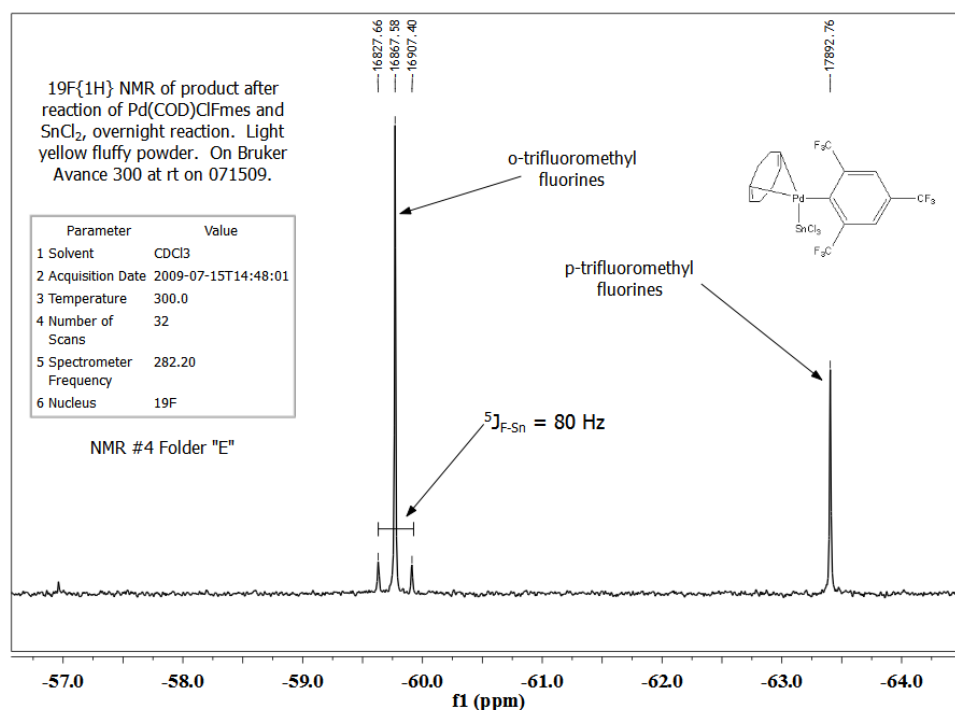


Figure 6-2. $^{19}\text{F}\{^1\text{H}\}$ NMR spectrum of (FMes)Pd(COD)Cl.

The above reaction still required an excess of tin(II) chloride, but the identification of the products was relatively straightforward due to the fluorine NMR analysis. An exchange of the cyclooctadiene ligand with phosphine was attempted, but for unknown reasons, the product appeared to have decomposed, giving a mixture by NMR analysis.

6.2.3. Summary

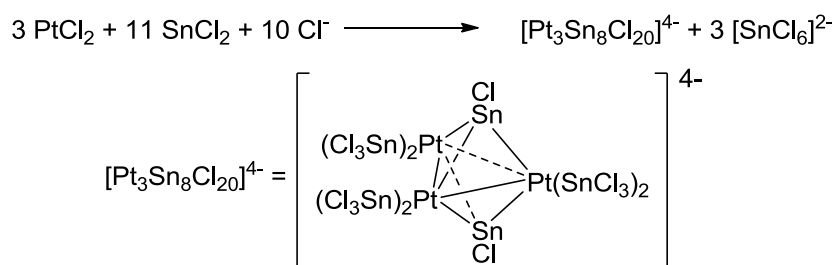
The insertion reaction of tin(II) chloride with a range of complexes was attempted. For all species examined, an excess of tin(II) chloride was necessary in order to realize full conversion to the trichlorostannyl-metal complexes. This has the downside of limiting the utility of any trichlorostannyl-complex formed due to the contamination and difficult removal of excess tin(II) chloride. Future reactions in this regard would have to find systems where the insertion is irreversible, and only one equivalent of tin(II) chloride per metal-chloride bond, to ease purification. Another issue possibly complicating the research is the relative lability of the trichlorostannyl- ligand; this is especially true for platinum complexes.⁴ Thus, a method of developing strong platinum-tin bonds for this ligand would also be necessary.

6.3. Attempted preparation of platinum-tin halide clusters.

6.3.1. Introduction

Another avenue that was explored for the preparation of appropriate precursors for thermolysis was to synthesize platinum-tin clusters, which researchers have studied even before the single insertion of tin(II) chloride.¹⁰ Generally, a platinum salt (Pt(II) or Pt(IV)) complex was reacted with tin(II) chloride in a hydrochloric acid solution or acetone. Then, a bulky neutral ligand or bulky cation was added (such as tetralkylammonium or tetraarylphosphonium salts), based on the charge of the platinum-tin clusters generated.^{10,11} Species generated from these reactions were usually complex, and were highly dependent on the concentrations of the reagents, and the concentration of the acid, if the reaction was performed in acidic media.^{11a} Nevertheless, researchers were at times able to isolate the main species of a reaction mixture for further analysis. For

example, Lindsey reported the reaction of platinum(II) chloride and tin(II) chloride in acetone under an inert atmosphere, which after reaction with tetraethylammonium chloride precipitated out a residue identified as tetraethylammonium hexachlorostannate(IV), and evaporation of the extracts from the above solid yielded a triplatinum compound, assigned as $[(\text{NEt}_4)]_4[\text{Pt}_3\text{Sn}_8\text{Cl}_{20}] \cdot (\text{acetone})$ based on EA and IR analysis. The reaction is shown in Scheme 6-4. Based on the products isolated, the tin(II) chloride participates in a redox reaction to generate the platinum-tin cluster and the hexachlorostannate(IV) anion.¹⁰



Scheme 6-4. The balanced redox reaction of platinum(II) chloride and tin(II) chloride to form the triplatinum-tin cluster.¹⁰

6.3.2. Attempted synthesis of a platinum tin cluster.

Four our research into platinum-tin clusters, an attempt to reproduce the reactions of Lindsey *et al.* was performed (Scheme 6-4). Thus, platinum(II) chloride was combined with tin(II) chloride in acetone under argon overnight, followed by filtration of the red solution directly into a degassed ethanol solution of tetraethylammonium chloride. Several attempts produced no discernible reaction products; however, using a different sample of platinum(II) chloride allowed for the exothermic behavior on combination with tin(II) chloride at the beginning of the reaction, as noted in the literature.¹⁰ Attempted workup of the latter reaction yielded a brown residue, which was recrystallized from

acetone to give light brown crystalline blocks; these were analyzed by powder XRD to be the hexachlorostannate(IV) salt. Evaporation of the supernatant yielded additional crystalline material that was analyzed by $^{119}\text{Sn}\{^1\text{H}\}$ NMR spectroscopy, and is shown in Figure 6-3. The splitting pattern does not look like the one expected for three platinum centers contained in a single complex, as the coupling constants are small and not of the correct intensity ratio, except for the first obvious coupling constant at 16 kHz ($^1J_{\text{Pt-Sn}}$). It was suspected that this species could simply be a monomeric $[\text{Pt}(\text{SnCl}_3)_x]^{n-}$ complex based on the splitting pattern observed.

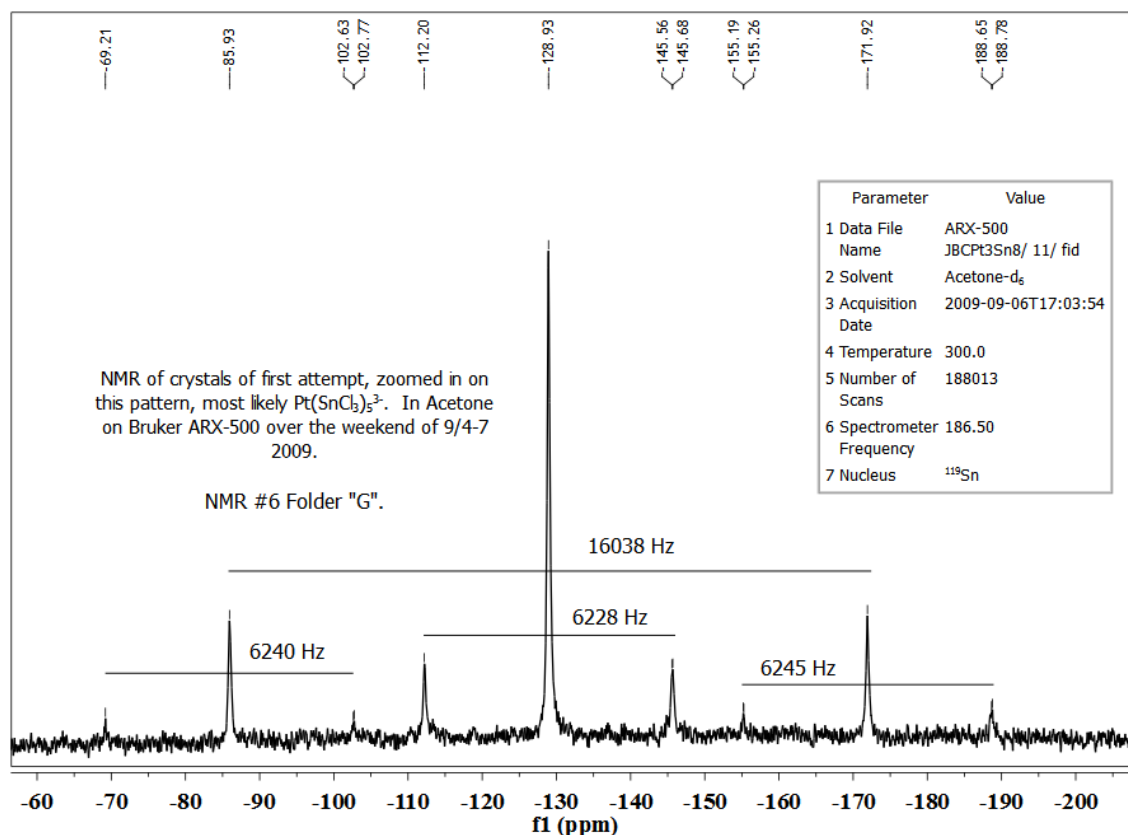


Figure 6-3. The $^{119}\text{Sn}\{^1\text{H}\}$ NMR spectrum of the crystalline species obtained from the reaction mixture reported in this section.

It was first suspected that the signals were due to the formation of $[\text{Pt}(\text{SnCl}_3)_4]^{2-}$, however the coupling constants reported for that complex are significantly different than the constants observed here, and are 30 kHz and 1835 Hz for the $^1J_{\text{Pt-Sn}}$ values and the $^2J_{\text{Sn-Sn}}$ values, respectively.¹²

After further research, the complex that most closely matched the splitting pattern and coupling constants observed was actually the five-coordinate $[\text{Pt}(\text{SnCl}_3)_5]^{3-}$ complex.¹³ The literature values for the coupling constants are 16 kHz and 6230 Hz for the $^1J_{\text{Pt-Sn}}$ values and the $^2J_{\text{Sn-Sn}}$ values, respectively, which is almost an exact match for the data in Figure 6-3; however, the literature reports a shift of -387 ppm from tetramethylstannane, while we report a shift of -128 ppm. This shift difference could be due to a calibration error on either machine, or both, but the splitting pattern and coupling constants are almost identical, therefore, our assignment is for the 5-coordinate trichlorostannylplatinate complex.

6.3.3. Summary

An attempt was made to replicate some prior work with platinum-tin clusters in order to evaluate their effectiveness for generating PtSn nanoparticles; the work was chosen for the relative simplicity of the reagents and conditions. Though the reaction observations matched literature reports on both the color of the solution and the exotherm that developed, the only isolable species were the hexachlorostannate(IV) salt and the pentakis(trifluorostannyl)platinate(II) complex. Further attempts at the reaction will likely have to investigate variations of caution with respect to the inert atmosphere, as well as assessing the purity of the reagents used.

-
- (1) (a) Hampson, N. A.; Willars, M. J.; McNicol, B. D. *J. Power Sources* **1979**, *4*, 191–201; (b) Wasmus, S.; Küver, A. *J. Electroanal. Chem.* **1999**, *461*, 14–31; (c) Alonso-Vante, N. *Fuel Cells* **2006**, *6*, 182–189; (d) Antolini, E. *Appl. Catal. B-Environ.* **2007**, *74*, 337–350.
 - (2) (a) Corey, J. Y.; Braddock-Wilking, J. *Chem. Rev.* **1999**, *99*, 175–292; (b) Corey, J. Y. *Chem. Rev.* **2011**, *111*, 863–1071.
 - (3) Anderson, G. K.; Clark, H. C.; Davies, J. A. *Organometallics* **1982**, *1*, 64–70.
 - (4) Holt, M. S.; Wilson, W. L.; Nelson, J. H. *Chem. Rev.* **1989**, *89*, 11–49.
 - (5) Rocha, W. R.; De Almeida, W. B. *Int. J. Quantum Chem.* **1997**, *65*, 643–650.
 - (6) (a) Momeni, B. Z.; Baleh, L. J.; Hamzeh, S.; Rominger, F. *J. Coord. Chem.* **2007**, *60*, 285–293; (b) Momeni, B. Z.; Moradi, Z.; Dianati, L.; Shahverdi, K. *J. Coord. Chem.* **2009**, *62*, 465–474.
 - (7) Bartolomé, C.; Espinet, P.; Villafañe, F.; Giesa, S.; Martín, A.; Orpen, A. G. *Organometallics* **1996**, *15*, 2019–2028.
 - (8) Batsanov, A. S.; Cornet, S. M.; Dillon, K. B.; Goeta, A. E.; Thompson, A. L.; Xue, B. Y. *Dalton Trans.* **2003**, 2496–2502.
 - (9) Cornet, S. M.; Dillon, K. B.; Entwistle, C. D.; Fox, M. A.; Goeta, A. E.; Goodwin, H. P.; Marder, T. B.; Thompson, A. L. *Dalton Trans.* **2003**, 4395.
 - (10) Lindsey, R. V.; Parshall, G. W.; Stolberg, U. G. *Inorg. Chem.* **1966**, *5*, 109–110.
 - (11) (a) Yurchenko, E. N. *Koordinats. Khim.* **1980**, *6*, 1731–1736; (b) Fässler, T. F.; Hoffmann, R. *Angew. Chem. Int. Ed.* **1999**, *38*, 543–546; (c) Tristram Chivers; Dana J. Eisler In *Tin Chemistry: Fundamentals, Frontiers, and Application*; Marcel Gielen, Ed.; John Wiley & Sons, Inc., 2008; pp. 53–67.
 - (12) Yamakawa, T.; Moriyama, H.; Shinoda, S.; Saito, Y. *Inorganic Chemistry* **1987**, *26*, 3347–3353.
 - (13) Nelson, J. H.; Alcock, N. W. *Inorganic Chemistry* **1982**, *21*, 1196–1200.